Synthesis, characterisation and transfer of CVD graphene for high-resolution structural analysis and surface force measurements



Judy L. Britton

St. Cross College

Department of Materials, University of Oxford

DPhil Materials

Trinity Term 2015

Supervisors: Dr. Rebecca Nicholls & Prof. Nicole Grobert

Declaration

I confirm that the work presented in this thesis is my own. Where I have consulted the work of others, it has been clearly stated.

Abstract

This thesis describes an alternative approach to graphene research. It puts forward that the concept of graphene as a “miracle” material largely differs from the reality. The thesis describes high-resolution characterisation of commonly seen imperfections in graphene and a new application for graphene that overcomes such defects.

The thesis is divided into two main areas; high-resolution transmission electron microscopy (HRTEM) characterisation of naturally occurring defects in CVD graphene; and the synthesis and transfer of CVD graphene for the creation of the first graphene surface force balance (gSFB). The HRTEM work focuses on the thorough characterisation of "real" graphene and hence analyses the quality of the graphene that is likely to be used in research laboratories and industry. The creation of the gSFB has not only provided an instrument for novel surface force measurements of graphene but has also provided a new ultra-smooth transfer technique which can be further used elsewhere. The work undertaken in both of these areas is beneficial, not solely in graphene terms, but also for other 2D materials. For example, the gSFB has the potential to be altered to measure 2D chalcogenides and hBN interactions, and similar high-resolution characterisation of common defects in other 2D materials will also provide information on their synthesis, transfer and hence feasibility of industrial production. The research in this thesis is positioned between the pristine, flawless graphene portrayed in the literature, and the real material which will eventually be used in applications on the larger scale.

Acknowledgements

This thesis would have not been possible without many people. To those people, I give my biggest thanks and appreciation.

Firstly, to my supervisors Dr. Rebecca Nicholls and Prof. Nicole Grobert. To Nicole, for giving me the opportunity to join the department, for bringing the best out in me and giving me confidence. To Becs, for taking me on and putting up with trigonometry discussions, endless TEM images and PhD planning.

To the Engineering and Physical Sciences Research Council for their funding of my Doctoral Training Award studentship.

To my research group; for their advice, discussion and entertaining lunches. Specifically to Juan, Adrian, Nataliia and Madhuri. To my collaborators in chemistry: Dr. Susan Perkin and her research group. Specifically to Nico and Christian for making PhD research that much more music filled.

To the technical support who make everything work. Notably to Greg and Gabriella for fruitful discussions and microscope fixes. To Judy Kim for TEM training, great ideas and optimism in times of beam-loss.

To my all my amazing friends in Oxford. Especially to Caro, Soph, Emma and Jess for making our homes the best places to live. Finally, to Mum, Dad, Laura and George, for your love and support throughout a long 4 years.

Thesis work contributions

Talks

"A graphene surface force balance" (Symposium of 2D Materials for Optoelectronics, Plasmonics and Photonics Grasmere, 2014)

"Ultra-flat transfer of CVD graphene for surface force measurements" (TMS 2014, San Diego, USA)

"Atomic resolution imaging of tungsten chalcogenide nanowires" (TMS 2014, San Diego, USA)

"Overcoming the challenges of up-scaling CVD graphene" (NanoteC 2013, Surrey, UK)

"Challenges to overcome for CVD graphene composites" (Department of Materials, University of Oxford, 2012)

Papers

"Rapid epitaxy-free graphene synthesis on silicidated polycrystalline platinum" (Nature Communications, 2015)

"A graphene surface force balance" (Langmuir, 2014)

"WS_2 2D nanosheets in 3D nanoflowers" (Chemical Communications, 2014)

"Thoughts on an education": Contribution to feature piece (Nature Nanotechnology, 2013)

"Probing the bonding in nitrogen-doped graphene using electron energy loss spectroscopy" (ACS Nano, 2013)

"*In situ* engineering of NanoBud geometries" (Chemical Communications, 2013)

Press releases

"Ultraflat transfer method for graphene surface force balance", Nanowerk Spotlight (Nanowerk, 2014)

Thesis work contributions cont...

Awards

5-Year Teaching Fellowship – Centre for Doctoral Training in Diamond Science and Technology, University of Warwick (2014) *Offered, not accepted.*

Best Junior Speaker - Symposium of 2D Materials for Optoelectronics, Plasmonics and Photonics , The Rank Prize Funds (2014)

Outstanding Outreach Contribution – Mathematical, Physical and Life Sciences Division, University of Oxford (2014)



Figure 1) Graphene brownie.

Table of Contents

Declaration ii
Abstract iii
Acknowledgements iv
Thesis work contributions v
Glossary 11
Preface 12
1 Introduction 14
1.1 Introductory literature review 14
1.1.1 What is Graphene? 14
1.1.2 The case for few-layer graphene 16
1.1.3 Synthesising graphene 16
1.2 Current outlook of CVD graphene 20
1.3 Conclusion and thesis aims 23
2 Experimental techniques & preliminary results 25
2.1 Part I: CVD & general graphene characterisation 25
2.1.1 Introduction to CVD of graphene 25
2.1.1.1 CVD Experimental 27
2.1.2 Graphene characterisation 29
2.1.2.1 Scanning electron microscopy 30
2.1.2.2 Raman spectroscopy 31
2.1.2.3 Atomic force microscopy 32
2.1.2.4 Electron back scattered diffraction 33
2.1.2.5 Energy dispersive X-ray analysis 33
2.1.3 Preliminary results 33
2.1.3.1 Controlling graphene synthesis 35
2.2 Part II: HRTEM & graphene transfer 42
2.2.1 Introduction to TEM 42
2.2.1.1 The benefits of TEM over STEM 43
2.2.2 CVD graphene transfer 44
2.2.2.1 Example transfer to silicon and other hard substrates 44
2.2.2.2 Transfer for TEM 46
2.2.3 Background to HRTEM 47
2.2.3.1 Aberration correction and monochromator use 50

2.2.4 HRTEM imaging of graphene 51
2.2.4.1 HRTEM experimental details 51
2.2.4.2 Common challenges in graphene imaging 52
2.2.4.3 Interpreting HRTEM Graphene Data 56
2.2.4.4 Accuracy and error in data collection from TEM images and FFTs 60
2.3 Summary 62
3 HRTEM of imperfect CVD graphene: Part I 63
3.1 Introduction 63
3.1.1 Motivation 63
3.1.1.1 Background literature 64
3.2 TEM imaging of imperfect graphene 67
3.2.1 Overlapping areas 68
3.2.2 Folded wrinkles 69
3.2.3 Simple wrinkle contrast 75
3.2.4 Periodicity along graphene planes 76
3.2.5 Sideline periodicity 78
3.2.6 Inter-graphitic plane contrast 83
3.2.7 Linear moiré patterns 86
3.3 Summary 99
4 HRTEM of imperfect CVD graphene: Part II 101
4.1 Imperfect domain boundaries 101
4.1.1 Introduction and motivation 101
4.1.2 Determining a grain boundary 106
4.1.3 Experimental observations of imperfect domain boundaries 108
4.1.3.1 Example 1 108
4.1.3.2 Example 2 109
4.1.3.3 Example 3 – Introducing overlapping domains 114
4.1.3.4 Example 4 120
4.1.3.5 Example 5 124
4.1.4 Summary 129
4.2 Part I and Part II summary 131
5 HRTEM of imperfect hBN 133
5.1 Introduction 133
5.2 HRTEM analysis of hBN 137
5.2.1 Sample synthesis and TEM grid preparation 137

5.2.2 HRTEM characterisation 138
5.2.3 HRTEM defect contrast in hBN 141
5.2.4 hBN imperfect domain boundaries 145
5.3 Summary 147
6 Graphene surface force balance development 149
6.1 An introduction to a surface force balance 149
6.1.1 Multiple beam interferometry 151
6.1.2 A SFB with surface potential control 156
6.2 Approach 1: Few-layer graphene synthesis and direct epoxy transfer 159
6.2.1 Few-layer graphene synthesis 159
6.2.2 Polymer epoxy transfer to SFB lenses 160
6.3 Approach 2: Graphene synthesis on thin films 162
6.3.1 Substrate preparation 163
6.3.2 Graphene growth 166
6.4 Approach 3: Substrate Electropolishing 177
6.4.1 Graphene growth on electropolished foils 179
6.5 Approach 4: Substrate pressing 181
6.5.1 Substrate preparation 181
6.5.2 Graphene growth on pressed substrates 183
6.6 Overall analysis of Approaches 1-4 for SFB modification 186
6.7 Approach 5: New ultra-flat transfer technique 188
6.7.1 Ultra-flat transfer of FLG 188
6.8 SFB results 193
6.8.1 Proof-of-principle experiment 193
6.8.2 SFB Summary 196
6.9 Chapter summary 197
6.10 Experimental details 197
6.10.1 General graphene synthesis via CVD 197
6.10.2 Cu/Mica substrate preparation 198
6.10.3 Cu pressing 198
6.10.4 Cu electropolishing 198
6.10.5 Ultra-flat transfer of CVD graphene from Cu foils onto glass/Ag lenses 198
6.10.6 SFB measurements 199
7 Further work 201
7.1 Further experiments 201

7.1.1 Graphene daggers investigation 201
7.1.2 Graphene synthesis analysis using ultra-flat transfer 202
7.1.3 Graphene/hBN HRTEM further work 203
7.1.4 Thin film synthesis - Solid precursor investigation 203
7.1.5 Hot-pressing Cu 205
7.1.6 Graphene SFB investigations 205
7.2 Broader outlook 206
7.2.1 Overlooked parameters 206
7.2.2 Other 2D nanomaterials 206
7.3 Concluding remarks 207
8 List of Figures/Tables 208
9 Appendix 216
9.1 Appendix A: Further explanations of experimental techniques 216
9.2 Appendix B: NanoBud publication 220
9.3 Appendix C: Five further examples of imperfect merging domains 223
9.4 Appendix D: Additional information from Chapter 6: Approach 2: Cu/mica thin film synthesis 226
9.5 Appendix E: gSFB publication 237
10 References 245

Glossary

AFM: atomic force microscopy

BSE: back scattered electrons

CNT: carbon nanotube

CVD: chemical vapour deposition

DI: de-ionised water

EBSD: electron back scattered diffraction

EDL: electrical double layer

EDX: energy dispersive X-ray analysis

FFT: fast-Fourier transform

FLG: few-layer graphene

gSFB: graphene surface force balance

hBN: hexagonal boron nitride

HRSTEM: high-resolution scanning transmission electron microscopy

HRTEM: high-resolution transmission electron microscopy

RMS: root mean squared

SEM: scanning electron microscopy

SFB: surface force balance

STEM: scanning transmission electron microscopy

STM: scanning tunnelling microscopy

SWNT: single-wall nanotube

TEM: transmission electron microscopy

TMC: transition metal dichalcogenide

Preface

This thesis is largely split into two sections; high-resolution characterisation (Chapters 3-5) and the creation of the graphene surface force balance (the larger Chapter 6). Chapters 1 and 2 are introductory chapters that also contain some preliminary results. Due to the nature of the work in this thesis, specific literature reviews have been included at the beginning of the relevant chapters rather than a larger literature review in Chapter 1. To communicate the structure of the thesis, brief chapter outlines are as follows:

- Chapter 1: Introduction - an introductory literature review of the broader graphene field to present both the driving force behind the work and the key aims of the thesis.

- Chapter 2: Experimental techniques & preliminary results - an outline of the relevant experimental techniques that have been used in this thesis. Some preliminary results have been introduced in this chapter to enable easier understanding of results in subsequent chapters. It will include a HRTEM section which will detail how HRTEM has been used in this thesis including data interpretation and experimental techniques specifically related to graphene samples.

- Chapter 3: HRTEM of imperfect CVD graphene Part I – the first results chapter introducing the high-resolution characterisation of CVD graphene. Results in this chapter steadily build in complexity to ensure that methods of interpretation are understood.

- Chapter 4: HRTEM of imperfect CVD graphene Part II – the second results chapter focussing on five examples of imperfect domain boundaries in CVD graphene. Results in this chapter use methods of interpretation related to previous observations outlined in Chapter 3.

- Chapter 5: HRTEM of hBN – the final HRTEM results chapter which mimics the characterisation used for graphene for CVD hBN.

- Chapter 6: Graphene surface force balance development – the largest results chapter outlining the experiments and results that lead to the development of the graphene surface

force balance. This was kept as one chapter to ensure the key aims and explanations were not lost when dividing the work into smaller sections.

- Chapter 7: Further work – a summary of some future experiments that could be taken forward from the results in all chapters of this thesis followed by some concluding remarks.

1 Introduction

This chapter introduces the key literature surrounding the field and outlines the driving force behind the research described in this thesis. Subsequent chapters will contain more specific literature reviews therefore this chapter will broadly describe the importance and capabilities of graphene together with the holes in the research where this thesis is aimed.

1.1 Introductory literature review

1.1.1 What is Graphene?

Monolayer graphene is a one atom thick honeycomb network of carbon atoms and is the thinnest known material ever produced[1]. Until recently, graphene was presumed to be too unstable to exist due its delicate 2D nature and the spontaneous formation of related carbon derivatives such as carbon nanotubes (CNTs) and fullerenes[2–4]. The term "graphene" was merely used as a term to explain such structures, it being the fundamental building block of fullerenes, CNTs and graphite (Figure 2). However, since its unequivocal isolation in 2004 by Novoselov *et al.*[2], research into graphene and its relatives has grown exponentially. This has ensured that over just 10 years, research into this area has uncovered a wealth of information about a material that had originally been deemed too unstable to exist.

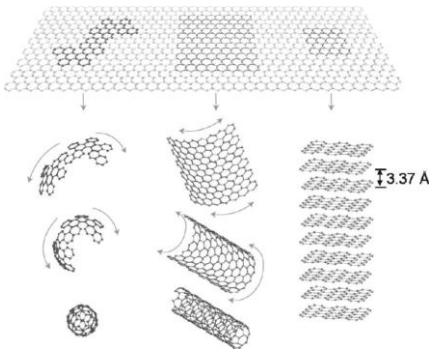


Figure 2) Graphene is viewed as the building block of other carbon nanomaterials such as fullerenes, CNTs and graphite. Reproduced with permission from ref[5]

In this thesis, the term "graphene" in general will be defined as <10 layers of the monolayer material, as after >10 layers properties start to mimic bulk graphite[6,7]. Few-layer graphene

(FLG) typically refers to between 3-10 layers[8]. Graphene therefore exhibits strong covalent bonding between the sp^2 hybridised carbon atoms and weak van der Waals interactions between graphene layers[9].

Graphene has been shown to exhibit hugely interesting and diverse properties. As well as its impressive strength[10], monolayer graphene is impermeable to almost all gases[11] and has a thermal conductivity even higher than that of copper[12]. Its zero band gap ensures its unique "massless" dirac fermions[13] conduct electricity with an unrivalled carrier mobility[14]. In addition to this ballistic conduction, graphene also exhibits a room temperature quantum hall effect[15], an ambipolar field effect[2], and demonstrates a breakdown of the adiabatic Born-Oppenheimer approximation[16,17]. Additionally, it is optically transparent[18] and flexible, displaying even elastic properties[6].

These properties have made graphene a target for applications in areas spanning throughout all science disciplines such as: field effect transistors[19–26], transparent electrodes[27–32], transparent gas barriers[33–36], light absorbers in solar cells[37–40], energy storage[41–45], and enhancement of mechanical properties of other materials[46–48]. Furthermore, graphene also has the ability to detect single molecular signals making it ideal for new sensor technology[49]. Moreover, graphene has been shown to shield from electromagnetic radiation[50], to harvest energy from water flow[51] and can be used in the production of both corrosion protective coatings[52] and conductive inks[53]. CVD graphene has also been speculated to be a prime material to replace indium tin oxide (ITO) as a cheaper and more widely available version of transparent, conducting electrodes[29,30].

However, since the publication by Novoselov *et al.* in 2004, a primary focus of graphene research has still been its synthesis. Graphene sales were predicted to grow from $196,000 in 2008 to $59 million in 2015[54]. But as yet, a full proof synthesis method has not been defined. Investigations to find a method to reliably synthesise graphene with the desired properties, whilst still ensuring a feasible scale up are still ongoing.

1.1.2 The case for few-layer graphene

It could be argued that for applications, few-layer graphene is more useful to industry than monolayer graphene[55]. Although monolayer graphene exhibits remarkable properties, it has been shown that FLG may be more useful in the fabrication of devices. It has been reported that FLG can exhibit electronic properties comparable to those of monolayer graphene[56–60]. Additionally, increasing layers of graphene has been shown to open up the band gap[61] (which is crucial for electronic applications) and exhibit a lower sheet resistance and higher conductivity with the increased layers across a film[28,62].

Many of the properties described in section 1.1.1 are limited to "pristine" graphene, i.e. an isolated area of monolayer graphene lattice on the nanometre scale that is completely defect free and perfectly clean. This could typically include only a few-hundred atoms. It could therefore be argued that those properties are not wholly representative of the usable material. Studies on FLG are much more limited[55] and therefore there is scope for a further understanding of the more usable, and more easily obtained, graphene material that may be the primary material used in future graphene applications.

1.1.3 Synthesising graphene

As previously described, much of graphene research has been directed towards synthesis methods. Novoselov and Geim won their noble prize in 2004 after cleaving layers of plain graphite with Scotch tape to eventually yield monolayer and few-layer graphene[2]. This is now referred to as mechanical exfoliation and although provides very high-quality graphene (as it is derived directly from graphite) it is not a suitable method to sustain graphene research and development.

"High-quality" graphene will be referred to in this thesis as graphene which is largely void of significant defects such as non-uniformities in lattice structure (e.g. dislocations) and large amounts of contamination. Quality can be analysed by a combination of characterisation techniques such as scanning electron microscopy (SEM) and Raman spectroscopy. These techniques will be outlined in more detail in Chapter 2, but can indicate the extent of defects in a

sample. However, it is noted that the quality of any material is dependent on its resulting application.

After 2004, research focussed into finding new ways to make graphene. Techniques now include: CVD[63,64], epitaxial growth[65,66], arc discharge[67,68], liquid exfoliation[69,70], mechanical thinning of pencil lead[71], carbon nanotube opening[72,73], organic routes[74,75] and even growth from food, insects and waste products[76].

A brief summary of the most studied and promising techniques to synthesise graphene are detailed in Table 1.

Technique	Brief description	Product, size	Advantages	Disadvantages
Mechanical exfoliation	Graphite layers cleaved using Scotch tape	Mono-few layered graphene flakes µm – cm	High-quality graphene, low number of defects Simple Cheap	Non-uniform number of layers Very small scale production Inconsistent
Silicon carbide epitaxial growth	Evaporation of Si on SiC wafers at high temperature	Mono-few layer graphene films cm	Low number of defects Up to cm in size Controlled thickness	Expensive, limited scalability Can be low yield, small scale
Confined organic self -assembly	Organic polymerisation of pyrrole	Monolayer films Up to 100nm.	Controlled thickness	Defective graphene Small scale (nm-µm) Organic contaminations
Liquid exfoliation	Graphite layers cleaved in specialised solvents during ultrasonication to create graphene liquid dispersion	Mono-few layer graphene suspensions Up to µm	Quick and easy method High concentrations Graphene oxide suspensions easily produced Large areas obtainable Cheap and scalable	Non-uniform in layers and size Significant defects Separation from solutions an issue Little control
Chemical reduction from exfoliated graphene oxide	Graphene oxide exfoliated in solvents then chemically reduced	Mono-few layer graphene suspensions Up to µm	Large area Can be stored in water	Often hazardous chemicals involved Final product only stable in hydrophilic polymers
Arc discharge	Arc discharge of carrier gases	Single-few layer graphene 100 nm- µm	High production rate (up to 10 g/h)	High % carbonaceous impurities High concentration of FLG vs. monolayer Little control
Nanotube opening	Un-zipping of nanotubes via various techniques such as chemical, catalytic and electrical cleavage of C-C bonds	Single-few layered graphene nanoribbons Few µm	Size controlled with known sized nanotubes Confirmed nanoribbons	Expensive Small scale production (<mg) Impractical for industry
Chemical vapour deposition	CVD of graphene from a gaseous carbon source on a metal substrate at high temperatures	Single, bi, few layer graphene cm-m	Wide range of substrates, variable method Access to monolayer graphene Large area up to cm uniform films Online control Scalable	High temperatures (>900°C) Potentially low pressures Multiple nucleation points

Table 1) A summary of graphene synthesis methods using information from refs[54,63,64,66–69,71–74,77]**.**

The table outlines some basic advantages and disadvantages of some of the most common graphene synthesis methods. To summarise; mechanical exfoliation, although produces high-quality graphene, is inherently impractical for large scale production; both SiC epitaxial growth and nanotube opening are a very expensive means of production and hence not ideal for industry; organic growth from pyrrole leads to speculations of quality and potential contaminations and arc discharge can produce a large amount of graphene, but along with many other derivates and impurities in the yield.

Liquid exfoliation however (together with subsequent chemical reduction if necessary) is a technique which does have industrial potential. It can be cheap, produce large quantities of high-quality graphene and can be stored in solution which is often useful for some applications. However the number of layers in the graphene product is arbitrary and not easily controlled. In addition solvent removal can be problematic, leading to an increase in cost. Liquid exfoliated graphene is an ideal candidate for graphene "fillers", but working towards a uniform, large area sheet of graphene is where CVD graphene excels.

CVD synthesised graphene demonstrates the largest area, most easily controlled, high-quality graphene that can be up-scaled easily, based on the industrial CNT production that is already dependent on the same set-up. It is an unrivalled candidate in this sense and hence should be a primary target for applications. Additionally, due to its control, FLG graphene can be more consistently synthesised by CVD than other methods.

CVD graphene has already been shown to be a promising material for use in applications. In 2010, roll-to-roll processing by Bae *et al.* produced the largest area use of graphene to date (30 inches), demonstrating a flexible material with resistances and transparency improved when compared to ITO[30](Figure 3). They claimed an "unlimited scalability", which, although in practice may not be without complications, indicates that CVD grown graphene has the potential for large-scale industrial production.

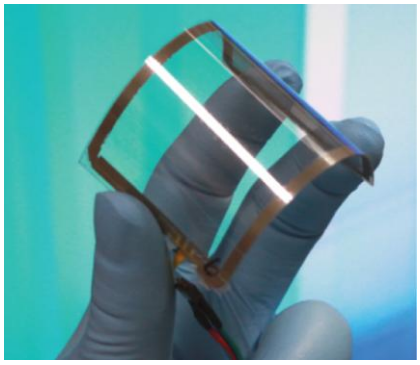


Figure 3) A PET/graphene touch panel assembled by Bae *et al*. demonstrating flexibility and transparency. Reproduced with permission from ref[30]

In addition, layered CVD synthesised graphene composites can be used to build devices. Haigh *et al*. created graphene-boron nitride heterostructures[78] and Karys *et al*. reported that stacking CVD graphene films with nitric acid exposure effectively p-doped the layered graphene, decreasing resistance[27]. CVD graphene layered with PET has been shown to act as efficient transparent conducting electrodes in flexible alternating current electroluminescence devices[79]. Chung *et al*.[80] have used CVD graphene to enhance the production of GaN films and hence was used in a layered composite to produce a platform for visible light-emitting diodes. In addition, Li *et al*. produced some unique results in using CVD to produce graphene in meshes and hence embed and improve the properties of polymer matrices[81].

These few examples demonstrate the scope for possibilities of new materials and applications of CVD graphene. CVD graphene has some of the most promising industrial potential compared to other graphene synthesis methods and consequently research into fully understanding this industrially useful material is paramount.

1.2 Current outlook of CVD graphene

As previously discussed, often publications describing the properties of graphene are focussed on a very small area of sample due to the nature of the characterisation methods used. Therefore, it could be argued that some characterisation is unrepresentative of the larger material system. The aim of this thesis was to therefore undertake some more representative characterisation of the material that may be used in applications.

This aim was further driven by the primary findings obtained from a sample of commercially available graphene. It is known that graphene, like any material, contains defects and irregularities which are likely to affect resultant properties. However, the broader recognition of this information is overlooked in the literature. Graphene is often referred to as the "miracle" material; however this term is usually referring to the pristine graphene at the nanometre scale. To demonstrate the antithesis of this, a SEM image of a sample of readily used commercially available graphene, as advertised on the website ("Single layer graphene [...] films are grown [...] continuous across copper") is shown in Figure 4.

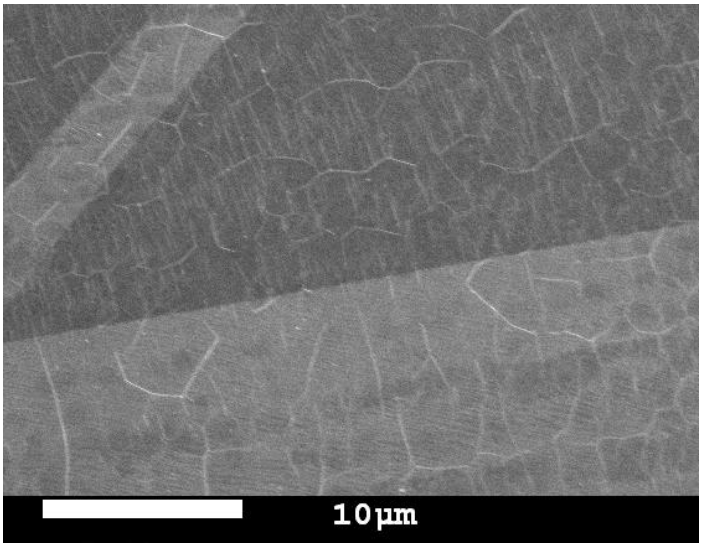


Figure 4) SEM image of a sample of commercially available graphene as advertised[82].

Figure 4 shows an SEM image of the as-synthesised graphene on Cu. The surface looks initially clean, and a lack of an "island" contrast indicates full-coverage (continuous film) of graphene across the Cu foil. There are also wrinkles present in this coverage as can be seen by white lines in the image. Although these wrinkles will affect the electronic structure of the graphene sheet[83,84] the image looks largely as the company describes.

However, as part of the investigations in this thesis, SEM analysis was undertaken on a purchased sample of the same advertised graphene. It is worth noting that visually both sides of the foil looked different. One side appeared shiny (Side 1) and another fairly dull (Side 2). SEM images that were taken at low and higher magnifications are shown in Figure 5.

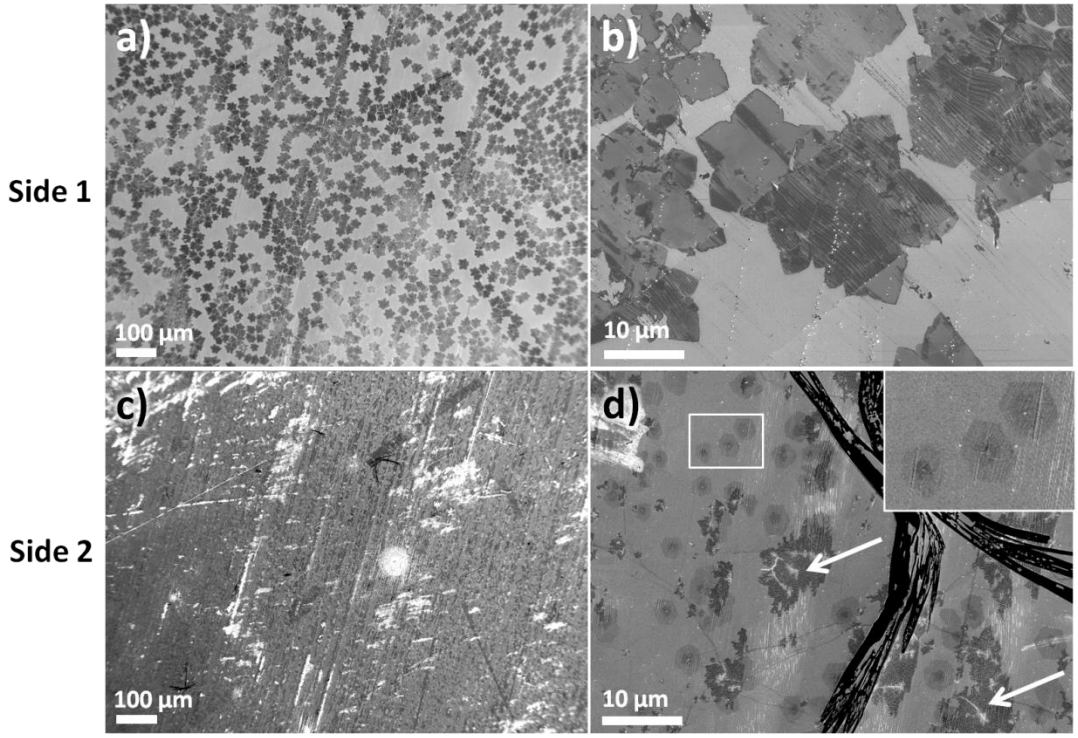


Figure 5) SEM images of both sides of a sample of commercially available CVD "monolayer" graphene grown on Cu foil. Inset of d) is the magnified image of the area of the white box highlighting the presence of areas of FLG growth.

Firstly, it can be noted a stark difference between Figure 4 and Figure 5. The shinier Side 1 consists of an "island" contrast which denotes less than full-coverage of graphene on the surface. The flower-shaped "domains" are islands of graphene. This observation differs from the advertised product and hence if transferred, no conductivity would be present across a surface. Conversely, Side 2 shows a hugely contaminated sample, both in large quantities (white residue in Figure 5c) and in a dark, amorphous contamination as highlighted by white arrows in Figure 5d. This darker contamination was seen to be present in samples synthesised in this thesis when graphene samples had been stored for a relatively long period (>6 months), therefore it may be indicative that this commercial sample was not newly produced.

The Raman analysis of these samples (the background to which will be described in Chapter 2) indicates that Side 1 is few-layer graphene and Side 2 is likely mainly mono layer graphene, with additional few-layer areas. These areas can be indentified within the full-coverage monolayer as small hexagonal graphene domains as shown in the inset of Figure 5d.

Therefore, Side 2 is in fact largely full-coverage of graphene monolayer, as advertised. However, the extent of contamination is considerable. Additionally, the cleaner side of the sample, although exhibits less contamination, is a distinctly different graphene product to that advertised. This is perplexing as there is no mention of any difference between either side of the foil on the data sheet of the product.

These results fuelled a large part of the work undertaken in this thesis. This initial characterisation demonstrated both the state of some commercially available graphene, but also a disregard for characterisation and quality. Figure 5 is not an example of a miracle material.

Additionally, even when CVD graphene is devoid of significant contamination and is synthesised under more control, it still differs from the pristine graphene that is largely characterised. It is imperative that imperfections in graphene are fully understood and a wider recognition of those features is known to the scientific community.

It is important to understand the naturally occurring defects in CVD graphene before materials can be synthesised or exploited fully. An application of "defective" graphene, the gSFB, will be discussed in Chapter 6 and a method of overcoming the defects is discussed. Gaining the most of a material, despite the naturally defective nature should be the larger goal for graphene, especially when removing defects entirely is either very expensive or simply impossible.

1.3 Conclusion and thesis aims

In summary, graphene research has tremendous scope to shape our future technologies. CVD is evidently a contender for scalable industrial production as it demonstrates many advantages over other techniques and has already proven worth at the larger scale.

This thesis looks at graphene research from a different approach. It will examine graphene as an "imperfect" material, rather than focus on its pristine nature. As graphene moves towards up-

scaled production, it is believed that such an approach will enable the characterisation to be more realistic and representative of some of the graphene used in applications.

Therefore, the key aims of this thesis are:

- To analyse the initial challenges in graphene synthesis that can effect graphene growth.
- To characterise naturally occurring defects in transferred CVD graphene to highlight the differences between characterised pristine graphene and the practical material used on a larger scale.
- To apply this characterisation approach to an additional 2D material, hexagonal boron nitride.
- To demonstrate a use of "imperfect" graphene by actively overcoming the naturally occurring defects in the material and creating a new graphene application, the graphene surface force balance.

2 Experimental techniques & preliminary results

This chapter will outline the key experimental techniques utilised in this thesis and some preliminary results that help both to demonstrate the delicate nature of CVD graphene synthesis and characterisation, and lead to easier interpretation of work in additional chapters. The chapter is divided into two main sections; Part I: CVD & general graphene characterisation, and Part II: HRTEM & graphene transfer.

Part I will first outline the CVD process alongside some experimental considerations, before describing the lower-resolution characterisation techniques used in this thesis. Some initial observations that have shaped the research in this thesis will then be introduced.

Part II will detail the experimental procedures behind the HRTEM work in this thesis, introducing first the transfer of CVD graphene (together with the difficulties in the transfer process as a prelude to Chapter 6) followed by an introduction to HRTEM and aberration correction. Some basic imaging and interpretation tools that have been used for specifically graphene imaging have then been described, including an outline of several difficulties of HRTEM graphene imaging.

2.1 Part I: CVD & general graphene characterisation

Initial synthesis experiments and work on overlooked parameters described in this section were conducted in collaboration with Dr. Adrian Murdock.

2.1.1 Introduction to CVD of graphene

As described in Chapter 1, graphene grown from CVD is large area, controllable and produces high-quality graphene using a simple synthesis technique. In this thesis, graphene is synthesised via CVD which involves a gaseous carbon source being passed over a hot metal substrate which decomposes and adsorbs onto the surface[85,86] (Figure 6). Graphene nucleates and then grows in "domains" which eventually knit together to form a graphene film[25,87].

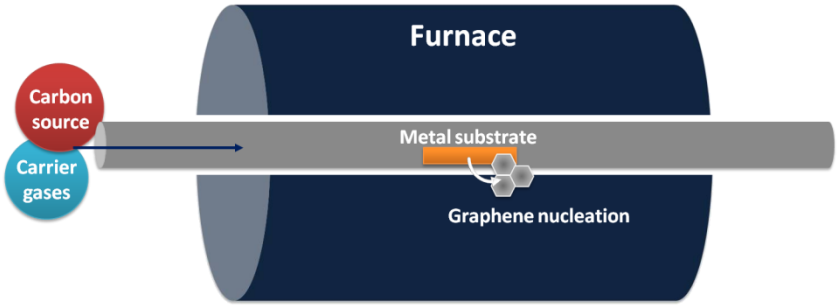


Figure 6) Schematic of the basic principles of CVD graphene synthesis.

The process can be tailored with changes in temperature, pressure and the concentration and flow rates of the gases to optimise the growth. In addition, there is commonly an annealing period under hydrogen prior to growth to encourage a clean metal surface for nucleation and larger Cu grain sizes[25,88].

The metal substrate plays an important role in graphene growth. By 2011, CVD research had largely focussed on rubidium[89,90], iridium[91,92], platinum[93,94], nickel[95,96] and copper[25,97,98] substrates. Platinum has shown the largest graphene domain growth, producing up to millimetre sized, individual graphene domains[99]. However, copper is widely available, easily produced in different purities and cheaper than many other metal candidates, notably platinum, for CVD graphene growth. In addition, copper has a lower carbon solubility compared to nickel, decreasing surface segregation and hence making graphene growth more controllable[25]. In 2009, the first high quality graphene growth on copper was shown[25]. Since, research has rapidly expanded into this field, and in 2010, Bae *et al.*[30] produced 30 inch films of CVD grown graphene as previously described in Chapter 1.

The Cu substrate, which acts as both the substrate and a catalyst for graphene nucelation[64,100] , can significantly influence the graphene growth. Research has shown that the grain size, orientation, purity and cleanliness of the copper have an effect on graphene domain size, number of layers and hence the quality of the resulting graphene film [64,101,102]. Examples of these effects will be discussed in more detail in subsequent sections.

2.1.1.1 CVD Experimental

In this thesis, graphene was synthesised using CVD of methane on Cu foil. An experimental set up is shown in Figure 7. This method was chosen from proven procedures that produced high-quality graphene, obtained previously both in the laboratory and in the literature[30,64,100,103,104].

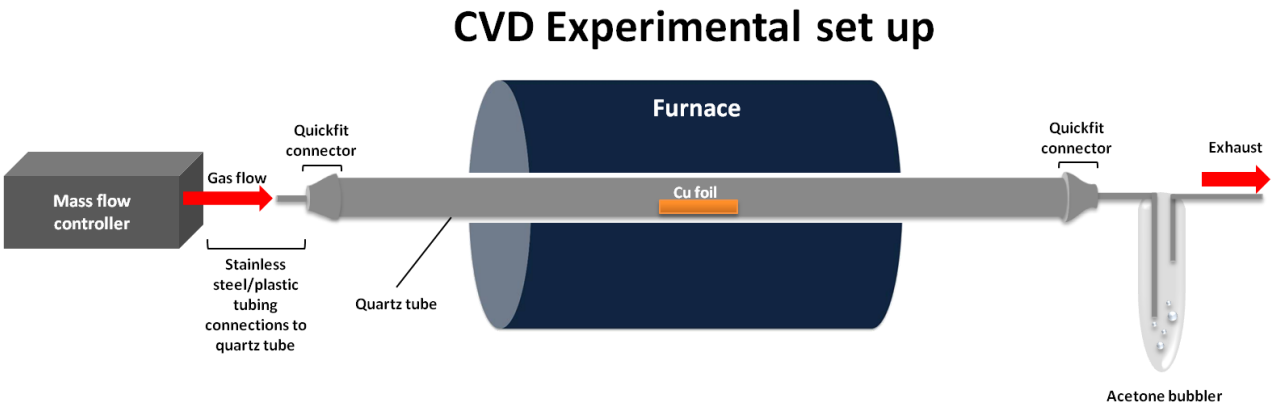


Figure 7) Schematic of the CVD experimental set up.

Graphene samples were synthesised using the set up shown in Figure 7 at atmospheric pressure. The CVD system consisted of a quartz tube (20 mm inner-diameter) located inside a horizontal, cylindrical, single heating zone furnace. A mass flow controller was used to control gas flow through the system which was connected to the quartz tube via stainless steel and plastic tubing. An acetone bubbler was connected to the end of the quartz tube before the gas was exhausted. Approximately 10 x 25 mm Cu foils (*Alfa Aesar,* 99.8 %, 25 µm thick unless otherwise stated) were first cleaned to remove contamination from supplier processing[105]. Substrate cleaning was undertaken as follows: 10 minutes sonication in deionised water (DI), 10 minutes sonication in acetic acid, 10 minutes sonication in DI followed by drying with a nitrogen gun. Clean Cu foils were then immediately placed inside the quartz tube at the centre of the furnace at 1035 °C and annealed for 30 min in the presence of 500 sccm H_2 unless otherwise stated. The CVD system was purged with argon before hydrogen was introduced. Graphene growth was then undertaken by introducing CH_4 in the presence of H_2 at tailored flow rates. During any non-annealing, non-growth or substrate cooling times the system was kept under 200 sccm Ar.

The specifics of gas flow, time and temperature for each experiment will be described in the relevant chapters. These factors are often altered to tailor graphene synthesis towards specific criteria (such as layer number or domain size) which is a complex process. In this thesis it has been necessary to obtain tailored graphene growth on different substrates; hence experimental parameters have had to be thoroughly investigated.

The graphene nucleation mechanism from the CVD of methane on Cu is a complex process that is not yet fully understood. However, it is now largely accepted that it occurs over five main processes; (i) the binding of atomic hydrogen to the Cu surface, (ii) the adsorption of methane and dissociation into active carbon species, (iii) the precipitation and transport of active carbon species, (iv) graphene nucleation and growth from active carbon species and (v) the etching of the grown graphene domain via hydrogen[86,106–109]. Obtaining nucleation on new substrates (or in new CVD systems) is often undertaken by initially using a high methane concentration with respect to hydrogen. This will likely enable some carbon deposits on the substrate due to the increased concentration, although graphene growth is likely to be poor quality. Tailoring the methane/hydrogen ratio can be investigated after this initial nucleation to obtain a specific quality of graphene.

The ratio of methane to hydrogen is a key step in controlling and tailoring graphene synthesis. It is suspected that hydrogen plays multiple roles in the CVD graphene growth. Hydrogen has been shown to act as both a graphene etchant and nucleation aid in the CVD process[86,107]. Vlassiouk *et al*. showed that the hexagonal shape of the domains occurs due to preferential hydrogen etching to produce the more thermodynamically stable zig-zag edge.[86] In addition, Zhang *et al*. showed that atomic carbon does not play a role in graphene nucleation as it is unstable on the Cu surface, and its hydrogen activated species that are the thermodynamically stable form of carbon that drive graphene synthesis[107]. Hence, the hydrogen can both promote nucleation but also reduce the size and growth on graphene domains. Therefore a delicate balance must be achieved.

As well as gas parameters, many additional factors must be controlled to obtain reliable graphene synthesis. Examples of these factors will be described in 2.1.3 Preliminary results.

2.1.2 Graphene characterisation

Tailoring graphene synthesis is only achieved alongside accurate characterisation of the material. As mentioned in Chapter 1, graphene characterisation can often be limited to small, pristine areas. Larger scale characterisation can give a broader picture of the quality of the graphene produced. It can identify potential applications and create new methods of distinguishing samples. However, systematic characterisation in necessary to make valid conclusions and a combination of techniques is normally used to ensure consistency between results.

Graphene has been characterised in this thesis primarily by scanning electron microscopy (SEM), Raman spectroscopy and transmission electron microscopy (TEM). The TEM experimental method will be discussed in detail in Part II. There are multiple techniques used to characterise graphene, however, in this thesis, it was necessary for characterisation techniques to satisfy the following criteria:

- ✓ Graphene layer determination (SEM, Raman, TEM)
- ✓ Defect determination (SEM, Raman, TEM)
- ✓ Fast and non-destructive techniques (SEM, Raman)
- ✓ High resolution (TEM)

Therefore, a combination of these three main characterisation techniques was sufficient for graphene analysis. These primary characterisation techniques have been detailed and other experimental techniques used have also been briefly outlined. Background to the characterisation techniques used in this thesis has been described in Appendix A.

2.1.2.1 Scanning electron microscopy

SEM was first used to characterise CVD graphene growth on Cu in 2009[25] and is now a widely used technique for graphene characterisation. SEM is especially useful for characterising CVD synthesised graphene as it can provide valuable information on the graphene growth such as the extent of nucleation and an indication of the quality and morphology of the graphene. Furthermore, SEM does not require graphene transfer from the substrate. An example SEM image is shown in Figure 8 to demonstrate how SEM images are interpreted and what data they can provide. The image highlights typical features: the Cu substrate, a graphene domain, a Cu grain boundary and contamination particles. When graphene domains grow larger over time and eventually knit together, "full-coverage" across the substrate surface is obtained.

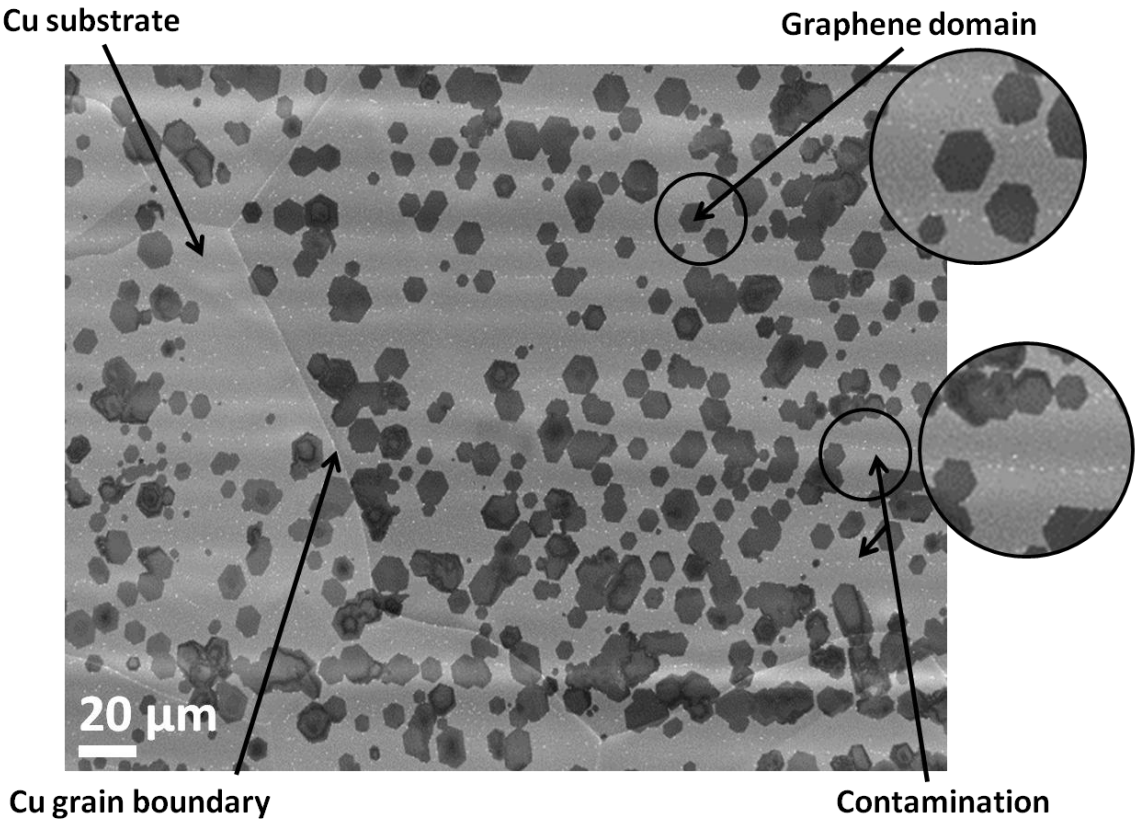


Figure 8) Example SEM image of graphene grown on Cu foil with key features highlighted: Cu substrate, Cu grain boundary, a graphene domain and contamination particles.

In SEM, different materials produce different signals; different contrasts are observed for the Cu substrate and graphene, with visible contrast also apparent between graphene layers[86]. Additionally, SEM can determine full-coverage growth and the extent of large-scale wrinkles

and defects across metallic grains. However, SEM is limited to growth analysis and it is not possible to absolutely define the number of layers with SEM alone.

In this thesis, a JEOL JSM-6500F field emission SEM was operated at 5 kV to obtain images. 5 kV with a small working distance was necessary to gain the resolution and surface sensitivity required in the SEM without damaging the graphene.

2.1.2.2 Raman spectroscopy

Raman is a spectroscopic technique that can quickly define the quality and number of layers of a graphene sample[110–113]. In addition, Raman has the ability to distinguish between doped and functionalised graphene[114] and provide information on graphene edge structure[115].

There are three widely recognised Raman peaks that are characteristic of graphene. These are the D peak at 1350 cm^{-1} (corresponding to the breathing modes of six-atom rings activated by a defect), the G peak at 1580 cm^{-1} (corresponding to a signal resulting from sp^2 carbon-carbon stretching bonds) and the G' (or 2D) peak at 2640-2720 cm^{-1} (corresponding to 2nd order phonon modes of the D peak, that do not need a defect for activation)[111]. Therefore, the D peak can provide information on graphene quality, and hence is often referred to as the "defect peak". This peak appears due to the presence of edges, tears and significant bonding defects (e.g. dislocations) and hence is usually present in chemically exfoliated or functionalised samples. A Raman spectrum of both graphene and graphite are shown in Figure 9. D peaks are not present in either spectrum, denoting a high-quality material, devoid of defects.

Combining the Raman spectrum with a visualisation technique to characterise graphene, e.g. SEM, an assumption of graphene quality can be made. If a Raman spectrum does not exhibit a D peak and corresponding SEM images indicate uniform growth without significant defective features (e.g. significant contamination or tears, as seen in the commercially available sample in Chapter 1), the sample can be considered as high-quality.

The ratio of the G and G' (2D) peak can be used to quantify the number of graphene layers[63]. In addition, the shape and intensity of the G' (2D) peak can also help indicate the layer

number[110,111,116]. Generally, a 1:1 ratio indicates bi-layer graphene, a smaller G peak indicates monolayer graphene (as shown in Figure 9a) and a smaller 2D peak indicates few-layer graphene. Peak broadening can be observed with increasing layers due to splitting of the electronic band for few-layer samples, leading to a broad peak that eventually becomes indistinguishable to that of bulk graphite (Figure 9b-d).

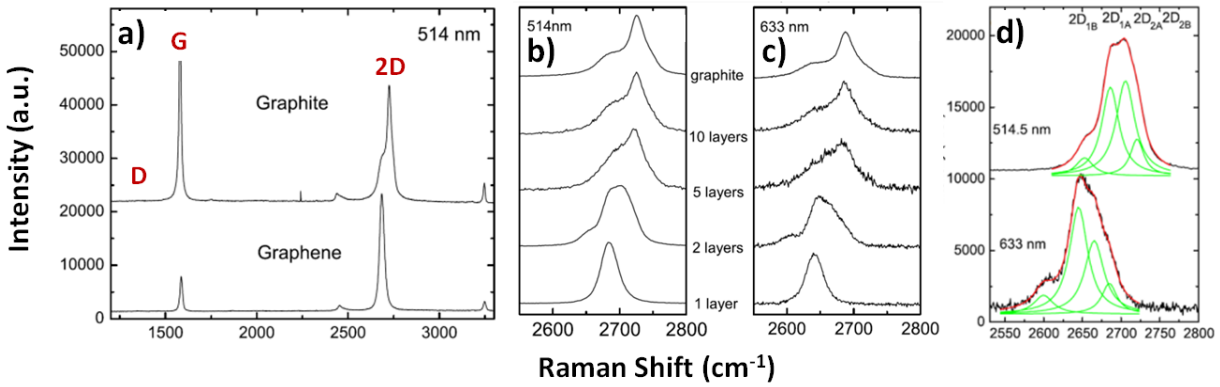


Figure 9a) Raman spectra at 514 nm comparing bulk graphite and graphene. b) Changes in Raman spectra at 514 nm with increasing number of graphene layers. c) Changes in Raman spectra at 633 nm with increasing number of graphene layers. d) Development of four components of the G' peak in bi layer graphene at 514 and 633 nm, explaining the development of an increasing band with increasing layers. Reproduced with permission from ref[110].

In this thesis, Raman spectroscopy was conducted at room temperature using a JY Horiba LabRAM Aramis Raman spectrometer equipped with a 532 nm laser. Accumulation times were optimised for each sample scan.

2.1.2.3 Atomic force microscopy

Atomic force microscopy (AFM) has been frequently used to characterise graphene[31,87,117–122]. AFM can deduce the number of graphene layers using the graphene interlayer spacing and the step height of graphene layers. Scanning large areas of a sample also provides information on topographical features (both from the graphene and the metal substrate from CVD synthesis) and domain size and structure. Similarly to SEM, AFM has the added advantage that the sample does not have to be transferred from the metal substrate.

In this thesis, AFM was used to determine the roughness of graphene surfaces in Chapter 6. AFM images were obtained used a NanoScope MultiMode AFM in contact mode using Nanosensors PointProbe® Plus Contact Mode probes.

2.1.2.4 Electron back scattered diffraction

Electron back scattered diffraction (EBSD) can be used to determine the crystallographic orientation of metals in conjunction with SEM. EBSD has been used in this work to study metallic substrates used for CVD graphene synthesis. EBSD maps are produced by scanning the sample and obtaining point measurements which provide an overall picture of large area changes in crystallographic orientation.

In this thesis, EBSD was used in conjunction with a JEOL JSM-6500F field emission SEM operated at 15 kV. A TSL EBSD system was used and Hough-based analysis was employed to index patterns and create orientation maps using EDAX OIM data analysis software.

2.1.2.5 Energy dispersive X-ray analysis

Energy dispersive X-ray analysis (EDX) can be used to determine the elemental composition of materials. EDX is used in conjunction with SEM by taking advantage of the interaction of the electron beam with a sample and analysing the characteristic X-rays emitted. Thus, X-rays are directly interpretable to the constituent elements within a sample. In SEM, EDX is not an accurately quantitative technique and therefore can only provide an indication of elemental presence.

In this thesis, EDX analysis was conducted in conjunction with a JEOL JSM-6500F field emission SEM operated at 15 kV using an EDAX detector and EDAX Genesis software for elemental assignment of signals.

2.1.3 Preliminary results

Due to the number of changeable parameters in CVD, it is possible to synthesise a range of graphene products that in turn exhibit different properties. Figure 10 summarises some examples of different types of CVD grown graphene and introduces some preliminary results. Figure 10a-c shows SEM images of few-layer graphene (FLG) growth, Figure 10d shows largely monolayer growth and Figure 10e shows an example of full-coverage, FLG.

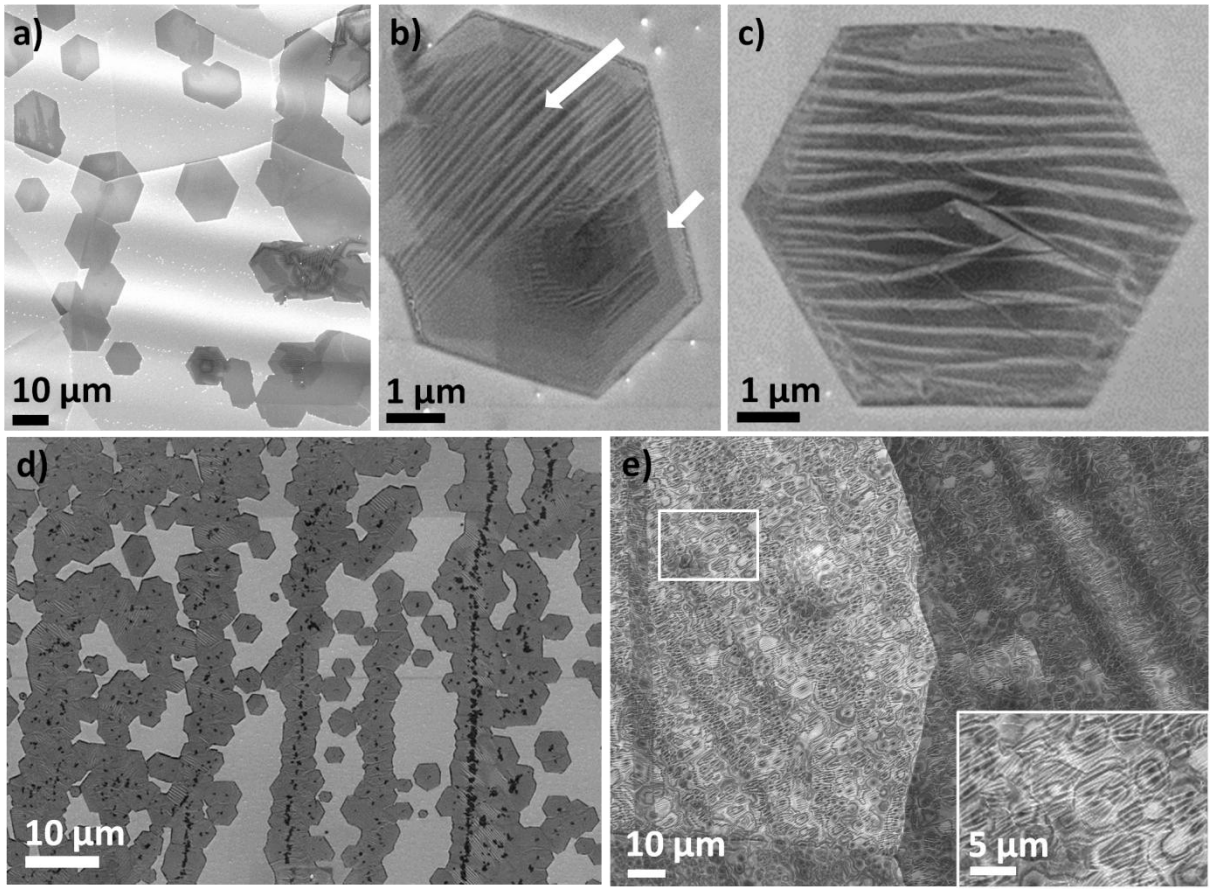


Figure 10) SEM images of example CVD graphene grown in Cu foils. a) Hexagonal graphene growth. b) and c) Individual hexagonal domains with FLG growth visible within the domain. White arrows in b) highlight two growth points in one domain. c) Example of possible "spiral" FLG growth. d) Hexagonal growth of largely monolayer graphene. e) Full-coverage FLG with white box highlighting area of magnified inset.

Hexagonal growth of graphene domains is a commonly observed morphology from atmospheric pressure CVD (Figure 10a-d). Angles of hexagonal domains are usually regular, exhibiting 120° on average, but can range from 105-150°. Discrepancy could be due to few-layer growth within individual domains (white arrows in Figure 10b highlight two separate growths within a hexagonal domain) and the ability for hexagonal domains to exhibit "spiral growth" as observed in Figure 10c.

Wrinkling in graphene can also be observed in individual domains (Figure 10b,c) and within full-coverage (Figure 10e inset). Wrinkling can occur due to contamination interactions[123], interfacial instabilities with the substrate[124] and has been proven to occur due to differences in thermal expansion between graphene and the metallic substrate upon cooling[125]. Therefore, varying degrees of wrinkling can be observed across different Cu grains. Wrinkle formation is

an extremely common occurrence in CVD graphene synthesis and will be discussed further in subsequent chapters.

2.1.3.1 Controlling graphene synthesis

During this work, it was necessary to produce consistent FLG samples. It became apparent that inconsistencies arose between experiments of the same conditions and that there were some additional parameters that had been overlooked in the literature which may have been causing discrepancies. Parameters such as gas flow and temperature are commonly controlled but additional factors can significantly affect graphene growth. Parameters such as substrate position within the furnace, the substrate supplier and contamination effects will be introduced in this section to demonstrate the difficulty of obtaining precise CVD graphene synthesis. These results firstly highlight the complexity of CVD graphene growth but also enabled further understanding of CVD synthesis to ensure precise and thorough investigation in subsequent experiments.

2.1.3.1.1 Substrate position

Firstly, an investigation was carried out into how the substrate position within the furnace effects graphene growth. A long Cu foil was placed inside the entire length of the furnace for graphene synthesis. A selection of results from key areas is shown in Figure 11.

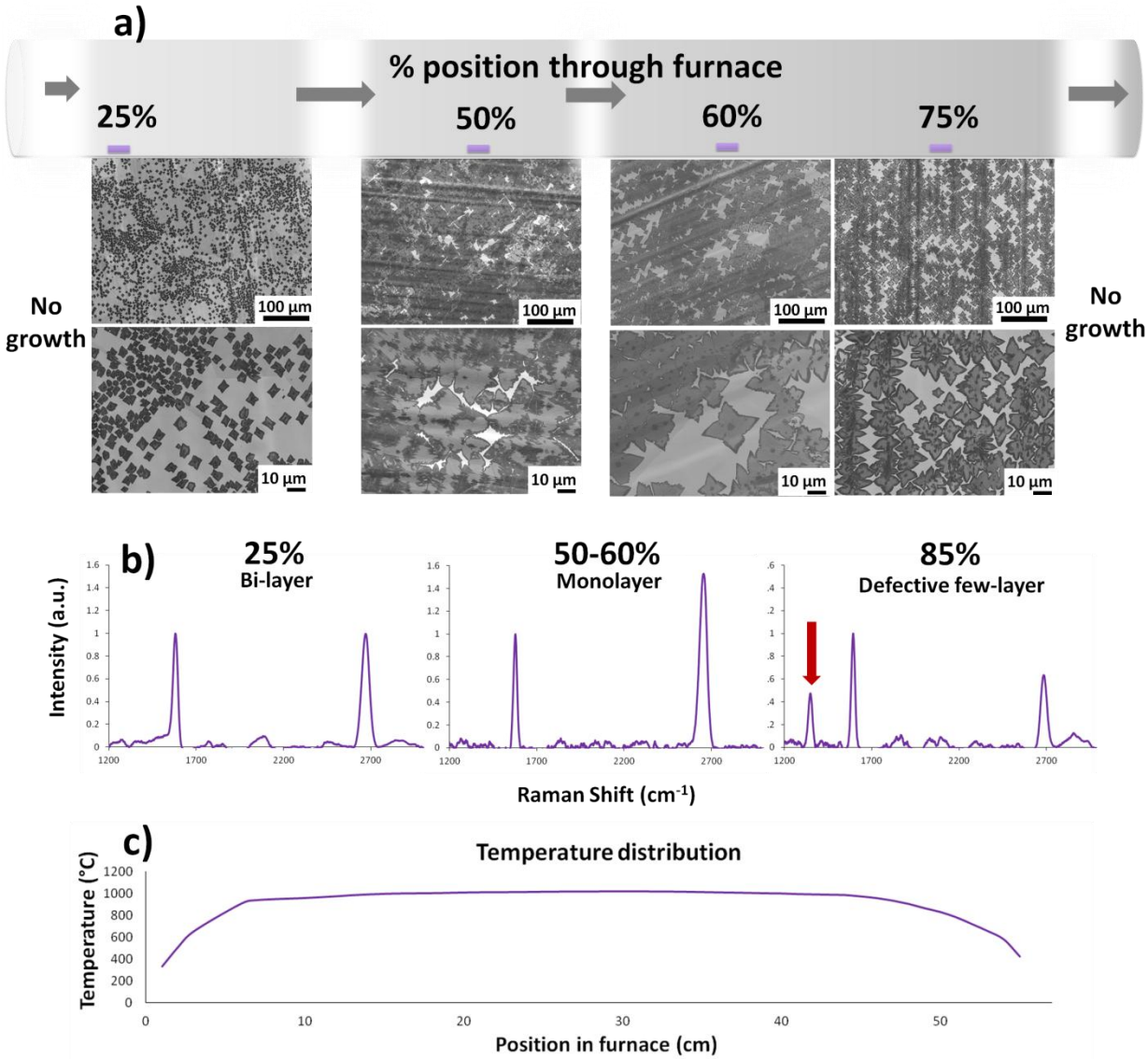


Figure 11) Difference in graphene growth across CVD furnace due to substrate position. a) Example SEM images shown from 25%, 50%, 60% and 75% through the furnace. b) Corresponding Raman spectra taken from samples 25%, 50-60% and 85% through the furnace. Raman data shows the evolution of graphene growth from bi-layer to monolayer to defective FLG throughout the furnace. A red arrow in the Raman spectrum for 85% highlights the D peak. c) Temperature distribution of CVD furnace which is likely to be a factor that influences the changes in graphene growth.

From the SEM and Raman data (Figure 11a and b) it can be shown that at 25% through the furnace, low coverage bi-layer graphene is present. At 50-60%, monolayer graphene is present at notably higher coverage and larger domain size. Towards the end of the furnace at 85%, lower coverage and more defective graphene is present. The D peak is highlighted by a red arrow in Figure 11b.

As well as gas concentration effects, the differences in growth are likely due to the variation in temperature across the furnace as shown in Figure 11c. Between 25-75% in the CVD furnace, it

is possible that the change within 10°C contributed to significant differences in graphene growth. This is an important observation in context of the industrial production of graphene as it demonstrates that with a small temperature change, or a few cm shift in substrate position, notably different graphene is produced.

This finding ensured that substrate positions of all subsequent CVD experiments were precisely measured within the furnace and an additional thermocouple was used to confirm the temperature.

2.1.3.1.2 Substrate supplier

Substrate choice inevitably influences graphene growth. Figure 12 shows some examples of how the Cu substrate can influence the synthesised graphene.

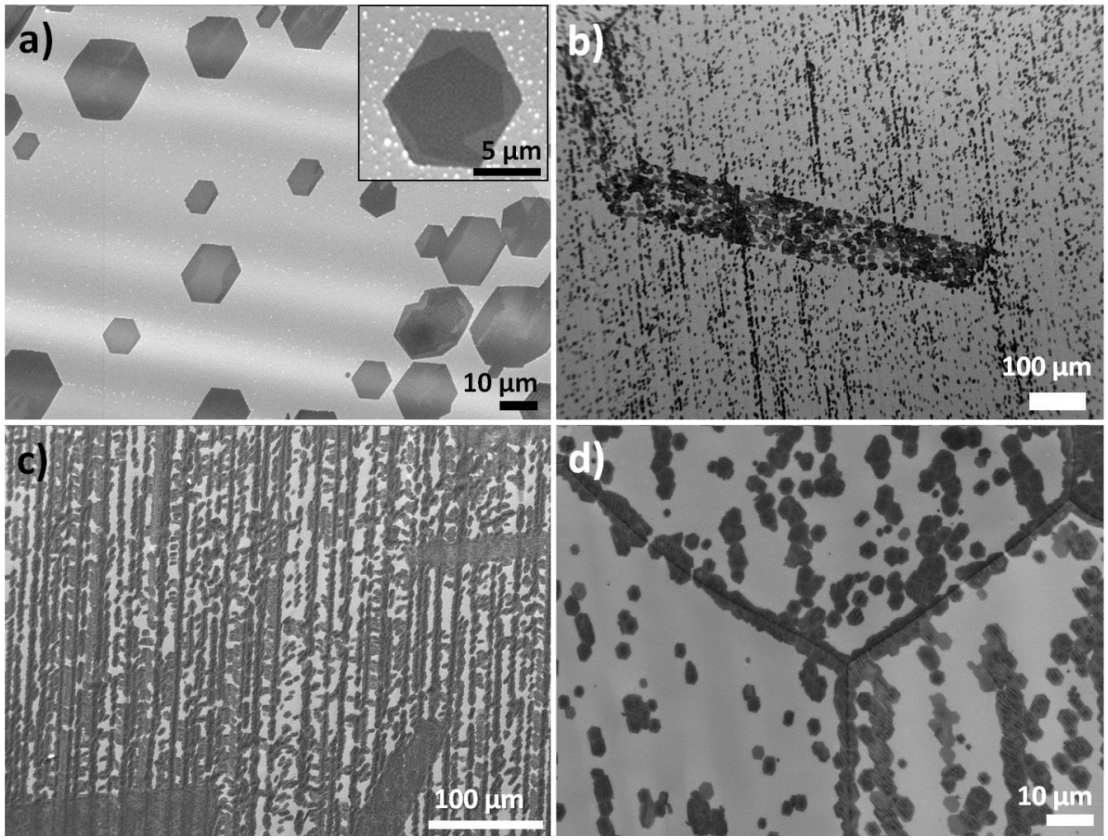


Figure 12) SEM images of varied graphene growth due to influences from the Cu substrate. a) Alignment of hexagonal domains in one Cu orientation. Inset shows a graphene domain with an additional graphene domain, at a different orientation, within it. b) Example of different graphene growth on different Cu grains. c) Graphene growth dominated by Cu processing lines. d) Graphene growth more prevalent on grain boundaries between Cu orientations.

Figure 12a shows the orientation of hexagonal graphene domains in the same Cu grain. Work has shown that for some Cu grains, graphene domains orient themselves along preferential axes to lower the energy of the system[62,104,121]. In addition, the inset in Figure 12a shows an example of two orientations within one hexagonal domain. It is suspected that AB Bernal stacking (see Figure 77, Chapter 5 for schematic) does not always occur as the secondary layer is also influenced by the Cu substrate, not solely the first graphene layer[86]. Figure 12b shows an example of how graphene nucleation and growth can differ with different Cu orientations, with one Cu orientation exhibiting increased nucleation compared to the surrounding Cu grains. Figure 12c shows how graphene nucleation is preferential on Cu roughness, in this case the Cu processing lines. A similar behaviour is shown in Figure 12d where Cu grain boundaries have also shown preferential nucleation. Furthermore, during these experiments, it was observed that upper and lower faces of the substrate can produce different growth hence both sides of the substrate must always be analysed. This phenomenon was also apparent in the sample of commercially available graphene, discussed in Chapter 1.

Figure 13 demonstrates the significant differences between copper substrates from two different suppliers. EBSD scans indicate a large difference in the Cu grains across the foils which have therefore produced contrasting graphene growth from the same experimental parameters. In this example, Cu from Supplier 1 (*Alfa Aesar, 99.98 %*), exhibiting a largely Cu (001) surface, has produced poor graphene growth at a very low coverage, whereas Cu from Supplier 2 (*Goodfellow, 99.9%*), exhibiting closer to a Cu (111) surface, has produced near-full coverage, hexagonal, FLG growth. It was also found in these primary investigations that interestingly the most expensive substrates (e.g. the highest purity, 99.9999%) did not necessarily produce the highest quality graphene growth, which may be of interest in cost-effective industrial synthesis.

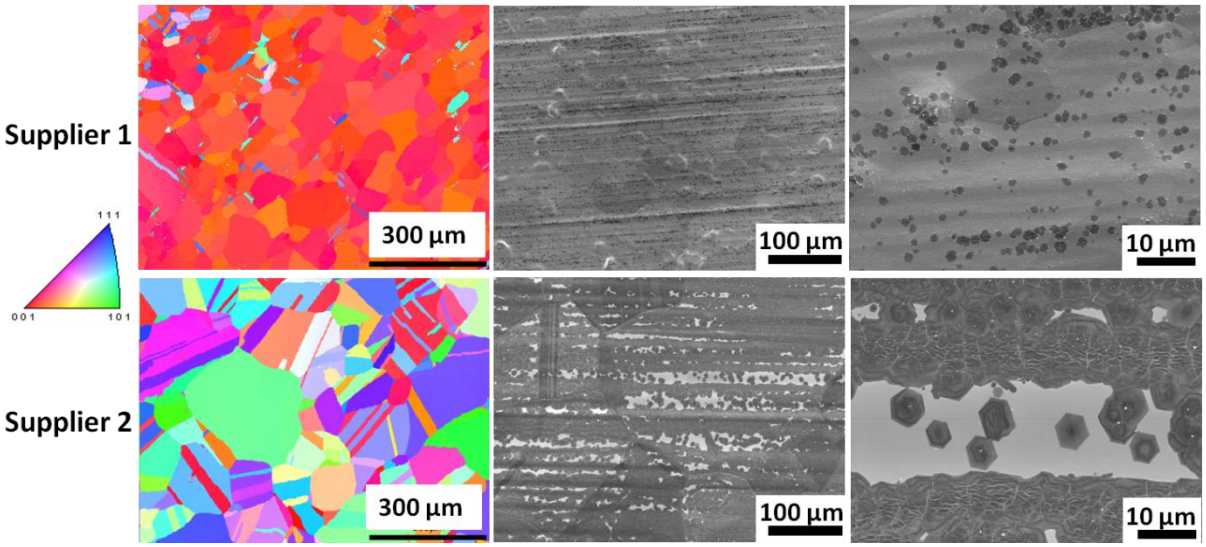


Figure 13) EBSD scans of Cu foils from two copper supplies with corresponding SEM images of graphene grown from the same synthesis conditions.

These results lead to the use of one consistent type and supplier of Cu foil where possible for all subsequent CVD experiments, and cleaning procedures ensured that topographical features such as processing lines had negligible effects on graphene growth.

2.1.3.1.3 Contamination

Regardless of the substrate material, contamination in the CVD graphene synthesis is very common. SEM images demonstrating examples of contamination effects have been shown in Figure 14. Figure 14 shows that contamination can be evident on top of the synthesised graphene (Figure 14a), across the substrate (Figure 14b) and can be shown to both induce (Figure 14c-e) and inhibit (Figure 14e inset) graphene nucleation.

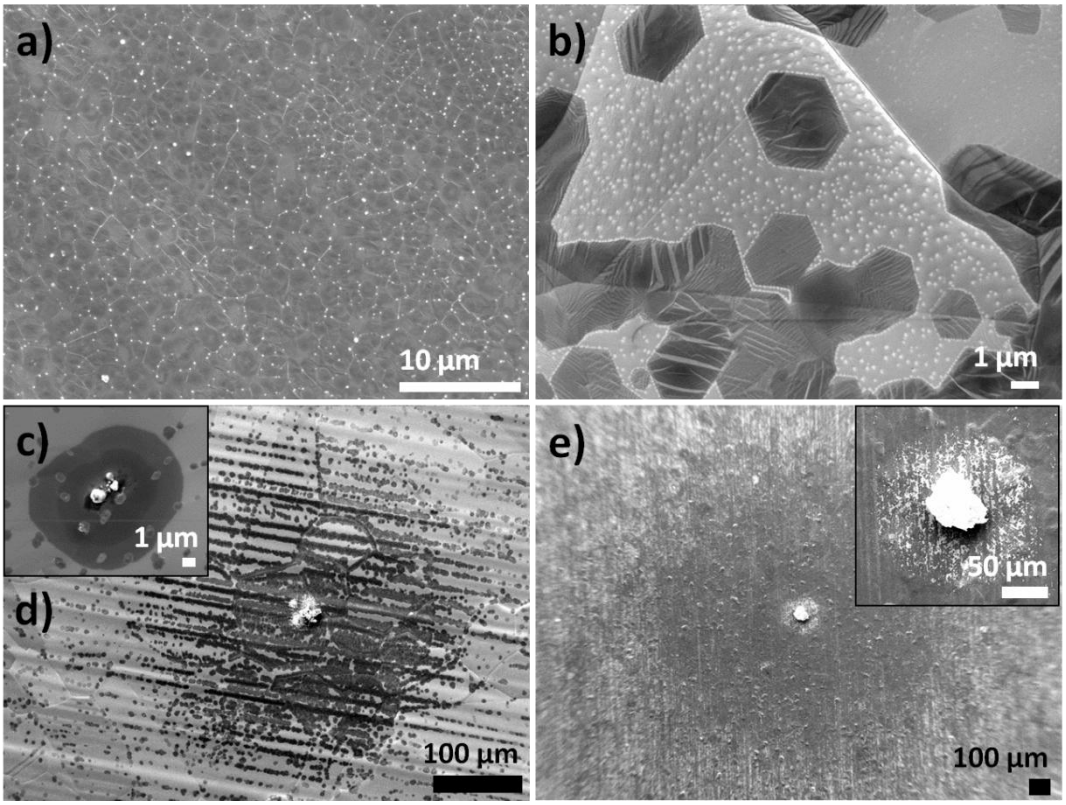


Figure 14) SEM images of contamination observed after graphene growth on Cu foils. a) Full-coverage graphene with contamination particles visible as a continuous deposit on top of the graphene. b) Contamination visible on Cu foil and bordering graphene domains. c) and d) Examples of large contamination particles inducing substantial nucleation. e) Large contamination particle both inducing nucleation and hindering growth (inset at higher magnification).

Preliminary EDX analysis of contamination particles indicates the presence of Ca, Si and Al, as well as carbon and oxygen; all of which are commonly found in Cu processing chemicals. During the first investigations in this thesis, an interesting phenomenon, which has been referred to as the appearance of graphene "daggers", arose due to contamination particles as shown in Figure 15.

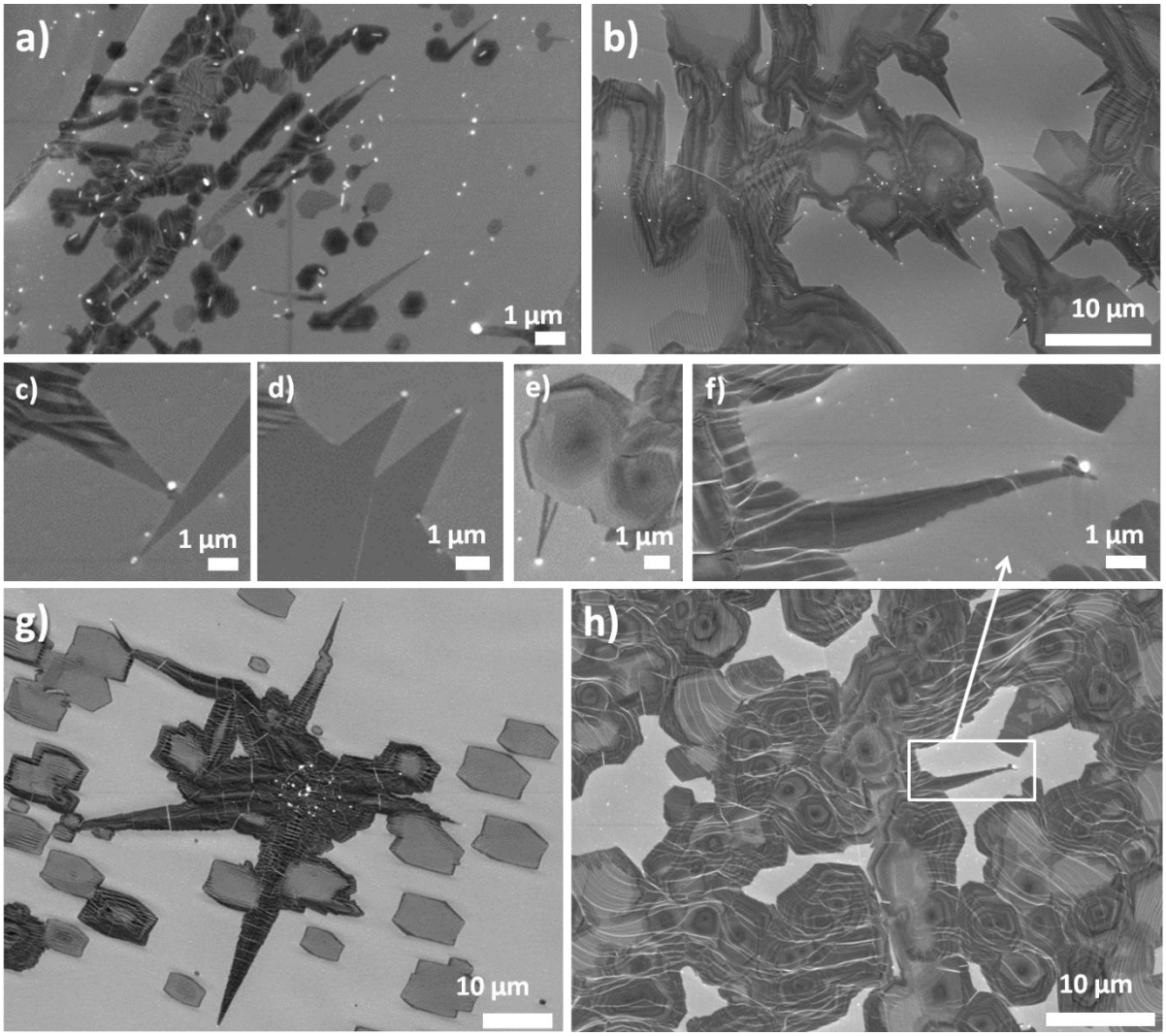


Figure 15) SEM images of graphene daggers. a-f) Examples of graphene daggers terminating in contamination particles. c-f) Examples of graphene daggers at higher magnification. g-h) Examples of graphene daggers occurring within regular FLG growth. Inset of h) is shown at higher resolution in f).

Daggers are likely to be contamination driven. SEM evidence shows that graphene daggers are always terminated with a contamination particle. It is likely that, compared to the rest of a graphene domain, a graphene "dagger" experiences an increased growth rate which may be due to a contamination particle that could decrease the activation energy for the growth of graphene. This could occur by (i) lowering the energy barrier for attachment of adsorbed species to the graphene edge, (ii) lowering the energy barrier for decomposition of the methane on the Cu foil at the site of the contamination particle, or (iii) increasing the concentration of carbon at the graphene edge.

As shown in Figure 14 and Figure 15, contamination therefore can significantly alter graphene growth and controlling, or working around, contamination is of considerable importance if controllable synthesis is to be achieved. Thus, as previously described, thorough cleaning of substrates and experimental equipment was undertaken for all experiments in this thesis and any experimental techniques that consistently yielded increased contamination were avoided.

These initial results of overlooked parameters show a few examples of how simple factors can be crucial in determining the quality of the graphene produced. For example, a simple change in position or choice of substrate could alter an experiment and the final product significantly. Optimum combination and awareness of these influences was vital for ensuring high-quality graphene production for the work in this thesis and is of interest to both graphene research in general and industrial production.

2.2 Part II: HRTEM & graphene transfer

To further investigate graphene quality, graphene was characterised in this work at higher resolution using HRTEM. Similarly to Part I, this section includes some preliminary data that aids in the explanation of the results described in subsequent chapters. All TEM data in this chapter was collected during this thesis investigation unless otherwise stated.

Work on NanoBuds was undertaken in collaboration with Dr. Rebecca Nicholls (please see the peer reviewed article[126]: "*In situ* engineering of NanoBud geometries" in Appendix B).

2.2.1 Introduction to TEM

Transmission electron microscopy (TEM) can provide structural information of graphene at much higher resolution than SEM. TEM enables imaging down to angstrom resolution and can provide evidence of atomic structure, graphene layering and hence explanations of growth mechanisms and properties of the synthesised materials.

Imaging larger atomic spacings, such as graphite stacking in CNT walls (0.335 nm), is much easier and hence can be done with less advanced microscopes. Resolving much smaller distances, like carbon-carbon atomic spacings (0.142 nm), is more difficult as it requires a highly aligned, aberration corrected electron beam. Both TEM and scanning-transmission electron microscopy (STEM) can utilise aberration correction and hence are capable of the higher resolution that can provide atomic scale data on carbon nanomaterials.

2.2.1.1 The benefits of TEM over STEM

STEM has a different contrast mechanism to TEM, relying on atomic number, Z. Contrast in STEM images is directly proportional to Z and therefore thicker samples or heavier elements appear brighter in STEM images. For specialised instruments, with the addition of aberration correction, high-resolution STEM (HRSTEM) can resolve atomic spacings in a graphene lattice, and due to the nature of the contrast mechanism can easily visualise dopants. Zhou *et al.*[127] has shown a Si atom substituted into a graphene lattice (Figure 16a). Additionally, HRSTEM has been shown to resolve even a contrast difference between a nitrogen and carbon atom as shown in Figure 16b and c by Nicholls *et al.*[128]

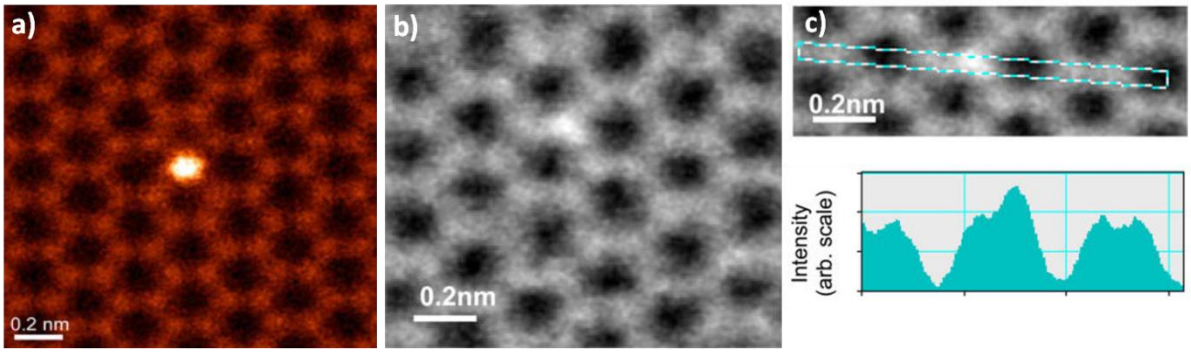


Figure 16 a) HRSTEM image of substitutional Si dopant in graphene lattice, with two adjacent five-fold rings. Reproduced with permission from ref[127]. b) HRSTEM image of substitutional N dopant with c) corresponding line profile illustrating the contrast difference between carbon and nitrogen atoms. Reproduced with permission from ref[128].

However, in terms of imaging the effect of defects on a slightly larger scale, STEM is not as versatile. TEM can image larger areas more easily than STEM which was beneficial for the samples in this thesis which contained naturally occurring defects that could span across several microns. Additionally, contamination can often be more prevalent during STEM imaging

which would have been more problematic when imaging samples of defective FLG which already contain areas of amorphous carbon and foreign particles from the transfer and synthesis procedure. HRTEM provides a clearer insight into graphene imperfections and layer structuring by way of both graphitic spacings that have a distinct contrast difference to bulk graphene in TEM, and how layer edges are more easily observed within full-layer coverage. In addition, variations in TEM imaging can provide indications of sample strain, as will be discussed in the following chapters.

2.2.2 CVD graphene transfer

To analyse CVD graphene using TEM, it is first imperative to transfer the graphene samples from the metallic substrate to a TEM grid. Transferring graphene is necessary for a multitude of applications including electronics, composites and further characterisation. Transferring graphene can induce folds, tears and contamination into the system, all of which can be detrimental to the final material properties. Folds and tears originate from the procedure itself whereas contamination can occur from the substrate (notably from etching), any chemicals used in the transfer procedure and any contaminants from the atmosphere, including those from storage containers.

The transfer procedure must attempt to retain the high quality graphene that has been achieved through controlled synthesis. It is important to stress the difficulties in this process; adhesion of the substrate used for growth has to be overcome and handling one of thinnest materials is an intricate process.

2.2.2.1 Example transfer to silicon and other hard substrates

An example of a typical transfer method is shown in Figure 17. A well established method is the use of a polymer support which is bound to the graphene prior to etching of the metallic substrate[28,129–131]. The polymer is dropped or spin coated onto the graphene/metal substrate and left to dry or cured at a higher temperature (Figure 17). Thicknesses of the polymer vary with how researchers have chosen to attach the polymer.

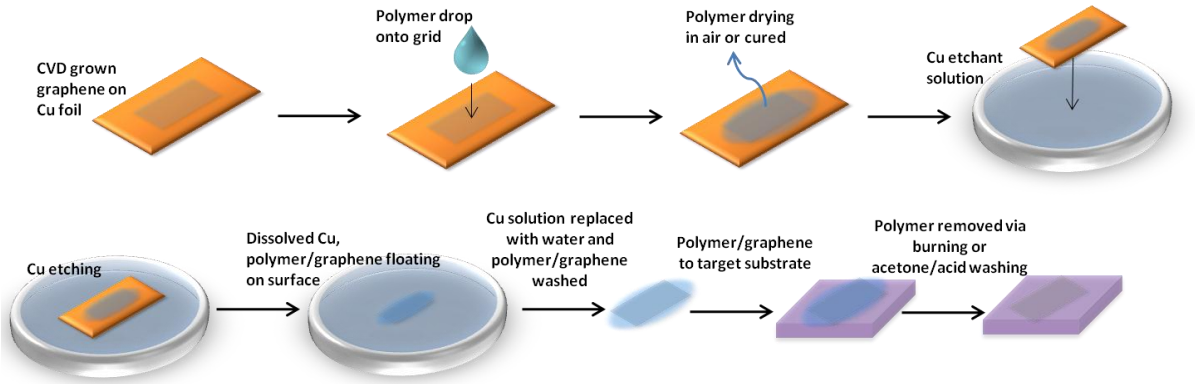


Figure 17) Schematic of general polymer transfer of CVD graphene onto a different substrate.

Poly(methyl methacrylate)(PMMA) is often used because of its ease and flexibility of use; it can be easily dissolved and stored in varying solution concentrations and dries quickly. However, one large disadvantage of using a polymer support is the residual contamination on the graphene surface, even after removal as shown in TEM images by Lin *et al.* in Figure 18. Polymer contamination has been shown to be detrimental to graphene properties, notably the carrier mobility[14]. Optimum polymer removal techniques have been researched[28,129–132]; including curing, acetone and acid washing, but none can claim 100 % polymer removal. Publications tend to loosely cover the issue of polymer contamination; this is likely because it is so difficult to completely remove.

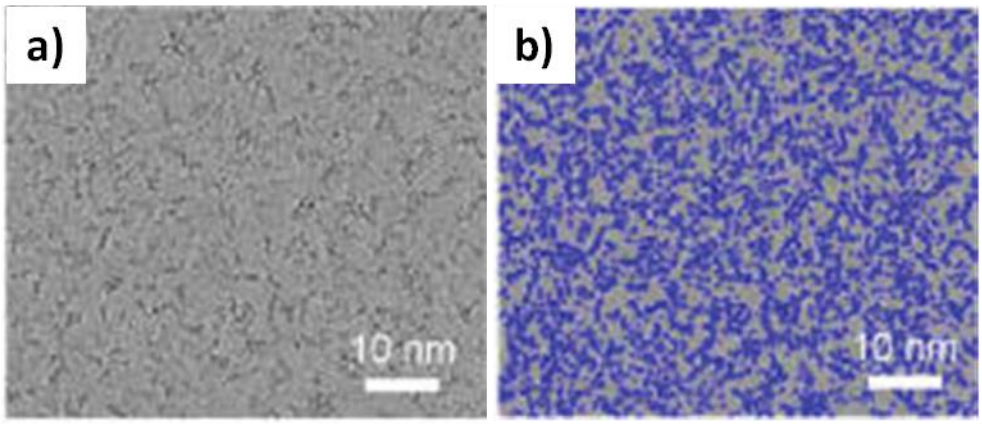


Figure 18a) TEM image of graphene exhibiting polymer contaminating after PMMA support was used for graphene transfer and annealed for removal. b) shows corresponding false colour image with polymer contamination highlighted in blue. Reproduced with permission from ref[132]

In addition to this contamination, the etching of the metal substrate introduces metal residues[132] which can also cause changes in material properties.

Transfer techniques must therefore try to avoid significant contamination and any defect-inducing procedures. This information is relevant in the development of a new transfer technique, outlined in Chapter 6.

2.2.2.2 Transfer for TEM

The use of the polymer method as shown in Figure 17 can also be used for TEM transfers by using the grid as the secondary substrate, but inevitably at the cost of contamination. Regan *et al.*[133] described a method for graphene transfer specifically for TEM involving the direct adherence of a TEM grid to the metal/graphene substrate, followed by substrate etching, using the same principles that the graphene then adheres preferentially to the TEM grid as the substrate on which graphene has been grown has been dissolved. This scheme is shown in Figure 19. The key step in the success of this procedure is the adherence of the grid to the graphene/Cu using isopropanol (IPA) evaporation.

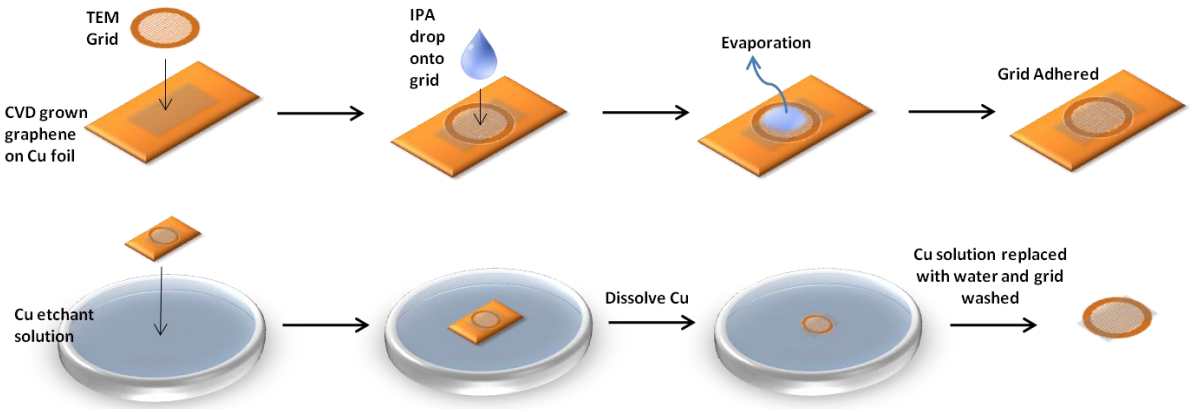


Figure 19) Schematic of graphene transfer process for TEM using process from ref[133]

In this thesis, graphene was transferred onto Au TEM girds (*Agar Scientific*) with holey carbon. IPA (*Sigma-Aldrich*) was dropped onto the grid/graphene/Cu and left to evaporate at 80°C on a hotplate. The Cu substrate was dissolved in an etchant solution of 1M ammonium persulphate (*Sigma-Aldrich*, ≥98%) and the grid was washed thoroughly with DI before being dried in air over a hotplate.

This technique became a simple and effective method to transfer graphene for TEM, if well executed, and most importantly avoids the use of a polymer support and its associated contamination.

2.2.3 Background to HRTEM

What differentiates HRTEM from TEM is the appearance of an additional contrast mechanism, known as phase contrast, which can enable high-resolution imaging. In short, the origin of the contrast stems from the interference of multiple electron waves travelling through a sample, which each exhibit a different phase. Multiple beams therefore interfere and contribute to the final image contrast and hence often large (or no) apertures are used during imaging.

The subsequent discussion follows the work and terminology put forward by Williams and Carter[134].

HRTEM can be optimised by understanding how much information is transferred from the sample to the image. This can be described by the contrast transfer function (CTF) or *H(u)* which is defined by:

$$H(u) = A(u)E(u)B(u)$$

Where *u* is the spatial frequency (which denotes the resolution of the microscope; high resolution requires high spatial frequencies), *A(u)* is the aperture function (defining the spatial frequencies cut off by a specified aperture), *E(u)* is the envelope function (or the attenuation of the wave) and *B(u)* is the aberration function. *A(u)* and *E(u)* are both properties of the microscope and therefore (once an aperture has been selected) these cannot be controlled by the user to manipulate the contrast transfer function. Therefore to exhibit any change in *H(u)*, *B(u)* must be controlled. *B(u)* can be expressed as:

$$B(u) = \exp(i\chi(u))$$

χ is known as the phase-distortion function or the Scherzer factor. It is necessary to generate a phase shift to obtain a contrast difference in a HRTEM image. Phase shifts can be induced by adding or subtracting the amplitude of phases which is denoted by χ, expressed as:

$$\chi = \pi \Delta f \lambda u^2 + \frac{1}{2} \pi C_s \lambda^3 u^4$$

Where λ is the electron wavelength, C_s denotes the spherical aberration and Δf is defocus. Thus, assuming λ remains constant, χ can be controlled using defocus and controlling spherical aberration. Hence, χ is dependent on the microscope and is not related to the sample. As graphene is very thin, it behaves as a weak-phase object and therefore *B(u)* can be approximated to:

$$B(u) = 2 \sin \chi(u)$$

Therefore, to visualise the contrast transfer function, sinχ is plotted against *u* to provide an indication of resolution capability of the system. An example plot is shown in Figure 20.

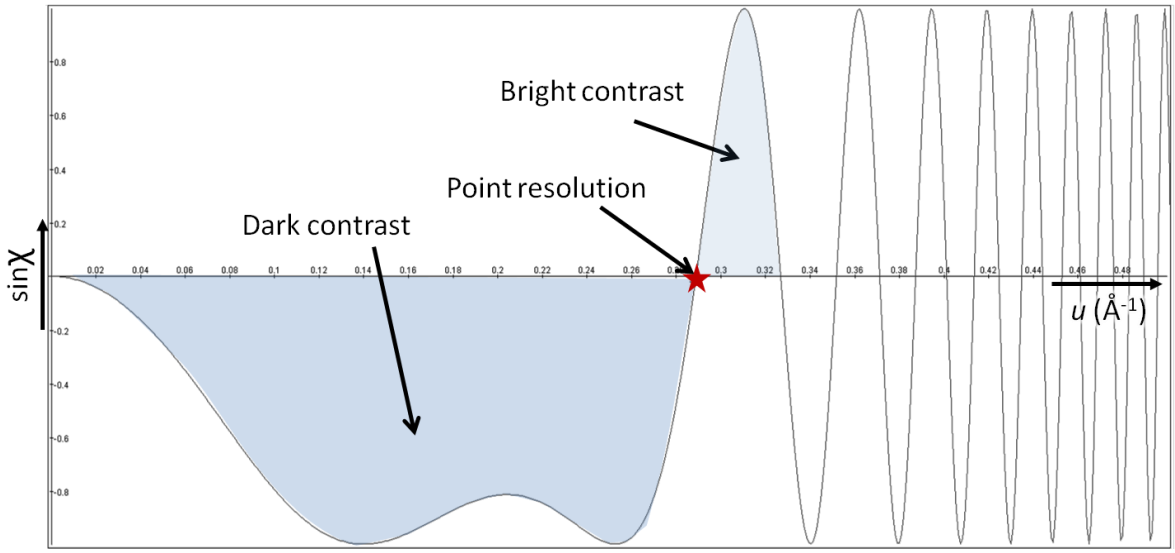


Figure 20) Example of a visualisation of a CTF from a HRTEM. Point resolution is highlighted by a red star.

Figure 20 was created using CTF simulation software designed by Jiang *et al.*[135]. This plot indicates the maximum point resolution of the microscope under certain conditions, highlighted by the red star in Figure 20.

This information can be used to maximise the interpretability of the data taken. Figure 20 demonstrates how contrast changes in high-resolution images can be obtained and explains how dark and bright contrast in an image can occur. When sinχ is negative (giving a positive phase contrast), atoms appear dark, whereas when sinχ is positive (giving a negative phase contrast), atoms appear bright[134]. In short, a small change in focus (which changes sinχ) can denote the type of contrast that is gained, as demonstrated in Figure 21 which shows the same area of graphene imaged at slightly different defocus values to produce both dark and bright atomic contrast.

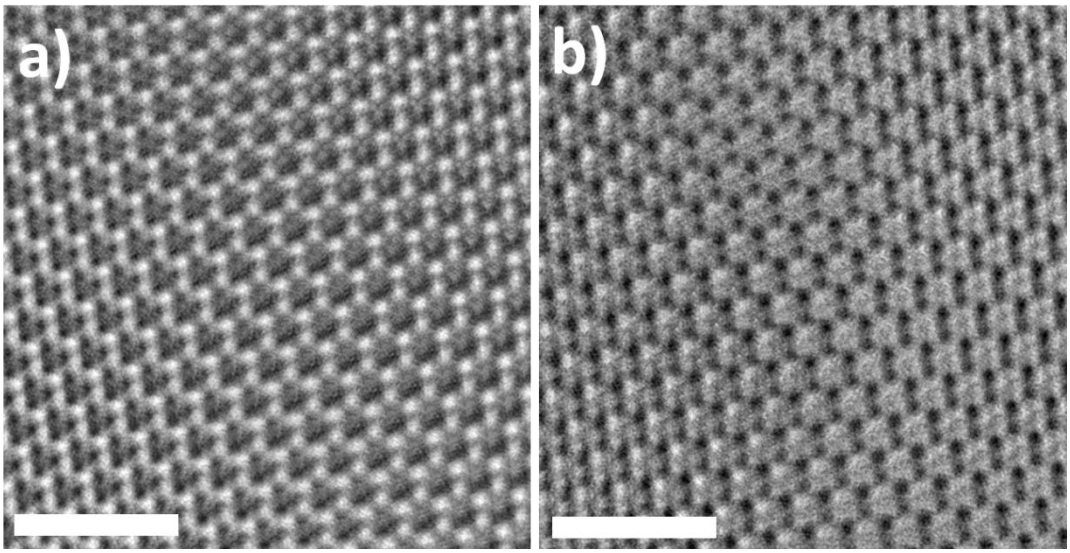


Figure 21) HRTEM images of graphene at different focuses resulting in a) bright atomic contrast and b) dark atomic contrast. All scale bars are 1 nm.

Higher accelerating voltages can provide higher resolution due to the de Broglie relation, however, graphene is susceptible to beam damage so imaging is limited to 80 kV[136]. Therefore high-resolution imaging, and the maximum point resolution, is heavily reliant on both aberration correction and defocus. Objective lens stability is especially important as lens aberrations cause a significant reduction in resolution. Some aberrations can be easily corrected, such as 2-fold astigmatism and coma, however higher-order aberration correction is more difficult.

In this thesis, it was not necessary to gain the resolution shown in Figure 21 as larger scale imperfections in graphene were being characterised. Figure 21 does however demonstrate the capability of the microscope used.

2.2.3.1 Aberration correction and monochromator use

Aberration correction refers to the extra tuning ability of a microscope to produce a more coherent electron beam for imaging and hence is a method for further improving resolution. It has already been shown that the phase-shift and hence microscope resolution is directly affected by spherical aberration, C_s. As well as C_s, aberration correction software can tune additional aberrations that hinder resolution in practice. Corrector software analyses the extent of aberrations in the electron beam, detecting up to 6-fold aberrations using the FFT of the image. The aberration analysis can then be assessed and those aberrations that are hindering the ideal beam shape are then corrected for. The corrector analysis produces a "tableau" of smaller FFTs that have been taken from various tilt angles as shown on the right in Figure 22. This tableau was taken at a tilt angle of 35 mrad.

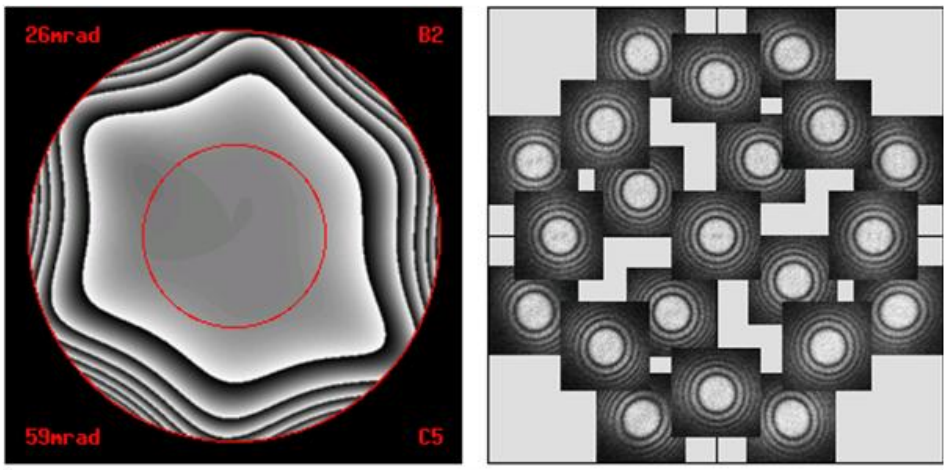


Figure 22) Left – aberration corrector software analysis of Right – tableau of FFTs to produce a sweet spot of 26 mrad. Outer tableau limit (maximum tilt angle) was 35 mrad.

The average of the aberrations detected in the FFTs produce the analysis shown in the left in Figure 22 which details how much of the beam is coherent, denoted by the size of the red circle, or "flat phase". The more uniform and symmetrical the FFTs are across the tilt angle analysis, the larger the flat phase or "sweet spot" for imaging.

Higher spatial frequencies can also be gained by using a monochromator which can further reduce the energy spread of electrons. This is a mechanical addition, at the very top (or bottom) of the microscope that acts similarly to an aperture. It is a small "slit" positioned shortly after the emitted electrons that immediately "cut off" a large part of the electron beam, resulting in a more uniform beam of electrons with a reduced energy spread. Combining this with aberration correction results in a highly-aligned electron beam capable of the highest resolution atomic imaging. Without a monochromator to initially reduce the energy spread before beam alignment, C-C spacing contrast (like that observed in Figure 21) would be difficult to obtain.

In this thesis, both a monochromator and aberration correction were used to obtain high-resolution data.

2.2.4 HRTEM imaging of graphene

This section will first outline the experimental details of the HRTEM work undertaken in this thesis followed by an outline of some common challenges that can occur during HRTEM graphene imaging.

2.2.4.1 HRTEM experimental details

2.2.4.1.1 TEM operation

In this thesis, graphene samples were analysed using a JEOL JEM-2200 MCO field-emission gun TEM operated at 80 kV. Aberration correction was undertaken using a CEOS system and a monochromator was used with a 3μm slit which reduces the energy spread to approximately 143 meV. When a monochromator was used, an additional aperture was not needed. Images were recorded using a Gatan Ultrascan CCD Camera with optimised acquisition times for the sample.

2.2.4.1.2 Graphene synthesis and transfer for TEM

For HRTEM analysis, FLG was synthesised using the CVD system described in Chapter 2. Clean Cu foil (*Alfa Aesar*, 99.999%) was annealed for 30 min under 500 sccm H_2 at 1035°. The growth

stage was then undertaken for 15 minutes under 5 sccm CH_4 and 300 sccm H_2 before cooling under argon at room temperature. The time was kept to 15 minutes to produce hexagonal domains of slightly below full-coverage so that graphene domain boundaries could be more easily identified at low magnification. This resulted in a sample of FLG with some areas of monolayer graphene.

A sample of commercial monolayer CVD graphene was obtained from Graphene Supermarket (2x2 inches, on Cu foil). All graphene samples were transferred to TEM grids by the method described previously in Figure 19. Prior to imaging, graphene samples were baked overnight in vacuum at 180 °C to limit amorphous contamination.

2.2.4.2 Common challenges in graphene imaging

Before explaining how HRTEM graphene data is interpreted, it is worth mentioning the difficulties involved in the HRTEM imaging of graphene.

Firstly, graphene transfer to a TEM grid is a delicate, and often unsuccessful process, as described previously. Additionally, different TEM grids can yield different results. Most grids have areas of amorphous material (such as carbon or silicon nitride) that provide support for the sample, but over which high-resolution imaging is problematic as the extra amorphous background makes the atomic structure unresolvable. Holey carbon grids, like those used in this thesis, have holes in the amorphous carbon where high-resolution graphene imaging is possible.

This thesis aimed to characterise specific areas of graphene samples containing features already existing, such as merging graphene domain boundaries. It is difficult to ensure areas of interest lie over carbon "holes", and it is common to find areas of interest that lie over amorphous carbon, so it is often pot-luck whether certain areas can be effectively imaged.

2.2.4.2.1 Sample damage and contamination

Finding a potentially interesting and imageable area is only the first stage in the imaging process. Graphene, like most materials, can gain amorphous contamination over time. It is often common practice to "beam shower" an interesting area of the sample with the electron beam to

remove and immobilise some of the amorphous carbon contamination for more efficient imaging. This is done by irradiating a larger area of sample at a lower magnification before high-resolution imaging is undertaken. However, it was found that there was a threshold of time when beam showering proved either beneficial or detrimental. In cases where either the beam shower was too long or in areas where contamination was too great, the beam irradiation not only attracted more contamination, but cause damage to the sample. Figure 23 demonstrates how a beam shower has destroyed an area of graphene. Both amorphous and metallic nanoparticle contamination was present in this area prior to irradiation. It is possible to see that the damage that has occurred is limited solely to the area where the sample was being irradiated and mimics the shape of the imaging beam itself (Figure 23a and b). It is possible that, due to the increased metallic contamination in this area, the particles catalysed the degradation of the graphene and hence caused the breakdown of the lattice as shown in Figure 23c.

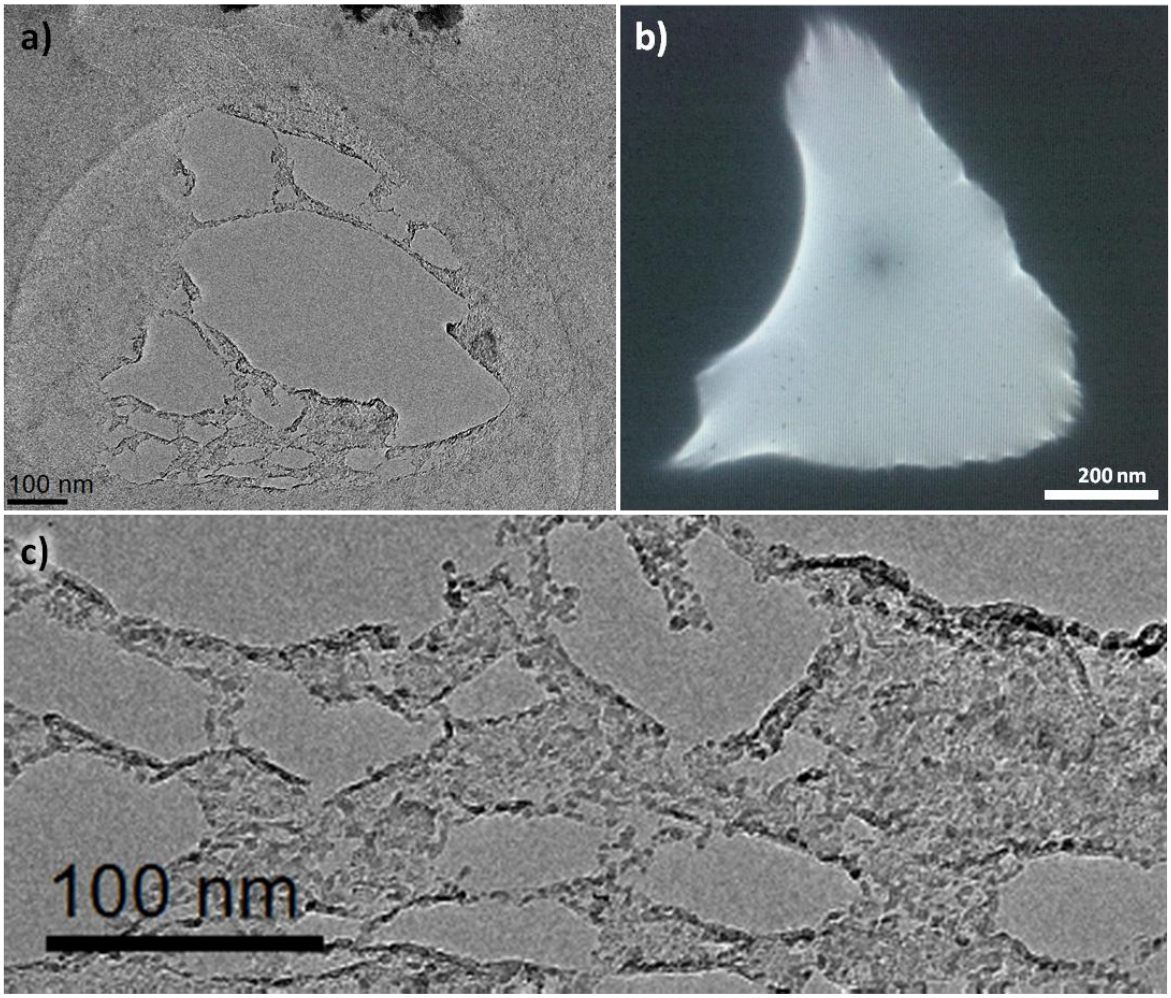


Figure 23 a) Beam damage observed in the exact shape of b) the electron beam used during beam showering. c) Higher magnification image of accumulation of nanoparticles in damaged area of graphene.

Foreign metallic particles are a common feature in TEM samples of carbon nanomaterials. Nanoparticles can originate from the synthesis process or, in the case of graphene, from the etching process of the metallic substrate during graphene transfer. Similarly to carbon nanomaterials, nanoparticles can also be unstable under the electron beam. Figure 24 shows the rapid movement of a particle during beam irradiation. This image was taken from an area of the damaged graphene shown in Figure 23. The fact that these particles are so mobile suggests that their reactivity under the electron beam catalysed the graphene damage.

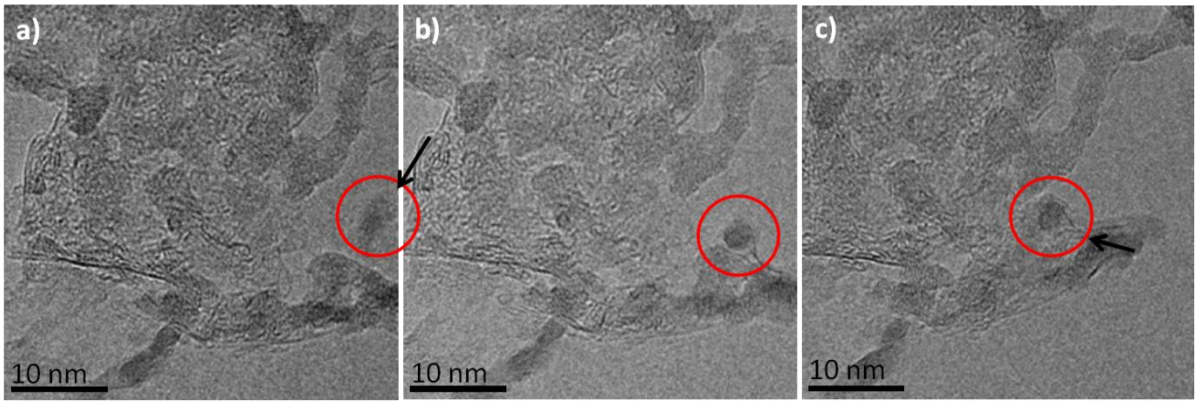


Figure 24 a-c) Sequence of nanoparticle mobility; red circles highlight the position of one moving nanoparticle, black arrows illustrate the direction of movement.

Beam irradiation can have an effect on many materials regardless of contamination. During this thesis, an *in situ* study of carbon NanoBuds was undertaken to determine more information on the bonding nature of the fullerene to the single-wall CNT. It was observed that the NanoBuds evolved over time under beam irradiation[126] (Figure 25, reproduced with permission).

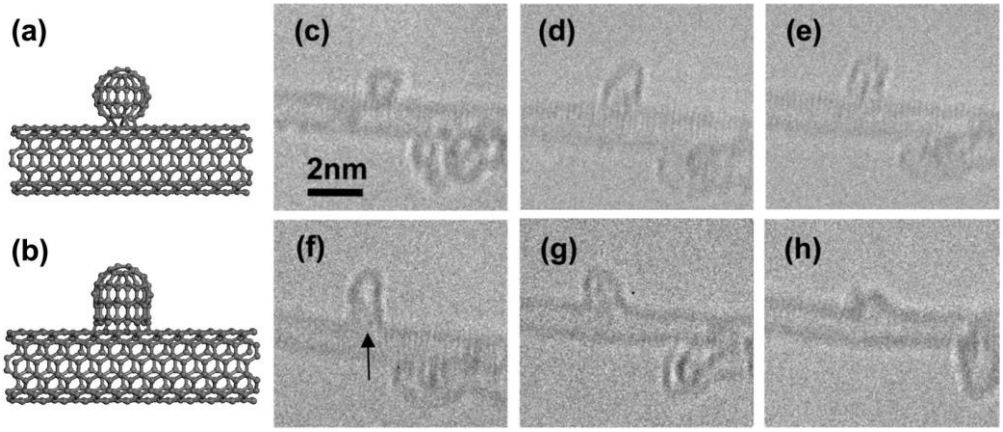


Figure 25 a) Representation of a NanoBud (fullerene attached to a SWCNT), corresponding with c) starting material. b) Representation of transient structure of evolved NanoBud (c-h) TEM images of evolution of NanoBud structure under electron irradiation.

Previously, it has been shown that imaging defect-free single-wall nanotubes (SWNTs) and graphene using an accelerating voltage of 80 kV reduces knock-on damage caused by the electron beam[136], however defective SWNTs and fullerenes are still vulnerable to damage[137–140]. Therefore, it could be expected that carbon NanoBuds would be susceptible to damage via electron irradiation. Figure 25 shows how a NanoBud was observed to evolve into several geometries over time, without the presence of any visible catalyst, apart from that of the

electron beam. This result indicates that, using electron irradiation, carbon NanoBuds could be a useful precursor in the synthesis of nanotube junctions.

Similarly, beam damage in graphene is not always catalysed by nanoparticles. It is common practice to irradiate a graphene lattice to produce a defect and image the outcome[141,142]. Figure 26 shows how a hole in FLG evolves over time under beam irradiation and hence demonstrates the sensitivity of graphene whilst imaging, even at 80 kV, if defects are present.

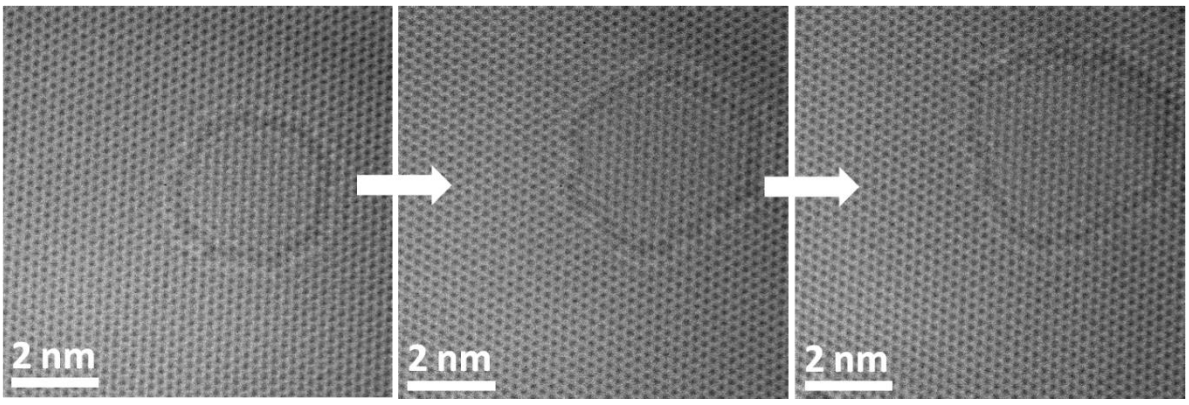


Figure 26) HRTEM images of evolving hole in FLG during beam irradiation.

Thus, beam catalysed damage was an additional obstacle to overcome during TEM imaging in this thesis, especially as defective regions were often the areas of interest.

In summary, excluding electron beam alignment and aberration correction, the challenges for graphene imaging in this work have been four-fold: success of the graphene transfer, obtaining an area of interest over a vacuum hole, sample contamination and damage from beam irradiation. These obstacles along with electron beam alignment and aberration correction ensured data collection was both complex and often problematic.

2.2.4.3 Interpreting HRTEM Graphene Data

Contrast in TEM images can be difficult to interpret. This is especially the case when imaging phenomena which have not yet been fully characterised. Clean, monolayer graphene is easier to interpret than areas of FLG for example, or areas of overlapping and wrinkles. It is therefore necessary to employ other methods of gaining more information to start probing more detailed structure. Although a TEM image alone can provide valuable information on a sample, there are

techniques that can be used to gain more detailed data than just the raw image. These techniques can also enable images of poorer sample areas to be interpreted.

Firstly, and perhaps most simply, the use of z height in imaging can provide vital structural information. Not only can it result in opposing contrast for the same sample as previously shown in Figure 21, imaging the same area of sample through various heights, identifying how the image comes in and out of focus at different points, indicates the z structure of the sample and can hence provide information on the layering of different features and sample thickness.

Another valuable tool for image interpretation is the use of the FFT of the image. At high resolution, FFTs provide reciprocal space information from local regions, some examples are shown in Figure 27. The number of hexagonal patterns in the FFT can indicate layer number and provide information on the stacking of graphene layers. Figure 27a shows an example of a monolayer FFT with indexed lattice spots. Unless otherwise specified, all other FFTs in this thesis have been assumed to be indexed in this way. Figure 27b shows an example FFT from misaligned FLG, with multiple sets of hexagonal lattice spots visible. Figure 27c demonstrates how Meyer *et al.*[143] showed how the intensities of lattice spots in the diffraction pattern of graphene differ for monolayer and aligned bi-layer graphene. For monolayer graphene, the lattice spots in the centre-most ring of the FFT are more intense that those in the outer ring, and vice versa for bi-layer graphene. This contrast difference enables identification of layer number in TEM when mono or bi-layer graphene exhibit very similar contrasts.

Additionally, the distances between lattice spots provide information on lattice strain as they are directly related to the reciprocal lattice parameters between planes. The use of a white dotted circle was used frequently in this thesis to visually demonstrate areas of strain in images by highlighting the lack of perfect symmetry in the reciprocal lattice (as demonstrated in Figure 27d and e, where Figure 27e shows a deviation in the (01-10) direction outside the dotted circle). It is noted that small changes in a FFT could be attributed to other factors (e.g. beam aberrations). However, further use of this method in this thesis to identify changes in lattice

parameter has proven to fit with expected values, and therefore it has been accepted that measured values from FFTs can be trusted. The use of FFTs is therefore an invaluable tool in HRTEM graphene imaging and notably in this thesis in determining defect structure.

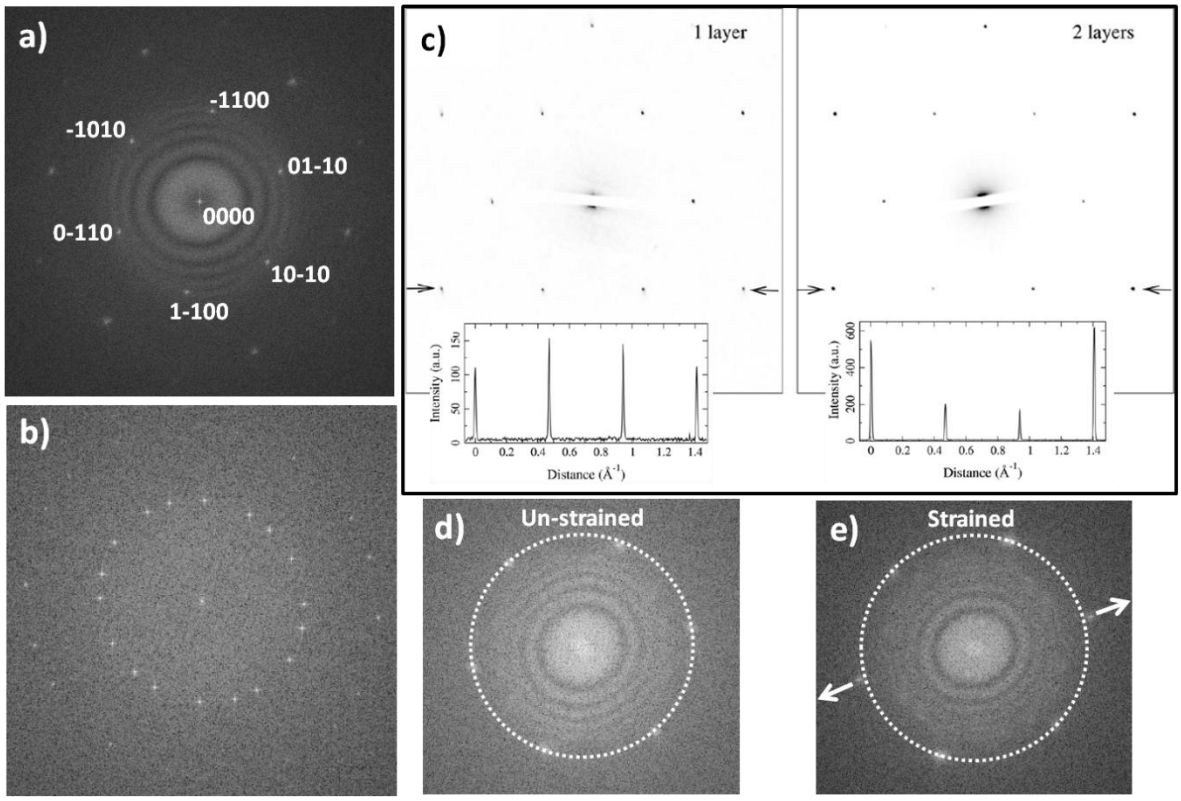


Figure 27a) Monolayer FFT with indexed diffraction spots. b) FFT of misaligned FLG. c) Reproduced with permission from ref[143]. Diffraction of monolayer and bi-layer graphene with corresponding contrast profiles of arrowed regions in the diffraction pattern. d) FFT of an un-strained graphene lattice. e) FFT of a strained graphene lattice with a deviation from the symmetry of the white dotted circle, highlighted by white arrows.

Portraying digital images as FFTs is an incredibly useful tool as other algorithms can be applied to extract as much data as possible. An extreme example is outlined in Figure 28 to illustrate the capabilities of this technique. Figure 28a and b show an image and its corresponding FFT respectively. Figure 28a appears un-interpretable due to a layer of amorphous contamination, and it is only the use of the FFT that indicates the presence of a graphene lattice. The FFT in Figure 28b indicates misaligned graphene layers as well as rings of amorphous material which is the contamination that can be seen in the image. By selecting solely the diffraction spots from the FFT (Figure 28c-d), masking the data from the amorphous background (Figure 28e), the inverse FFT can be calculated to reveal the graphene lattice without the amorphous contamination (Figure 28f and at higher magnification in Figure 28g).

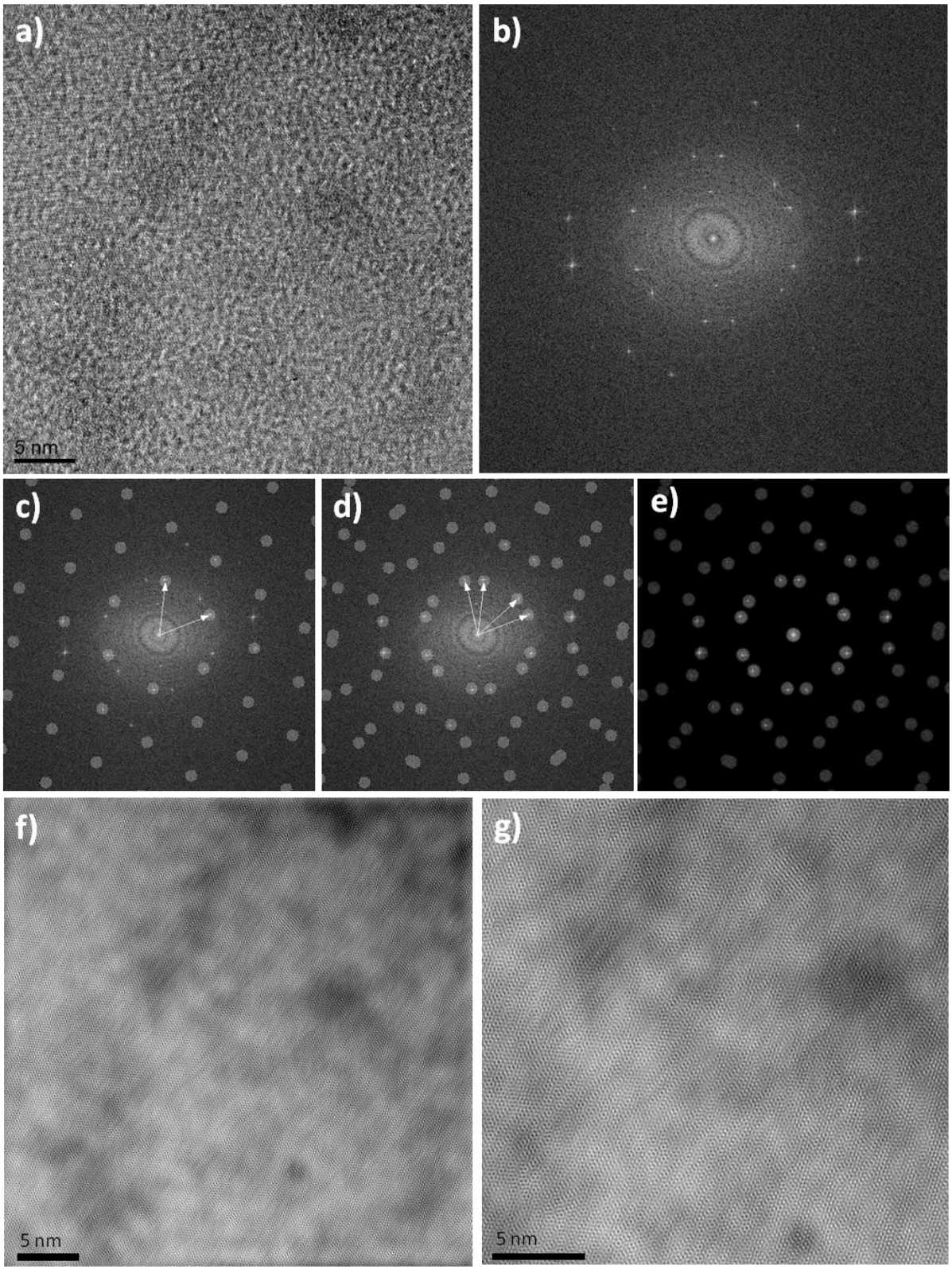


Figure 28a) Raw TEM image where a graphene lattice is not visible through amorphous contamination. b) FFT of image a). c-d) Procedure of masking of lattice spots. e) Final modified FFT with masks in place. f-g) Inverse of masked FFT to produce image visualising lattice. g) Higher magnification image of inversed masked FFT, showing moiré fringes and confirmation of misaligned bi-layer graphene, previously invisible in raw data a).

The resulting image (Figure 28f-g) distinctly shows a lattice structure, and corresponds to the misaligned graphene layers. The residual data that remains in the new image is more useful to the experimentalist, and highlights features that may not have been visible previously. Similarly, specially designed filters can be applied to FFTs to "polish" the data or further highlight interesting areas. Applying extreme filters to highlight areas of interest is a useful tool; however they are not commonly used to make final conclusions if the resultant images are significantly altered compared to the raw data.

The combination of these interpretation techniques enables the extraction of the maximum information possible from one TEM image. These procedures are used throughout the data analysis in Chapters 3, 4 and 5 with the raw data and corresponding FFT analysis being most commonly used and masking filters applied only to initially interpret images.

2.2.4.4 Accuracy and error in data collection from TEM images and FFTs

A large amount of information can be obtained from HRTEM data, both using the raw image and by utilising the FFT as demonstrated previously. However, as with most measurements, there is a question of accuracy.

The information ultimately recorded in an image is determined by its pixel resolution. In turn, the information extracted from an image is limited by the ability of a programme to measure and extract information from the number of pixels. HRTEM images in this thesis are 1024x1024 pixels.

To extract reliable data from images, accurate calibration is imperative, which can be constructed using known values and corresponding features in images; such as graphitic spacings or bond lengths. Unfortunately this calibration is limited to the assumptions that the observed spacings are equivalent to values from the literature and that they are not for example, distorted bond lengths or a different material entirely. However, these distortions are likely very small and are negligible when calibrating most images. It does mean however, that the calibration is as accurate as the value that has been used, i.e. if 2.13 Å has been utilised as

the calibration value, distances can only be quoted to a maximum of two decimal places. For the highest resolution images, it is possible to be this accurate with calibrations as atomic spacings are visible. However, for lower magnifications this detail is not easily seen therefore one decimal place is often used.

Calibration at low magnifications cannot utilise known material spacings as these features cannot be seen. In this thesis, the 2200MCO TEM that was used was calibrated for low magnification images by using a calibration sample (Au cross grating) of known spacings at various magnifications. These calibrations are then extrapolated by the imaging software, Digital Micrograph, for additional magnifications in between. For low magnifications where material spacings are not apparent this accuracy is sufficient. Although these calibrations can be extrapolated for higher magnifications, it is good practice to recalibrate images where known spacings are seen for higher accuracy.

Accurate calibration is what limits distance measurements in images. However, measuring angles are limited by the pixels, calibration and capabilities of the software. Digital Micrograph, the software used to process TEM images in this thesis, is limited to a 0.2° increment. Therefore the accuracy and error in measurements is constrained by this limitation. However, an accuracy to 0.2° is a fairly good indication of structural changes in a sample and by taking measurements multiple times, sometimes either side of a point if necessary, average angles can be calculated. This has been a reliable method as throughout this thesis the data using such accuracy corresponds well to expected theories.

It is also worth noting that with any measurements and calibrations undertaken on images, an element of human error is present. In this thesis, measurements were taken multiple times to eliminate this error as a large contributing factor. In addition, measuring distances was done using contrast line profiles, making it easier to distinguish the centre of features being measured. In FFTs, angles and distances were measured utilising both spots of the same symmetry. This way, the drawn line must cut through three separate points.

2.3 Summary

This chapter has described the key characterisation techniques used in this thesis and how graphene has been synthesised and transferred. The challenges associated with graphene synthesis, transfer and TEM characterisation, along with variations that can be observed in graphene synthesis, have also been introduced to ensure the full interpretation and understanding of results described in the following chapters. This preliminary work allowed a thorough understanding of CVD synthesis and graphene characterisation prior to undertaking further investigations.

3 HRTEM of imperfect CVD graphene: Part I

This chapter describes Part I of the high-resolution characterisation of imperfections in graphene by TEM. A brief literature review will detail the background to current research after which defects observed during this thesis investigation will be discussed. Results are divided into two chapters; Part I and Part II. The first section analyses common imperfections observed in graphene and the TEM contrast they can produce, hence ensuring that Part II is more easily explained and understood. The second section analyses several examples of "imperfect" graphene domain boundaries, detailing the differences between what has been observed in this thesis and published work.

A note on terminology: The term "defect" in this thesis will not refer to vacancies or dislocations on the smaller scale in the material, but will refer to the larger imperfections that can occur. The terms "defect" and "imperfection" have been used interchangeably to describe any area of graphene that is not a pristine lattice.

3.1 Introduction

3.1.1 Motivation

As shown in Chapters 1 and 2, most CVD synthesised graphene contains defects such as wrinkles. A large majority of the experimental literature on defects is governed by those which are induced artificially, via electron beam irradiation. This thesis aims to examine the imperfections which naturally occur in graphene samples and to therefore produce characterisation that is representative of the real material. CVD graphene is grown and almost always transferred off the mother substrate. Therefore, defects from both synthesis and transfer procedures are likely to be present in any resulting sample and hence neither must be overlooked.

This chapter will analyse the presence of imperfections in two CVD graphene samples; FLG and monolayer graphene. The aims are to define the structure of the characterised features, recognise correlations and differences with the literature and determine the capability of HRTEM as a characterisation technique to help define defective graphene. It is believed that the features discussed in this chapter will be relevant to both monolayer and FLG due to the high presence and probability of defects in all graphitic material.

As previously discussed, FLG is largely under-characterised compared to monolayer graphene, but is still useful for many applications. It is therefore of interest to further characterise this material and understand any common imperfections that may be occurring. In addition, the synthesis of FLG is prone to more defects at domain boundaries than monolayer synthesis due to the fact that more layers must atomically bond on merging. Imperfect domain boundaries will be discussed in Part II.

Characterising defects in monolayer graphene was also a sufficient starting point for analysis as the results are more easily interpreted in TEM. The monolayer sample that was characterised in this chapter was from a commercial supplier. This was done to understand the imperfections present in even the commercial market.

3.1.1.1 Background literature

As previously described in Chapter 2, imperfections in graphene can be induced by various processes, such as during growth, transfer or from interaction with foreign materials such as nanoparticles. It is worth noting that publications on graphene defects increased in 2014, which may be indicative that defect characterisation is gaining recognition and is becoming more important in the research field.

The large majority of publications on graphene defects are based on computer simulations to either predict a change in properties or the defect structure. From these papers, it is now widely accepted that defects such as wrinkles affect the electronic, mechanical and functional properties of a perfect graphene sheet[144].

Work that has simulated wrinkle structures[145–151] has generally defined three types of graphene wrinkle that can occur, as shown in Figure 29. From these publications, most simulations therefore focus on these three main types of defect.

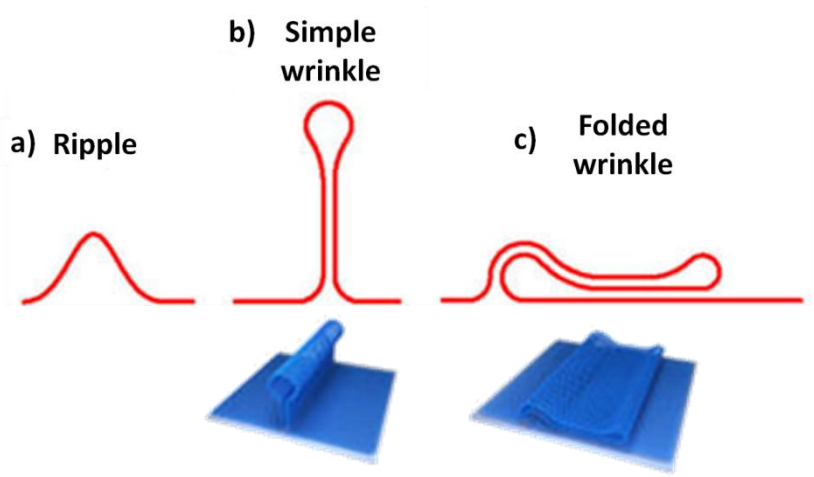


Figure 29) Reproduced and adapted with permission from refs[84,152]: three defect structures of graphene. a) a ripple, b) a simple wrinkle and c) a folded wrinkle.

Figure 29a shows a ripple in a graphene sheet and Figure 29b shows a simple wrinkle. A ripple becomes a simple wrinkle when it becomes more stable for the distance between the raised lattices either side to equate to the van der Waals spacing (0.335 nm). Figure 29c shows a possible consequence of Figure 29b; a folded wrinkle. The driving force for a folded wrinkle is thought to be a competition between van der Waals forces and the elastic bend in the graphene lattice[147,148].

From these and similar structures, changes in electronic structure have been both predicted and experimentally shown[89,145,153–156]. Examples include; a difference in thermal conductivity[157,158], decreased corrosion and oxidation resistance[159,160] and change in catalytic activity[161]. Wrinkles have shown to be more prone to hydrogen etching after growth[162] and have been used as nanoparticle binding sites to more easily identify the defects within the graphene sheet[152], demonstrating the difference in binding energies and the overall chemistry of defects compared to the bulk.

Both scanning tunnelling microscopy (STM)[151,163] and atomic force microscopy (AFM)[83] have been used to further characterise defects. However both techniques have not provided conclusive structural information on exact defect structure.

Raman spectroscopy has been used to visualise defects and the defective lattice by mapping the G band as shown in Figure 30; it demonstrates how wrinkles seen in the corresponding SEM image yield a varying Raman signal, indicative of a change in quality over defective areas. However, Raman, along with SEM and optical microscopy, is still limited by resolution in determining the finite structure and hence type of defect. (Resolution being the smallest distance that can be distinguished between two points.)

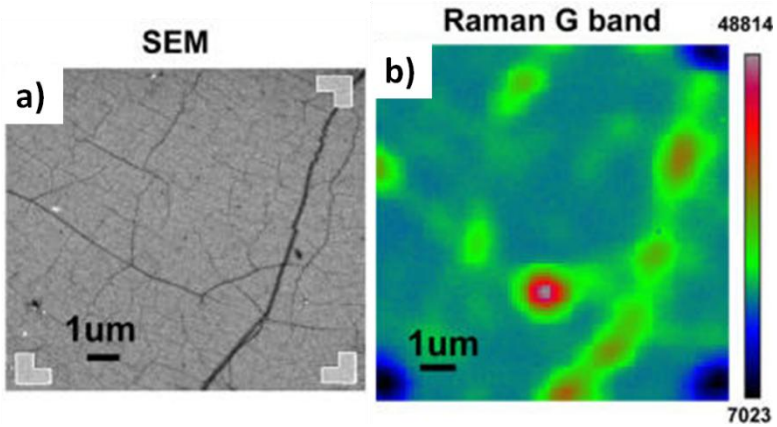


Figure 30) Reproduced with permission from ref[84]. a) SEM image of CVD graphene on SiO_2/Si substrate. b) Raman G band intensity map of the same area demonstrating a change in Raman signal over wrinkles.

High-resolution TEM characterisation can yield detailed structural information from both the image contrast and the FFT information. As yet, HRTEM analysis has not been widely used to characterise graphene defects[125,164–167], with even fewer papers using the technique to help define structure[164–166]. Some examples have been shown in Figure 31.

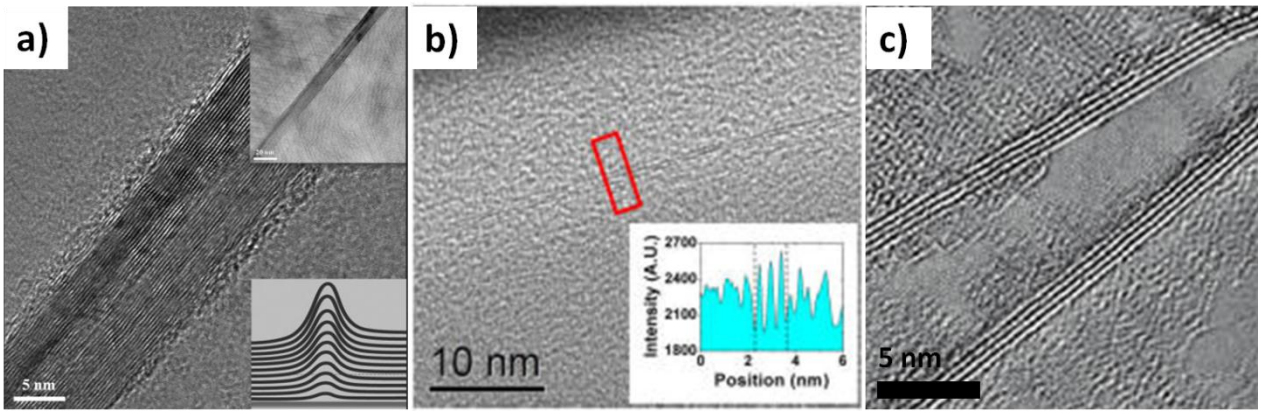


Figure 31) TEM characterisation of wrinkle defects in the literature. a) Reproduced with permission from ref[125] b) reproduced with permission from ref[84] c) reproduced and adapted with permission from ref[164].

Figure 31a and b are examples of graphene wrinkle characterisation where the image is used as a confirmation of a defect with a speculation on structure. Figure 31c is an example of a folded wrinkle that has been discussed in detail and will be referred to later in the chapter in comparison with some experimental results.

The capability of HRTEM to interpret defect structure is much more promising than the use of other techniques and has therefore been used as the primary characterisation technique to investigate defect structures in this project.

3.2 TEM imaging of imperfect graphene

The results of Part I will focus on more interpretable, simple features found in graphene samples before going on to analyse more complex areas. It will be split into several sections:

- Overlapping areas
- Folded wrinkles
- Simple wrinkle contrast
- Periodicity along graphitic planes
- Sideline periodicity
- Inter-graphitic plane contrast
- Linear moiré patterns.

3.2.1 Overlapping areas

Overlapping in graphene can occur through the transfer process or the merging of individual graphene domains (as discussed in more detail in Part II). Figure 32 shows some examples of overlapping areas and demonstrates how FFT analysis can provide valuable information to determine the structure of the feature. Upper and lower FFTs refer to FFTs taken above and below each of the line features in Figure 32a-c.

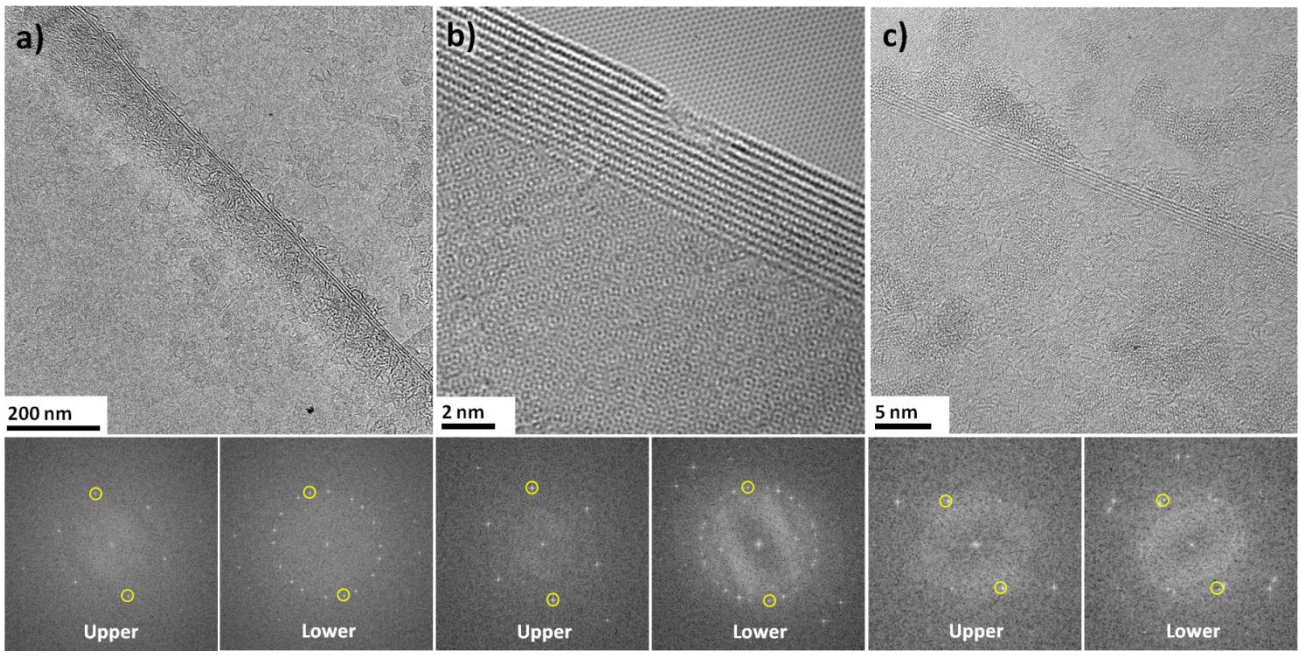


Figure 32a-c) TEM images of overlapping areas of monolayer and few-layer graphene. Corresponding FFTs of above (upper) and below (lower) the overlap are pictured below the relevant image. In all cases, the FFTs from below the feature show more lattice spots, along with those seen in the above FFT (highlighted by yellow circles), indicating an overlapped region.

The FFTs in Figure 32 show how the upper lattice is also seen in the FFT of the lower lattice (highlighted by yellow circles), indicating a continuous layer across the entire image and hence an overlapping structure. The graphitic contrast on the edge of a fold can imply layer number of the overlapped region, but may also be a folded region that is overlapped. The TEM image in Figure 32b clearly exhibits a moiré pattern on the overlapped area indicating a difference in graphene lattice stacking in this region. Overlapping graphene was commonly observed throughout all graphene samples characterised and can be easily interpreted using FFT analysis.

3.2.2 Folded wrinkles

Figure 33 shows an example of a folded wrinkle in monolayer graphene, as previously shown schematically in Figure 29c. In this case, it has also been shown more simply in Figure 33c to help visualise the structure.

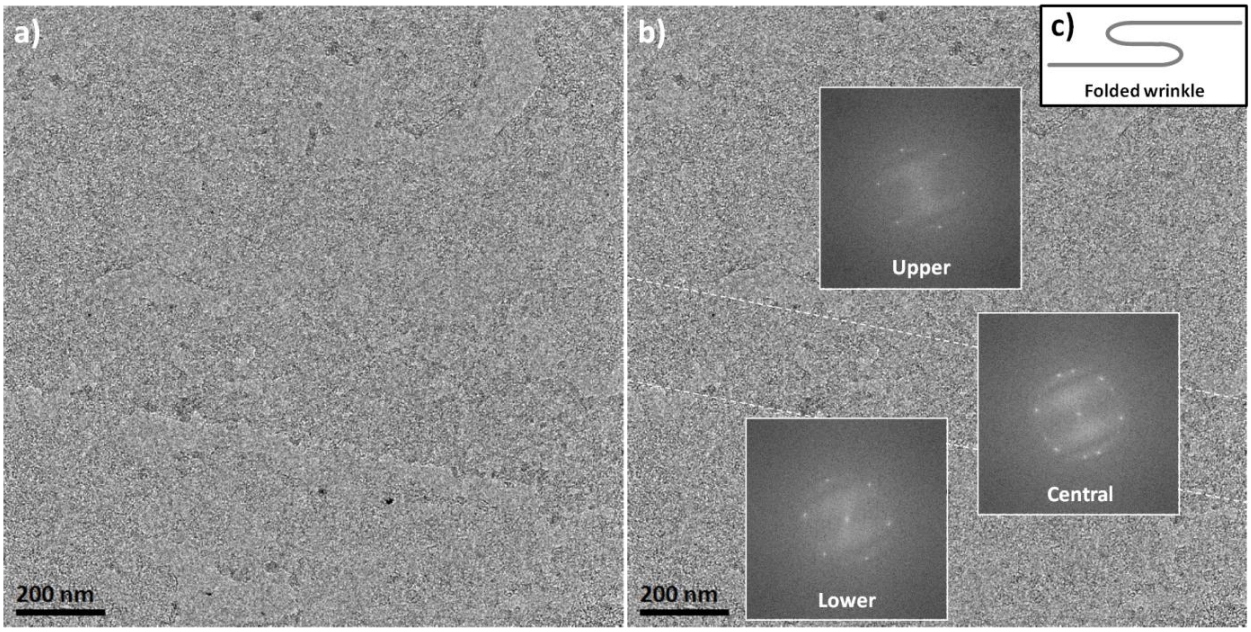


Figure 33a and b) TEM image of area of folded wrinkle. The lines of the fold are highlighted in b) by white dotted lines. The insets in b) are FFTs of the above, central and below areas of the feature. c) Schematic of a folded wrinkle.

The two-line contrast in Figure 33 is parallel and the FFT analysis shows that the lattice remains unchanged above and below the central feature, with an additional set of lattice spots observed in the central region. This is indicative that this feature is occurring within the same graphene flake. This additional lattice is rotated by 19.5° ± 0.7 which implies that the fold rotated by this much upon collapsing, without changing the rotation of the bulk lattice either side. Although such defects are common, often the line contrast is not parallel, as shown in Figure 34.

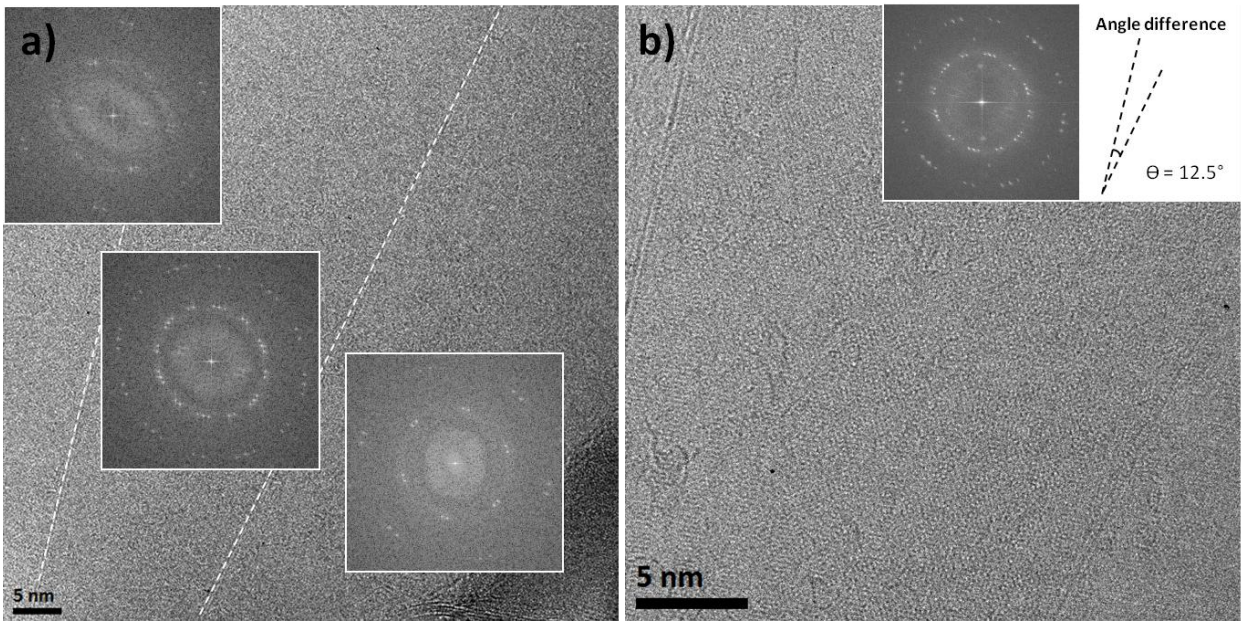


Figure 34a) TEM image of a non-parallel folded wrinkle with FFT insets from respective areas in the image. b) TEM image of the same area at higher resolution showing a moiré pattern in the central area with corresponding FFT of whole image. Inset indicates angle difference between the non-parallel two-line contrast.

Similarly to Figure 33, the FFTs in Figure 34a show additional lattice spots on the central feature of the fold. However, the remaining FFTs also differ. Both FFTs show two sets of lattice spots rotated from each other by 24.2° ± 0.5. This rotation change could be assumed to be two different graphene flakes, however the central feature can provide additional information to disprove this. The FFT patterns either side of the feature are both present in the central FFT, along with an additional set of spots. The additional set of lattice spots is indicative of a fold taking place, as in Figure 33.

The difference in rotation between the non-parallel line contrast of the central feature is approximately 12.5° as shown in the inset of Figure 34b. Measuring the angle difference between the line contrast could enable calculations to determine the change in rotation of the graphene lattice. This has been described previously[164] and is shown in Figure 35.

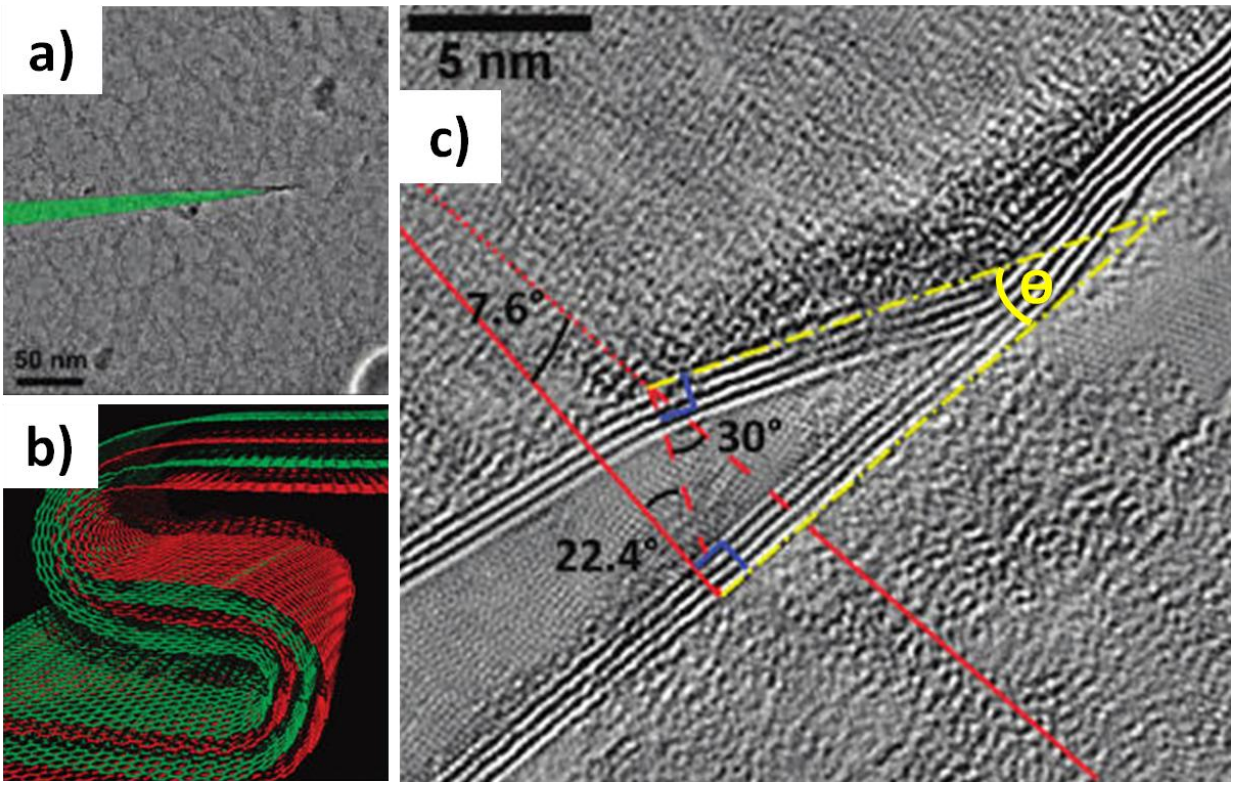


Figure 35) Reproduced and adapted with permission from ref[164]. a) Low magnification TEM image of folded wrinkle, highlighted in green. b) Schematic of likely structure of the rotation fold in a tri-layer graphene sheet. c) High-resolution TEM image of tip of folded wrinkle, highlighting change in rotation between the two rotated lattices.

Robertson *et al*. took FFTs from the regions across a folded wrinkle in Figure 35c, similarly to those in Figure 33 and Figure 34. From these measurements, it was found that the two lattices above and below the fold were rotated from the extra central lattice spot by 22.4° and 30° respectively. The difference between these rotations is 7.6°, which equates to the total rotation change between the lattices either side of fold. Taking parallel lines from the line contrast at the tip of the fold (Figure 35c: yellow dotted lines follow the fold contrast and red lines are taken at right angles to these lines), and then marking the rotation changes from the extra central lattice spot (22.4° and 30°), the lines match up with the overall change in 7.6°. Trigonometry is therefore used to determine that the angle between the yellow dotted lines, and hence the tip of the fold, denoted by θ, is equivalent to the 22.4° angle, or the rotation change in one lattice.

This would therefore imply that in similar defects, a change in rotation angle from the extra lattice spots on the central feature compared to one of the original FFT lattices is equal to the angle at the end of the fold. However, in Figure 34, the lattice rotations from either side of the

central fold were rotated from the extra lattice spot by 5.6° ± 0.6 and 32.1° ± 2.2, neither of which equate to the measured angle of the contrast in Figure 34 of approximately 12.5°. Therefore there must be some discrepancy in the angle measurement. Figure 36 shows more examples of similar features and demonstrates the difficulty of determining an accurately measured angle at the tip of a fold.

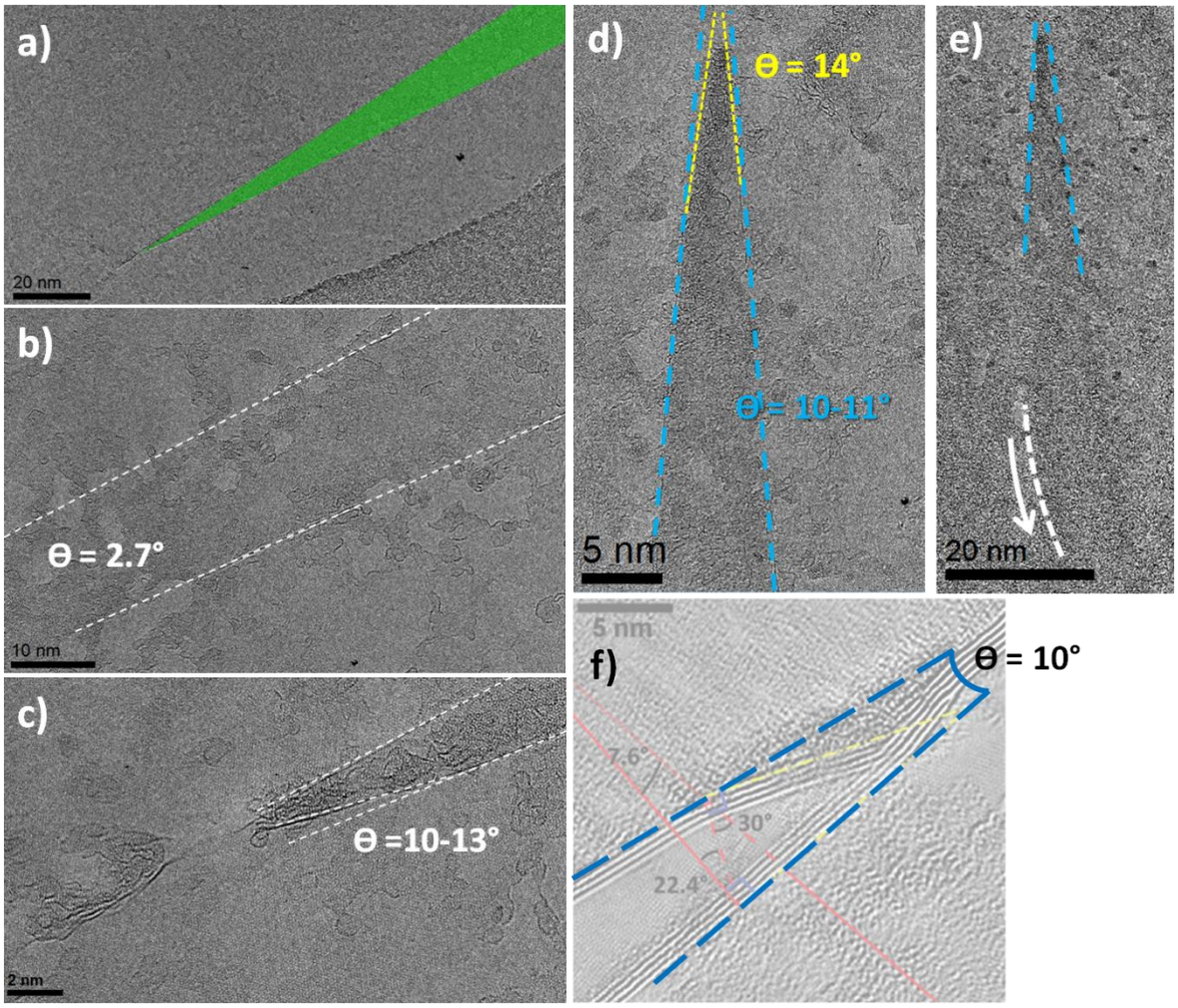


Figure 36) Images depicting the change in angle measurement across non-parallel folded wrinkles, including the discrepancy in determining the angle at the tip of the fold. a) Low magnification TEM image of a rotated folded wrinkle, highlighted in green. b) and c) Higher magnification images of the middle and end of the feature shown in a). d) and e) Second folded wrinkle with various rotation angles highlighted. e) Feature in d) at lower magnification highlighting the curvature that occurs lower down the feature. f) Image from Figure 35c with alternative rotation highlighted equating to 10°. This angle differs from that denoted by the yellow dotted lines equating to 22.4°.

Figure 36a-c shows the same fold imaged at different points. The angle between the line contrast at the centre of the fold in Figure 36b equates to 2.7° whereas the angle measured at the tip of the fold in Figure 36c can be measured to be between 10-13°. Additionally, in Figure

36d and e, the yellow dotted lines measure 14° compared to the blue dotted lines measuring between 10-11°. The FFT measurements from these images using the technique outlined in Figure 35 also predict a value distinct from that which is measured.

It can therefore be concluded that measuring the angle at the end of the fold is not a conclusive indication of the change in rotation between the two lattices, and is especially inaccurate at the centre of a fold. It is clear from these images that after the initial fold, a change in angle is almost immediate. In the case of Figure 36e, even a curvature in the fold can occur, as highlighted by the white arrow. Although the paper by Robertson *et al*. was successful in matching the angle at the end of the fold to lattice rotation, in multiple examples observed in this project this was not the case. Additionally, Figure 36f shows the figure from Robertson *et al*. with an additional angle from the end of the fold highlighted. This further emphasises the ability to define various angles in a TEM image; in this case from 10-22.4°. Therefore for folded wrinkles, FFT analysis (ideally from multiple regions of the defect) must be relied upon to accurately determine the changes in lattice orientation. Hence either HRTEM or accurate electron diffraction is necessary to reliably define defect structure.

As described in Chapter 2, FFT analysis can also provide information on the strain in a system. Predictably, Figure 37 shows that, in the case of a non-parallel folded wrinkle, the most strain is observed around the apex of the fold.

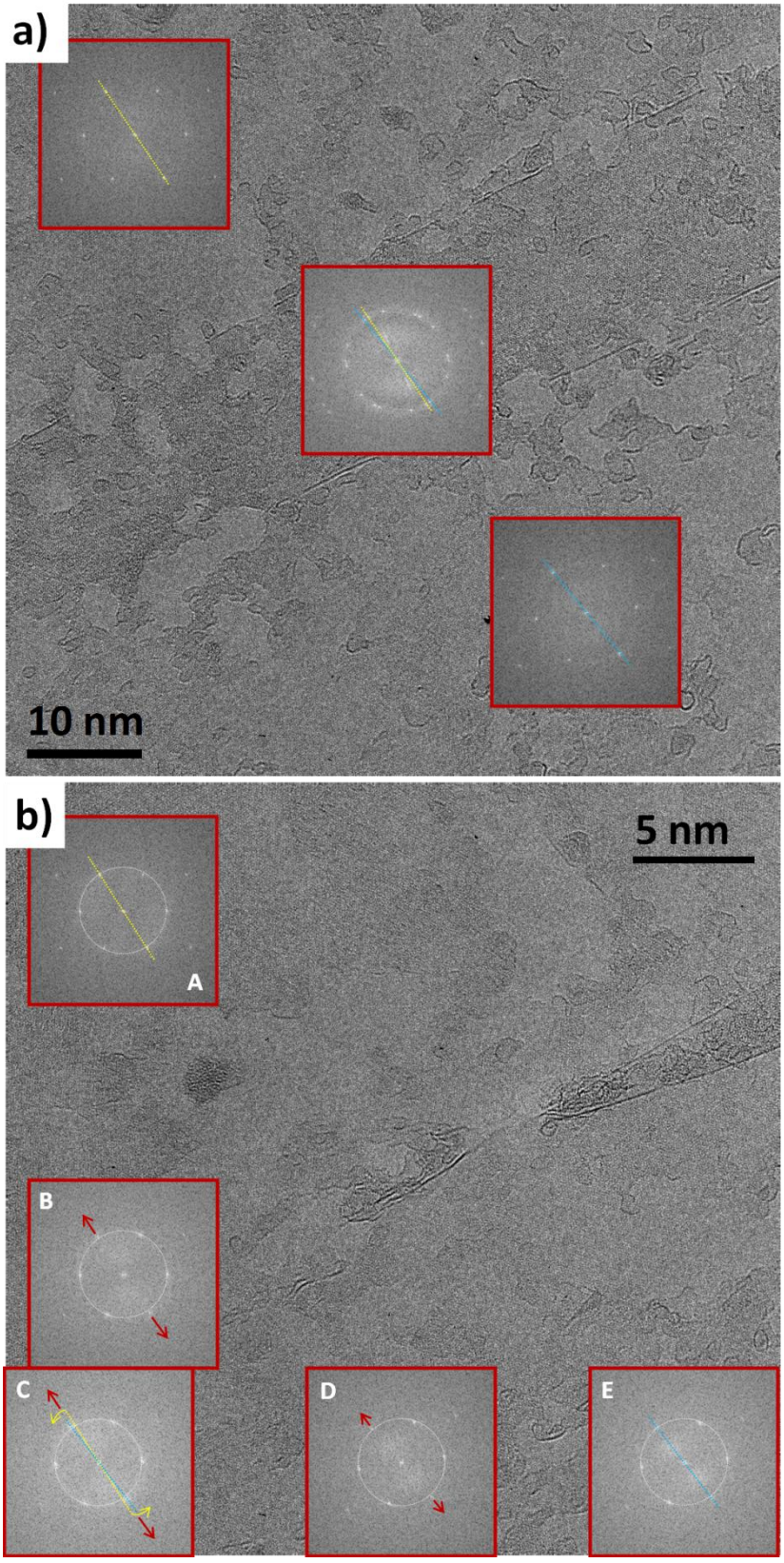


Figure 37) Non-parallel folded wrinkle with FFTs showing change in lattice rotations and strain. a) TEM image of rotation fold with corresponding FFTs from above, central and below fold. b) TEM image of same fold at tip, showing corresponding FFTs. White dotted circles mark a regular, un-strained lattice with red arrows highlighting non-uniformity in the FFT. Yellow and blue lines highlight the angles of the top and bottom lattices either side of the fold respectively.

In Figure 37b, blue and yellow lines highlight the different lattice orientations which are rotated from each other throughout the image between 5.3°-7.6°. Strain can be observed in the FFTs around the area of the fold where there is significant lattice rotation (highlighted by yellow arrows in the FFT). White dotted circles and red arrows help to visualise a deviation from the perfect lattice. FFT measurements indicate more regular lattices in FFTs A and E, those furthest from the rotated fold. In FFTs B-D, changes in lattice parameter have been measured between 6-11%. This change decreases in the FFTs closer to the positions of A and E. What is not clear is whether this strain was the consequence or driving force of the folded wrinkle. However, what is apparent is the discreet change in the strain in a very small area, and the clear resolve of larger strain away from the initial fold. Such effects will undoubtedly have an effect on graphene properties.

Although it has been shown that graphene folds can be eradicated by "stretching out" a wrinkled graphene sheet[168] , it is likely that on an industrial scale defects such as folded wrinkles will still remain. Defects produced from these phenomena , such as lattice wrinkling, can be further examined with HRTEM to extract more detailed structural information.

3.2.3 Simple wrinkle contrast

Wrinkles in graphene sheets can provide useful information on the structure and quality of a graphene sample. Wrinkles in graphene are dominated by the contrast observed for the graphitic planes, similar to that observed in the walls of CNTs. An example of a simple wrinkle in FLG is shown in Figure 38.

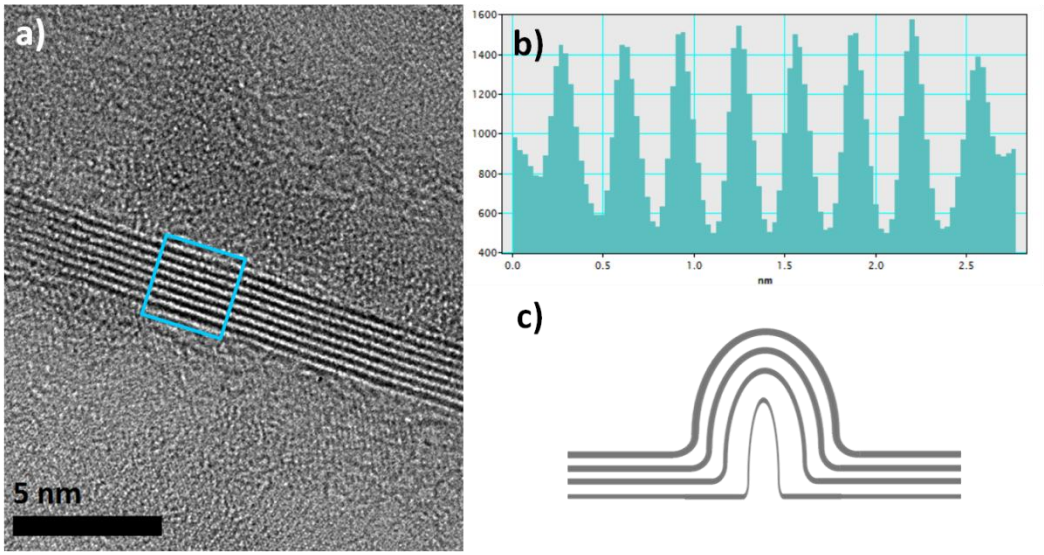


Figure 38a) TEM image of wrinkle in FLG with turquoise box highlighting area where b) line profile was taken. b) Indicates the contrast of the 8 lines. c) Schematic of a similar wrinkle feature.

In Figure 38, the contrast profile from the turquoise box on the centre of the wrinkle shows the distinct periodicity of the wrinkle feature. The spacing is equal to the graphitic plane spacing of 0.34 nm. An 8-layer contrast can be observed in this image, and it is likely that the wrinkle structure is similar to the schematic shown in Figure 38c: a simple wrinkle in 4-layer graphene. Therefore, wrinkle contrast can also give an indication to the number of graphene layers in a sample, as well as the type of defect that is occurring.

3.2.4 Periodicity along graphene planes

During characterisation of defects such as wrinkles, an additional contrast was observed within the main graphitic spacing of graphene layers. This contrast was consistently observed across several samples, including in h-BN which will be further discussed in Chapter 5. The contrast was the appearance of an alternative periodicity, often appearing as aligned spheres or ellipses, separated by a spacing of approximately 0.2 nm, appearing along the graphitic planes separated by the expected 0.34 nm separation. Some example images are shown in Figure 39a and b.

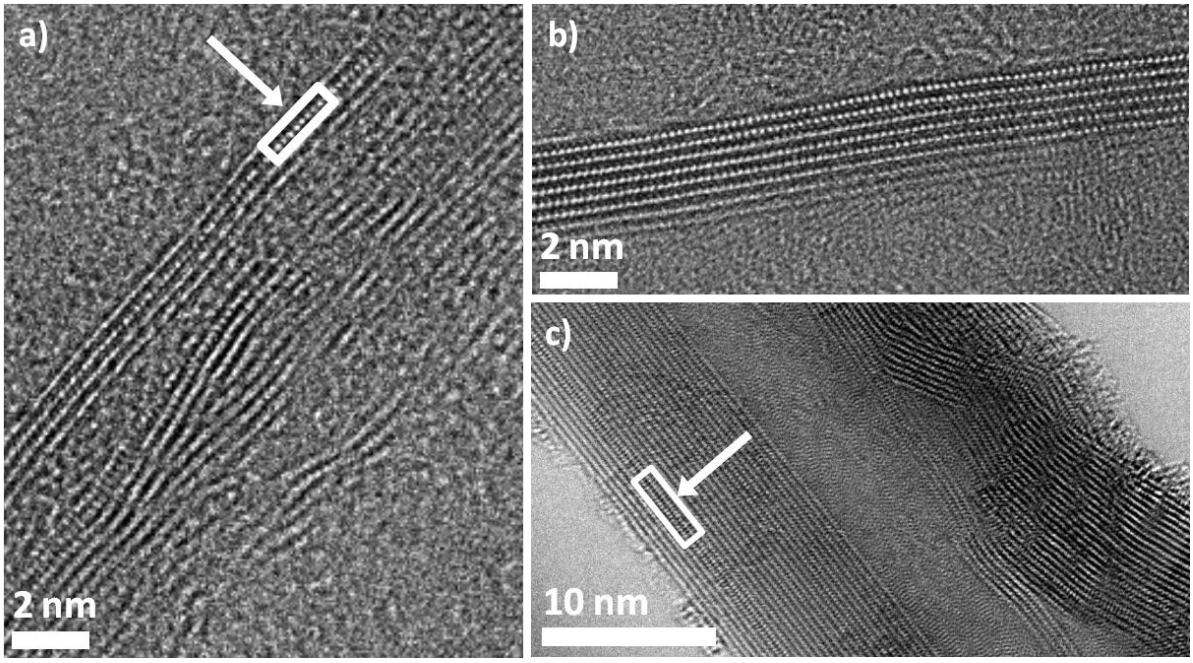


Figure 39a-b) TEM images of graphene wrinkles where a periodicity can be observed within the contrast of the graphitic layers. c) TEM image (courtesy of Dr. Rebecca Nicholls) of a CNT where a white arrow highlights a similar contrast.

Figure 39a shows this periodicity along one graphitic plane, whereas Figure 39b shows this periodicity consistently present throughout a wrinkle feature. The periodicity was often observed on edges as well as on wrinkles and folds. This contrast can also be seen in CNTs, as highlighted by the white arrow in Figure 39c (this image is courtesy of Dr. Rebecca Nicholls). In all cases, the spacing of the graphitic planes still remained consistent at 0.34 nm. Therefore, it can be deduced that this is a characteristic of TEM imaging in graphitic materials as a whole.

Typical periodicity spacings that have been observed are in the range of 0.18 nm-0.23 nm, but most often correspond to between 0.21-0.22 nm. This spacing would be the equivalent of a contrast mechanism made up of two carbon atoms along the zig-zag axis, blurring, to form one column separated by 0.213 nm, as shown schematically in Figure 40.

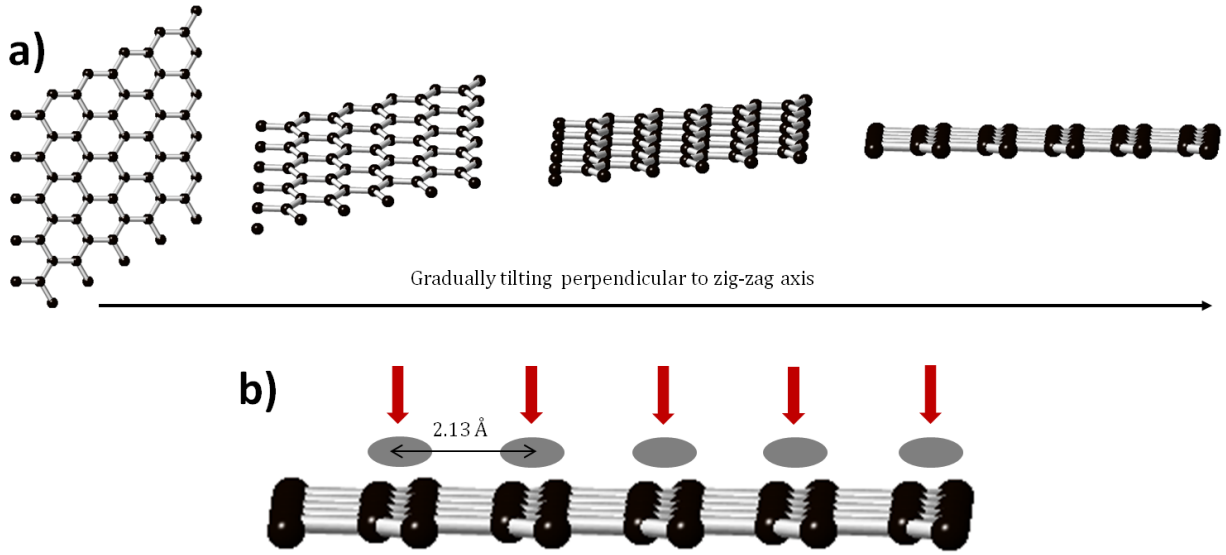


Figure 40a) Schematic of a graphene lattice gradually titling perpendicular to the zig-zag axis. The last diagram in this series is enlarged in b) where the contrast and spacing corresponding to the contrast observed experimentally is highlighted.

Figure 40a visually demonstrates that gradually tilting perpendicular to the zig-zag axis yields a periodicity between columns of atoms, separated by 0.213 nm, as shown in Figure 40b. Therefore, this periodicity corresponds to observations down the (01-10) zone axis of the graphene lattice and any discrepancy in spacing is likely due to a tilt effect.

Although this contrast can be observed in multiple publications, explanations of origin are not often the focus of the published science. Norimatsu *et al*. however reported on a very similar contrast, observed from a cross-section of FLG grown expitaxially on SiC. Using theoretical simulations, they also concluded that the contrast originated from two carbon atoms observing from the (01-10) zone axis[169].

3.2.5 Sideline periodicity

An additional contrast, commonly seen in these samples but reported only once in the literature, was observed as a line periodicity on the edge of some graphene defects. This contrast has been described as “sidelines”. Some examples are shown in Figure 41a and b.

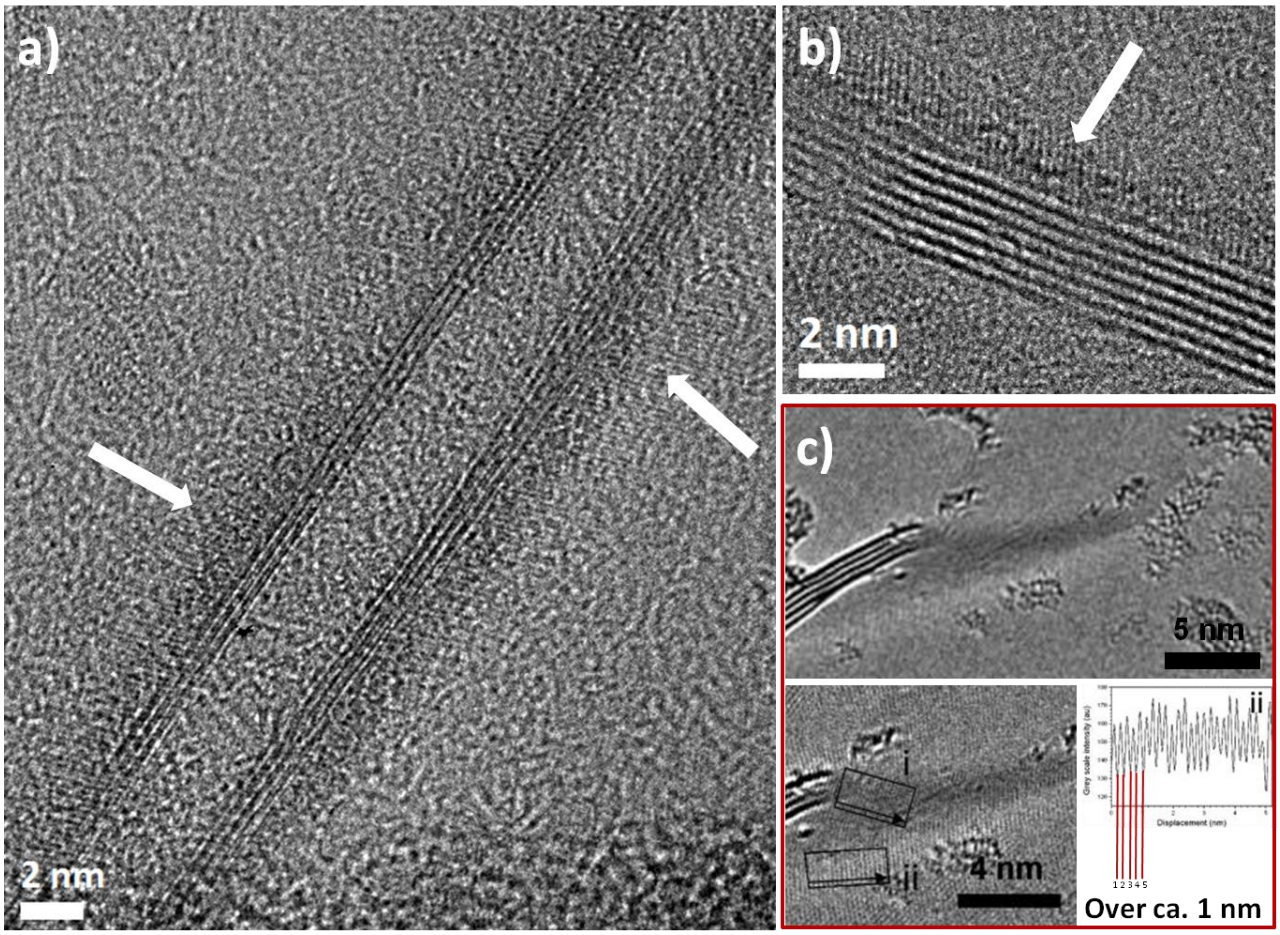


Figure 41a and b) TEM example images of periodic "sideline" spacing seen in FLG. White arrows highlight some areas of this contrast. c) possible sideline example images from literature ref[164]. Bottom image is feature at higher magnification with corresponding line profile of area ii. Spacing in the paper is quoted as 0.12 nm. From the image, it seems that in *ca.* 1nm, 5 spacings occur, indicative of a *ca.* 0.2 nm spacing.

Figure 41a shows sidelines either side of a folded wrinkle (as previously defined) in FLG and Figure 41b shows sidelines on one side of a simple wrinkle in FLG. The spacings of the sidelines in both examples equal between 0.20-0.21 nm. This spacing is in the same range as the previously discussed periodicity along graphitic planes. To the best of current knowledge, Figure 41c shows the only other example in the literature of a similar sideline contrast[164]. Similarly to the samples in this thesis, the sidelines appear around a defect feature in FLG however they quote the spacing, as shown in box ii, as 0.12nm. The contrast profile, as shown in the white box next to the TEM image, suggests a five-spacing periodicity within an approximately 1 nm distance. This would yield a more similar 0.2 nm spacing. It is likely that the initial value was miscalculated, although it is possible that sample tilt provides a variety of angular measurements. In this paper, the appearance of this contrast is not the main focus and

they postulate that its origin is similar to a thickness effect, with an out-of plane distortion of the graphene leading to an apparent change in bond length[164]. It could be speculated that the appearance of sidelines is simply a delocalisation effect as a result of using a field-emission gun TEM, however further evidence would suggest otherwise. Delocalisation refers to the phenomenon whereby a location of a lattice fringe does not necessarily correspond to the correct location of a lattice plane[134].

Sidelines were sometimes observed to continue after or around, but not next to, the main defect feature. After the consistent appearance of these features, it became of interest to further understand their origin. Figure 42 aims to help explain their formation.

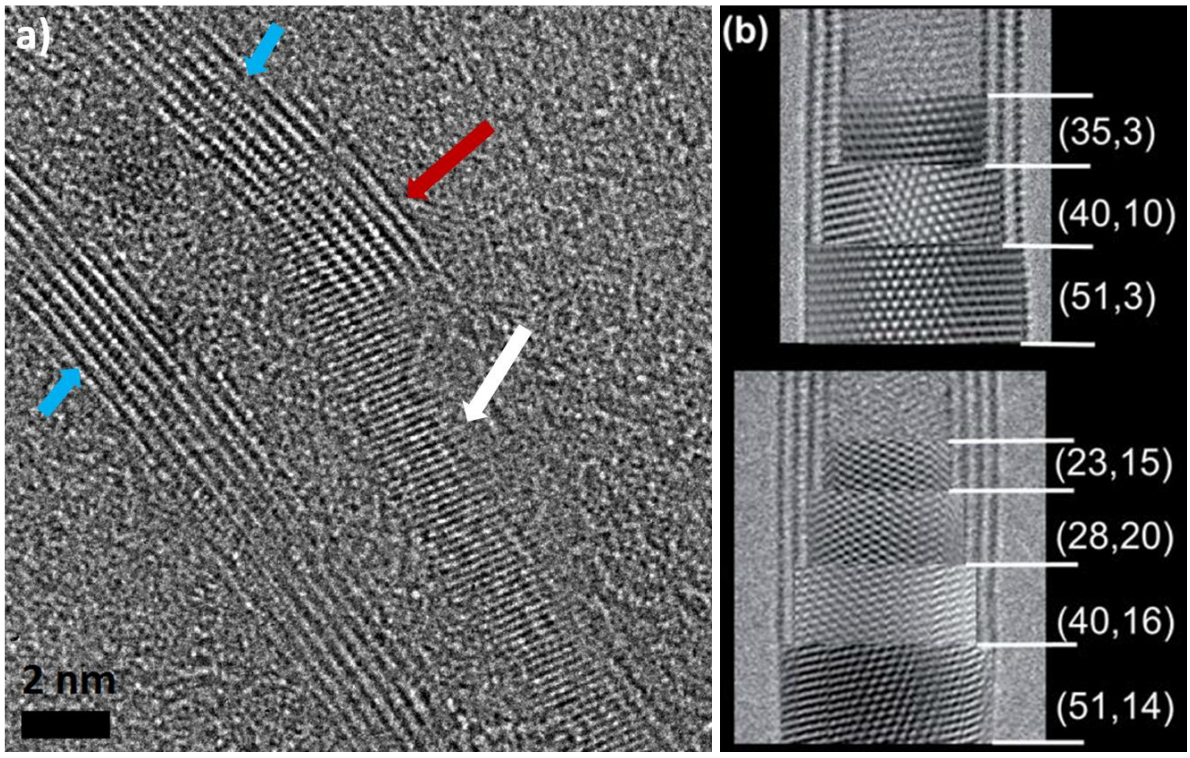


Figure 42a) TEM image of area of sidelines showing interesting contrast similarities between the periodicity along graphitic planes and the sidelines contrast. The white arrow highlights an area with prominent sidelines, the blue arrows highlight areas of periodicity along graphitic planes and the red arrow highlights an area where it appears one feature derives from the other. The spacings of all periodicities in this image equate to *ca.* 0.2 nm. b) Reproduced with permission from ref[170], simulation of multi-wall CNT TEM image at various chiral indices showing appearance of similar sideline contrast on the side of a CNT.

Figure 42a shows an additional sideline example. Blue arrows highlight a periodicity akin to the periodicity along graphitic planes, as previously discussed, and the white arrow highlights regular sidelines. The red arrow highlights an area where the periodicity along graphitic planes

and sideline periodicity cross over, with one seemingly being produced from the other. Both the spacings of the sideline periodicity and periodicity along graphitic planes equate to *ca*. 0.21-0.22 nm, with interestingly the same larger range of between 0.18-0.23 nm. Although this is a fairly complicated feature, and the exact structure is difficult to speculate, it provides evidence of the similarities in contrast mechanisms between the sidelines and the periodicity along graphitic planes.

Therefore, as this contrast is derived perpendicular to the (01-10) direction, it implies the area of lattice containing sidelines is changing in orientation with respect to the bulk, much like the tilting lattice schematics shown in Figure 40.

In the literature, a similar contrast with a very similar spacing was found on TEM simulations of multi-wall CNTs[170], as shown in Figure 42b. The simulations were carried out for various chiral indices of CNTs and what is apparent is that there is a distinct line-contrast observed on some of the simulations (notably for indices; (40,10), (51,3), (40,16) and (51,14)). It is noted that the line contrast appears on the curve of the CNT, not in the centre of the CNT.

It is likely that the origin of these contrasts is very similar. Appearance of sidelines in a system therefore implies a different orientation with respect to the imaging axis. As sidelines only appear in one area of an image, it shows that this area is off axis compared to the bulk, implying a change in orientation, and indicating a change in height and curvature at this point, much like where curvature is seen in CNTs. Such a phenomenon would also fit with the areas where sidelines are observed: larger, more 3D defect features in a graphene sheet.

If this is the case, as well as indicating curvature in a system, the appearance of sidelines can also be exploited to deduce the approximate angle of incline of the lattice area. By measuring the length of the sidelines in the TEM image and the range of defocuses at which they appear, an incline angle can be estimated, as shown in Figure 43.

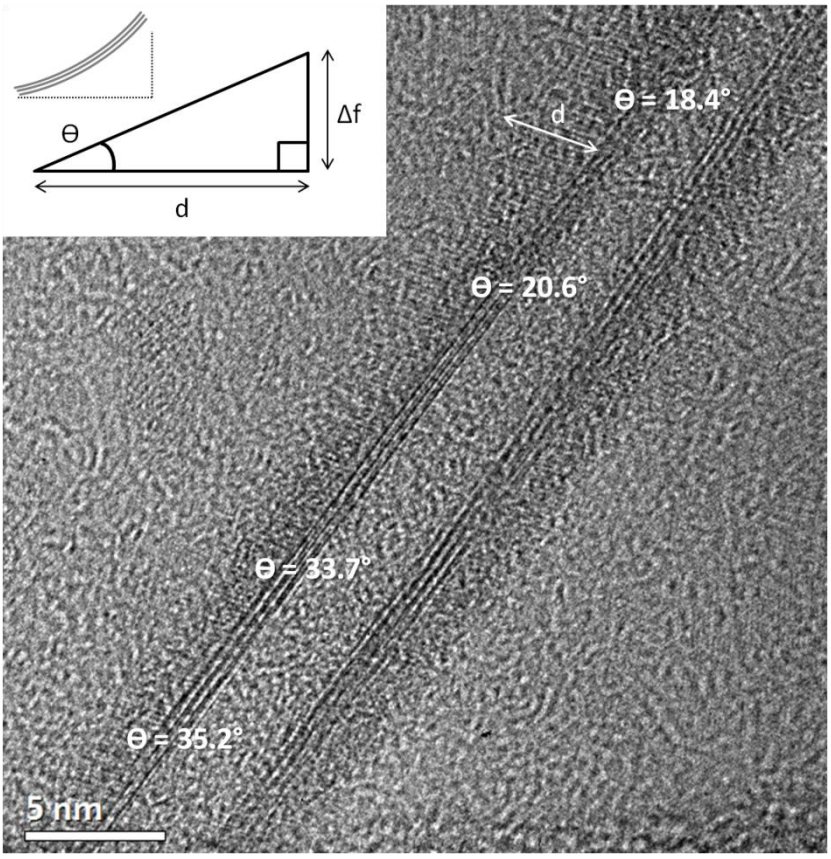


Figure 43)TEM image of a folded wrinkle with sideline features. Inset shows how the angle of incline can be calculated if the change in focus and length of the sidelines is known. The top left of the inset depicts how this could relate to the arrangement of FLG in this scenario. Angles on the image depict how the change in incline has been calculated throughout the image.

This principle has been applied to sideline features seen alongside a folded wrinkle as shown in Figure 43. In this image, the length of the sidelines change along the side of the feature, but the defocus change stays the same. Therefore the angle of incline is likely to change throughout the image and has been calculated to be between 18.4-35.2°, with a gradually increasing angle of incline towards the lower part of the fold.

This information can provide an insight into how "tight" the binding is within a feature and further understand graphene defect structure. If for example sidelines are in focus for a larger range of defocus values, it would suggest that the defect is very large, and could therefore have increased effects on graphene properties compared to a smaller feature. The appearance and understanding of sidelines can therefore provide TEM users with an immediate indication of defect size and structure.

3.2.6 Inter-graphitic plane contrast

A third contrast that was observed during defect imaging was that of an inter-graphitic plane contrast, observed in between the graphitic plane spacings of 0.34 nm. This contrast was only observed on wrinkle and fold features, not on edges. Some examples have been shown in Figure 44.

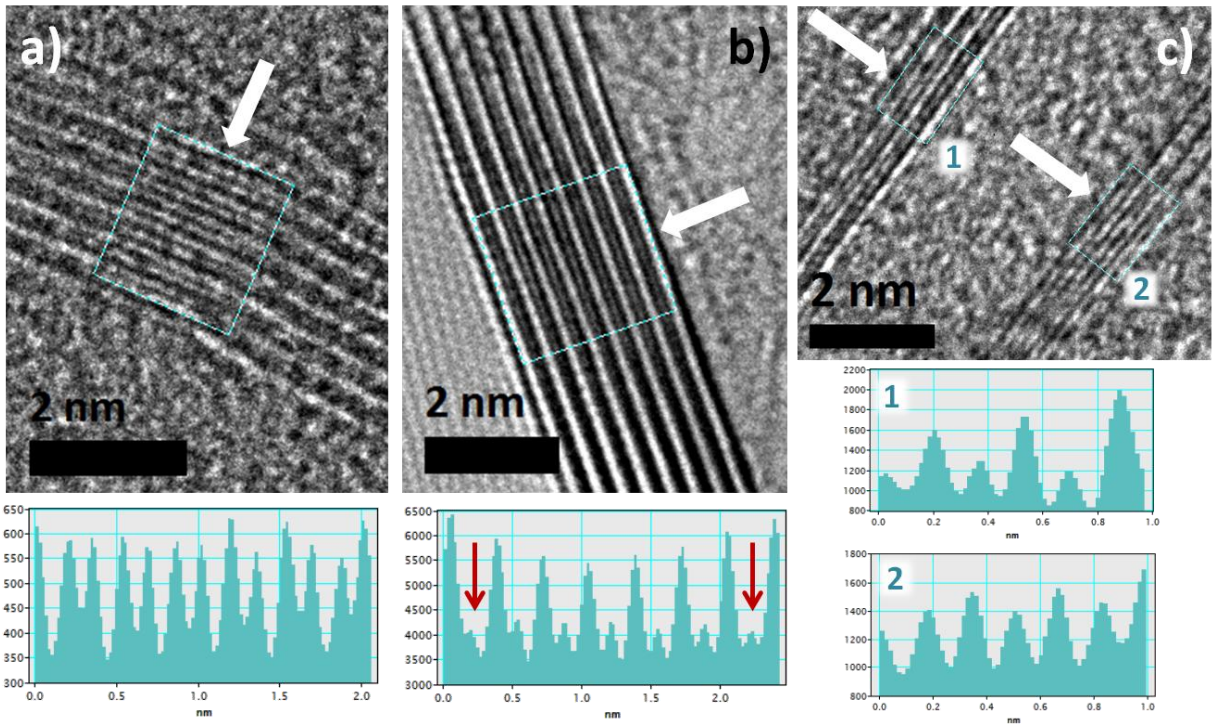


Figure 44a-c) TEM images and corresponding line profiles (below each image) of areas highlighted by a turquoise box. White arrows point to areas of inter-graphitic plane contrast between the graphitic plane spacing. a) and b) Images of a simple wrinkle features. c) Image of a folded wrinkle, both sides of which exhibit an inter-graphitic plane contrast. In c) line profiles 1 and 2 correspond to the numbered boxes in the image. The red arrows in the line profile for image b) highlight two sets of contrast; off-centre and central.

The examples in Figure 44 show a TEM image with a corresponding contrast profile of the area showing an inter-graphitic plane contrast. The contrast is observed in between the graphitic plane spacing both perfectly central between layers and often off centre, as highlighted by red arrows in Figure 44b; showing an evolution of the contrast from the left towards the centre in between the graphitic layers. Central spacings are, predictably, around 0.16-0.17 nm (central to the 0.34 nm graphitic layer spacing). The inter-plane contrast was not observed consistently along some wrinkle features, as shown in Figure 45.

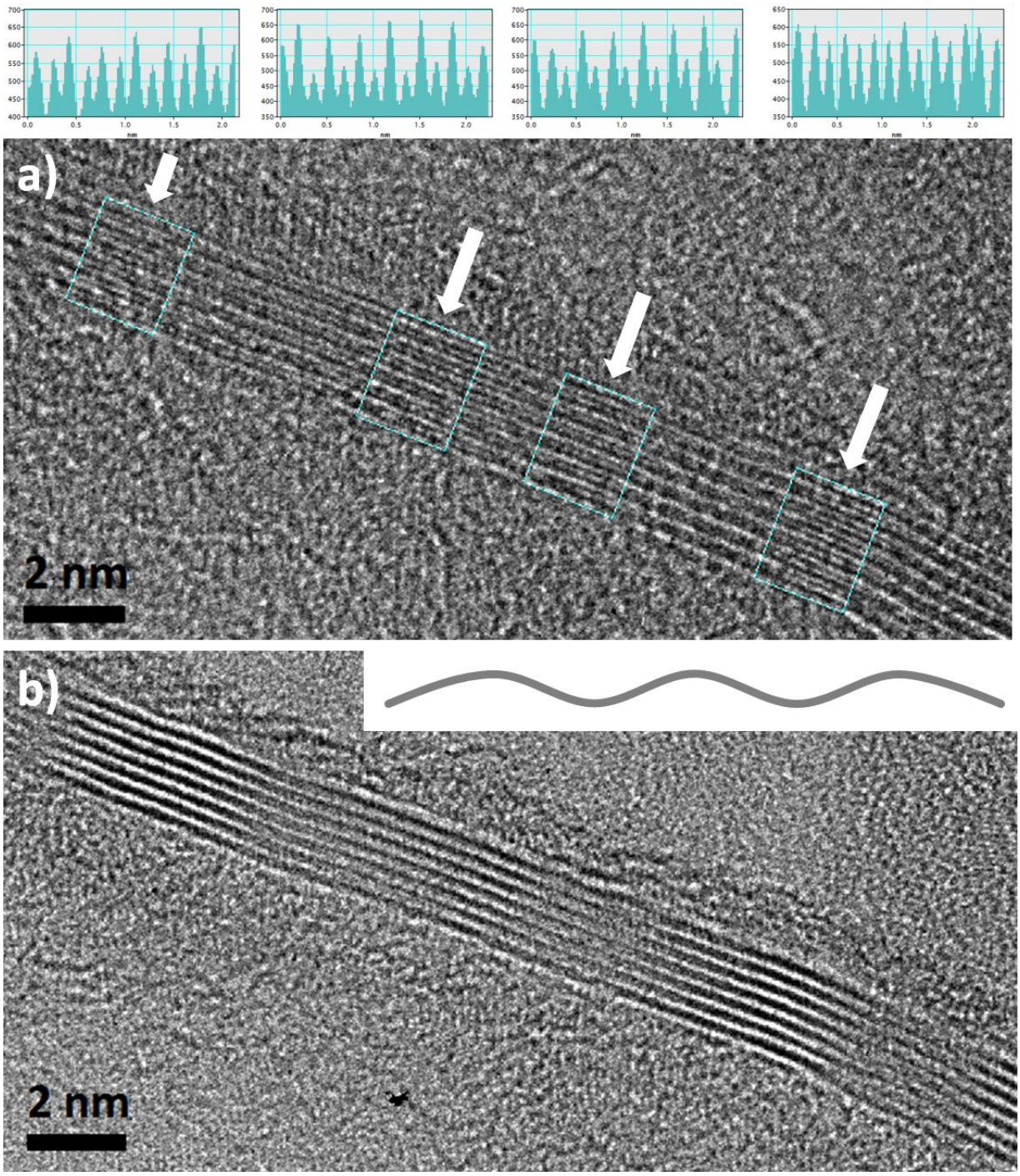


Figure 45a) TEM image of wrinkle with several examples of inter-graphitic plane contrast, highlighted by white arrows. Turquoise boxes correspond to the contrast profiles above the image. b) TEM image of the same area at different focus highlighting the change in focus across the feature. Inset shows a schematic of similar periodic change in height over a lattice.

Figure 45 shows TEM images of the same feature under slightly different focuses to highlight the difference in contrast and therefore height changes in the wrinkle. In Figure 45a, the areas of inter-graphitic plane contrast are highlighted with turquoise boxes, the contrast profiles of which are shown above. The inter-graphitic plane contrast is seen at various points across the

wrinkle and so is likely to be a feature of a change in focus, demonstrating that the wrinkle in Figure 45 is undulating in and out of focus, shown more clearly in the TEM Figure 45b (the inset shows how the wrinkle might look from the side). Figure 46 shows an additional feature with a central contrast in between the graphitic plane, however in this case the central contrast also exhibits its own periodicity.

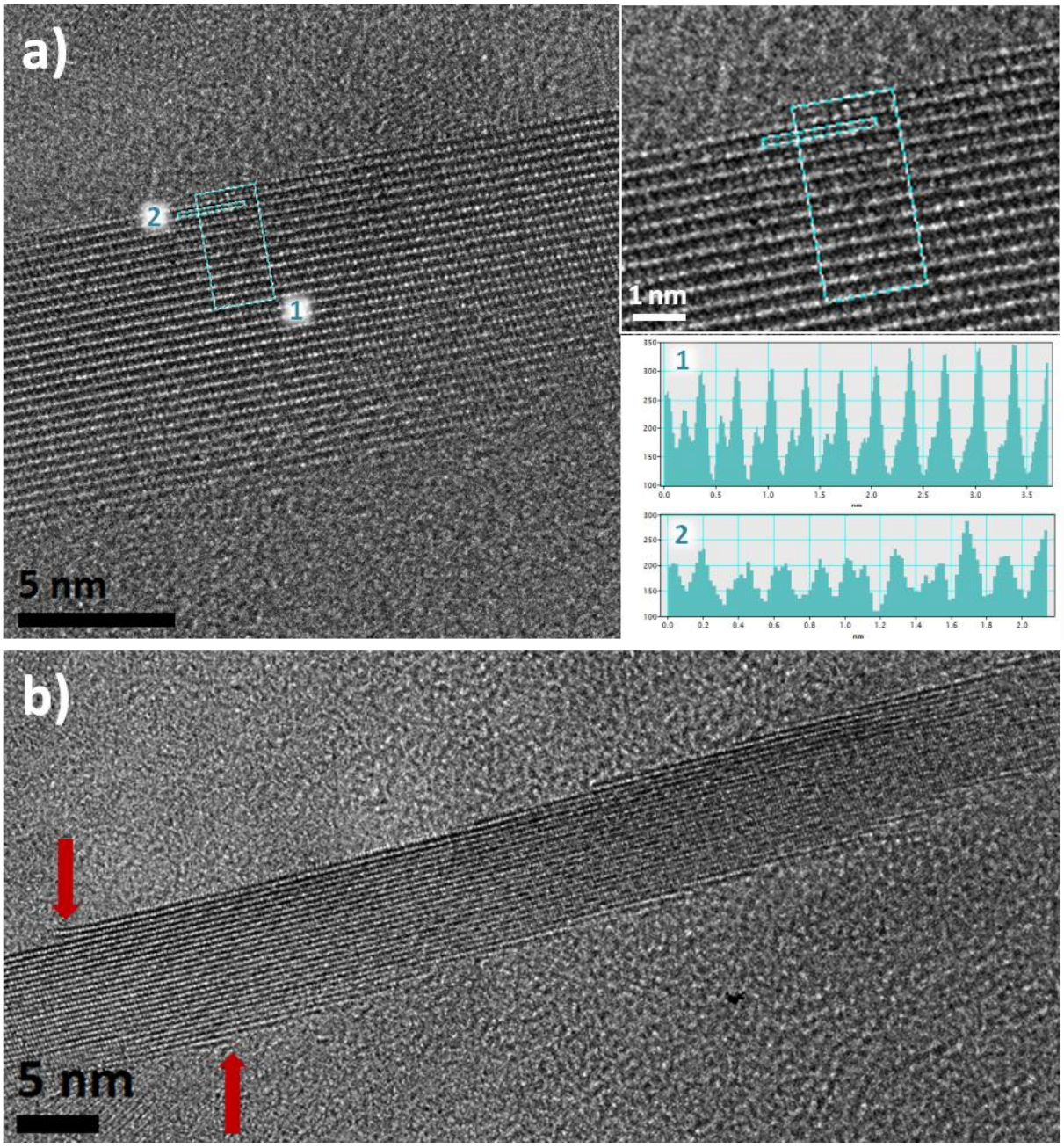


Figure 46a) TEM image of large wrinkle feature with turquoise boxes highlighting numbered contrast profiles; 1 and 2 (insets). b) TEM image at lower magnification of the same area, with red arrows highlighting graphitic layers appearing and disappearing from contrast.

Figure 46a shows an image of the feature that exhibits the periodicity along graphitic planes consistently along the graphitic layers indicating a highly tilted structure towards the beam direction. At the highest resolution this spacing was measured to be 0.213 nm, matching exactly the predicted value. A version of the inter-graphitic plane contrast is observed in this feature, as shown in contrast profile 1 of the inset in Figure 46a (showing a gradual centre to off-centre contrast). However, the difference in this example is that the contrast observed between the graphitic plane spacings exhibits its own periodicity along the graphitic planes as shown by contrast profile 2. This spacing has also been measured at 0.213-0.214 nm.

At lower magnification in Figure 46b, it can be observed that graphitic layers step on/off the feature, highlighted by the red arrows. This is indicative of a wrinkle with an angular tilt that is slightly askew to the lattice. Measuring the angle between the step-layers can indicate the tilt angle, which is this case is approximately 44°. This would explain why the contrast is only seen at certain parts of the feature.

To obtain the 0.213 nm spacing within the inter-graphitic plane contrast indicates that the feature is tilted close to perpendicular to the beam direction, indicating a very sharp defect. The large number of layers observed in this feature could create a large 3D feature compared to the bulk 2D sheet and may also contribute to the increased contrast.

It is therefore concluded that the inter-graphitic plane contrast is indicative of an off-axis area of a wrinkle. Its origin is focus and tilt related and is likely a contrast observed when the wrinkle feature is slightly off axis from the beam direction at a specific tilt angle, similar to the periodicity along graphitic planes as previously discussed.

3.2.7 Linear moiré patterns

The final feature of TEM defect imaging that will be discussed in this section is the observation of linear moiré patterns.

During HRTEM analysis of graphene where few-layer or overlapping areas are possible, it is common to observe moiré effects in TEM images as shown previously in Figure 32b and Figure

34b. Moiré patterns can occur when two or more regular patterns are overlaid at an angle, in this case, two or more graphene lattices stacked on top of each other at different rotations, which yields a commonly observed rotational moiré pattern.

The first moiré pattern of graphite was observed by Kuwabara *et al*. in 1990 using scanning tunnelling microscopy (STM)[171]. Kuwabara *et al*.[171] defined the relationship for the observed rotational moiré pattern using the resultant superlattice spacing and the inter-planar lattice spacing:

$$D = \frac{d}{(2\sin\theta/2)}$$

Equation 1

Where:

D = observed moiré spacing

d = inter-planar lattice spacing (0.213 nm)

θ = angle of misorientation

Using this equation, it is possible to simply work out the rotation of two graphene lattices using the spacing of the moiré pattern alone.

Studies of rotational moiré patterns of graphene have been governed by their visualisation in STM[90,91,172–179], whereas HRTEM studies are less common. This is likely due to the large majority of HRTEM work studying solely monolayer graphene.

Moiré patterns have been used to predict strain in graphene[172], and can also provide information on how layers of graphene are stacked. Stacking orientation will change the electronic properties[180] and Luican *et al*.[174] showed how varying angles of misorientation can lead to strong electronic coupling or decoupling between graphene layers, highly depending on the degree of rotation. Through understanding the cause of moiré effects, and extracting

specific data from TEM images, it is possible to gain structural information and hence predict changes in electronic properties throughout the material, helping to define the overall quality.

Figure 47a is an image of bi-layer graphene and an example of a commonly seen hexagonal moiré pattern, produced from two graphene lattices rotated off-axis from each other. The FFT (Figure 47c) implies that it is a bi-layer region, slightly misaligned by *ca*. 2.5°±0.3. Using

Equation 1 and defining the unit cell of the moiré pattern as in Figure 47b, the spacing and the measured rotation was calculated and fits well with the expected values (D = 4.88 nn when θ = 2.5°, observed D≈4.93 nm).

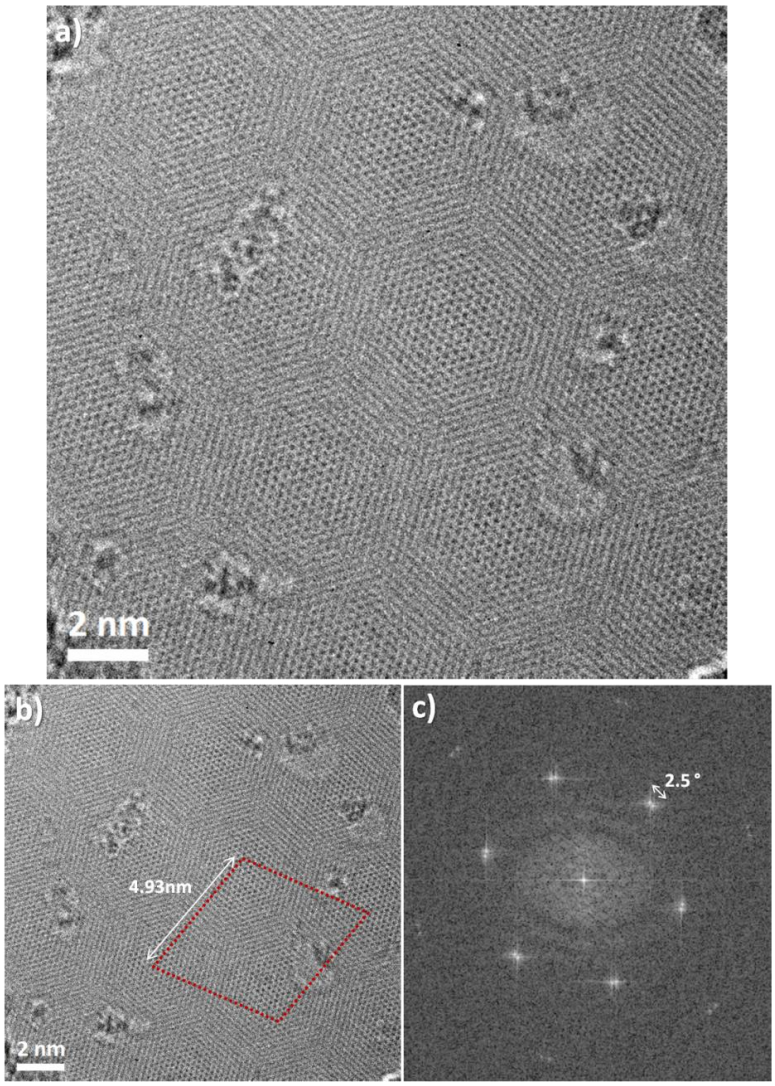


Figure 47a) Hexagonal moiré pattern observed in bi-layer graphene. b) the same moiré pattern with unit cell of superlattice highlighted and defined with superlattice constant, 4.93 nm. c) FFT of a) showing lattice rotation of 2.5° ±0.3.

Figure 47 depicts a well established moiré effect with the commonly observed hexagonal symmetry in bi-layer graphene. However, some moiré effects observed in FLG in this project did not exhibit this symmetry. Figure 48a and b show a raw and filtered TEM image of linear, regular features from a FLG sample that do not correspond with any other imaging phenomenon other than that of a moiré effect.

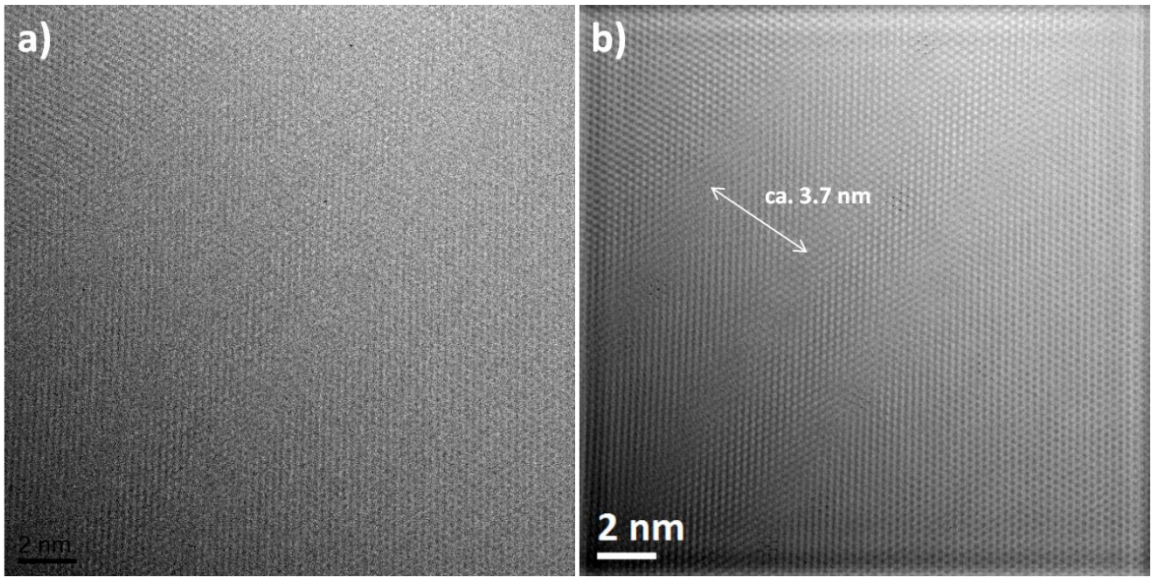


Figure 48a) Raw data of observed linear Moiré pattern. b) Filtered image of a) to highlight linear Moiré features with a spacing of *ca*. 3.7 nm.

The moiré effect in Figure 48 exhibits a spacing of approximately 3.7 nm. It is worth noting that due to the difference in size of the moiré effect and the lattice, the moiré spots on the FFT could not be seen to reliably measure. Hence, the moiré spacing must be estimated from the image for subsequent analysis.

Experimental observations of a linear moiré effect in graphene has been reported in only one previous paper; Jasinski *et al*.[181] observed both a hexagonal and linear moiré effect in the same graphene bi-layer flake (Figure 49). They put forward that the linear features were due to a distortion in one of the graphene lattices, and that this distortion caused the change from the normal hexagonal moiré effect to the linear pattern, without any bond breaking. Upon modelling this theory, they produced a similar, linear moiré pattern (Figure 49c).

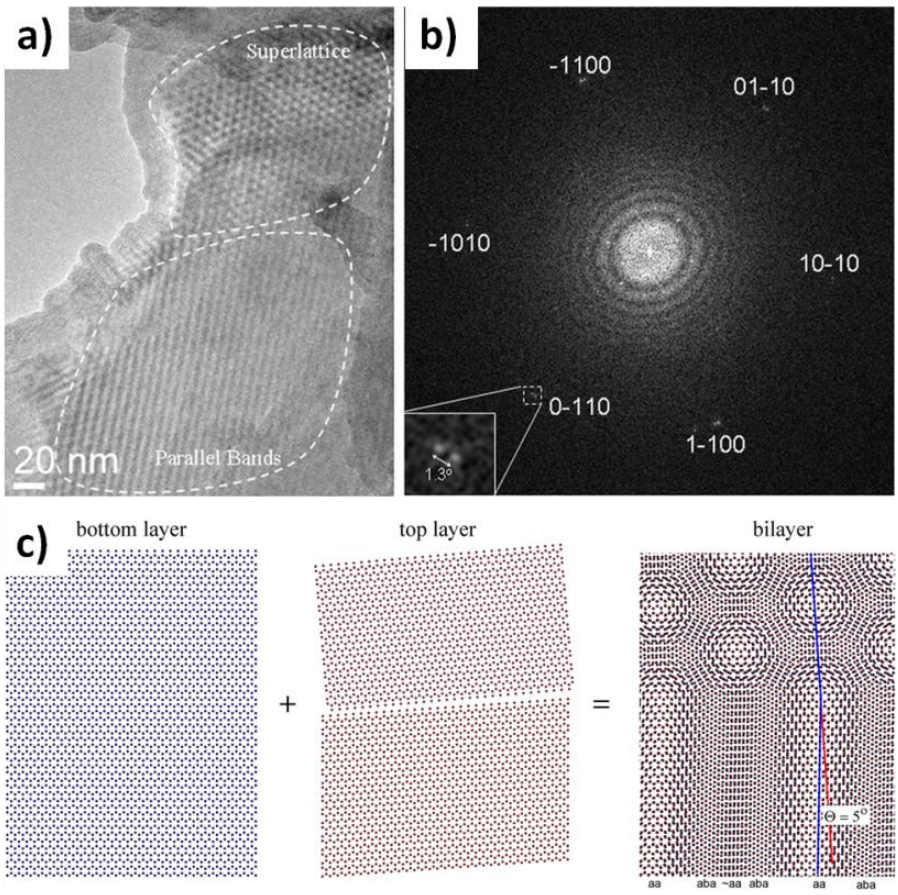


Figure 49) Reproduced with permission from Jasinski *et al.*[181] a) Hexagonal and linear moiré patterns observed in a TEM image of bi-layer graphene and b) corresponding FFT measuring a 1.3° rotation between the two layers. c) Modelling demonstration of how a distorted graphene lattice can produce a linear moiré effect without bond breaking occurring. The modelled distorted lattice is distorted by 5 °.

By adapting the method by Jasinski *et al.*, it was possible to analyse the cause of the linear moiré pattern observed in the experimental data in this thesis. This was done by attempting to reproduce the linear pattern by constructing a distorted lattice of a known distortion angle. From herein, "*x* °" distortion is defined as in Figure 50. From this procedure, new unit cell parameters could be calculated and distorted graphene lattices could be produced.

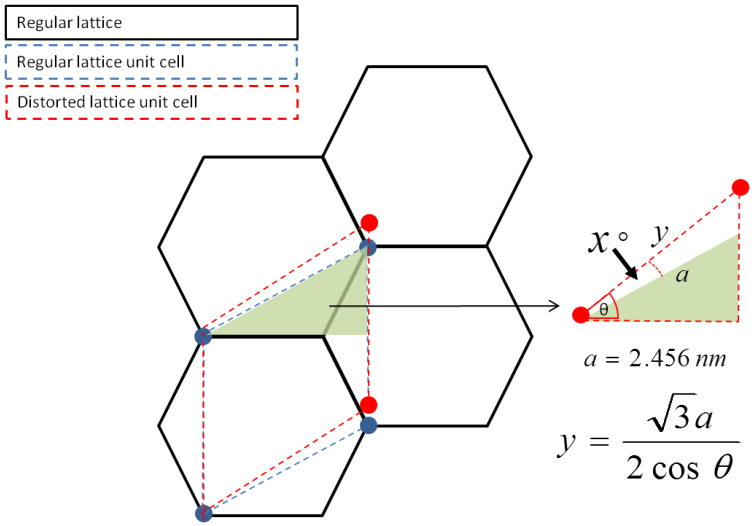


Figure 50) General procedure for the distortion of a graphene lattice in this thesis and corresponding calculation method for new unit cell parameters. The distorted graphene unit cell is highlighted in red dashed lines on the lattice. As θ is changed, *x* is also altered to result in a distorted graphene lattice.

However, on repeating a similar procedure with the data from Figure 48, it was almost impossible to recreate the observed spacing with the measurements obtained from the experimental data. On additional analysis of the FFT of Figure 48a, it became apparent that it differed from the observations made by Jasinski *et al*. From measuring angles on the FFT that would ordinarily equate to 60 ° in a non-distorted lattice, it is clear that in Figure 48, both lattices are distorted (Figure 51b-d). As shown by the approximate measured angles in Figure 51c and d, Lattice 1 is less distorted than Lattice 2. The possible origin of this particular distortion will be discussed later in this section.

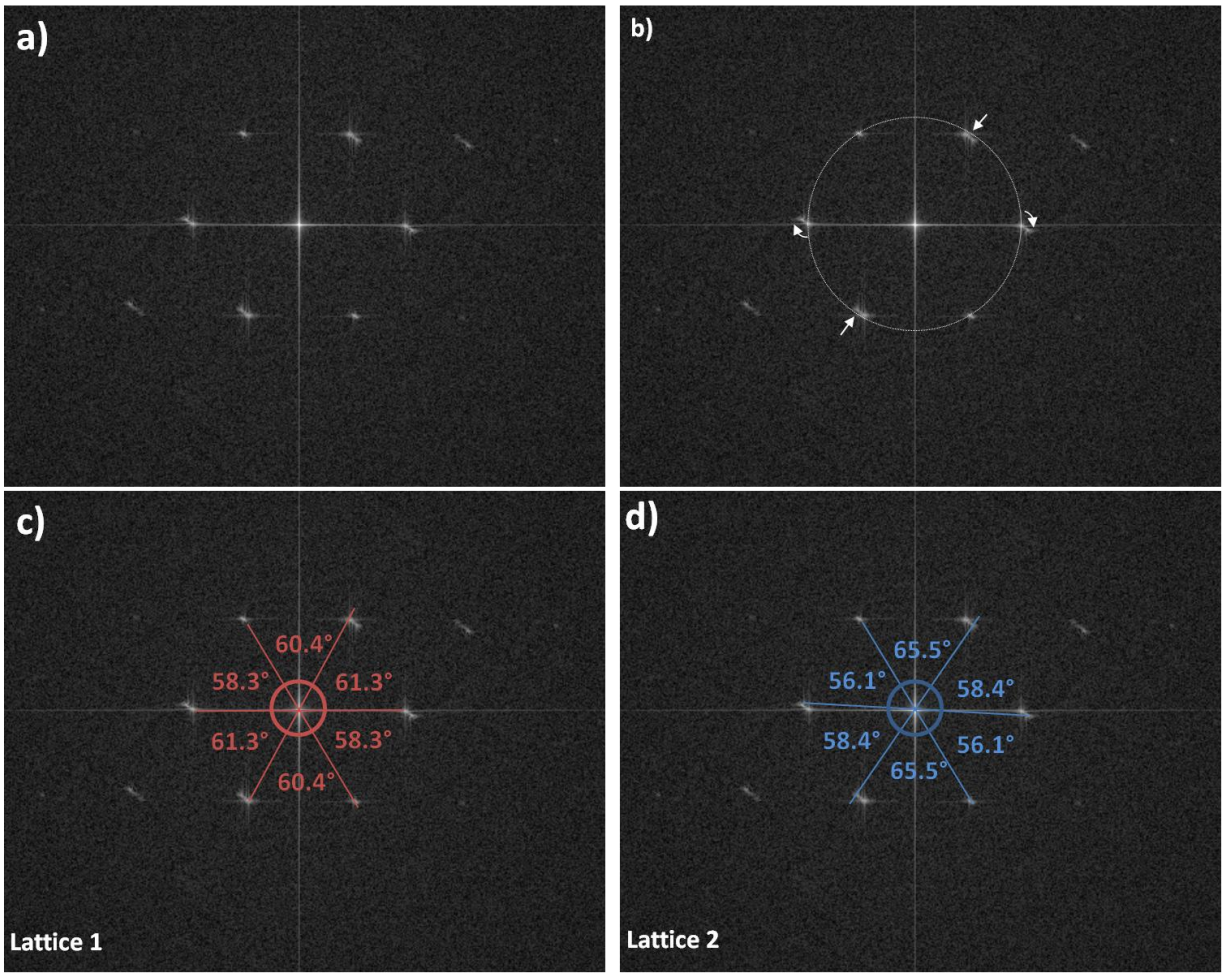


Figure 51a) FFT of raw data shown in Figure 48. b) Symmetrical circle drawn over FFT to emphasise the distortion visible in both sets of lattice spots. White arrows highlight how some lattice spots do not lie within this symmetry so could therefore be evident of a distorted lattice. c) FFT angle measurements from Lattice 1, the least distorted lattice. d) FFT angle measurements from Lattice 2, the most distorted lattice. All angles in c) and d) respectively total 360°.

Figure 51b highlights the non-uniformity of diffraction spots from a regular hexagon. It is possible to rule out that this effect is due to sample tilt as spots move in alternate directions. From further FFT measurements, the changes in lattice parameter indicate up to a 5% change in Lattice 2, and 4% in Lattice 1. Using the measured angles in Figure 51c and d, it is possible to construct unit cells for both distorted lattices using the method by Jasinski *et al*. outlined in Figure 50. Recreating a close match to both of these lattices and overlaying them also produces a linear moiré pattern (Figure 52).

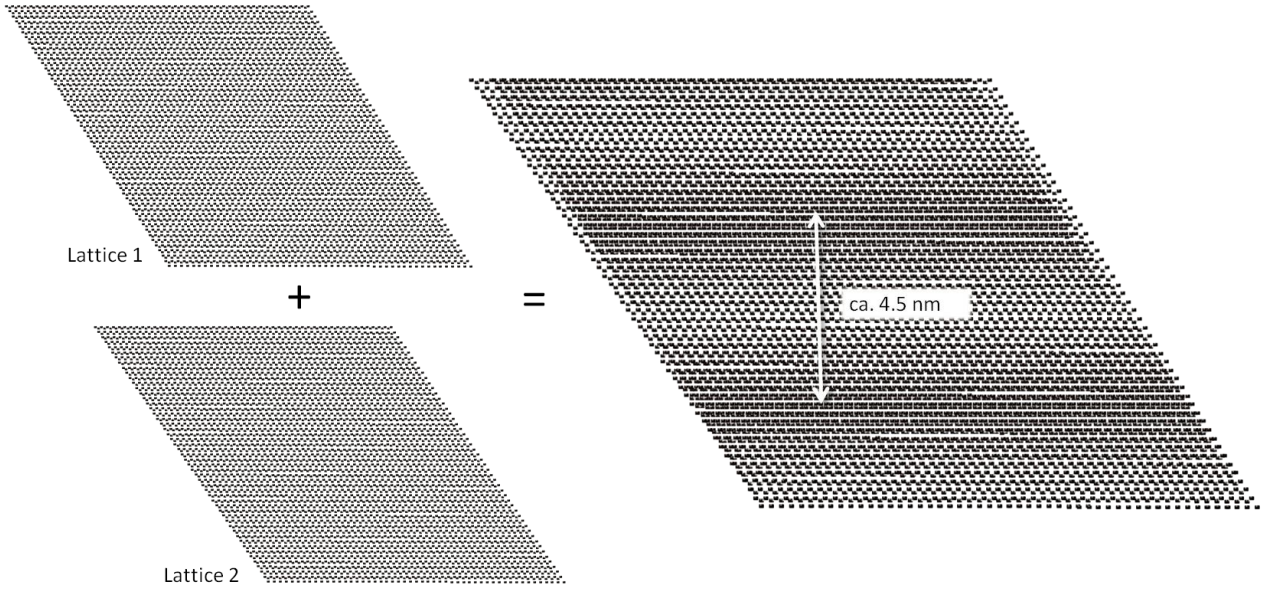


Figure 52) Modelled linear moiré pattern of distorted lattices recreated from measurements in Figure 51. Resulting linear spacing is *ca*. 4.5 nm.

The linear spacing of 4.5 nm observed in Figure 52 is not an exact match to the experimental data spacing of 3.7 nm. It does however illustrate that a similar linear moiré pattern forms when both lattices are distorted.

It is worth noting that a small change in $x°$ distortion using the method in Figure 50 can lead to a significant change in the observed lattice spacing. This may be a reason why Jasinski *et al*. did not reproduce the same spacing in their model as that observed in their images. To illustrate this, Figure 53 shows models of a set of lattices with both a 2° and 1.94° distortion. It demonstrates that with a change in just 0.06° in distortion between two models, the resultant moiré patterns would produce a *ca.* 4 nm change in the observed spacing. Therefore, even the slightest change in lattice distortion can affect the resulting moiré pattern substantially. This may be the reason for the mismatch with the experimental data observed in Figure 52.

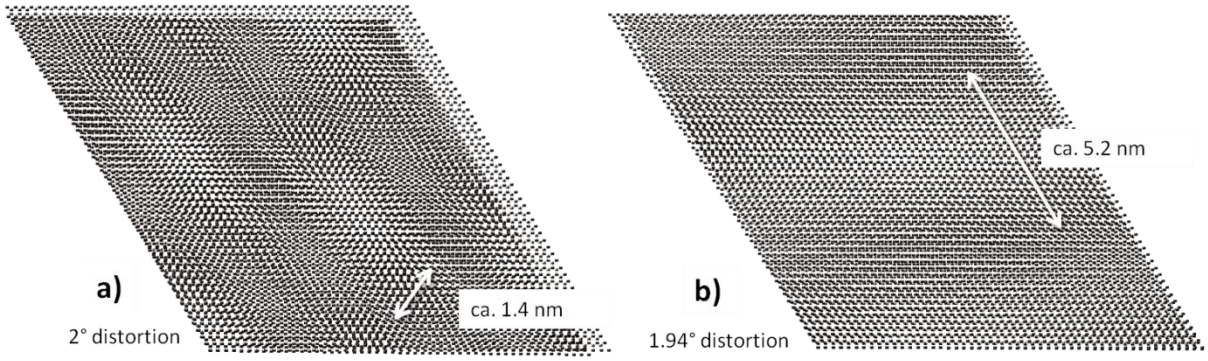


Figure 53) Modelled linear moiré patterns with one regular graphene lattice and a) with a 2° distorted lattice overlaid, resulting in *ca.* 1.4 nm spacing, compared with b) with 1.94° distorted lattice overlaid, resulting in a *ca.* 5.2 nm spacing.

Figure 52 was reproduced from measuring just the angles of the FFT, it is worth noting that recreating the lattices from the perpendicular distances measured between diffraction spots also yielded the same moiré spacing when using distances measured to 1 decimal place. However, moving away from the method used by Jasinski *et al.*, is it possible to confirm the presence of the linear moiré pattern and link it directly with the observed distortion. Outside of the graphene literature, a parallel moiré effect is known as a translational moiré pattern, the spacing of which can be defined by:

$$D = \frac{d_1 d_2}{d_1 - d_2}$$

Equation 2[134]

Where D is the planar moiré spacing and d_1 and d_2 are inter-planar spacings for the two overlaid lattices. Using values measured from the FFT in Figure 51, (d_1= 0.2157 nm, d_2= 0.2034 nm), D= 3.57 nm. This value is very similar to the spacing that has been experimentally observed (D≈3.7nm). Not only do the closely matching values provide evidence that Figure 48 is indeed an example of a translational moiré pattern created from two distorted lattices, but it also supports the accuracy of FFT measurements in demonstrating lattice strain and distortion, even for measurements exhibiting < 10% strain.

From the fit with Equation 2, we can deduce that Figure 48 is an example of a solely translational moiré pattern with negligible rotation and that the linear moiré pattern has

originated from more than one distorted lattice. It has been shown that linear moiré patterns can change considerably with very little change in strain and hence it is necessary to include FFT analysis to make any accurate predictions of lattice distortion and electronic properties.

To understand the origin of the lattice distortion in this example, Figure 54 shows images of the area of sample adjacent to the area where the linear moiré pattern occurs (the inset in Figure 54a shows where the linear moiré pattern was imaged in relation toFigure 54a).

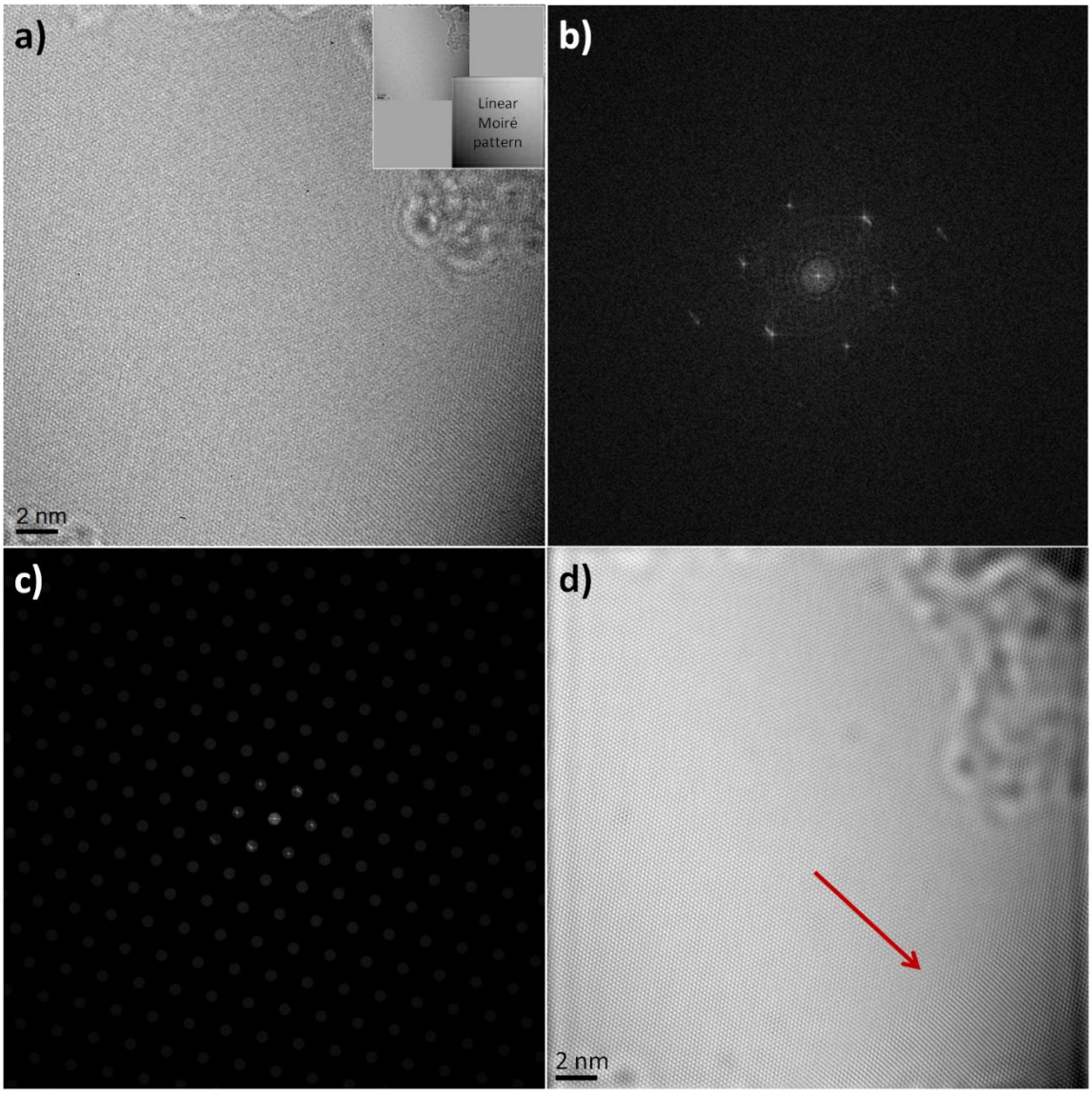


Figure 54a) Raw image of the sample area top left of observed linear moiré pattern. Inset shows where the linear pattern was observed in relation to a). b) Reduced FFT of raw data shows two sets of spots similar to the FFT of the linear moiré pattern. c) Masking of FFT of a) to produce d) an inverse FFT image which highlights the change in the lattice in the bottom right hand corner, highlighted by the red arrow, where the linear moiré pattern is produced.

Masking the FFT of Figure 54a highlights a change in the lattice in the bottom right of the image (Figure 54d, red arrow). It is closely after this point that the linear moiré pattern starts to occur. The FFT of this area is shown in Figure 55d and is very similar to the FFT of the moiré pattern observed in the original linear moiré image (Figure 48). In both cases, a second set of lattice spots appear at a distorted angle. Before this distortion occurs, in the top left of the sample region, the FFT implies regular, monolayer graphene[143] as shown in Figure 55a and b.

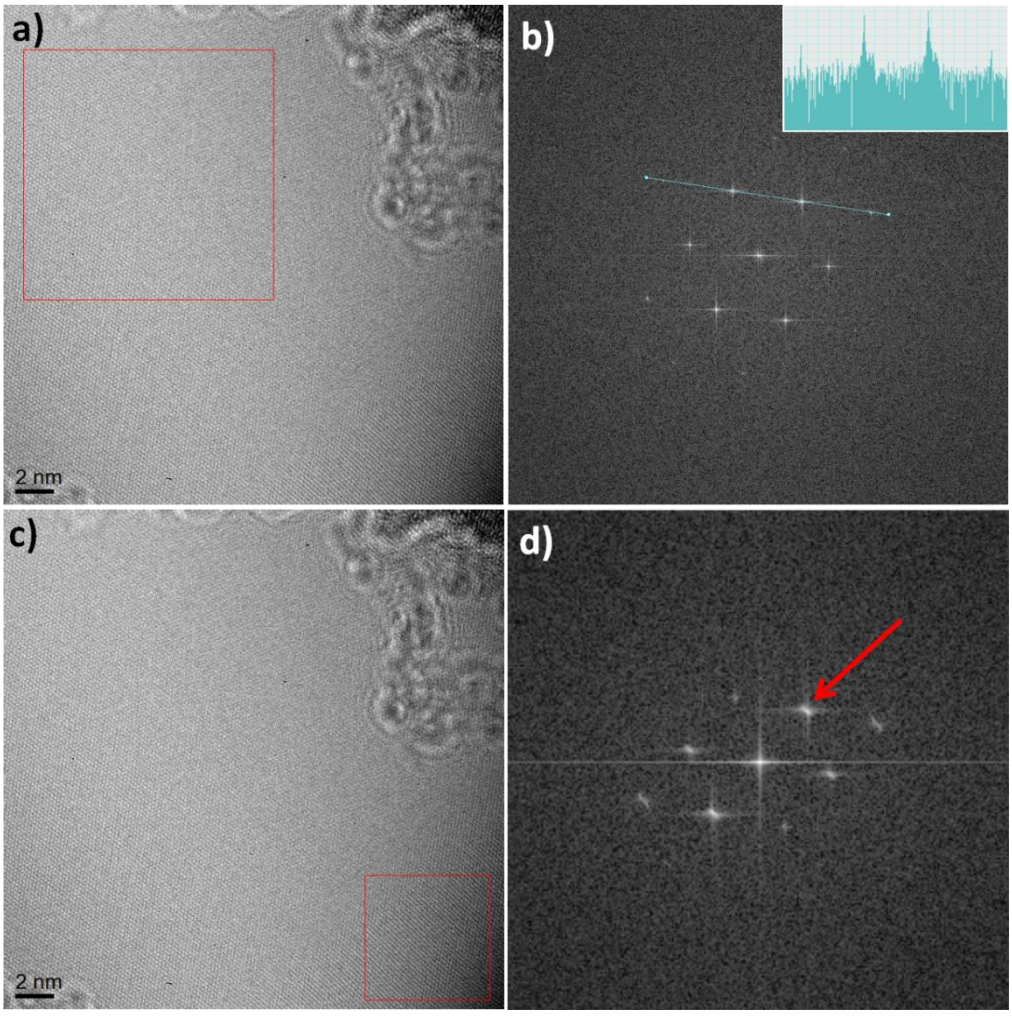


Figure 55a) Raw image with red box highlighting area where FFT b) is taken. FFT implies monolayer graphene from lattice spot intensity. Inset shows intensity profile of FFT lattice spots. c) Raw image with red box highlighting area where d) FFT is taken. Extra spots in the FFT highlighted by a red arrow imply an addition of another graphene layer, off-axis from the original monolayer.

From this additional data it is possible to speculate that this area of sample evolves from regular, monolayer graphene to a distorted bi-layer system and additionally that one of the distorted bi-layers was originally non-distorted, monolayer graphene (Figure 55a and b). In

addition, the image implies that the change in lattice distortion occurs without the breaking of C-C bonds, like in the example reported by Jasinski *et al*.[181]

This suggests that the distortion in the graphene lattices occurred due to the addition of a second lattice. This could have occurred during synthesis, either as a part of a single graphene domain or it could be an example of a domain boundary, where a bi-layer domain and a monolayer domain have merged together. However, as one set of lattice spots are coherent across both areas of the sample (the monolayer ≈ Lattice 1), it is likely that the two areas are within the same graphene domain, and nucleation of a secondary layer has occurred during synthesis. If this is the case, the secondary layer has distorted both the original monolayer and itself. Figure 56c shows a visual change on the image with the addition of the secondary layer (highlighted by black-red lines).

Comparing this observation to the SEM data, it is possible that this feature has stemmed from multilayer growth in one domain. Figure 56b shows a hexagonal, bi-layer graphene domain. The SEM shows that both layers are hexagonal, but at slightly different orientations. The inner hexagon highlighted in red in Figure 56c exhibits a hexagonal mismatch of between 1.5° and 10.5° compared to the outer blue hexagon. It is possible that the TEM data that produced this moiré effect is of a similar nature and the graphene lattices have distorted in response to a secondary nucleation.

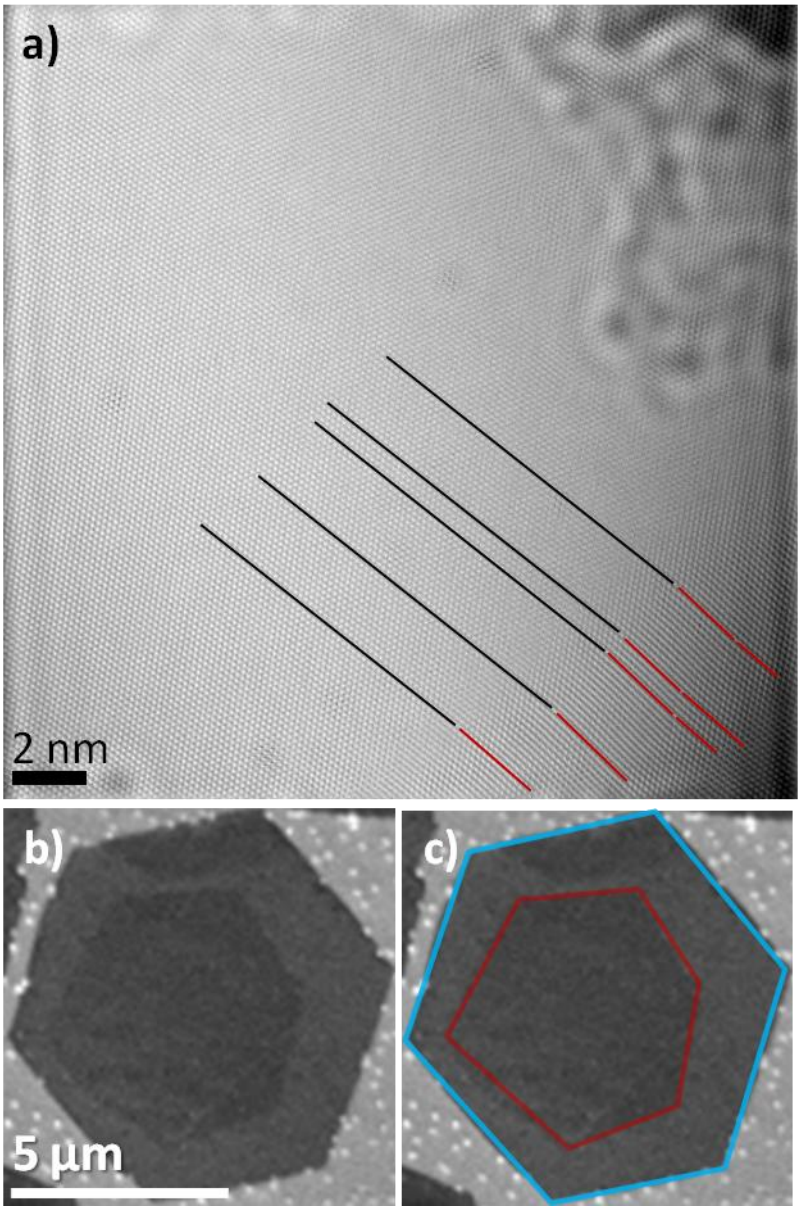


Figure 56a) TEM image as in Figure 55a with highlighted change in alignment of graphene lattice with the addition of a secondary layer. b-c) SEM image of a potential similar scenario; a bi-layer hexagonal domain in the grown sample with c) where two hexagonal layers are highlighted to emphasise the distortion. Distortion between the red and blue hexagons is between 1.5-10.5 °.

Hexagon-on-hexagon growth is not abnormal in CVD graphene synthesis and has been shown previously in Chapter 2. If this commonly seen feature of secondary nucleation can distort the original, high quality graphene monolayer, then it would be of interest to try and avoid it. This could also be possible in FLG growth and may pose challenges for FLG synthesis. Nonetheless, this observation of linear moiré patterns in TEM of bi-layer graphene has proved that they can be formed through not just one, but also two distorted lattices. Hence, linear moiré patterns can be used as an additional tool to quickly define the structure of a sample using HRTEM.

3.3 Summary

This chapter has introduced several examples of common imperfections that can be observed in CVD graphene. The analysis techniques and results shown in this chapter will help to discuss work described in Part II (Chapter 4)and Chapter 5.

In this chapter, the introduction to overlapping and folded areas of graphene demonstrates the use of the FFT to extract vital structural information about the changes in the graphene lattice. Such features can occur through transfer or synthesis and so although are relatively simple phenomena, prove to be a common feature of CVD graphene used in applications.

The slight differences in HRTEM contrast that have been discussed in this section: periodicity along graphitic planes, appearance of sidelines and inter-graphitic plane contrast, demonstrate how HRTEM contrast can provide information about sample strain, structure, and indicate the wider effect of the imperfections on the lattice on the slightly larger scale. It is noted that simulations are necessary to conclusively understand the contrast in these cases, however the prevalence of these phenomena demonstrate a consistency in similar imperfections across graphene samples.

Furthermore, the observation of linear moiré patterns in graphene has shown how HRTEM can indicate lattice strain, and importantly has proven a confidence in FFT measurement which matches well with theory. Additionally, the example discussed demonstrated how originally non-distorted graphene could exhibit lattice distortion in response to an additional graphene layer. This result is of interest to FLG synthesis and in modelling the changes in electronic properties in bi-few-layer systems.

In summary, Part I has introduced an approach to graphene analysis with HRTEM that characterises specifically naturally occurring defects as opposed to those induced via irradiation. This chapter begins to show evidence that despite pristine areas in graphene

samples; the larger product can contain significant, and as far under-discussed, imperfections that will affect the overall quality. Part II will continue to discuss this theme.

The broader application and outlook of this chapter will be summarised at the end of Part II of HRTEM imaging of imperfect CVD graphene.

4 HRTEM of imperfect CVD graphene: Part II

This chapter will continue the theme from Chapter 3 looking at naturally occurring imperfections in CVD graphene. It will describe the TEM characterisation of "imperfect" graphene domain boundaries.

4.1 Imperfect domain boundaries

Imperfect domain boundaries are those which have resulted in substantial defects during the domain merging process. They are unlike what has been described previously in the literature; differing from either simple overlapping or atomically bonded graphene domains. A brief literature review will provide the background and hence driving force for this work and will be followed by five examples of imperfect domain boundaries. A further five examples have been described in less detail in Appendix C.

4.1.1 Introduction and motivation

As described in Chapter 2, CVD growth of full-coverage graphene involves the nucleation of several graphene domains on a substrate which steadily grow with time and eventually knit together to form one sheet of graphene[25]. Where those graphene domains join is defined as a graphene domain boundary. At these boundaries, there is likely to be a slight change or anomaly in the graphene sheet as each graphene domain lattice will subtly differ. Differences include a change in lattice orientation or a variation in the number of graphene layers. Literature has shown that domain boundaries can often contain non-uniform carbon rings (Stone-Wales defects)[87,182], as shown in Figure 57. These defects are portrayed as minimal, seemingly causing no large change in the graphene sheet and hence can only be observed by atomic resolution microscopy. Yazyev *et al.* postulate that these "atomically bonded" domain boundaries provide a negligible effect to the overall electronic properties of the material[183].

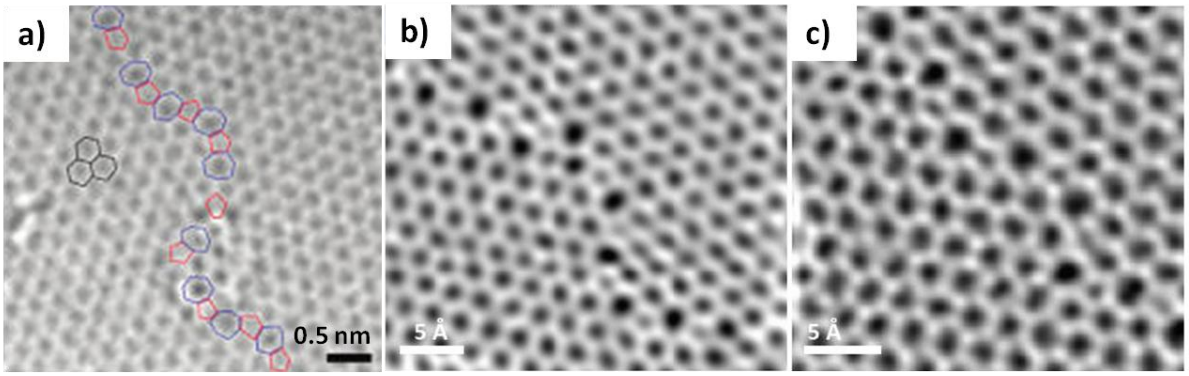


Figure 57a) HRTEM image of an atomically bonded graphene domain boundary, reproduced with permission from ref[182] b-c) HRSTEM images of similar graphene grain boundaries, reproduced with permission from ref[87]. All images show a change in carbon ring size at the domain boundary.

However, what is less established in the literature is the study of "imperfect" domain boundaries. It is often assumed that graphene knits together as shown in Figure 57 but, from the experiments carried out in this thesis, this is not always the case. Imperfect domain boundaries are those which do not perfectly knit together, unlike the examples shown in Figure 57. Example features can include overlapping domains, or strain induced effects such as buckling or wrinkling of the resultant graphene. Imperfect grain boundaries are likely to be more common in few-layer graphene where forming one uniform sheet involves bonding from several layers compared to a monolayer. If these defects are a common occurrence and are more prevalent than the literature suggests, the current characterisation may not be representative of the graphene that is being used in laboratories or material systems. Any change in layers or other defects in the graphene could lead to a change in properties and potentially make the material unsuitable for certain applications.

Papers documenting domain boundaries experimentally are fairly limited. This is likely due to the difficulty in finding such features in monolayer samples. Up until 2014, there was only limited literature[165,184] on domain boundaries that differed from the "minimal" domain boundaries shown in Figure 57. These two papers (one experimental, one theoretical) suggested as well as the atomically bonded boundary, an overlapping boundary also occurs (Figure 58c). The experimental paper on this different type of domain boundary was published by Robertson *et al*.[165] in 2011. They studied domain boundaries in FLG and hypothesised that

domains join via two principle processes: atomic bonding (as shown in Figure 57) and overlapping. In the case of overlapping domains, such a boundary could be described as imperfect. However, the paper suggests that even overlapping domain boundaries also have a very minimal effect on the resulting lattice; with no additional defects around the boundary region. In addition, only three examples of overlapping domains are given, two of which are areas of sample which have undergone high levels of beam degradation (Figure 58d-f). Figure 58f is particularly damaged and resembles an area of FLG where one layer has been sputtered away. An overlapping area in this image is highlighted in red and may have been a folded over area of graphene. In these examples, it could be suggested that there is little evidence to prove that the data is obtained is from two separate merging graphene domains and not just overlapping areas of the same lattice.

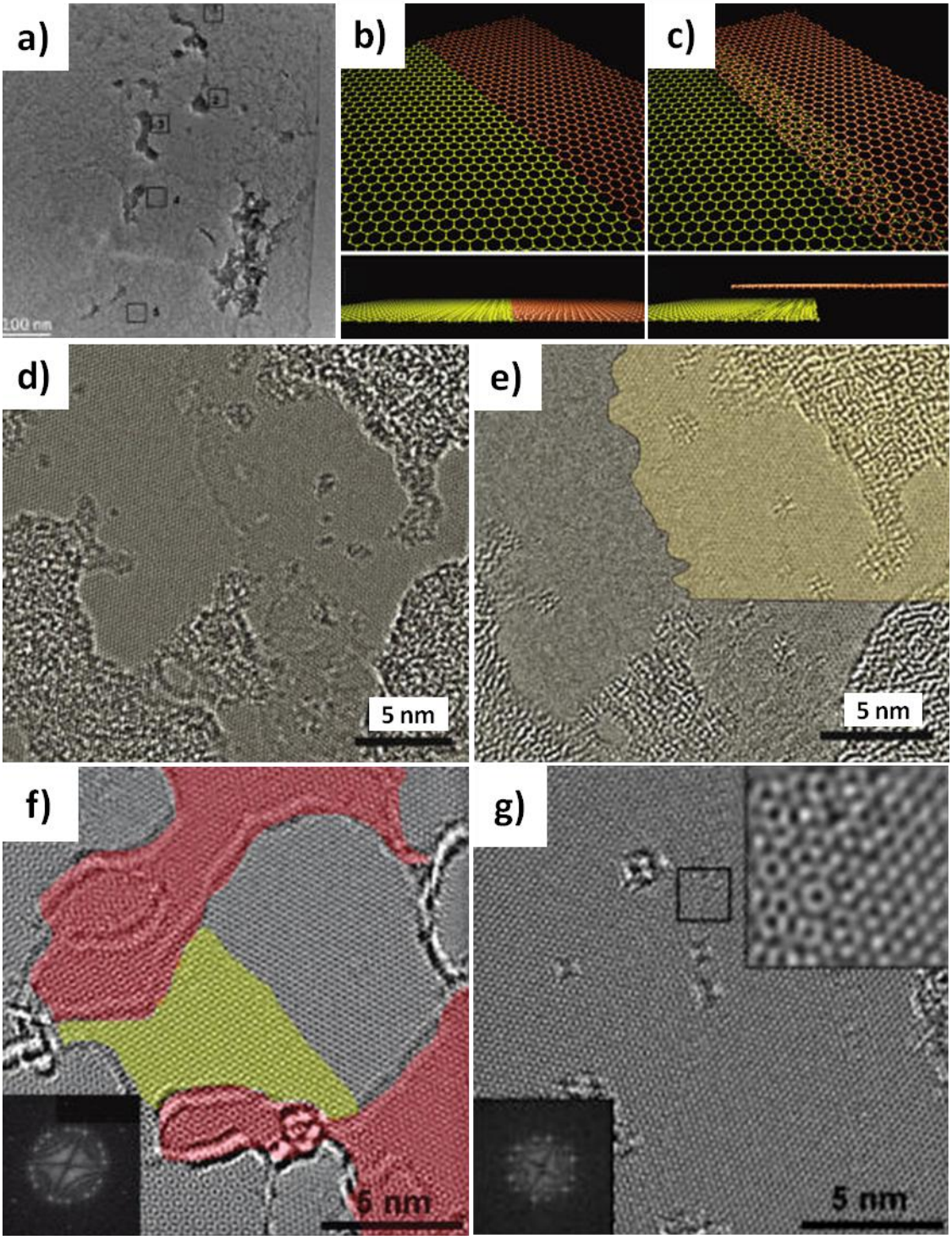


Figure 58) Schematics and TEM images reproduced with permission from ref[165]. a) Low magnification TEM image of an area of sample. b) and c) Schematics of atomically bonded and overlapping graphene layers respectively. d) and e) TEM images of one overlapping area with one layer highlighted in yellow in e). f) TEM image of FLG with several overlapping areas (highlighted by red and yellow). g) TEM image of overlapping example with inset showing the high-resolution Moiré pattern produced on one side.

The other overlapping example however, shown in Figure 58g, could be more consistent with two merging domains, with a very straight edge visible between the two areas. However, in all examples, no low magnification images are shown to support that the data was collected from

an area of a domain boundary. Figure 58a shows the only low magnification TEM image. From this figure it is not clear whether the image demonstrates merging graphene domains or simply a folded area of graphene. It would have been useful to show more than just FFT evidence to support the higher-resolution images.

Nonetheless, if it is assumed that both the examples in this paper are indeed examples of overlapping merging domains, the authors suggest that regardless of the overlapping, the material maintains perfect uniformity across large areas, indicating that domain boundaries contribute minimal defects in the resulting material. Hence, from this paper, subsequent theoretical studies focussed on two types of domain boundary; overlapping and atomically bonded, as demonstrated schematically in Figure 58b and c.

The literature in 2014 therefore finally recognised the addition of overlapping domains as a type of boundary, however, further experimental characterisation has only been undergone by SEM and Raman[185]. Apart from the previously discussed paper by Robertson *et al*. HRTEM characterisation is minimal.

During this thesis investigation, further characterisation of merging FLG domains was carried out by HRTEM. It was found that the literature is lacking in describing what can really occur at graphene domain boundaries and overlapping and atomic bonding boundaries may not be a sufficient explanation.

In this chapter, domain boundaries have been analysed from a sample of FLG, the synthesis of which is described in Chapter 2. This resulted in a sample of largely FLG hexagonal domains, with some areas of monolayer graphene, grown just under full-coverage to ensure easier identification of domain boundaries. In this sample, although it was possible to observe domain boundaries similar to those in Figure 57, multiple examples of imperfect domain boundaries were observed and the results are indicative of merging domains creating more distortion from the synthesis than the literature implies.

This chapter will discuss five examples of imperfect domain boundaries in detail, both analysing the evidence for a feature indeed being a domain boundary and then how it differs from previously published work.

4.1.2 Determining a grain boundary

Firstly, to make any conclusions on domain boundaries there must be sufficient evidence that the defect observed is from merging graphene domains as opposed to the transfer procedure.

This can be done by looking at low magnification TEM images and determining any features indicative of merging domains, such as two hexagonal features coming together (as shown in the SEM image in Figure 59) before imaging at high resolution. Then by observing the change in the FFT and hence any graphene lattice changes across a feature, a convincing picture of what is occurring can be hypothesised. Different graphene domains never produce exactly the same diffraction pattern. Un-changing graphene diffraction patterns, or FFTs, are commonly used to prove the existence of large, continuous graphene domains[103,186–189]. Therefore, if a change in the FFT is observed, it is very likely that more than one graphene domain is present. However, it is worth noting that during graphene transfer, a single graphene domain that folds, tears and hence rotates will also change the angles of lattice spots in the FFT. It is at this point that the low magnification images help to provide more evidence of what is occurring within a sample.

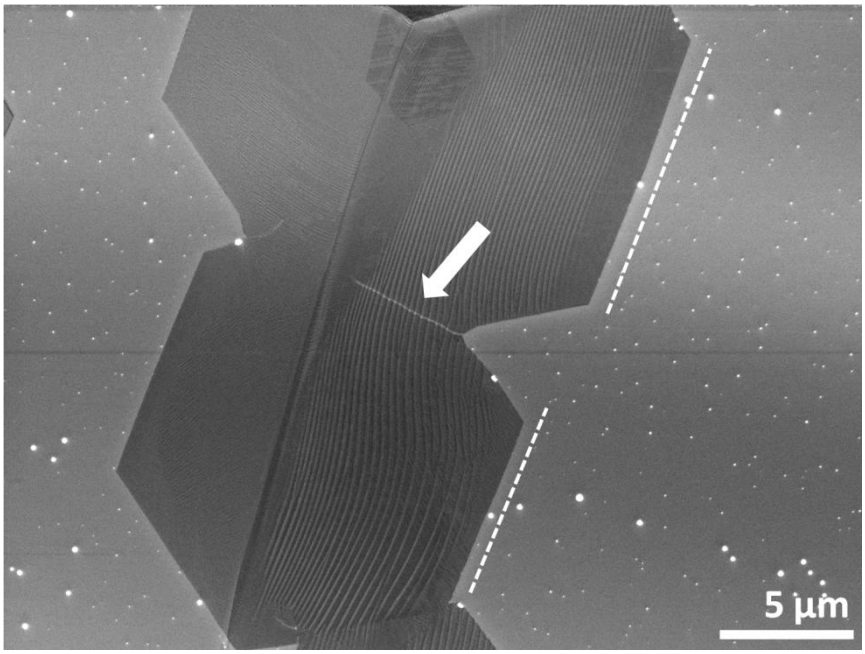


Figure 59) SEM image of two, on axis, hexagonal merging domains. White arrow highlights a feature which has likely resulting from the domain boundary.

Figure 59 is an example of a low magnification SEM image that depicts an imperfect domain boundary. Graphene domains often merge together, appearing to be on axis. Work has been undertaken to control the orientation of graphene domains in the hope that the impact of grain boundaries is lower[104,189,190]. It has been supposed that hexagonal domains would join more favourably as they have straighter, more uniform edges compared to some dendritic growth. However, even at low magnification, as shown in Figure 59, two, on-axis hexagonal domains (1° difference) have merged head on, creating an imperfection (appearing as a white line) between the domains, as highlighted by the white arrow.

In the sample characterised in this section, multiple examples of imperfect merging graphene domains have been observed and characterised by HRTEM. Some of the most interesting examples have been described and analysed in detail. A summary of findings will be discussed at the end of the section.

4.1.3 Experimental observations of imperfect domain boundaries

4.1.3.1 Example 1

Figure 60 shows the first example of an imperfect graphene domain boundary that has produced a defect. Large amounts of contamination prevented clean lattice imaging however reliable FFT data can still be obtained.

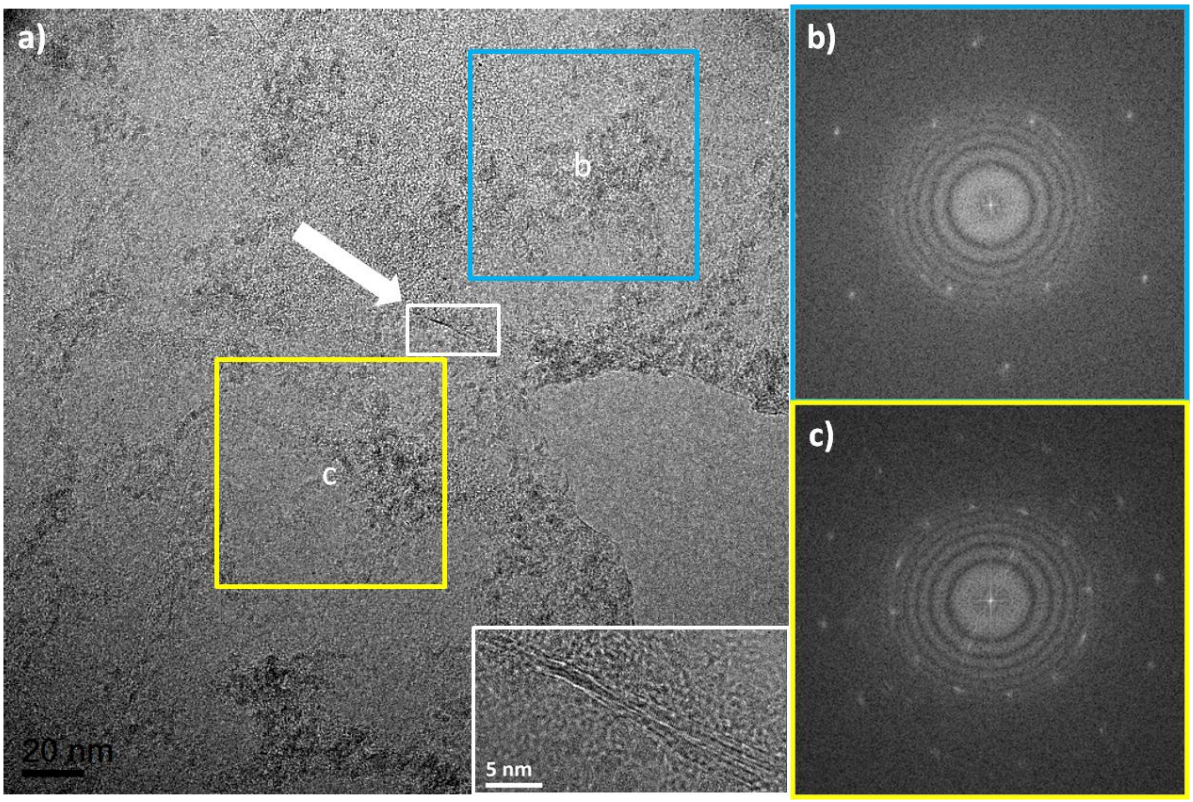


Figure 60a) Low magnification TEM image of merging domain area. White arrow highlights area of inset which shows a wrinkle at the boundary at higher resolution where the change in graphene lattices occurs. Yellow and blue boxes correspond to where FFTs b) and c) were taken.

This is the simplest example of an imperfect domain boundary where a small defective area can be observed at the join. Figure 60a shows a TEM image of the merging domain boundary with the inset highlighting the defect that can be observed at the join. FFTs change immediately above and below the join. FFT b implies an aligned graphene lattice whereas the lower domain, FFT c, exhibits an entirely different set of lattice spots, heavily implying an alternative graphene domain where neither lattice is aligned with FFT b. It is possible that the upper domain is a monolayer lattice and the lower domain is a misaligned bi-layer sheet, however the spot intensities from the FFTs could not be used to determine this in this case. The minimum lattice

rotation between both FFTs is 3.9°±0.9. This angle is distinctly smaller than in some future examples.

The white arrow in Figure 60a highlights the area where the inset is taken. The inset shows a wrinkle feature that has occurred at the boundary. This is likely due to sample buckling upon merging. Beyond this defect, no additional defect feature is observed and therefore it is likely that the atomic bonding boundary mechanism (as shown in Figure 57) is present here.

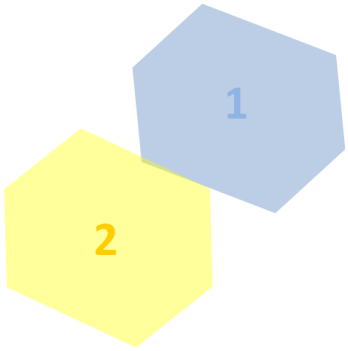


Figure 61) Schematic of potential domain boundary.

Figure 61 depicts the proposed schematic of the domain boundary as seen in Figure 60. The minimum rotation has been applied to the lower hexagon. The angle between both of these domains is similar to that which is observed in Figure 60. It is noted that nanoparticle catalysed degradation is also apparent on the domain edges next to the vacuum, where the imaging beam has been focussed. These edges were straight before high-resolution imaging took place.

4.1.3.2 Example 2

Figure 62 shows a low magnification image of an area of sample containing a graphene domain boundary. The white arrow highlights the area of sample where the majority of data was taken. The red arrow highlights a wrinkle feature that could be a result of what is occurring in the area of the white arrow.

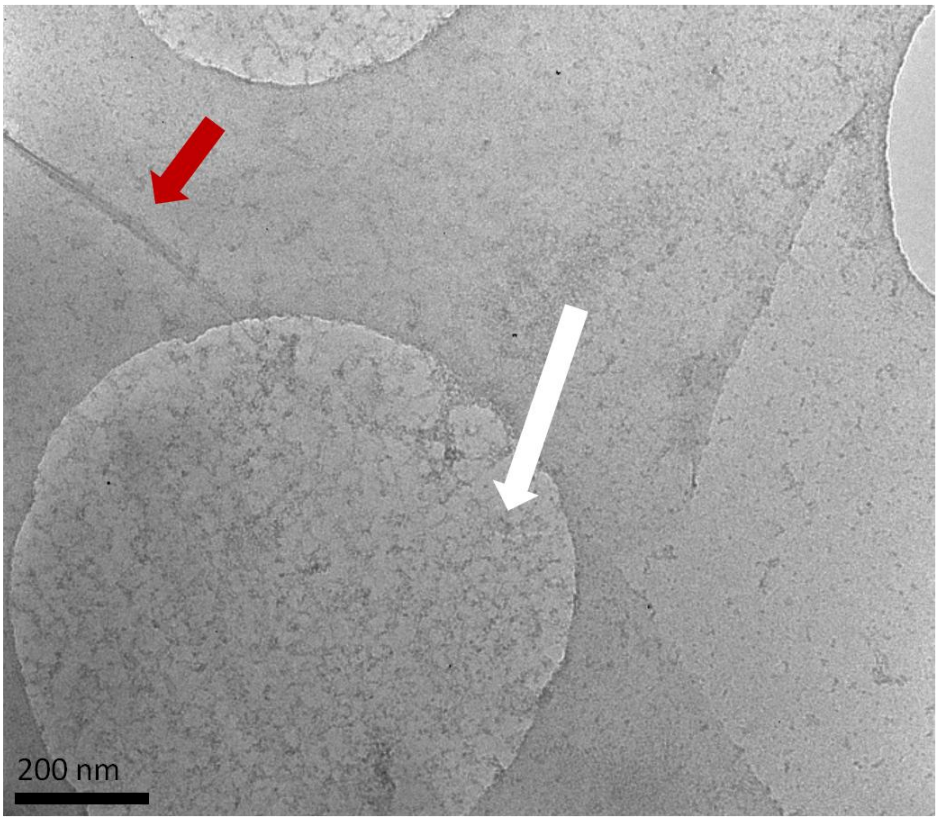


Figure 62) Low magnification TEM image of domain boundary. Red arrow highlights wrinkle, white arrow highlights the area where subsequent HRTEM data is obtained. It is possible to see a join here.

Figure 63 shows TEM images of the area highlighted by the white arrow in Figure 62. This white arrow is used in the same place in Figure 63a and b. In Figure 63b, the white arrow highlights a small "hole" in the graphene that is at the edge of the potential boundary, highlighted in the previous low magnification image. This hole, as can be also seen at higher magnification in Figure 63c-d, started off as an area of vacuum between two, straight edged, graphene sheets.

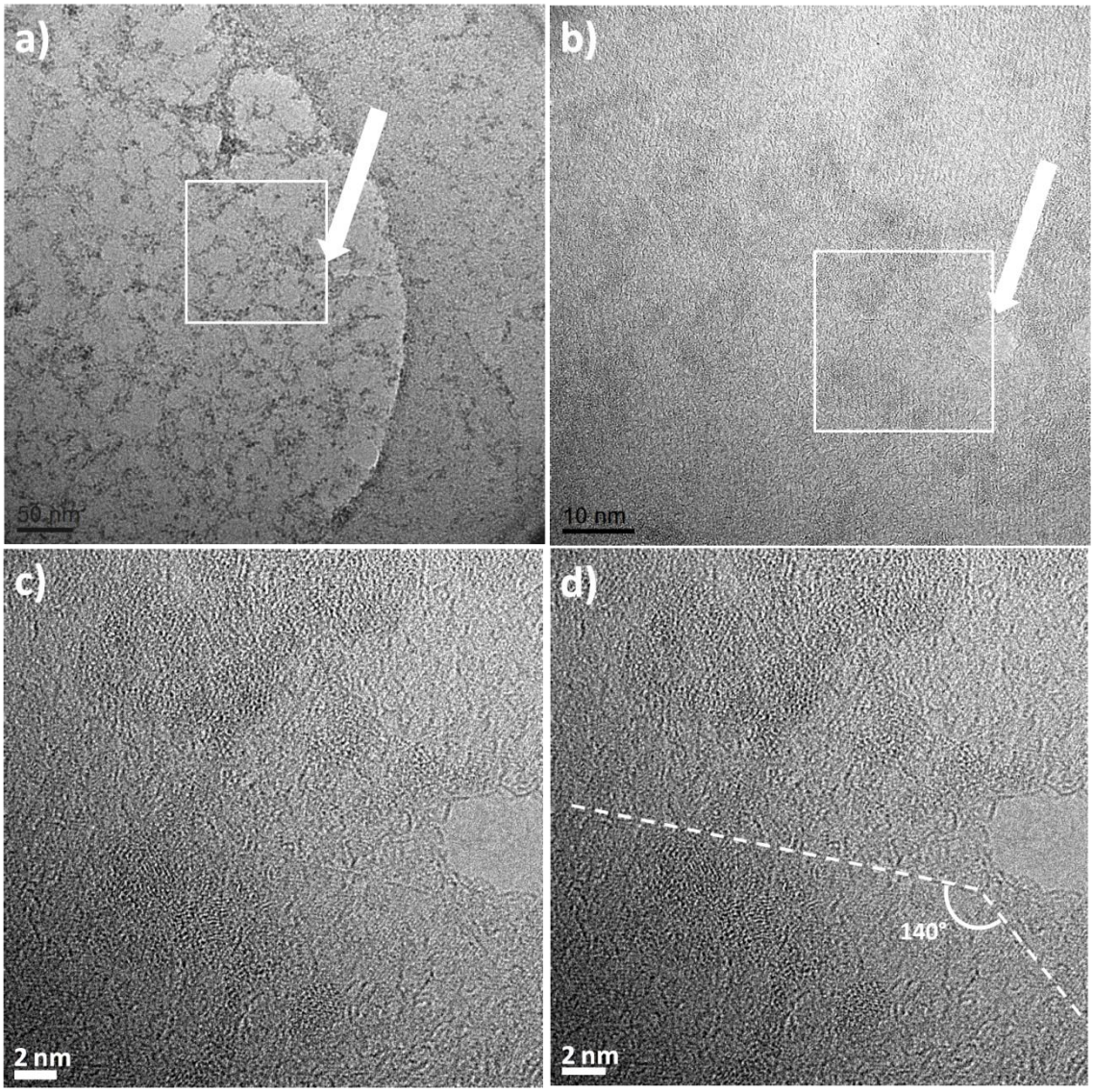


Figure 63) TEM images of potential boundary at higher magnifications. Inset in a) shows area of image b). Inset in b) shows area of image c). White arrows in a) and b) highlight region of the boundary. Image d) is the same image as c) but has highlighted a hexagonal feature which can be observed in c) equating to a *ca*. 140° angle. Graphene holes are apparent in b-d).

At the edge of the boundary, before excessive amorphous contamination occurred, it was possible to see a triangular feature in the TEM image (Figure 63c and highlighted by white dashed arrows in Figure 63d). The angle of this triangle measured *ca*. 140° which is consistent with an angle observed in a CVD hexagonal domain as described in Chapter 2. It is therefore possible that it is an apex of a hexagonal graphene domain. This triangular feature was susceptible to beam damage upon further imaging.

Figure 64 shows further evidence that this area of sample is a graphene domain boundary. Figure 64a shows the unprocessed image of the boundary, as previously shown in Figure 63b.

The white arrows follow a visible orientation either side of the domain boundary. Figure 64b is the FFT of this image and shows two hexagonal graphene lattices, slightly misaligned from each other by 1.8°±0.1 (inset).

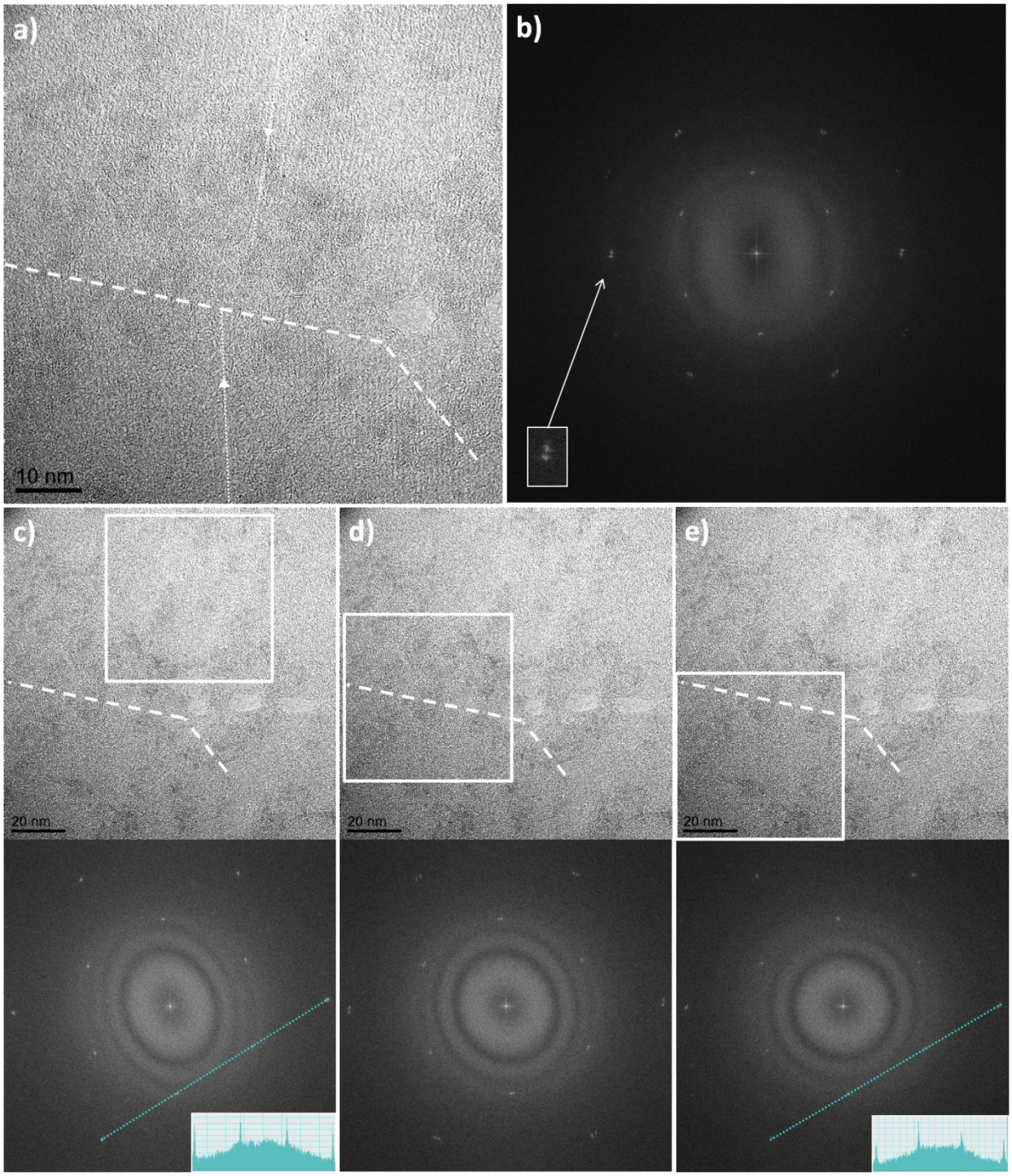


Figure 64a) TEM image of potential boundary with white dotted lines highlighting the change in direction as can be observed by eye on the image and the boundary. b) Corresponding FFT of a) showing two hexagonal lattices slightly misaligned, inset highlights the difference between two lattice spots. c-e) TEM image a) with white boxes corresponding to the relative FFT below. Insets in FFTs c) and e) correspond to spot intensity line profiles of monolayer graphene lattices.

Taking FFTs from smaller regions across the triangular feature(Figure 64c-e) it is possible to observe that the two sets of lattice spots correspond to either side of the boundary. Figure 64d shows how across the centre of the join, both sets of spots are visible. In addition, the spot intensities of the merging graphene lattices (insets of c and e) imply that both graphene lattices are monolayer. Therefore, these images correspond to merging monolayer graphene domains.

It is worth noting that only negligible, if any, strain in the lattices was observed and small enough that accurate FFT analysis would not have been reliable in this sample area. Initially the boundary exhibits very little imperfection, so it is likely that an atomically bonded boundary is what first occurs. In this case, two monolayer lattices are only misaligned by 1.8°±0.1. It therefore may be a simpler process to merge without significant stress compared to merging FLG domains.

However, at low magnification in Figure 62, the red arrow highlights a large defect in the graphene sheet. It is likely that the merging domains caused this buckling, as it is linked to the initial boundary through a visible contrast on the image (highlighted by the white dotted arrow in Figure 65b). Nanoparticle contamination is more common in this area between the boundary and the large defect feature. Previous research has shown that nanoparticles can preferentially bind to defects[152]. In which case, this could still be described as an imperfect boundary, despite the clean join that is observed in Figure 64.

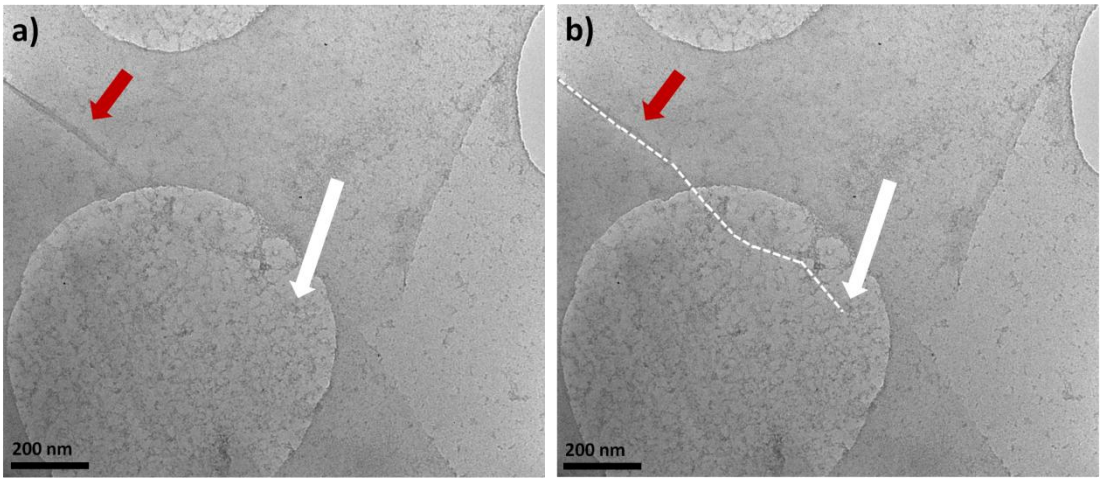


Figure 65) Low magnification TEM image of domain boundary. White arrow highlights area of join, red arrow highlights large defective area which has likely resulted from this join. b) Is image a) with a white dotted line highlighting the nanoparticle contrast that connects the two areas.

If this is the case, it brings into question the literature depicting images of cleaner domain boundaries. Finding a domain boundary in a TEM is a not an easy task and features such as wrinkles from domains merging would have aided this. It is possible that atomically bonded domain boundaries reported on in the literature also exhibited larger defects in close proximity.

4.1.3.3 Example 3 – Introducing overlapping domains

In this example, the boundary feature is observed within full coverage of graphene (Figure 66). At low magnification, a triangular contrast can be observed within the FLG sheet, as highlighted by the white arrow in Figure 66a. Additional similar features are also apparent in this area and resemble features that could be attributed to hexagonal domains from their angular measurements (Figure 66b).

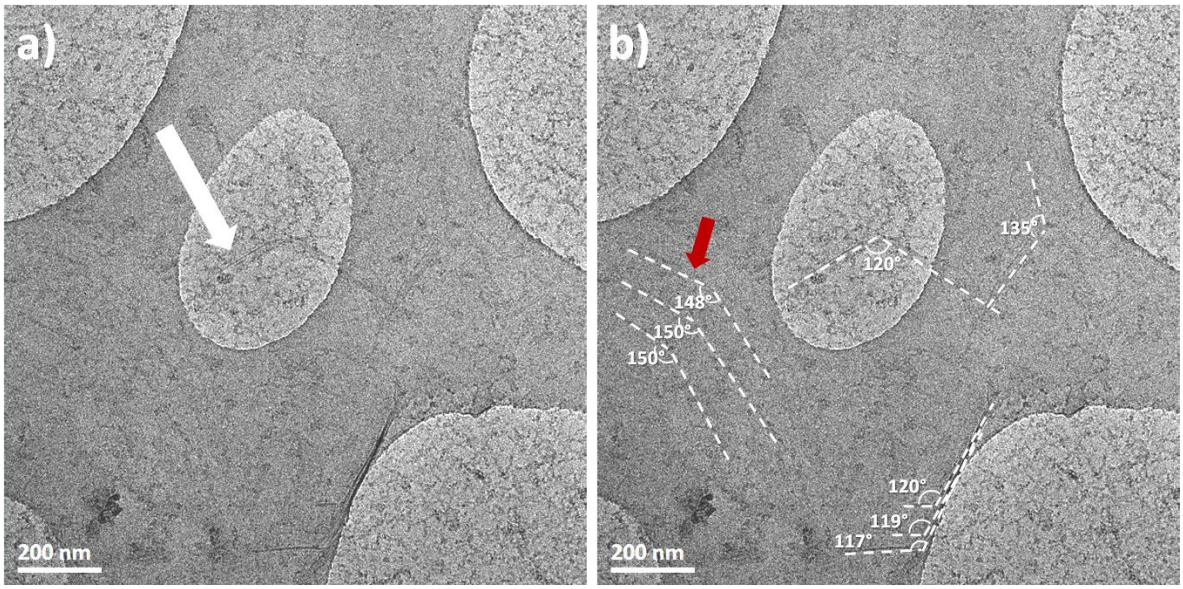


Figure 66a) Low magnification TEM image of feature, the white arrow highlights where subsequent data is obtained. b) is image a) with hexagonal features and corresponding angles highlighted. A small red arrow highlights features that are characteristic of FLG growth.

As shown in Chapter 2, hexagonal angles of graphene domains, although commonly around 120°, can range from approximately 105-150°. It is therefore plausible that the features observed in Figure 66 are multiple hexagonal domains merging together to form a continuous graphene sheet. In addition, the "step" features highlighted by the small red arrow in Figure 66b are akin to few-layer growth that has been previously discussed and observed with SEM imaging in Chapter 2. Unfortunately, only one area of sample was present over the vacuum hole in the holey carbon grid. This area of interest is highlighted by the white arrow in Figure 66a. Figure 67 shows higher magnification images of this area.

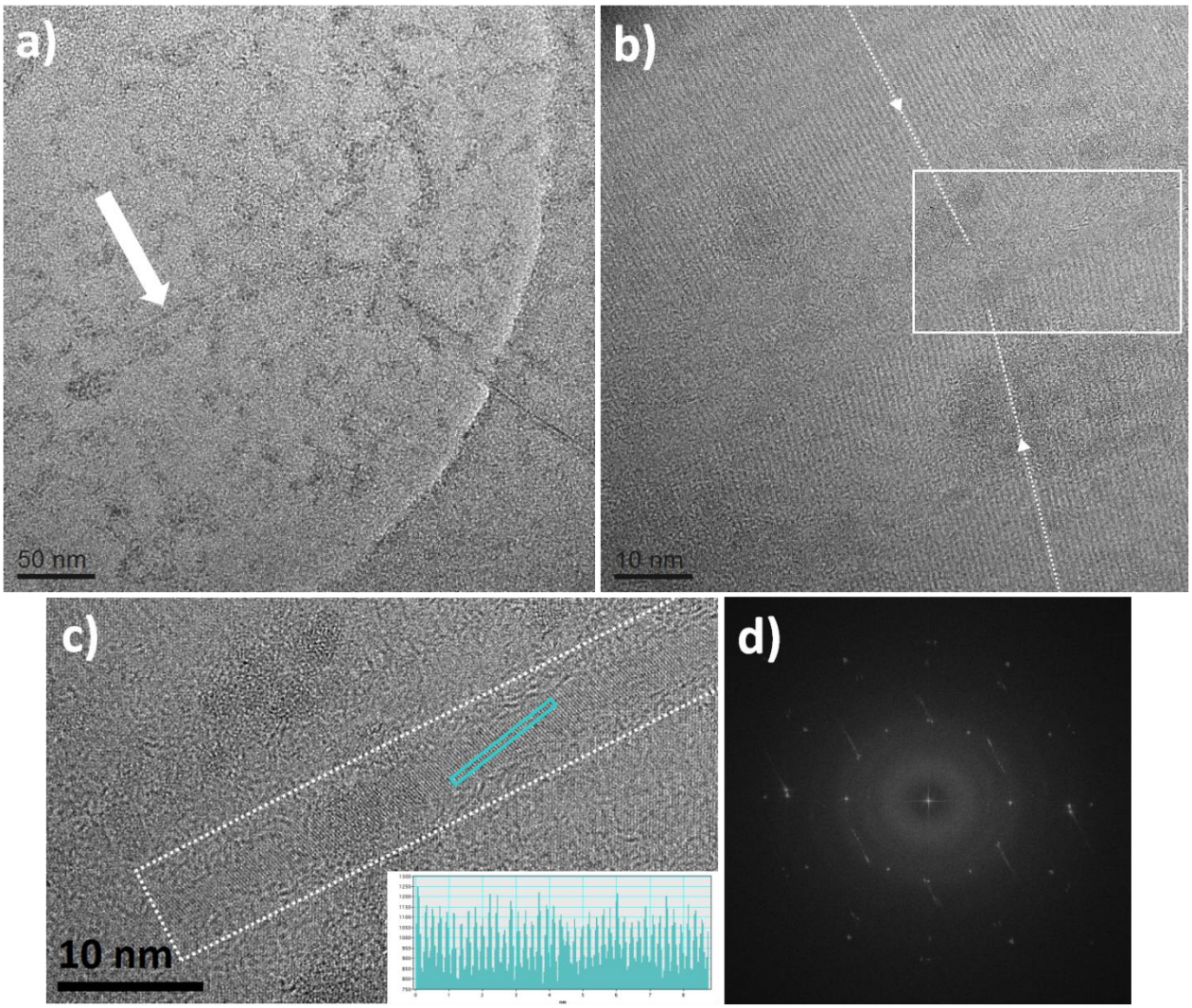


Figure 67a) Low magnification TEM image of area of interest with white arrow highlighting area where TEM image b) is shown at higher magnification. White dotted lines highlight visible misorientation. c) TEM image of the boxed area in b) where a white dotted box highlights a linear feature. The turquoise box highlights the region where the contrast profile (inset) is taken which shows the periodicity present within the linear feature. d) is the corresponding FFT of TEM image b).

Figure 67b shows white arrows that follow a visible orientation change either side of the boundary. The FFT in Figure 67d implies three sets of hexagonal lattices, and the streaks that appear in the FFT are attributed to a linear feature across the centre of the image as shown in Figure 67c. The periodicity observed in this feature is consistent with the spacing of the sideline periodicity as previously discussed. From those conclusions it indicates that there is a change in orientation of the graphene lattice at this point.

Figure 68a-f show areas of the TEM image shown in Figure 67b with corresponding FFT analysis. FFTs d and f of the upper and lower area of the image respectively appear to look very

similar to one another. Crucially, FFT e resembles the complete FFT of the image. To aid the interpretation of these FFTs, sets of spots from the complete FFT were masked to determine which spots corresponded to which lattice. Figure 68g highlights the sets of spots which were masked and are colour coded with the inverse-FFT results in Figure 68h-j.

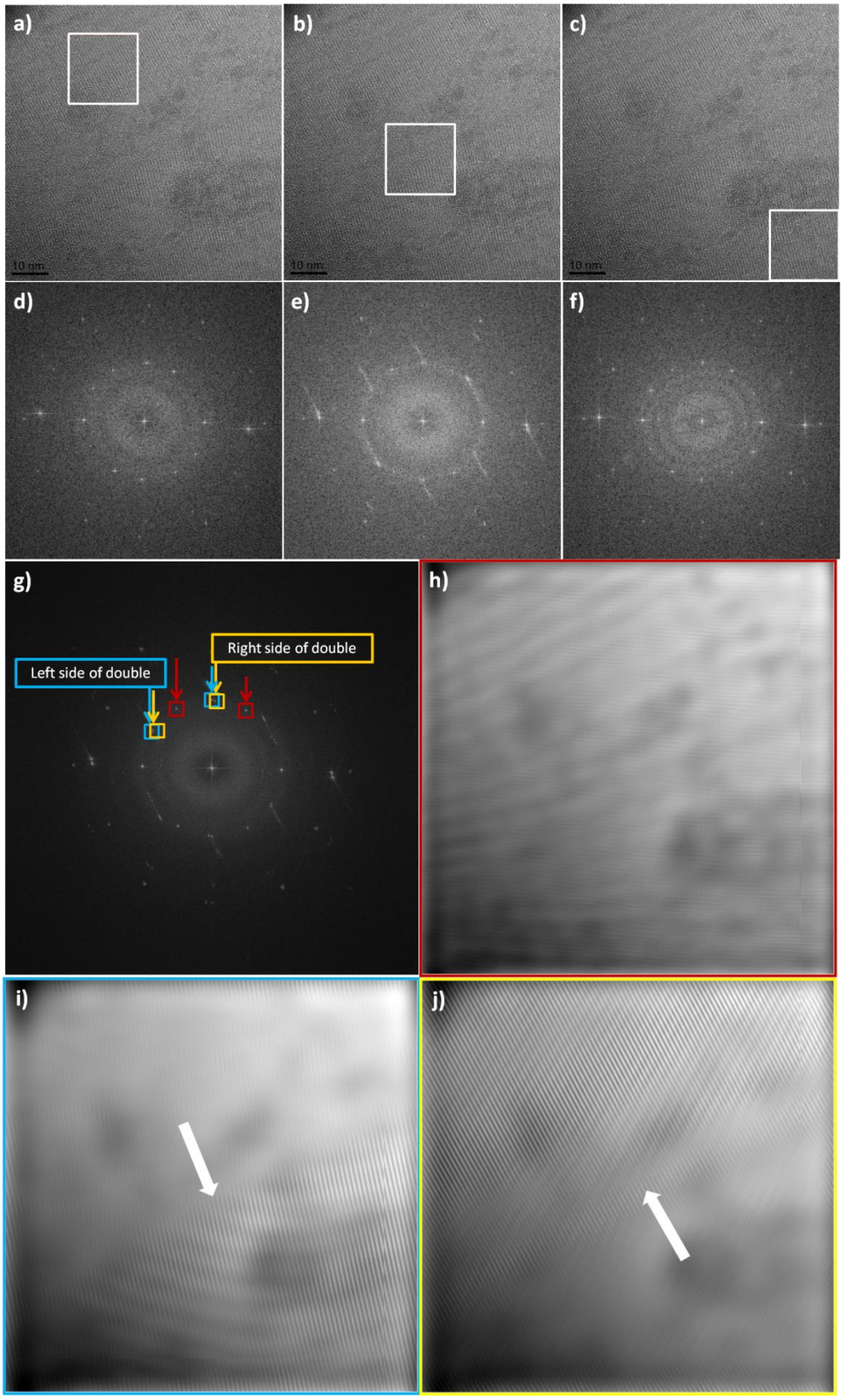


Figure 68a-c) TEM images of area of interest where white boxes highlight the areas of corresponding FFTs d-e). g) FFT of the entire image. h-j) IFFT images corresponding to positively masked sets of FFT lattice spots as highlighted in g). White arrows highlight the presence of one lattice in specific areas of the sample.

From this analysis it can be deduced that the red set of lattice spots (Figure 68h) is concurrent across the entire image. This implies a continuous graphene sheet throughout the area of the boundary. Blue and yellow sets of lattice spots (Figure 68i and j) correspond to the upper and lower lattices respectively. From their respective FTTs, these lattices are rotated from each other by 2.5°±0.6. This suggests that the upper and lower FFTs stem from two separate graphene domains and that this area shows an example of an overlapping domain boundary within full-coverage of an additional graphene lattice. Therefore, three graphene lattices are present at the join. Figure 69b demonstrates this schematically.

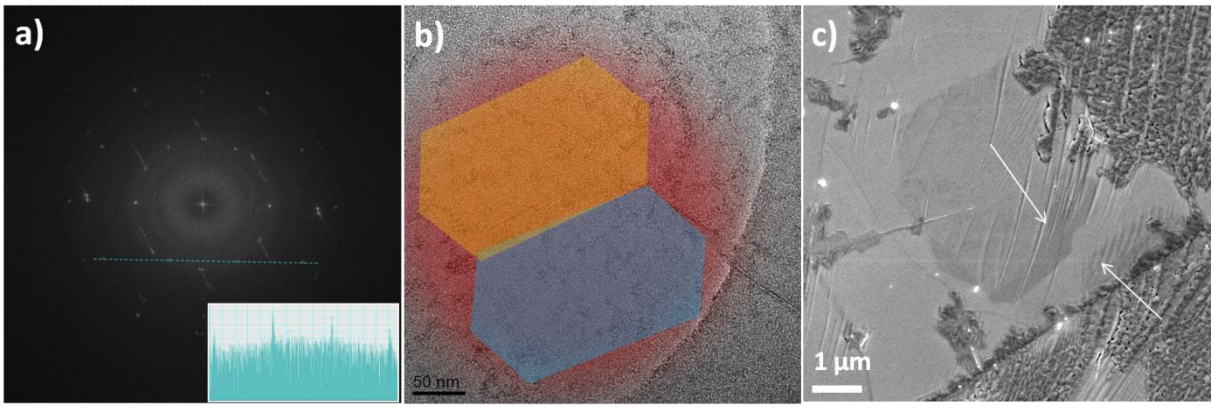


Figure 69a) FFT of Figure 67b. Inset shows the spot intensity line profile corresponding to the consistent monolayer lattice throughout the image. b) Schematic of possible domain boundary scenario. Red area represents the continuous monolayer. Yellow and blue hexagons represent merging graphene domains. c) SEM image of a similar feature that would be the prelude to his phenomenon, observed in a commercially available graphene sample.

The spot intensity line profile in the FFT of the continuous graphene lattice implies that it is a continuous monolayer sheet (inset Figure 69a). Figure 69b hence shows a schematic of two overlapping domains (yellow, blue) within an additional monolayer (red). The hexagons in this image are off-axis by 2.5° and demonstrate how the overlapping domains in the schematic closely resemble the feature observed in the TEM images.

Figure 69c shows the prelude to how this feature may have occurred. Figure 69c shows an SEM image of full-coverage monolayer graphene, with white arrows highlighting two additional graphene domains. If these domains merged, it could result in a very similar situation to what has been observed in this example. This image was taken from a sample of commercially

available graphene which may therefore indicate the presence of similar defects occurring in graphene currently used in industry.

Additionally, returning to Figure 66, the lower magnification TEM image shows that similar features to what have been characterised in this example are prevalent in the same area. This may be indicative of the extent of numerous, similar imperfections in some graphene samples.

4.1.3.4 Example 4

This penultimate example also concerns the analysis of a hexagonal feature within full-coverage. Unfortunately, in this particular area of the sample, nanoparticle contamination from the transfer to the TEM grid was abundant and sample degradation is visible. However, it has still been possible to gain reliable FFT data.

The area of interest is shown in Figure 70. Figure 70a shows a lower magnification image, the white arrow highlights where the first set of data has been taken. Figure 70b shows the same low magnification image, highlighting the hexagonal features with their corresponding angular measurements: 130° and 138°, indicating a hexagonal graphene domain. Figure 70c shows a TEM image at higher magnification of the area highlighted by a white arrow in Figure 70a. The two white arrows in this image are an aid to guide the eye to the hexagonal feature, which would correspond to the 130° angle in Figure 70b. Figure 70d is the corresponding FFT of Figure 70c. Multiple sets of lattice spots are present in this FFT, which will also include those from the crystalline nanoparticle contamination. Two white arrows however highlight two clear lattice spots which have hexagonal symmetry throughout the FFT. These sets of spots correspond to two different graphene domains as shown more clearly in Figure 71.

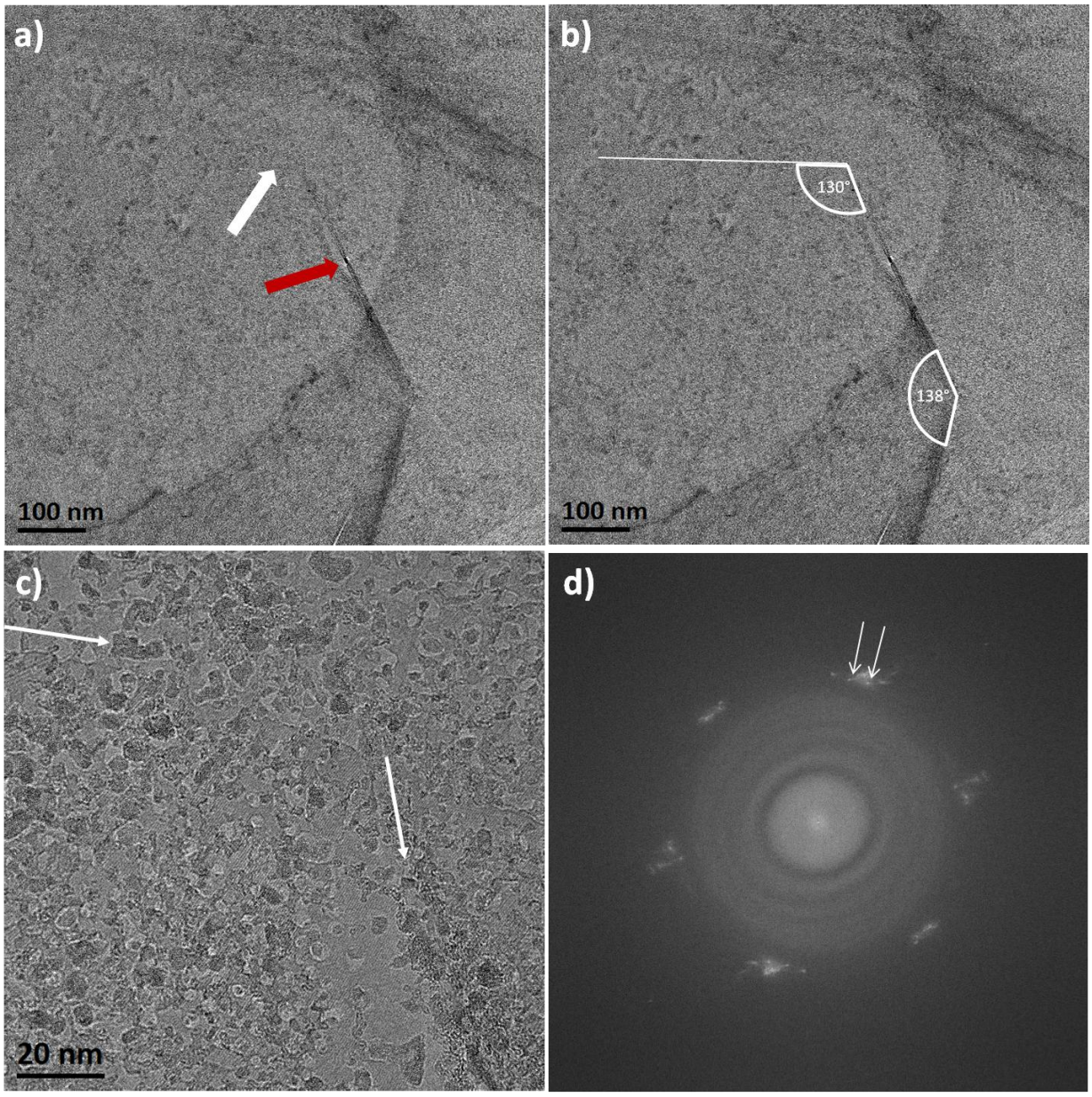


Figure 70a) TEM image at low magnification of merging domain area. White arrow highlights first area of interest, red arrow highlights second area of interest b) the same TEM image with hexagonal angles highlighted. c) TEM image of area highlighted by larger white arrow in a), white arrows highlight the directions of the hexagonal corner in the centre of the image. This area contains nanoparticle contamination which is caused sample damage. d) Reduced FFT of image c), white arrows highlight two strong lattice spots with hexagonal symmetry.

Figure 71 shows more detailed FFT analysis of the area of the boundary. Figure 71a and d, show FFT analysis of an area outside of the specified hexagonal domain, Figure 71b and e show FFT analysis towards the centre of the hexagonal domain and Figure 71c and f show FFT analysis within the hexagonal domain, but towards the edge and closer to a visible wrinkle, seen at lower magnification, highlighted by the red arrow in Figure 70. Nanoparticle contamination is more abundant towards this wrinkle which implies that the area may be more defective[152].

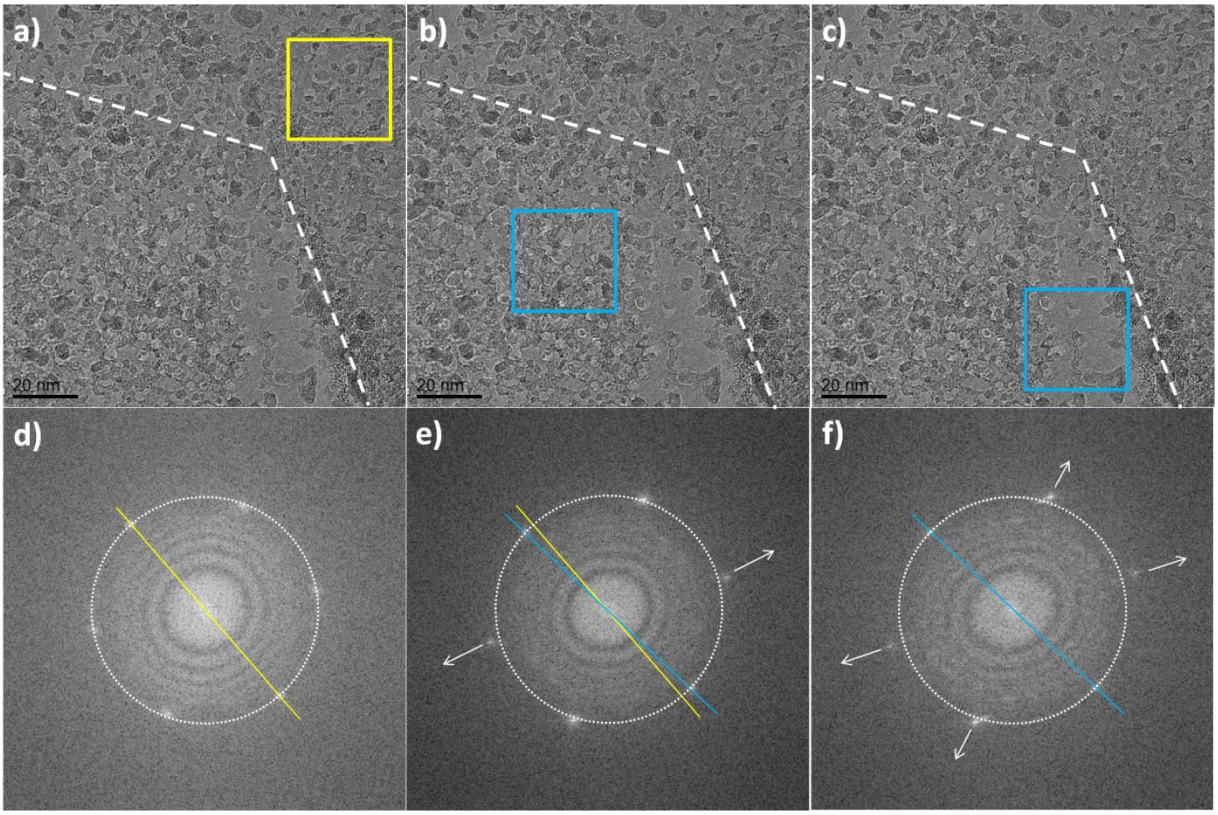


Figure 71a-c) TEM images of boundary region with yellow/blue boxes corresponding to where FFTs d-f are taken. More distortion in the FFTs is highlighted from d-f by variation from the perfect circle. Yellow/blue lines on FFTs indicate how different lattices are present either side of the boundary.

The FFT analysis confirms that two sides of the hexagonal feature exhibit different lattices and hence are different domains. Lattice spots between FFTs d-f change in rotation from 2.0-6.1°. The white dotted circles in the FFTs can show visually the distortion from a regular hexagonal lattice. The FFTs indicate more lattice distortion in the inner (blue) domain. Between 4-12% deviation in lattice parameter can be measured which increases towards the more defective area in FFT f (towards the area highlighted by the red arrow in Figure 70).The strain observed in FFTs e and f is likely to be the reason for the range in lattice rotation change from 2.0-6.1°.

To further analyse the area of distortion, analysis was undertaken in the area towards the wrinkle feature, highlighted by the red arrow in Figure 70. The wrinkle can be observed to consist of a number of discrete layers as shown in Figure 72b. Further FFT and image analysis is shown in Figure 72. Figure 72a shows the TEM image with coloured boxes corresponding to the areas where individual FFTs (Figure 72c-f) were taken. Figure 72b shows the wrinkle feature at higher resolution with insets showing line profiles of blue dotted lines 1 and 2 on the image.

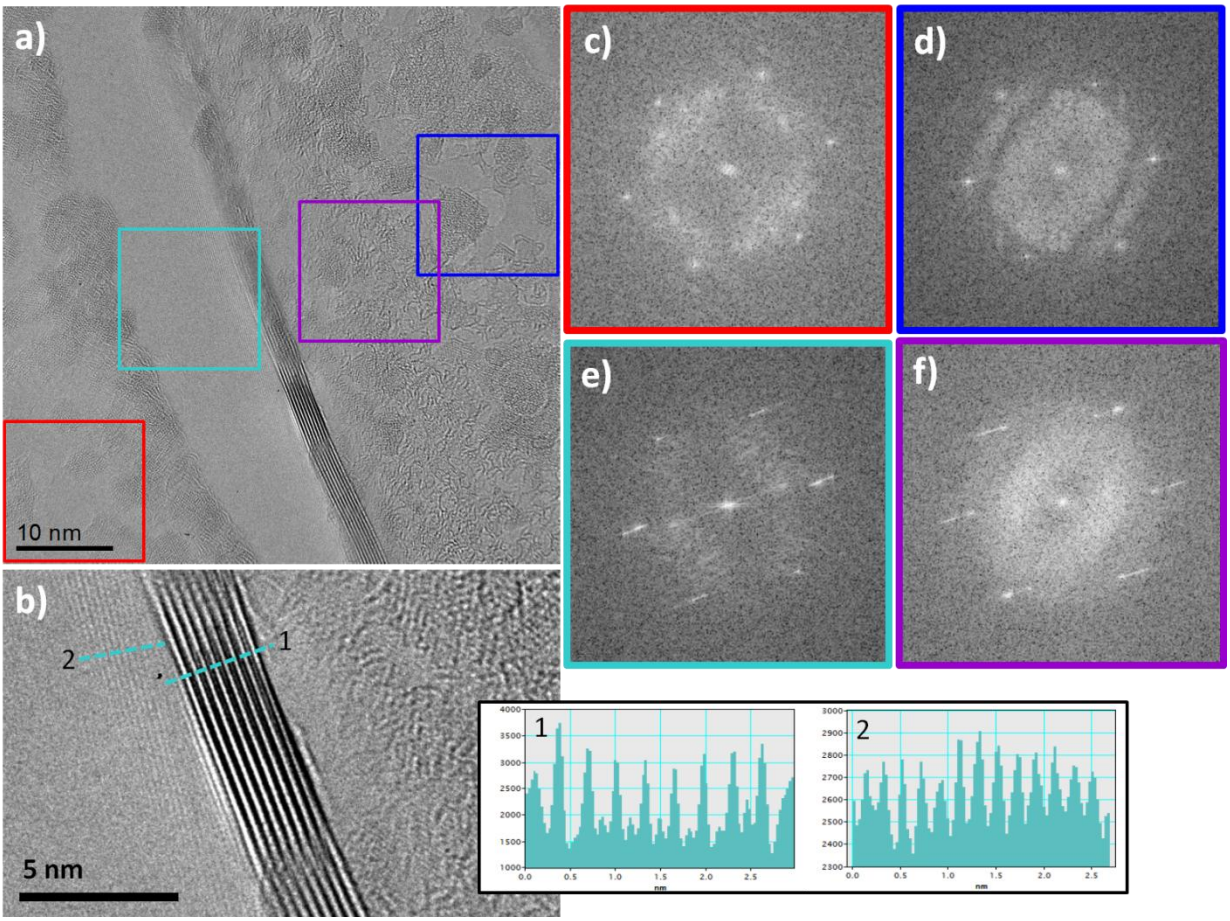


Figure 72a) TEM image of wrinkle feature, with b) at higher magnification. Insets are number line profiles across image. c-f) FFTs of corresponding coloured boxes in image a).

Line profile analysis in Figure 72b shows a contrast of 8 layers. In addition, Figure 72b shows that line profile 2 exhibits a sideline spacing of *ca*. 0.21 nm. This spacing seems to be often observed in defective areas and, as discussed previously, could be evident of a curve or off-axis arrangement of the graphene lattice. In addition, one area of the wrinkle also exhibits a inter-graphitic plane contrast, further suggesting a changing axis with respect to the bulk sample as previously discussed.

The FFT analysis across image Figure 72b compliments what was discussed previously in Figure 71; FFTs closest to the wrinkle feature exhibit more lattice distortion (FFTs e and f). FFTs e and f indicate up to an 8% strain in lattice parameter. FFT d exhibits negligible distortion and FFT c exhibits up to a 5% strain, comparable to Figure 71 where the FFTs within the hexagonal (left) domain were shown to consistently exhibit distortion. All other FFTs in this area exhibit streaks in similar directions. The streaks are likely due to the contrast of the linear bands measured in

line profile 2 in Figure 72b. These streaks could hence be indicative of lattice curvature in this area and provide structural insight into lattice arrangement. It could be expected that lattice curvature is more prevalent closest to the defect.

The number of graphene layers in this sample area could not be precisely deduced for two reasons i) high resolution FFT analysis that produce two rings of hexagonal spots could not be obtained, potentially due to contamination and ii) other edges of both flakes were within full-coverage so could not provide an indication on the number of layers. The 8-layer contrast observed could be the result of two bi-layers merging, each producing a simple wrinkle at the domain boundary. This would likely create a difference in orientation, and hence sideline contrast, as observed in the FFTs either side of the feature. It is possible that upon merging the two bi-layers collide and in doing so create a driving force upwards to form a tightly packed wrinkle. Such a wrinkle may not seem particularly probable; however it is worth noting that the 8-layer regular pattern is only observed for a relatively small distance compared to the size of the hexagonal flake. It is possible that in this small area, it was more stable for a wrinkle to form and the most stable C-C spacing is acquired (0.34 nm) in an attempt to lower the energy of the defect site. However, in this case, simulations would be necessary to confirm whether the TEM contrast observed is possible from the proposed scenario.

Nonetheless, this example again demonstrates that defective features have arisen upon the merging of two graphene domains, including wrinkle formation and lattice strain.

4.1.3.5 Example 5

This final example describes a more complicated imperfect domain boundary compared to Examples 1-4. Figure 73a, c-d show low magnification images consistent with a graphene domain boundary.

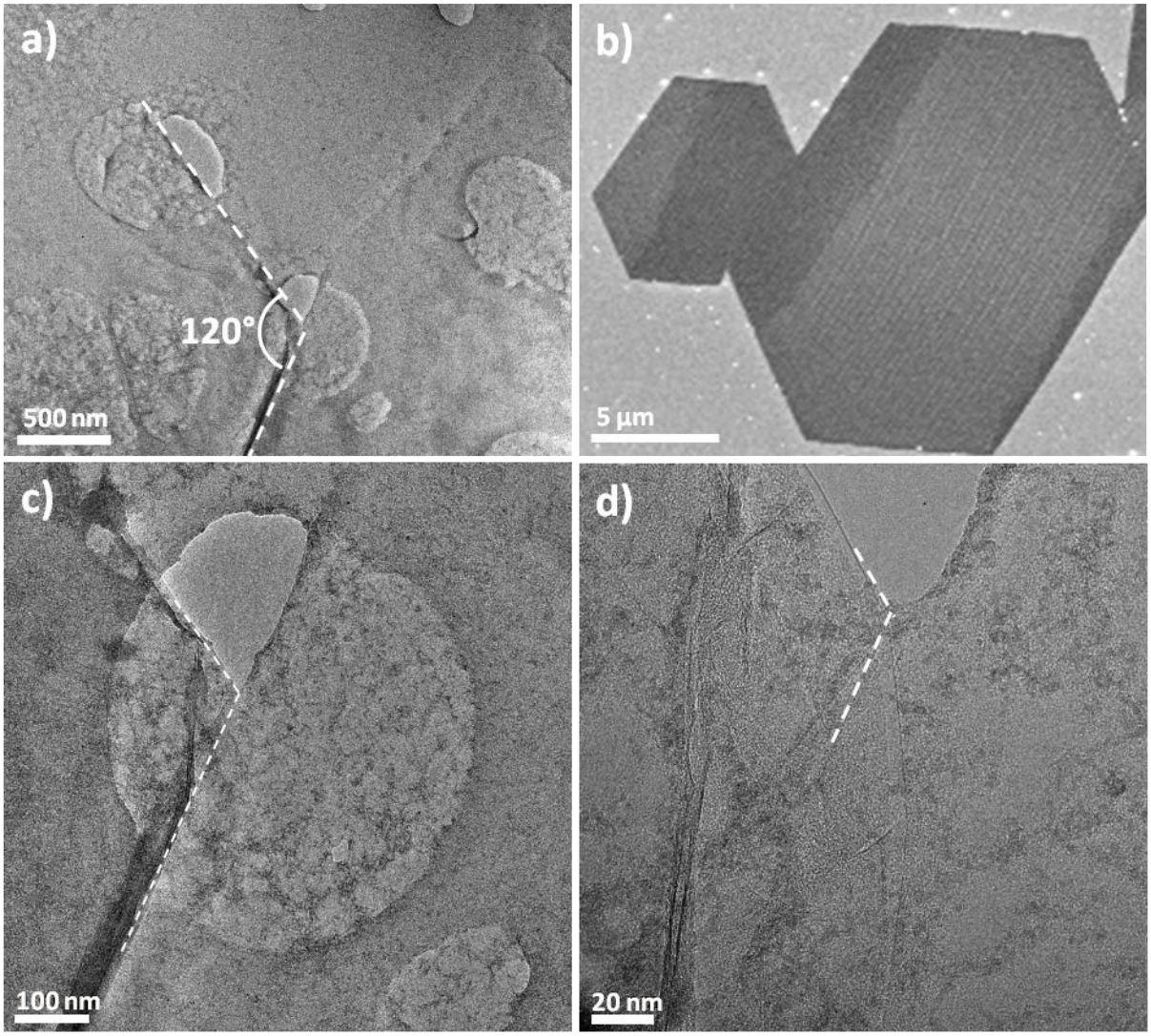


Figure 73a) Low magnification TEM image of graphene domain boundary. White lines highlight how features equate to a hexagonal angle of 120° b) SEM image of a similar feature. c) and d) increasing magnification TEM images of the feature, with more wrinkles becoming apparent as resolution increases.

Figure 73b shows a similar feature imaged with SEM. The first indication that this feature is likely to be a domain boundary is that the straight edge features on the left domain (as highlighted by white dotted lines in Figure 73a-d are at 120° to each other which is indicative of a hexagonal domain. The defined corner of this hexagon appears to exhibit buckling and multiple resulting wrinkles. FFT analysis at higher magnification has been undertaken in the area of Figure 73d and is shown in Figure 74.

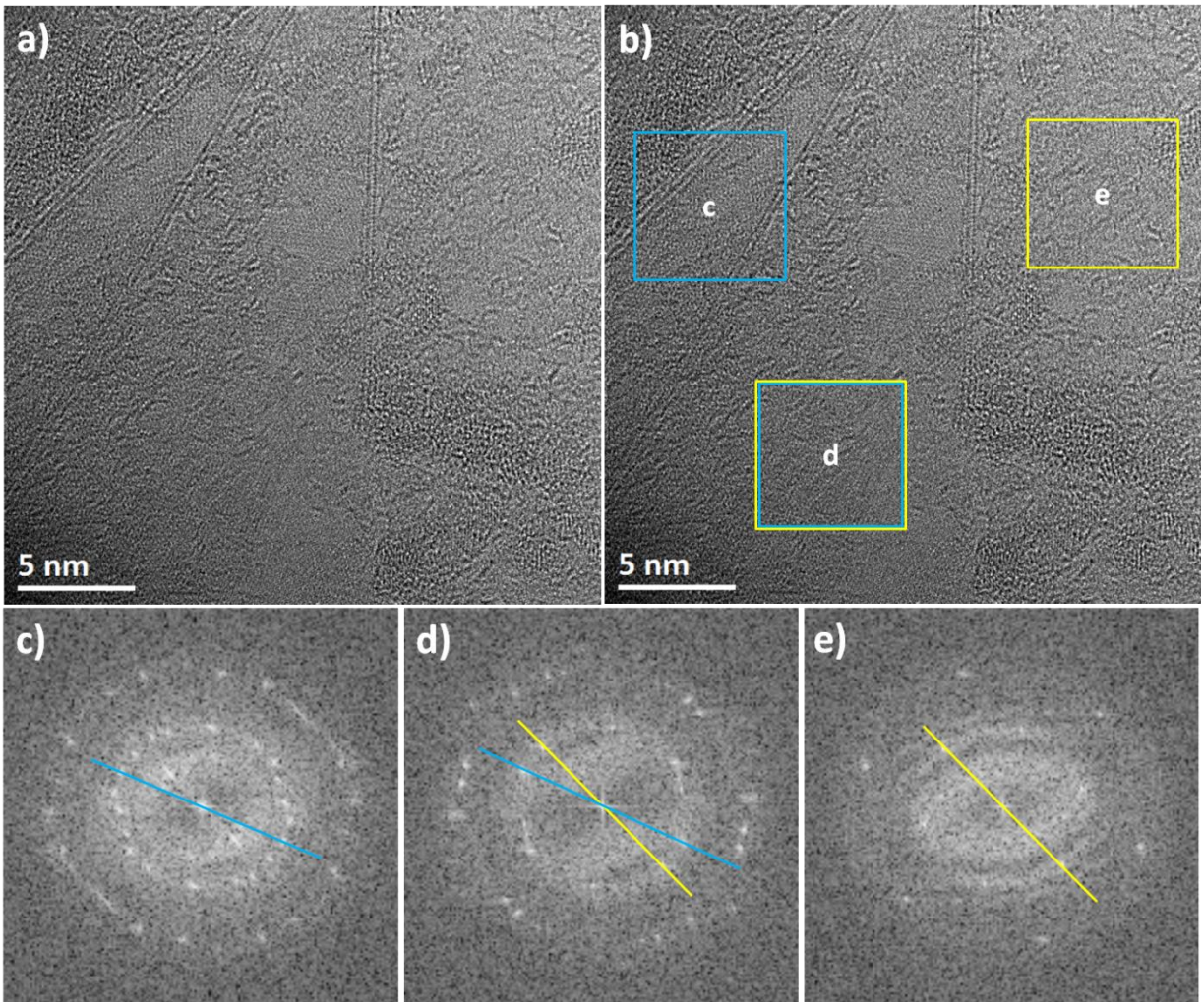


Figure 74a) High-resolution TEM image of domain boundary. b) Same TEM image as a) with insets highlights where FFTs c-e were taken. c-e) FFTs taken from respective places on b). Blue lines highlight a lattice that is present in FFTs c-d, yellow lines highlight a lattice that is present across FFTs d-e.

The FFT data taken from various points at the domain boundary (Figure 74c-e) implies that as well as multiple graphene layers being present, there is some overlap occurring. Figure 74a shows a higher resolution TEM image of the area, with corresponding FFTs highlighting the changes in the graphene lattices. By monitoring key points in the FFTs, it can be concluded that FFTs c and d contain one consistent lattice from the left side of the boundary (highlighted by the blue lines) and FFT d and e contain one consistent lattice from the right side of the boundary (highlighted by the yellow lines). FFTe may be monolayer graphene, bi-layer or aligned few-layer graphene, unfortunately, the spot intensities were not reliable in this case, likely due to the significant contamination present. It is also worth noting that both lattices either side of the

suspected domain boundary come into focus at different heights, further proving they are not uniformly bonded and are likely overlapping.

From measuring FFT d, the blue lattice is misoriented from the yellow lattice by 20.6°±0.2. This is the largest difference in misorientation compared to the previously discussed examples, and interestingly the most complicated and defective example. The bottom right inset in Figure 75 represents a simplified schematic of what could be occurring in this sample area, the colours of which are mirrored in the TEM image. The large white arrow at the top of the Figure 75 highlights a non-uniformity in the straight edge of the blue lattice. This edge discrepancy is likely due to the high concentration of nanoparticles on this edge, which as previously discussed in Chapter 2, can lead to sample degradation.

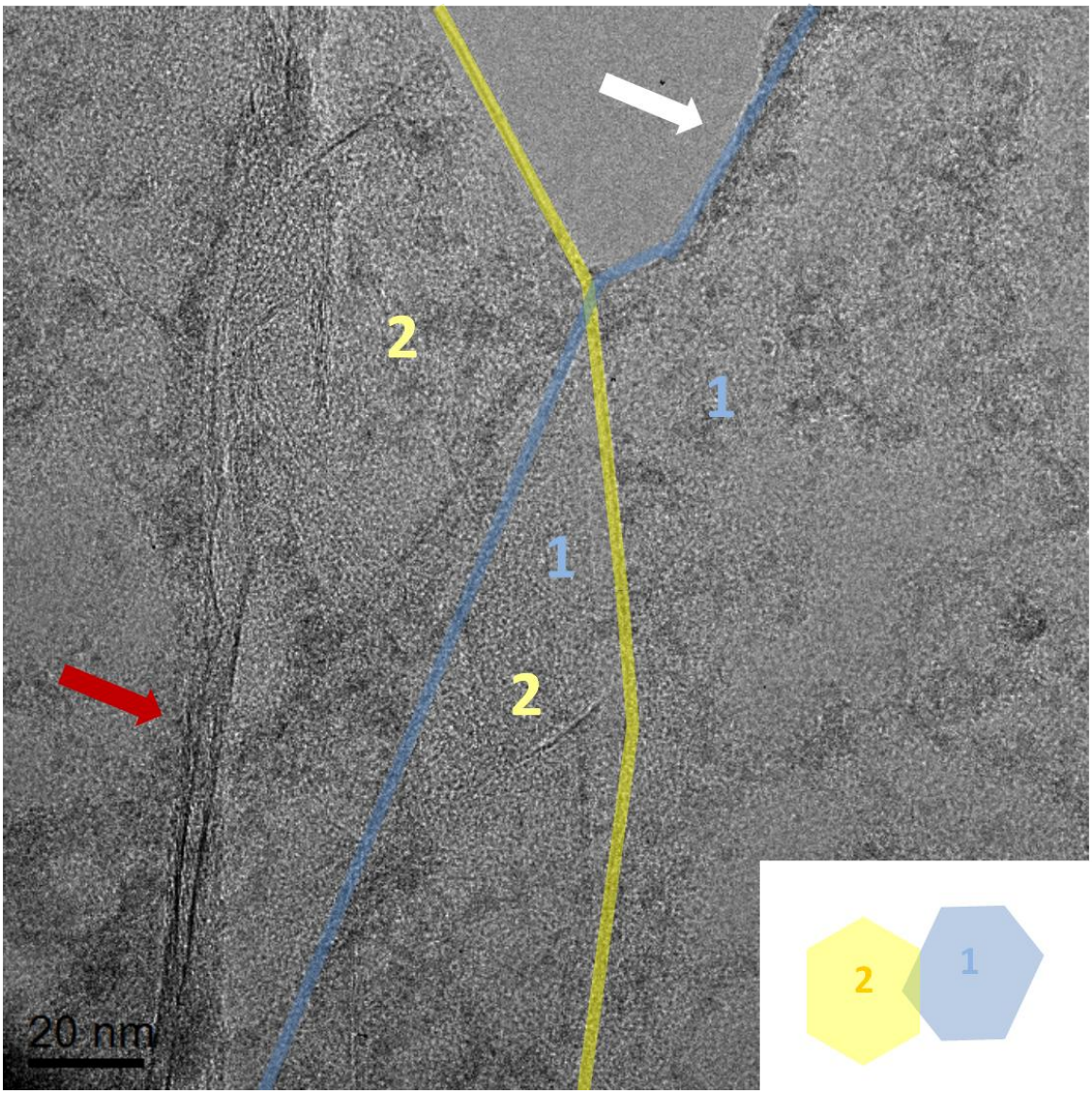


Figure 75) Low magnification TEM image of domain boundary with the arrangement of two merging domains highlighted, showing overlapping. White arrow – points to edge of 'blue' lattice which does not match up with the straight edge due to beam catalysed degradation during imaging. Red arrow – highlights the extra buckling occuring when the two domain are joining. Inset: Schematic of possible scenario occurring.

Comparing this overlapping domain boundary to the overlapping examples that have been discussed in the literature, it is evident that there is a clear difference. The red arrow in Figure 75 highlights an area of a large number of wrinkles. It is possible that the complicated merging of the two domains that has caused overlapping has also cause strain and buckling in the system. What is clear in this case is that this area is distinctly not a perfect graphene domain boundary and wholly unlike those which are reported in the literature.

4.1.4 Summary

What has been continually observed throughout the examples analysed in this section is that although some features may differ in terms of the number of layers, lattices rotations or overlapping features, all examples exhibit some form of larger imperfection that has not been reported in the literature. Graphene domain boundaries are assumed to have simpler defects, such as Stone-Wales defects or slight areas of overlapping that can only be distinguished with a contrast change seen at atomic resolution[165]. With the data analysed in this section, it is possible to deduce that multiple types of other domain boundaries exist, each slightly different and indeed less perfect than the literature implies. Domain boundaries that produce defects and lattice strain are much more likely to affect the overall properties of the material.

In the examples discussed, the change in rotation between the merging graphene domains ranged from 1.8° to >20°. The largest extent of imperfection, in terms of the highest presence of wrinkles and buckling, was observed in Example 5, where the largest change in lattice rotation between two merging domains existed.

In Examples 1-4, the angles of misorientation between merging domains was largely in the same range, and multiple types of imperfections could be observed. Both Examples 1 and 2 showed areas of atomically bonded domain boundaries, while also exhibiting wrinkle imperfections. Example 3 showed the first example of overlapping domains, which at high-resolution seemed to produce a fairly minimal overall effect, but caused large defective areas that were visible at low magnification in TEM. The same could be said for Example 4, where not only wrinkles were produced at the boundary but significant strain in the lattice could be observed at the point of the domain boundary.

Example 5 could be evidence to support the theory that on axis domains merge more preferentially, as the largest misorientation angle arguably produced the most defective domain boundary. However, all examples, even from a >2° misorientation have resulted in defective features such as wrinkles, overlapping or lattice strain. It is therefore integral to the field to

recognise such occurrences, and understand to what extent these features affect the final quality of the material. It has been shown that a deviation from the type of domain boundaries shown in Figure 57 has an effect on electronic properties[121,183,185]. However, this literature is limited to simple overlapping boundaries where overlapping is assumed not to coexist with any other defects. Therefore it is likely the properties of the five examples shown in this chapter would further differ.

Robertson *et al*. put forward that distinguishing between the type of domain boundary (overlapping or atomically bonded) is possible with HRTEM via a small contrast difference between the two mechanisms[165]. This contrast difference is very difficult to observe at low magnification. It is possible that features such as wrinkles alert researchers to the location of a domain boundary and the imperfections are not published in the final article. There is a need to provide more low magnification information to confirm the presence of a domain boundary as it is possible that more defective areas exist further afield from the boundaries reported in the literature.

It is understandable across all literature that scientists publish the highest-quality images of experiments, and hence only far from imperfect boundaries have been published to date. Even a more recent publication (Sept 2014) into overlapping domain boundaries still fails to comment on the other imperfections merging domains can cause[166]. If such analysis is unrepresentative of the material, it leaves a hole in graphene characterisation for the larger scale material, which will eventually be used in applications. If this is the case, the properties of imperfect boundaries are more likely to be what is reflected in the material used in industry and many laboratories. Experiments investigating changing properties will be discussed in Chapter 7: Further Work.

4.2 Part I and Part II summary

In summary, Chapters 3 and 4 discuss several defect phenomena that have been observed in graphene samples. The presence of overlapping and folded regions was concurrent with what has been seen in the literature and show the similarities to the samples synthesised in this thesis to those already characterised.

This chapter has included the investigation of several TEM contrast phenomena that can help define defect structure: periodicity along graphitic planes, appearance of sidelines and inter-graphitic plane contrast are all new investigations into the analysis of graphene defects in TEM imaging. In addition, the presence of linear moiré patterns was shown to be an additional indicator of graphene structure and has been shown to occur when both graphene lattices undergo lattice strain.

The characterisation of imperfect domain boundaries has shown that domain boundaries can be more defective than the current literature suggests. The imperfections observed can be seen at a lower magnification scale, and results suggest that imperfect boundaries may also be prevalent in other graphene samples. By further understanding the structures of defects at these boundaries, it can be translated to modelling schemes where changes in properties can be predicted and hence potential applications can be either identified or ruled out.

Defects clearly play a large role in defining the properties of the resulting material. Although some research has attempted to physically stretch out wrinkles[168], the fact still remains that through synthesis or transfer, the likelihood of wrinkles in a graphene system is very high.

From the increase in publications on graphene defects in 2014, it seems that the scientific community is gradually taking into account that graphene defects may be inevitable in the material system. In fact, Figure 76 shows some examples of low magnification SEM images of graphene in the literature where wrinkles and similar defects are clearly evident. (It is worth

noting that many of the papers referenced in Figure 76 did not include any comment on the presence of wrinkles or similar defects in their systems.)

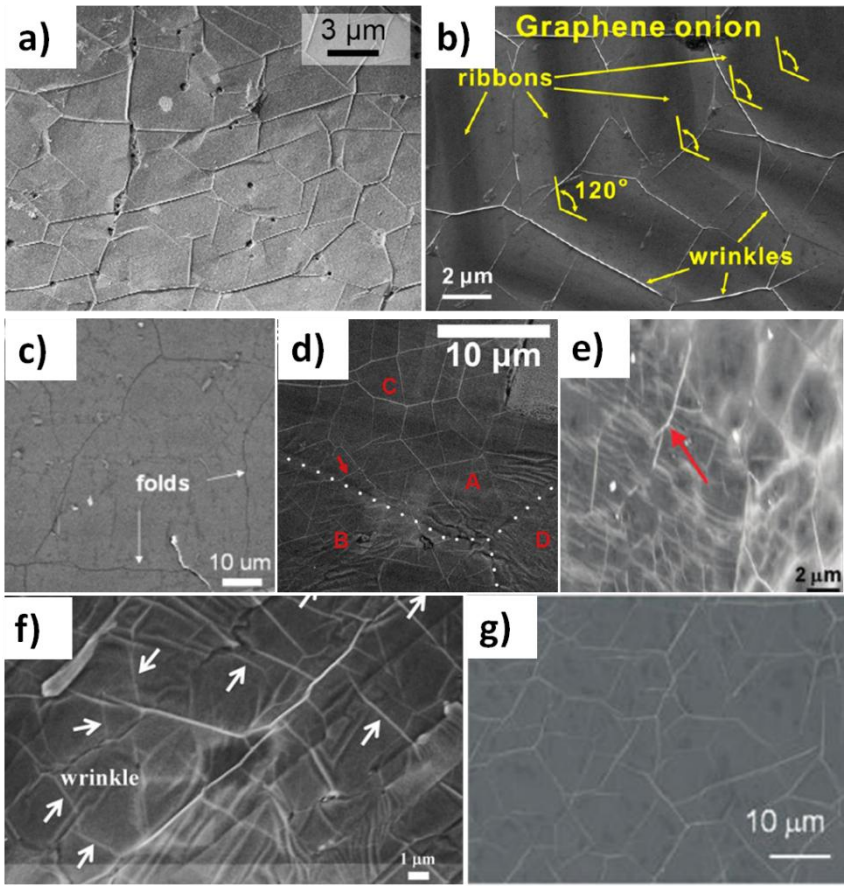


Figure 76) A sample of examples of SEM images from the literature of full-coverage graphene surfaces displaying defects. a) Reproduced with permission from ref[191]. b) Reproduced with permission from ref[192]. c) Reproduced with permission from ref[145]. d) Reproduced with permission from ref[193]. e) Reproduced with permission from ref[164]. f) Reproduced with permission from ref[125]. g) Reproduced with permission from ref[194].

It can therefore be concluded that defects are consistent across the literature and the need for further understanding, and an acceptance of graphene quality is necessary. This information is important to recognise the current state of graphene materials as a whole and how CVD graphene is to be used in industry in the future.

5 HRTEM of imperfect hBN

Similarly to Chapters 3 and 4, this chapter describes the defect analysis of a different 2D nanomaterial: hexagonal boron nitride (hBN). The results show strong correlations with what was reported for graphene in the previous chapters. HRTEM was used to deduce the similarities between hBN and graphene and hence also characterise naturally occurring defects found in hBN. With thanks to George Lane and Vitaly Babenko for hBN synthesis and grid preparation.

5.1 Introduction

hBN has a 2D crystal structure analogous to graphene but with boron and nitrogen atoms in place of carbon (Figure 77). There is less than a 2% change in the lattice spacings between graphene and hBN, with the B-N bond length equating to 0.144 nm and a hBN interlayer spacing of 0.333 nm[195]. In addition, the covalently bonded hBN preferentially exhibits AA' stacking[196] and multi-layer formation in this arrangement has been shown to stabilise the 2D structure as B-N stacking in the *c*-direction across layers has been shown to be more metastable than B-B or N-N[197].

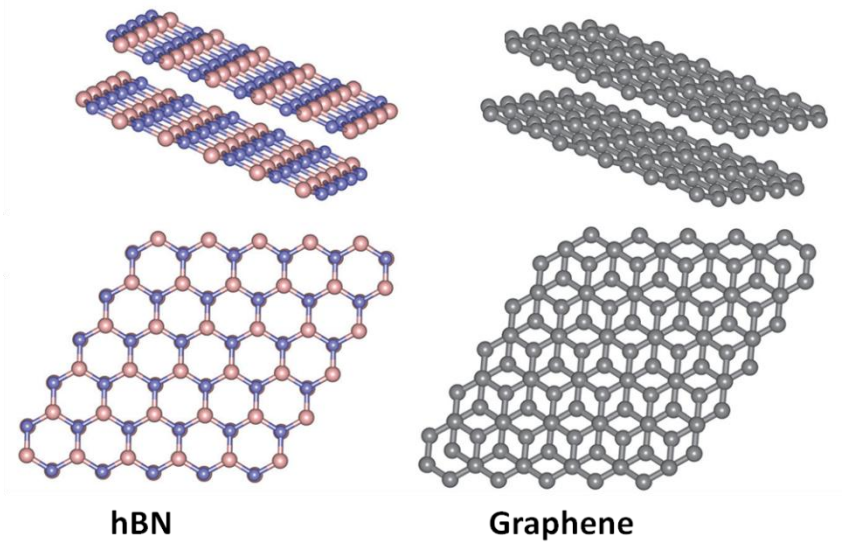


Figure 77) Schematics of hBN and graphene. Reproduced with permission from ref[198].

Like graphene, hBN exhibits strong covalent bonding along the basal planes and weak van der Waals bonding between layers. In this chapter, 'hBN' will refer to mono-to-few-layer hBN, similar to the graphene definition. hBN has a wide bandgap (5.0- 6.0 eV)[198,199] and is free of

dangling bonds and surface charge traps[200]. Hence, one of the most promising applications is its use as a superior dielectric for graphene devices compared to SiO_2. Using hBN as a substrate has allowed mobilities of graphene to reach an order of magnitude higher than with SiO_2 under the same conditions[201].

hBN shares similar synthesis methods to graphene, such as mechanical and chemical exfoliation[196,202–205] and boron nitride nanotube unzipping[206,207]. Furthermore, similarly to graphene, CVD is a promising technique for industrial production and has the added benefit of using the same system to synthesise both graphene and hBN simultaneously, enabling the formation of hetero-structures which can be used for devices[208]. CVD synthesis of hBN has been carried out on a variety of substrates including Pt[209,210], Ni[211–214] and Cu[211,212,215–223]. Although hexagonal domains have been reported[222], CVD synthesis largely produces triangular domains as shown in Figure 78a-d. This is likely due to the N-terminated edge exhibiting a lower energy [198,214].

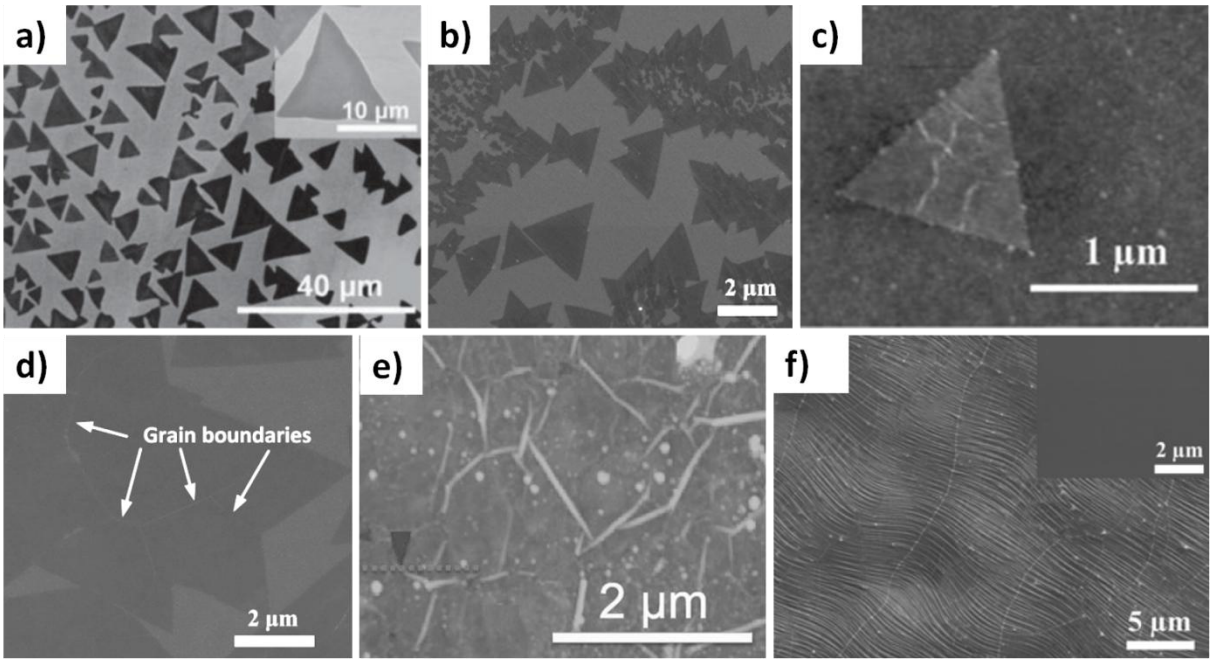


Figure 78) Examples of SEM images (except e which is an AFM image) of hBN domains and films from the literature. a) Reproduced with permission from ref[216], hBN domains grown on Cu foil. b) Reproduced with permission from ref[220], hBN domains grown in Cu foil. c) Reproduced with permission from ref[215], monolayer hBN domain on Cu foil. d) Reproduced with permission from ref[220]. hBN domains merging on Cu foil, with grain (domain) boundaries highlighted) Reproduced with permission from ref[219]. AFM image of few-layer hBN. f) Reproduced with permission from ref[224]. Few-layer hBN film on Cu. Images c-f) show visible wrinkles in the hBN film.

Similarly to graphene, imperfections in hBN can be seen in the literature but are often not the subject of published work. Figure 78c-f shows several examples of CVD grown hBN that exhibit visible defects such as wrinkling. Figure 78c shows wrinkles even in a single, as-grown monolayer hBN domain and Figure 78d highlights defects that seem to occur from hBN domain boundaries (highlighted as "grain boundaries" on the image).

TEM characterisation of hBN is generally used to determine the number of layers and confirm crystallinity[203,204,212,217–219,223,225–228] but thorough high-resolution characterisation is limited. Aberration corrected HRTEM has been used to distinguish between elements in hBN[229] and artificially introduced defects (created with the electron beam) have been investigated at atomic resolution[204,230,231]. Like graphene, hBN is also susceptible to damage due to beam irradiation[232]. Naturally occurring defects in hBN have not been largely studied.

Gibb *et al.* however studied a monolayer hBN domain boundary at atomic resolution[233] (Figure 79). hBN domain boundaries must take into account changes in lattice orientations, like graphene, but must also contest with elemental bonding differences. Homo-elemental bonding (B-B, N-N) is weaker compared with hetero-elemental bonding (B-N) and additionally leads to polar areas in the lattice which carry a net charge, creating a smaller bandgap[234]. These polar defects can occur with rings of 5-7 pairs in Stone-Wales defects. These 5-7 pairs have been experimentally observed in the example shown in Figure 79, highlighted by yellow and red rings respectively[233]. It is well known that Stone-Wales defects show changes in electronic structure and reactivity[234,235].

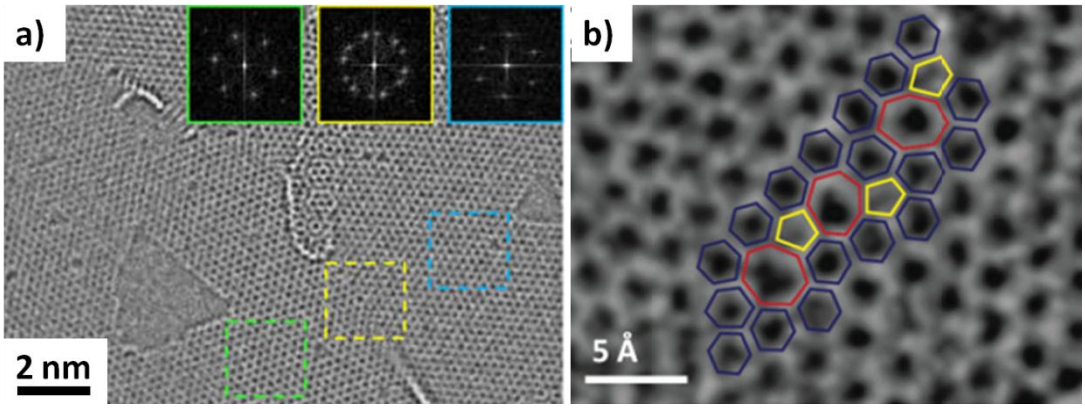


Figure 79) Reproduced with permission from ref[233]. HRTEM image of an atomically bonded domain boundary in hBN. a) Region of interest with FFTs showing the difference in two lattices. b) atomic resolution imaging of boundary seen in a) highlighting the 5-7 membered rings at the boundary.

Similarly to some of the graphene literature, this paper is limited to an atomically bonded domain boundary and does not include any discussion of additional boundary structures. In addition, this paper characterises monolayer hBN. Few-layer hBN is easier to produce and has been shown to work well for devices with graphene[221]; it is likely that monolayer hBN holds no advantage in this area. Therefore it could be argued that domain boundaries in few-layer hBN are of more interest to study. Few-layer hBN boundaries are likely to be more complicated than the atomic bonding shown in Figure 79, similarly to what has been discussed for FLG.

To the best of current knowledge, Figure 79 is the only example of HRTEM analysis of a naturally occurring defect observed in CVD grown hBN. This includes investigations into imperfections such as wrinkles or folds like those shown in Figure 78. Additionally, a recent review article on boron nitride which included a section entitled "Defect aspects", with the exception of the monolayer grain boundary shown in Figure 79, refers only to those defects which have been artificially introduced by beam irradiation at atomic resolution[198]. These defects are not representative of the material system on a larger scale.

It has been shown experimentally that fabricating devices with wrinkled hBN can reduce the stability of the device and induce power loss in the system[236]. This result is a direct reason for the need to further characterise such defects and understand whether the material can reach the potential to perform well in graphene-hBN devices.

Therefore, due to the limited work on defects in hBN and additionally HRTEM studies of those defects, it was a natural progression in this thesis to determine any similarities in this area between hBN and its sister material, graphene.

5.2 HRTEM analysis of hBN

In this section, the experimental procedures of hBN synthesis and TEM grid preparation are described. Similarly to graphene, hBN was synthesised using CVD on Cu foils.

5.2.1 Sample synthesis and TEM grid preparation

Few-layer hBN was synthesised using CVD of ammonia borane on Cu foils, similar to a method used by Song *et al.*[237]. The CVD system used closely resembles the set up shown in Chapter 2. A typical SEM image of the grown hBN film is shown in Figure 80a. hBN samples were synthesised for this study as follows:

Cu foil (25 μm, 99.8%, Alfa Aesar) was cleaned by sonicating in acetone for 5 minutes, rinsing with DI, sonicating for 10 minutes in nitric acid and rinsing again with DI before drying with a nitrogen gun. 100 mg of ammonia borane (99.8%, Sigma Aldrich) was placed in a vial that was connected to the CVD system and sealed. The Cu foil was placed in a quartz tube within a tube furnace and annealed under 500 sccm H_2 for 30 minutes. An oil bath at 100°C was raised under the vial of ammonia borane and 10 sccm H_2 was flowed through for 30 minutes (gas flow in the quartz tube was kept at 500 sccm H_2 for this time). After the 30 minutes, the oil bath was removed from the vial, the Cu was removed from the furnace and the flow rate was reduced to 200 sccm H_2 for 10 minutes to allow the substrate to cool.

hBN TEM grids were prepared by spin coating PMMA (M_w 15,000 followed by 960,000) to create a support for the hBN, similar to the transfer process outlined in Chapter 2. Delamination of the hBN/PMMA from the Cu was done electrochemically using a bias of 6V, similar to a set up used by Wang *et al.*[238] The Cu/hBN/PMMA was used as the cathode and bulk Cu foil was used as the anode, held in a 0.5M NaOH solution. H_2 bubbles formed at the cathode in between the Cu and the hBN causing them to peel apart. The hBN/PMMA stack was rinsed with DI and placed on

a gold TEM grid (*Agar Scientific)*. The PMMA was removed by submerging the grid in acetone for approximately 6 hours. A low magnification TEM image of the transferred hBN film on the gold TEM grid is shown in Figure 80b.

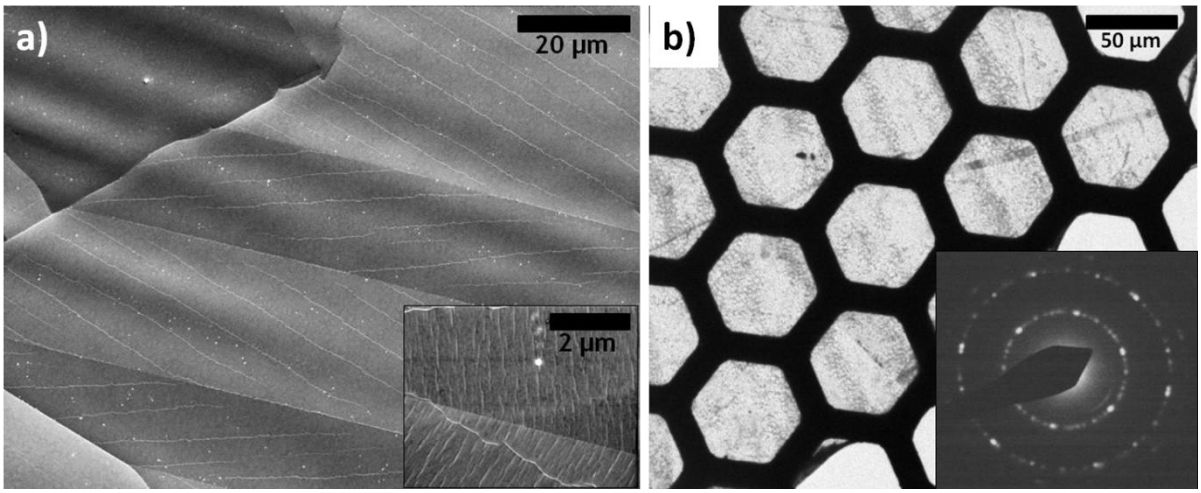


Figure 80a) SEM image of hBN film. Inset shows film at higher magnification. b) hBN film transferred to TEM grid with corresponding diffraction pattern. Images are courtesy of Vitaly Babenko and George Lane.

5.2.2 HRTEM characterisation

As previously described, HRTEM is used to determine the number of layers present in hBN by looking at the edges of samples. It was found in this thesis that often the edges of a hBN flake did not match up with the FFT information, for example; a hBN flake edge appeared monolayer when the FFT of the bulk flake showed multiple hexagonal lattice spots. This could have been due to folded edges or multiple small hBN domains that did not have matching lattice orientations. As hBN is often likely to exhibit AA' stacking, FFTs without the edge contrast cannot be used to conclusively state layer number. Unlike graphene, Odlyzko *et al.* showed that it is much more difficult to use the spot intensities of FFTs and electron diffraction patterns to distinguish monolayer hBN in TEM[239]. The hBN samples characterised in this thesis consisted of few-layer hBN with areas of the sample ranging from monolayer hBN to few-layer (< 10 layers, comparable to the definition of FLG) as shown in Figure 81.

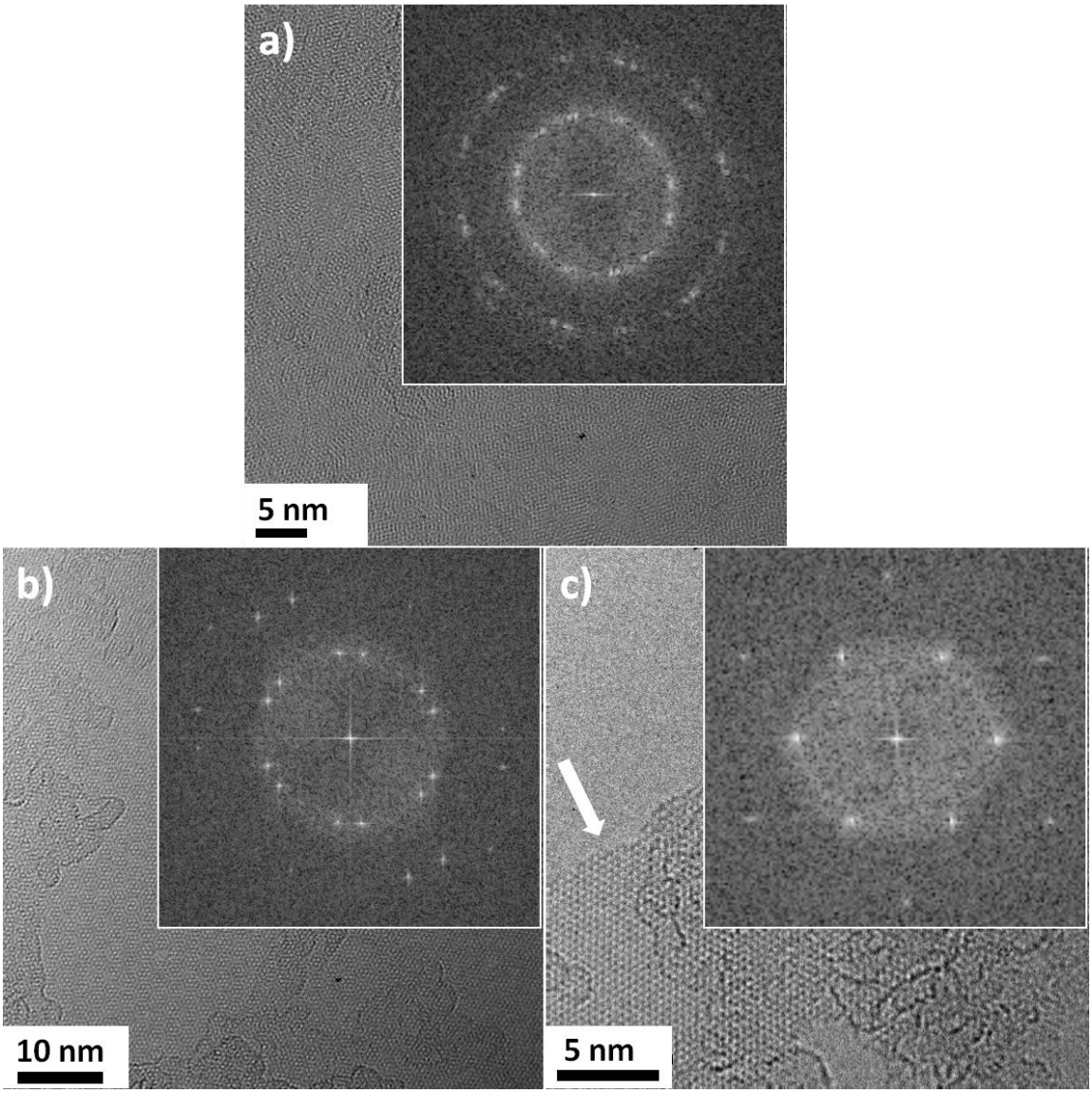


Figure 81) TEM images with corresponding FFT in the insets of a) Few-layer hBN, b) bi-layer hBN and c) monolayer hBN where a white arrow highlights the zig-zag edge structure.

Figure 81a shows an area of few-layer hBN with multiple rotations present. Figure 81b shows an area of bi-layer hBN rotated by 15.3°±1.7, causing a hexagonal moiré pattern (edge analysis also confirms bi-layer hBN in this area). This bi-layer region, and the few-layer region shown in Figure 81a, do not exhibit AA' stacking. Interestingly, similar misorientation has been shown in the literature[219,240], demonstrating how a deviation from AA' stacking in hBN can be often observed. Figure 81c shows an area of monolayer hBN terminating in a zig-zag edge configuration as highlighted by the white arrow. All images in Figure 81 were observed in the same hBN sample. Figure 82 shows two examples of how hBN layers vary by analysing the edge

of the hBN films. In the inset in Figure 82a, the green arrow highlights an additional layer appearing and the red arrow highlights a layer terminating.

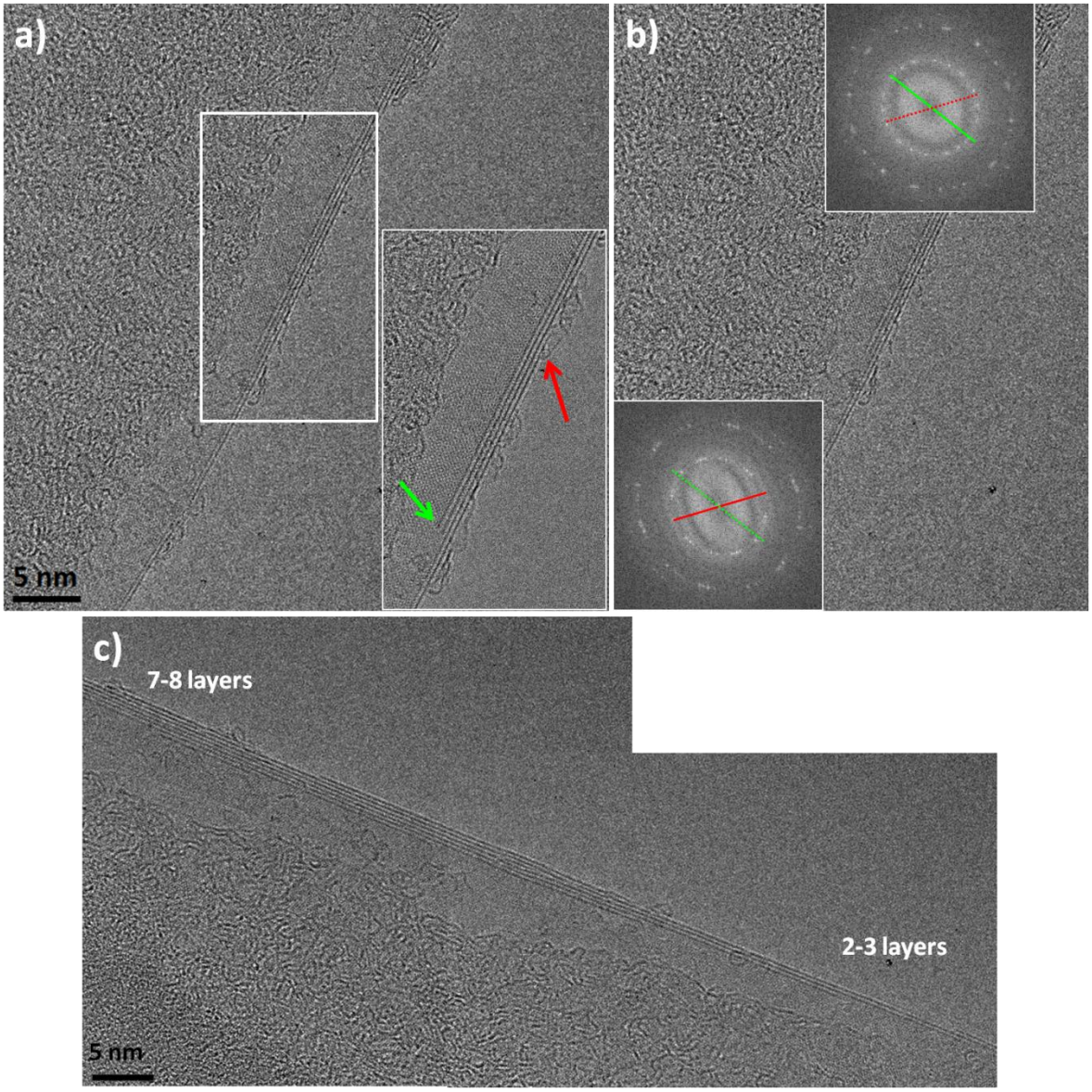


Figure 82a) TEM image of edge of hBN flake. Inset shows magnified area where green and red arrows highlight hBN layer additions and subtractions respectively. b) shows same TEM image as in a) with corresponding reduced FFTs. Green lines highlight common lattice spots with new additional layers, whereas a red line highlights lattice spots which are not present in the top FFT. c) shows another hBN edge showing the evolving change from 7-8 layers to 2-3 layers.

Figure 82b is the same TEM image as in Figure 82a but with the addition of FFTs in areas where the edge contrast has changed. The red and green lines in the FFTs highlight a lattice that has been lost and gained respectively. Dotted lines demonstrate the absence of that lattice in the alternate FFT. These changes in lattice spots correspond to the addition and subtraction of layers seen on the edge. This provides evidence that the sample is constantly varying in the

number of layers and often layers terminate and "add on" to existing layers. This indicates a synthesis mechanism where hBN layers grow and nucleate both on top and below additional layers. Figure 82c shows an additional example where a large change in layers is observed on a hBN edge from 2-3 layers to 7-8 layers over < 50 nm. In the literature, it is also common to observe a range of layers in a hBN sample[212,213,217–221,240]. These papers, together with Figure 81 and Figure 82, demonstrate how the number of hBN layers can vary considerably across a sample, and notably within a relatively short distance. Therefore, for conclusive layer number analysis, larger scale characterisation of hBN samples is necessary.

5.2.3 HRTEM defect contrast in hBN

Defect analysis was undertaken in the hBN samples and it was found there were some distinct similarities with the new imaging contrasts described in Chapter 3 for graphene. Concise examples have been described in this section and have been summarised in Figure 83.

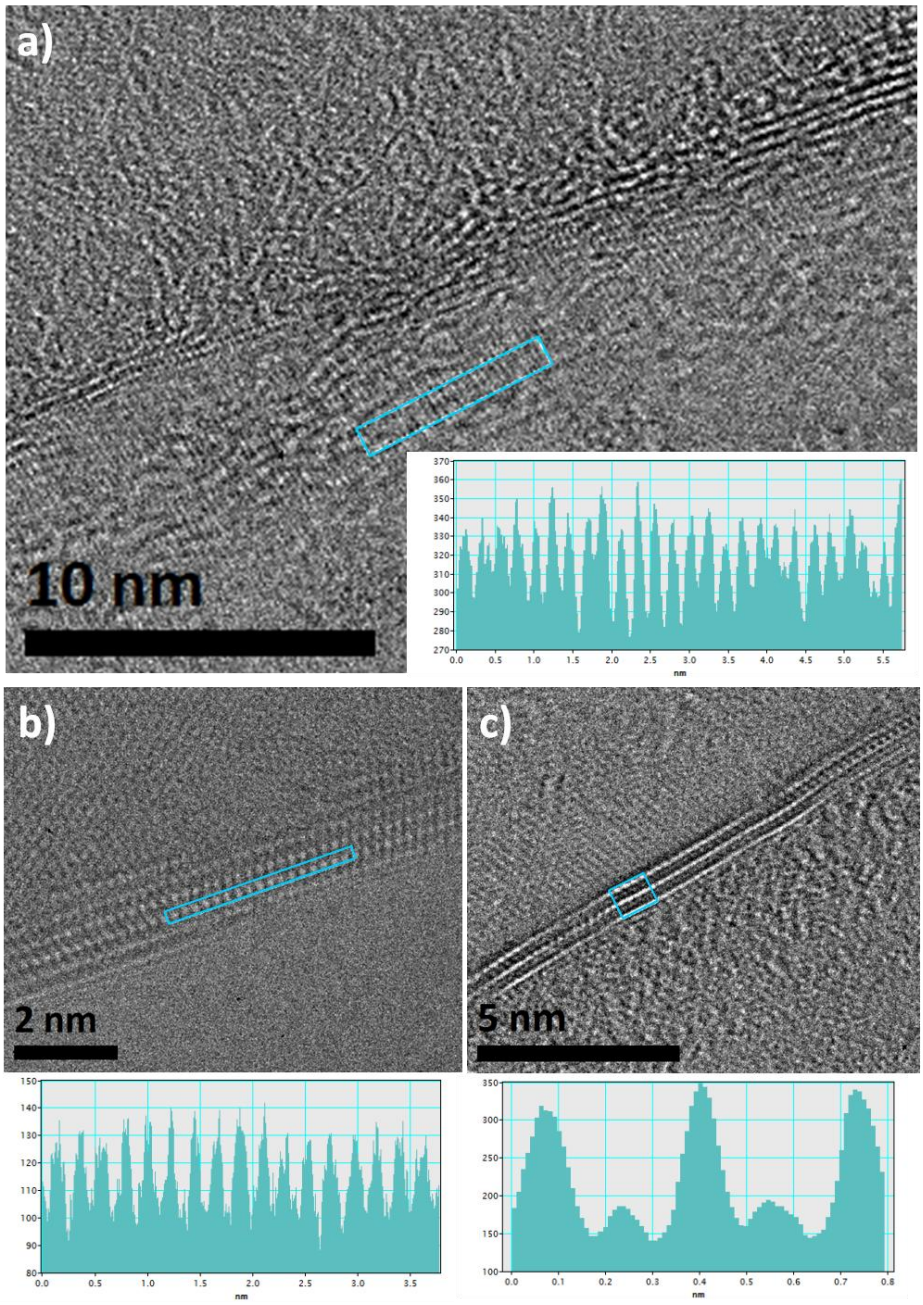


Figure 83) TEM images and corresponding line profiles of hBN examples of a) sideline periodicity b) periodicity along hBN planes, c) inter-hBN plane contrast

Figure 83a-c show examples of the sideline periodicity, periodicity along hBN planes and inter-hBN plane contrast. In hBN, the calculated spacing of the (01-10) zone axis is 0.217 nm (compared to 0.213 nm in graphene). Each feature in Figure 83 is consistent with this spacing with a measured range of 0.19-0.24 nm. Thus it can be deduced that defects in hBN can cause an off-zone axis distortion, which can be clearly observed using HRTEM imaging. Additionally, linear moiré patterns were also observed in hBN as shown in Figure 84.

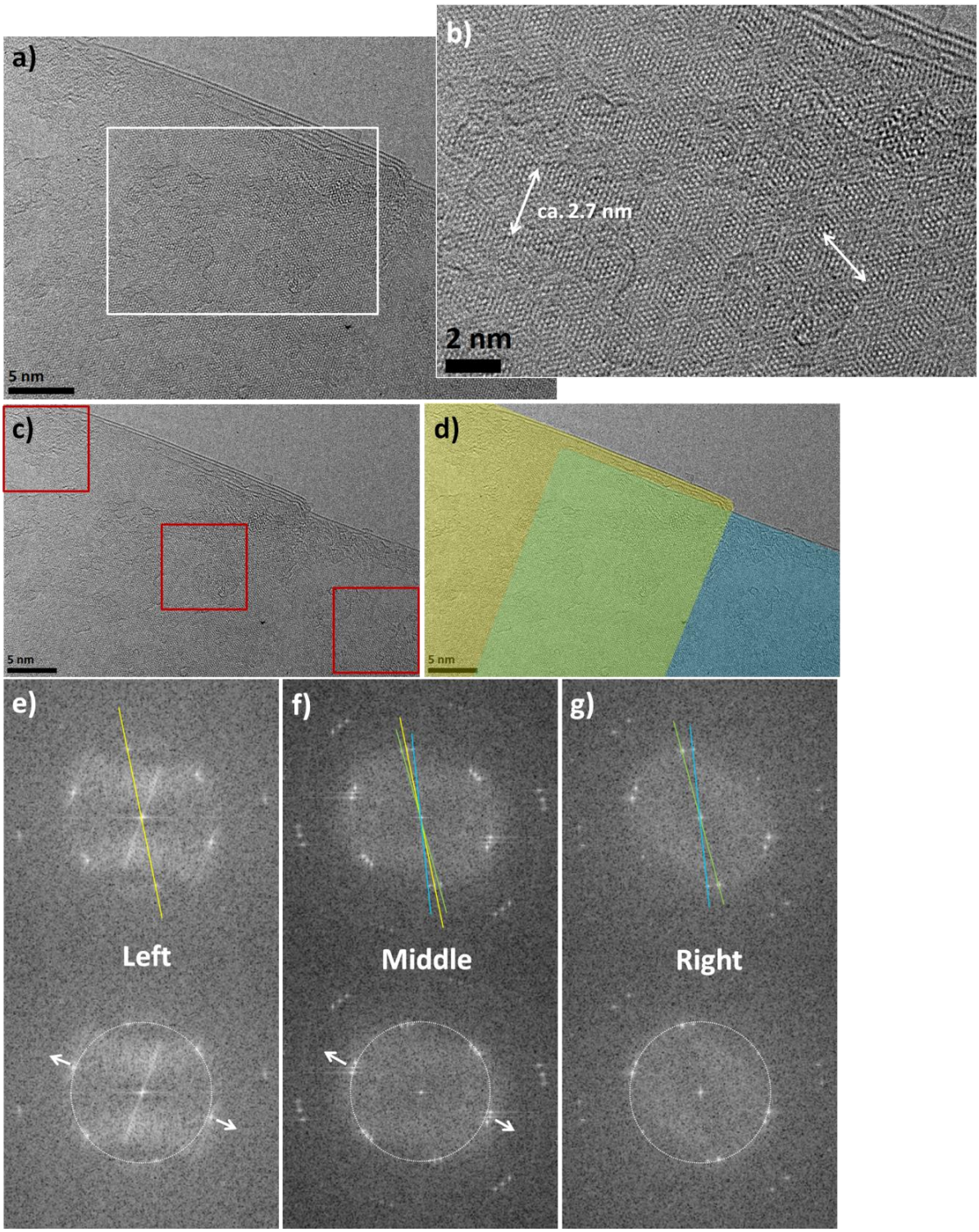


Figure 84a) TEM image of area showing a linear moiré pattern in hBN. The white box shows the area of b). b) Linear moiré patterns at higher resolution with arrows marking different spacings of two sets of linear features. c) TEM image of a) with red boxes corresponding to the areas where FFTs e-g) are taken. d) Schematic of the area demonstrating the overlapping of two lattices occurring, the left in yellow, the right in blue. e-g) FFTs from the image. The first row shows how the lattices from both left and right sides are in the central FFT. The last row shows the same FFTs with white dotted circles to demonstrate strain. White arrows highlight any areas of strain.

Figure 84a shows the unprocessed TEM image of an area of hBN exhibiting a linear moiré pattern. The inset highlights two linear spacings in different directions, demonstrating how

more than one linear moiré pattern exists in the same area. Using FFT analysis it can be deduced that this is an overlapping area of hBN, as shown schematically in Figure 84d. The yellow (left) lattice is likely monolayer hBN (from the FFT and edge contrast) and the blue (right) lattice is at least bi-layer hBN, rotated by 8.7°±0.2 (this rotation has also resulted in a hexagonal moiré pattern in the right of the image). As previously discussed in Chapter 3, linear moiré patterns occur in graphene when there is distortion present in one or more lattice. Using FFT analysis shown in Figure 84e-g it is possible to see strain in the left and middle FFT (shown by an arrow in the (10-10) direction). Between 2-3% strain can be measured in the lattices of the middle FFT. It is noted that the bi-layer lattice (from the right) follows this distortion in the middle FFT, despite being un-distorted prior to overlapping. The left lattice is misaligned from the right bi-layer by a maximum of 4.5°±0.5 and hence its diffraction spots lie in between the bi-layer spots.

In the example shown in Figure 84, both a change in rotation and lattice distortion is visible between the two interacting lattices. Therefore an additional moiré term must be defined to incorporate both changes:

$$D = \frac{d_1 d_2}{\sqrt{(d_1 - d_2)^2 + (d_1 d_2 \sin\theta^2)}}$$

Equation 3[134]

Where D is the planar moiré spacing, d_1 and d_2 correspond to the inter-planar spacings of the two overlaid lattices and Θ denotes the angle of rotation between the two lattices. Analysing the area of the linear moiré pattern that produced the *ca*. 2.7 nm spacing as highlighted in Figure 84b, measurements from each lattice in the FFT are consistent with Equation 3 (d_1=0.2096, d_2=0.2083 and Θ=4.5°) giving D=2.66 nm which fits well with the observed spacing.

Similarly to what was observed for linear moiré patterns in graphene (as described in Chapter 3), this analysis indicates that the overlapping of a distorted lattice (left) distorts an originally perfect, un-distorted lattice (right). The linear moiré pattern that is produced is therefore again

an example of two distorted lattices (but now of hBN) and the change in linear spacing indicates a further varying of strain throughout the overlapping area.

5.2.4 hBN imperfect domain boundaries

Additionally, examples of imperfect domain boundaries were found in hBN which were dissimilar to those that have been previously described in the literature[233]. It is worth noting that domain boundaries in these hBN samples were more difficult to observe experimentally due to the full-coverage films produced (Figure 80) and the triangular nature of hBN domains. Hexagonal domains of graphene are easier to distinguish in TEM. Nonetheless, two simple examples of imperfect domain boundaries have been shown in Figure 85.

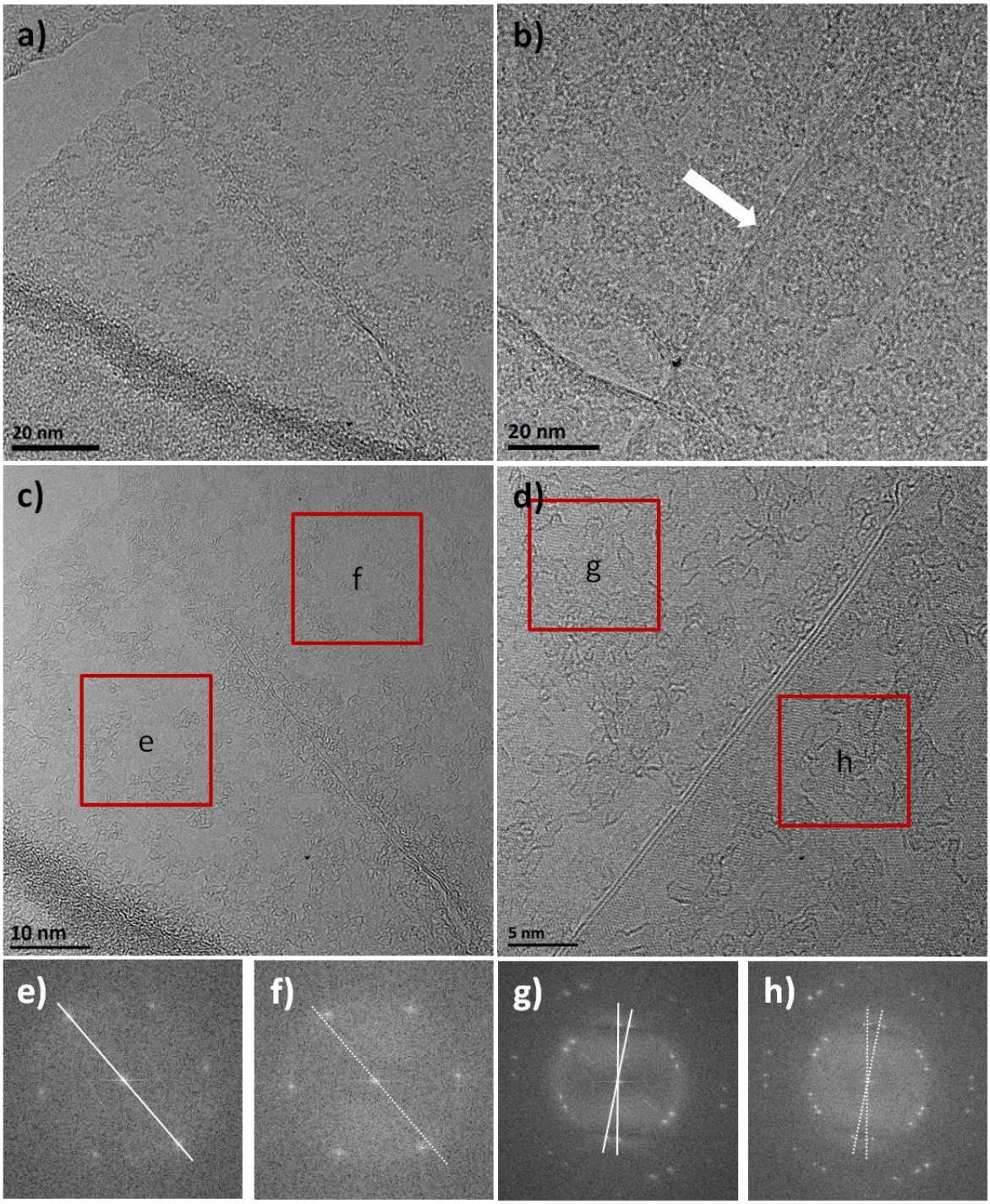


Figure 85) Two simple examples of imperfect domain boundaries in hBN. Left and right columns show different examples. a-b) Low magnification TEM images where the white arrow on b) highlights the long straight line of the boundary. c-d) TEM images at higher resolution showing boundary and red boxes where FFTs are taken. e-h) FFTs of areas either side of both boundaries where a white line on the lattice on the left FFT is shown in the right as a dotted line, demonstrating how the domains differ.

Similarly to the graphene characterised in Chapter 4, hBN has also shown defects such as wrinkles around grain boundaries. In the examples in Figure 85, domain boundaries consisting of a small number of layers have been demonstrated to simplify the FFT analysis as thicker few-

layer hBN is more difficult to interpret without the edge contrast. In each example, defects can be seen at the point of the boundary. In Figure 85a and c, the rotation difference between the two domains is 5.0°±0.4. It is likely atomic bonding is present at the boundary at the top of Figure 85c before wrinkle defects occur, notably becoming more prevalent towards the lower right of the image. In Figure 85b and d, it is possible that there is a continuing layer throughout the region as one set of spots closely matches another in the FFTs (approximately 1.2°±0.2 apart). However, the other lattice spots in FFTs g-h are distinctly different. Therefore it is likely this is either a domain boundary existing outright or a domain boundary with an additional continuous layer. Nonetheless, a distinct defect is observed along the domain boundary in the form of a simple wrinkle.

Compared to some of the more complicated imperfect domain boundaries for graphene described in Chapter 4, the examples shown here contain less imperfection. However, the boundaries observed in hBN are similar to the examples of graphene boundaries which involved the merging of domains of fewer layers, such as mono-or-bi-layer graphene. This similarity again demonstrates the consistent features across both 2D materials: like graphene, imperfect domain boundaries were observed in hBN which exhibit additional features compared to the Stone-Wales defects as reported in the literature.

5.3 Summary

This chapter has concisely summarised several features observed in hBN that are very similar to what has been observed in graphene. The results confirm the structural similarities between graphene and hBN and show that like graphene, hBN also contains naturally occurring defects, including those from imperfect domain boundaries. It is important to recognise such defects for full understanding of the material and notably, in the case of forming graphene/hBN hetero-structures, for devices to understand how to work with defects to ensure device performance[236]. As in graphene, defects change hBN properties. If defects can be controlled, hBN properties may be able to remain more stable, retaining the lack of charge traps and dangling bonds for

improved dielectric properties. This chapter has proven the defect similarities between graphene and hBN which can help enhance understanding of both systems and potentially lead to any defect controlling procedures to be recognised for the other material. For example studies in how to "smooth out" graphene wrinkles[168] is likely to also be applicable to hBN.

The distinct similarities between graphene and hBN observed over Chapters 3-5 could also lead to speculation of defect structure of other 2D materials such as MoS_2, WS_2 and other transition metal dichalcogenides. It is possible that 2D materials share more structural similarities like what has been observed for graphene and hBN and hence this work could be relevant for defect characterisation on a wider materials scale.

6 Graphene surface force balance development

This chapter will introduce a new instrument, the graphene surface force balance (gSFB). The gSFB is a new characterisation technique that will enable the measurement of surface forces under potential control. Additionally, it has the capability to both measure fundamental properties of graphene and also redefine the scope of conventional SFB experiments that have been largely unchanged since the 1970s.

The creation of the gSFB has involved the development of a new transfer technique for CVD graphene that works around and overcomes the common imperfections that occur in the material. It should be noted therefore that "imperfect" graphene is used in the formation of the gSFB and despite the evident defects, like those discussed in previous chapters, it is still an excellent material for the targeted application.

In this chapter, an introduction to SFB apparatus and key literature will first be outlined. Several approaches that lead to gSFB creation have then been summarised before describing a new ultra-flat transfer technique that ultimately lead to the formation of the gSFB.

Specific experimental details are included at the end of the chapter so as to not distract from the scientific argument in the main text. The SFB transfer work was done in collaboration with Professor Susan Perkin's group in the Department of Chemistry, University of Oxford, specifically with the help of Dr. Nico Cousens & Christian van Engers.

6.1 An introduction to a surface force balance

The surface force balance (SFB) was invented at the University of Cambridge in the 1970s[241,242], and provided the first direct measurement of van der Waals forces[241]. The SFB works on the principle of white light interferometry to measure the separation distance between two

atomically smooth lenses. Springs can then be attached to the lenses to determine normal and lateral force movements via Hooke's Law:

$$F = -kX$$

Where F is the force, X distance and k is the constant determined by the spring stiffness. Hooke's law therefore denotes that the force needed to act upon a spring by some distance is directly proportional to that distance. Therefore, the deflection of a spring can be measured which corresponds to the forces at the SFB lens surface as the surfaces are brought together. This enables forces such as friction and adhesion to be measured by monitoring the changes in the spring with separation distance.

The conventional SFB consists of two 1 cm^2 cylindrical, transparent lenses which, when held in a cross-cylinder geometry and brought close together, provide a single contact point which is equivalent to a sphere on a flat surface (Figure 86, left). White light is shone through these transparent lenses. Each lens is coated in a semi-transparent silver mirror which enables the incoming and reflected white light to interfere with itself. This interference is recorded as fringes which are directly interpretable to the distance between the two curved lenses. The power of this technique arises from the resolution that can be obtained from the interference fringes. As well as the silver mirrors, each lens is also covered with a thin, transparent, freshly cleaved layer of mica (Figure 86, right). Mica, being atomically smooth, can therefore ensure that the two lenses can come extremely close together and hence produce interference fringes of sub-angstrom resolution.

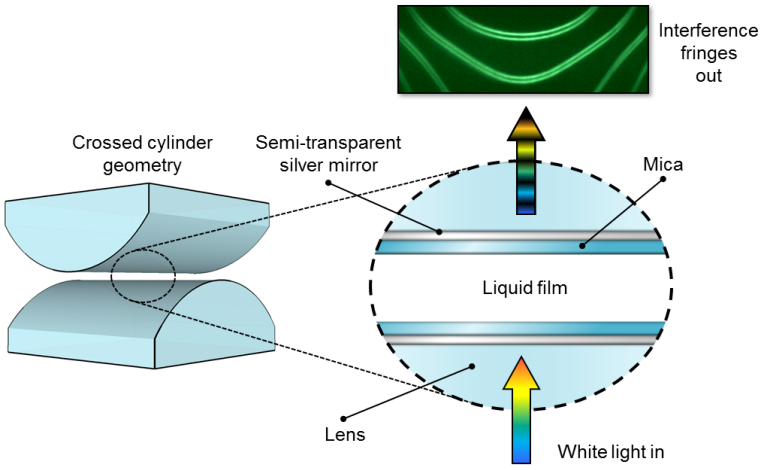


Figure 86) Reproduced with permission from ref[243]. Schematic of a simplified mica SFB set-up illustrating the cross-cylinder lens geometry of the silver and mica covered lenses. The semi-transparent silver mirrors allow white light interferometry to be used to measure the surface separation of the lenses using the interference fringes gained. Forces at the lens surface can be simultaneously measured by recording the deflection of a spring as the surfaces are brought together.

6.1.1 Multiple beam interferometry

The SFB utilises multiple beam interferometry (MBI) to determine the separation distance between the two SFB lenses. This is possible because both lenses are coated with a semi-transparent silver mirror which allows for multiple reflections between the two surfaces. The light is reflected multiple times between each mirrored surface, hence the probability of destructive interference is very high, and the signal of destructive reflections is lost.

Distance between SFB lenses will correspond to a specific wavelength of light. This wavelength will be seen as a strong, sharp signal in the spectrometer as demonstrated in Figure 87. The blue lines represent beams of incoming white light; the green represents constructive interference reflections and the red, destructive. The reflections are represented on top of one another to aid explanation. The wavelengths of light that interfere constructively, as shown in the top two examples in Figure 87, will keep amplifying with incoming light as the reflections occur over and over again. This can only happen if the distance corresponds exactly to a specific wavelength. If it does not, it leads to destructive interference, as shown in the bottom case in Figure 87. In MBI, destructive interference will occur even if the wavelength is just out of sync with the distance. This is due to the constant reflections occurring back and forth. In the bottom example in Figure 87, the reflections are numbered 1, 2 and 3. It is possible to see how in just 3

reflections, the wavelengths are significantly out of phase. This phenomenon ensures only the perfectly constructive reflections appear as signals in the spectrum, resulting in sharp peaks as shown in Figure 87. This is the reason for the high resolution ability of MBI as such sharp signals can be accurately indentified due to a lack of noise from destructive signals.

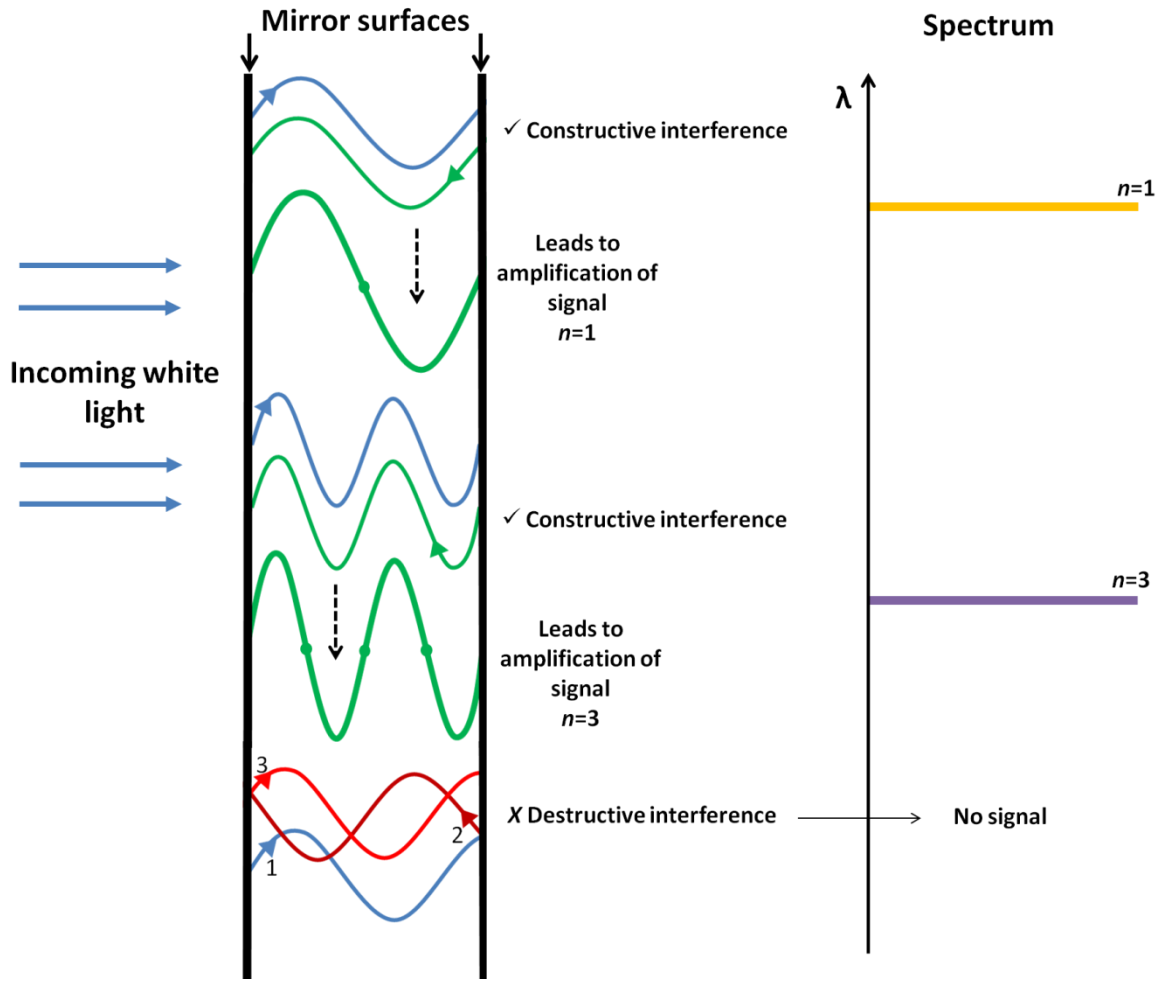


Figure 87) Schematic of MBI. Constructive interference leads to amplified, sharp signals. Destructive interference yields no signal. *n*= number of nodes present within waves, highlighted by green circles in amplified wavelengths.

The distance between the mirrors corresponds to the wavelengths of the constructive reflections, represented by their node number, *n.* The fringe that exits the interferometer is hence identified by this number and is described as the "chromatic order".

As shown in Figure 88, the "effective distance" between the mirrors is made up of smaller distances. In the mica SFB, the light must travel through the mica, as well as the medium in between. MBI is sensitive to refractive index which must be taken into account when calculating

the distance between the two SFB lenses. From herein, refractive index will be referred to as *R* as *n* has already been used.

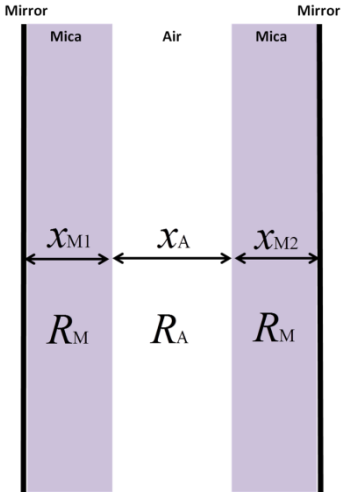


Figure 88) Representative schematic of mica-SFB lenses demonstrating how distance between lenses is calculated. X_{M1+M2} represent mica thickness and X_A represents lens separation. R_{A+M} represent corresponding refractive indexes.

The wavelength for the constructive interference (λ) between lenses can be used to deduce the effective distance between lenses based on:

$$\lambda = \frac{2}{N}(x_{M1}R_M + x_AR_A + x_{M2}R_M)$$

Where *x* is the thickness of the interferometer layers (X_{M1+M2} represent mica thickness and X_A represents lens separation), *R* is the refractive indexes of the interferometer layers and *N* is any integer. In this thesis, refractive indices of the materials used are well known, as well as the mica thickness. MBI is hence used to determine the distance between the mirrors and hence x_A can be found.

Figure 87and Figure 88 assume parallel reflective surfaces, however, SFB lenses are curved. This is the reason for the curve in the resultant fringes observed from SFB measurements (Figure 86). The fringe will move to longer wavelengths the further the distance from the contact spot. Hence, the fringes mimic the geometry of the interferometer, with each fringe representing one chromatic order, *n* (see Figure 89). Therefore, these fringes are referred to as fringes of equal chromatic order (FECO).

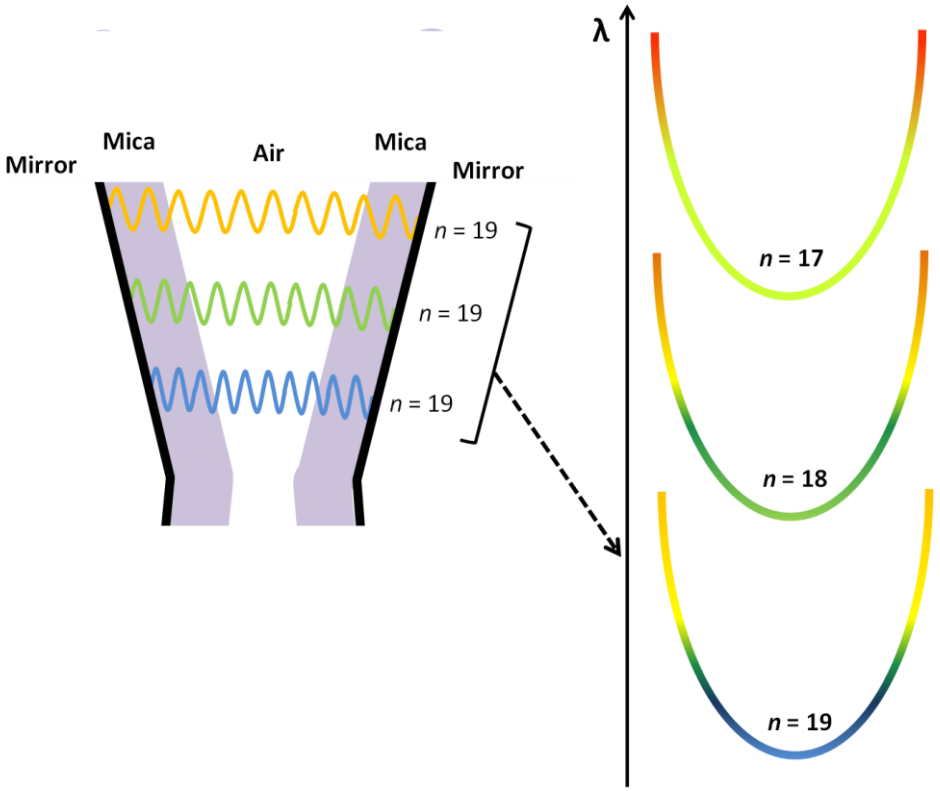


Figure 89) Schematic of MBI in the curved SFB set up demonstrating that the resulting fringes represent the local geometry of the interferometer.

An example data set from a SFB is shown in Figure 90. It demonstrates how the SFB can provide information on the the stacking of layers of ions in two different ionic liquids, and hence lead to predications of electrical double layers and ion self-assembly between two negatively charged surfaces. It demonstrates how, as the SFB lenses are brought closer together, layers of ions can essentially be“squeezed” out, leading to force oscillations on the surface force profile.

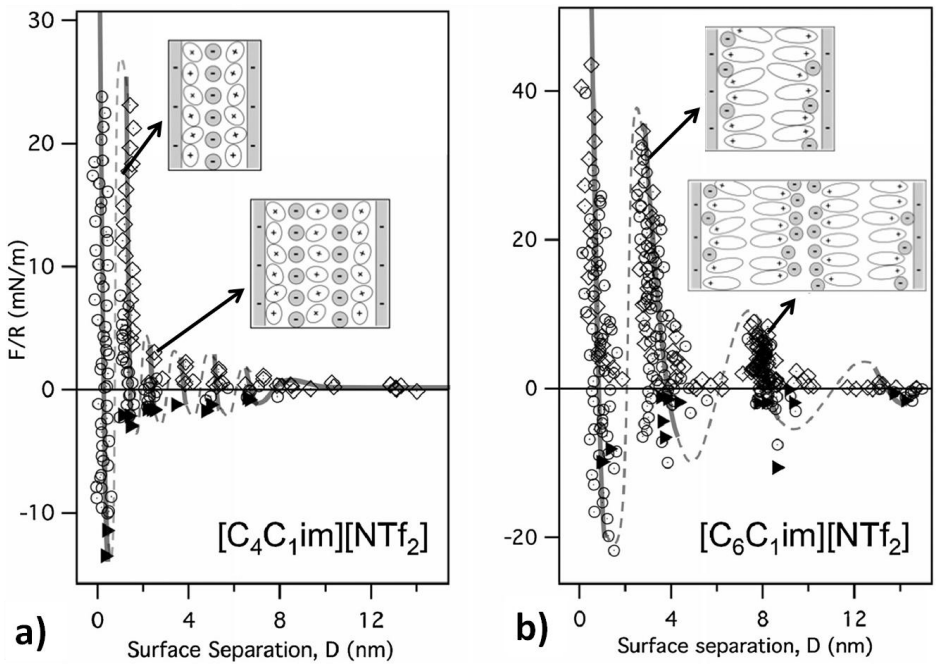


Figure 90) Adapted from refs[244,245]. Force profiles showing the interaction force as a function of film thickness between mica surfaces. a) and b) are surface force profiles from two different ionic liquids. Force oscillations indicate layered structures in the liquid film. Insets show possible example structures for different film thicknesses.

Figure 90 shows the difference between two surface force profiles of different ionic liquids. Predictably, the separation distance between oscillations is much larger for larger ions, as in Figure 90b. Such alternating layers of positive and negative ions of ionic liquids at the mica surface as shown in recent SFB studies[245,246] fit with what has been suggested by AFM experiments[247] and theoretical prediction[248].

Over the last 40 years the SFB has provided innovative measurements of a multitude of surface and colloidal forces in liquids:

- Liftshitz and van der Waals forces[241,249]
- Solvation forces[250]
- Electrostatic surface forces[251–253]
- Forces due to polymer adhesion[254,255]
- Forces due to biological molecules and surfactants[256]

These forces were all first characterised using this technique and demonstrate the capability of this instrument across a wide range of materials and scientific disciplines.

6.1.2 A SFB with surface potential control

Despite the pioneering measurements obtained from work with SFB apparatus, and the versatility of liquids and solutions that can be measured, the SFB has some inherent limitations.

To gain the integral smoothness, and hence the high resolution, in the vast majority of SFB experiments both SFB lenses are covered in a layer of mica[257], as shown previously in Figure 86. When using muscovite mica in solution, the surface becomes negatively charged as the potassium ions dissociate (Figure 91a). It is at this surface where ions can arrange themselves as electrical double layers (EDLs). However, at this stage, the surface potential of the SFB lenses are solely limited to an unspecified negative charge which is largely uncontrollable.

If SFB lenses exhibited surface potential control, all SFB experiments to date could be repeated and reinvestigated at changing potential, as well as entirely new experiments formulated. Monitoring changes in EDLs and ion-layering in ionic liquids through potential change could be undertaken, changes in lubrication properties at different surface charges could be measured, and processes that mimic electrochemical devices could be investigated. The huge range of new experiments that could be achieved with a surface potential controlled SFB is the driving force behind the development of a conductive SFB.

Although there have been several attempts[258–262], it has not yet been possible to replace both lens surfaces with a conducting material that exhibits similar roughness to mica and hence usable resolution over the area required. Template stripped gold lenses have been produced[258], which although initially exhibited a very smooth roughness of root mean squared (RMS) 0.2 nm, the gold surface rapidly roughened in solution (Figure 91b-c) which proved unusable for the vast majority of SFB experiments that require high-resolution. To study processes such as ion arrangement in ionic liquids, such roughness from the metal surface is insufficient and is a consistent problem with thin metal surfaces employed in this technique. There is a need for reliable “sub-molecular” roughness, akin to that of mica.

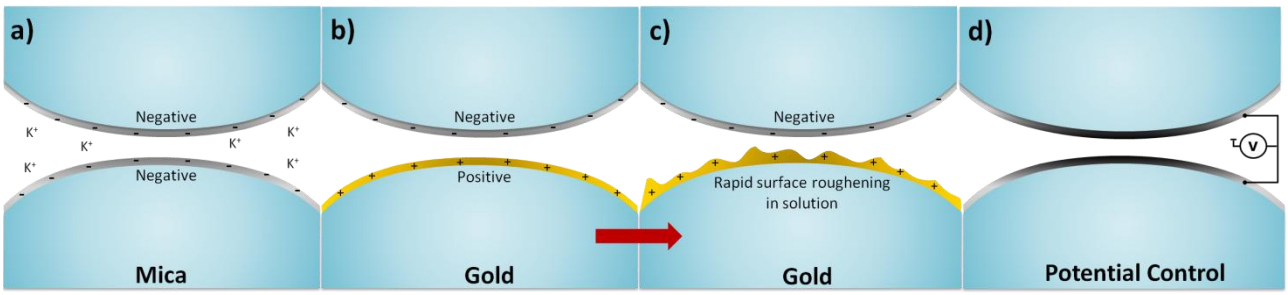


Figure 91) Schematics of various pairs of SFB lenses. a) Conventional mica SFB depicting formation of negatively charged lens surfaces after potassium ion dissociation in solution. b) and c) SFB with one lens replaced with a gold surface holding a positive charge. The red arrow depicts how the gold surfaces exhibit increasing roughness in solution. d) The target lens set up for SFB potential control. The material on the lenses should be smooth, transparent and conductive, akin to mica but with the ability to support potential control.

A completely potentially controlled SFB has therefore never been reliably accomplished. The key challenge is manufacturing a conductive material that will replace mica and coat the SFB lenses whilst retaining the high quality and reproducibility that mica provides.

The essential criteria for such a material for the SFB lenses are as follows:

1. The material must be electrically conductive to support an externally applied potential.
2. The material must be transparent enough to allow the use of white light interferometry.
3. The material must completely cover the lens so the underlying lens materials are not probed during measurements.
4. The material must be high-quality and clean so contamination does not interfere with experimental results.
5. The material must be incredibly smooth, on the order of < 5 nm to achieve a usable resolution.

When considering a material that embodies transparency and conductivity, graphene is an obvious contender. However, although graphene is sufficiently transparent and conductive, criteria 3, 4 and 5 must still be achieved, and the graphene must be applied to the SFB lenses in such a way that it can be used effectively.

In addition, in the case of using graphene, a sixth criterion is necessary:

6. Graphene must be thin enough to allow transparency, but thick enough to ensure there is no underlying effect from the silver mirror or additional materials underneath.

Rafiee *et al*.[263] have shown that monolayer graphene is essentially transparent to other van der Waals forces. Therefore, to use graphene in a SFB, full coverage, few-layer graphene (FLG) is the ideal material. FLG is thin enough to retain transparency, but thick enough to screen underlying forces from other lens materials.

CVD graphene is a prime candidate for graphene synthesis in this case as it is easily controlled and can be synthesised to be very high quality, as described in Chapter 1. However, Chapter 1 also provides evidence that commercially available CVD graphene is not ideal as it is primarily monolayer with large amounts of contamination.

The most difficult obstacle in this work was overcoming criterion 5, the need for sub-molecular roughness. Five approaches were employed to try to solve this problem, all of which involved CVD synthesis to produce FLG.

A summary of the approaches to obtain smoother graphene are as follows:

- Approach 1: FLG synthesis and direct epoxy transfer – FLG synthesis on un-treated Cu foils and an adaption of the PMMA transfer described previously in Chapter 2.
- Approach 2: Graphene synthesis on thin films – synthesis on evaporated Cu substrates aiming to produce very smooth FLG.
- Approach 3: Substrate electropolishing – synthesis of FLG on smoother, electrochemically treated Cu foils.
- Approach 4: Substrate pressing – synthesis of FLG on pressed Cu Foil.

In the following sections, the results from Approaches 1-4 are discussed. After the results from Approach 1, Approaches 2-4 come from the avenue of first creating the smoothest graphene on

modified copper substrates in the hope that such smoothness would carry through to the SFB lenses. A summary after Approach 4 analyses the progress of the project after the first approaches and outlines the thought process that lead to the final Approach 5, which in turn lead to the creation of the first graphene SFB:

- Approach 5: New ultra-flat transfer technique –transfer of FLG from Cu foils to eliminate detrimental roughness.

Although all approaches did not directly produce successful results to form the gSFB, results from each avenue may be of interest in the wider graphene field and have inevitably lead to the ideas that formulated the formation of the gSFB in Approach 5. All approaches were recognised as potential solutions and were conducted in parallel until a successful, low-roughness solution could be obtained.

6.2 Approach 1: Few-layer graphene synthesis and direct epoxy transfer

6.2.1 Few-layer graphene synthesis

As it was concluded that the necessary material for this work was few-layer graphene, reliably synthesising such samples was the ideal starting point in this work.

Parameters that can affect CVD graphene growth on Cu foils have been outlined in Chapter 2. It was found that high quality, FLG could be grown using the following experimental procedure:

Cu foil	Cleaning	Annealing	Growth	Product
			> 300 sccm H_2	
	> 10 min sonicate D.I.	> 500 sccm H_2	> 5 sccm CH_4	
Alfa-Aesar 99.8%	> 10 min sonicate acetic acid	> 1035°C	> 1035°C	
25 µm thick	> 5 min sonicate D.I.	> 30 min	> 50 min	Full coverage across foil of few-layer graphene

Table 2) General experimental procedure for full-coverage, few-layer graphene synthesis on standard Cu foils.

This procedure yielded high quality, FLG that exhibited full-coverage approximately 70 % of the time (Figure 92). The samples that did not produce usable material may have produced less than full coverage, or poorer quality graphene. This may have been due to extra contamination

present across some Cu foils, or a change in acid batch for cleaning for example. These overlooked parameters have been introduced in Chapter 2.

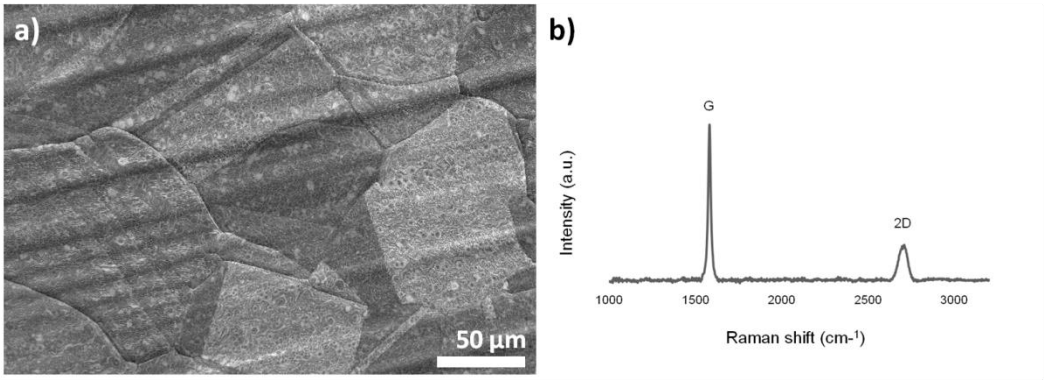


Figure 92a) SEM image of typical FLG synthesised using the experimental procedure outlined in Table 2. b) Corresponding Raman spectrum of the as synthesised graphene on copper. No D peak at 1350 cm^{-1} is indicative of very high quality graphene. The 2D to G ratio is characteristic of FLG.

The graphene produced as shown in Figure 92 is an ideal thickness and quality for use in a gSFB. The Raman is indicative of very high-quality FLG that has a low defect density as indicated by the lack of D peak in the Raman spectra.

Due to the successful synthesis of the ideal form of graphene, this material and its synthesis scheme was therefore used as the starting point for all following experiments.

6.2.2 Polymer epoxy transfer to SFB lenses

Adhering the ideal material to the SFB lens was another hurdle that had to be overcome. Using epoxy to adhere the graphene to a SFB lens was a viable option as it is transparent to white light and the thickness can be easily controlled by spin coating. In addition, epoxy can mechanically exfoliate graphene sheets[264], therefore proving it adheres well to the target material.

Because mechanical exfoliation of graphene is widely used, it was hypothesised that simply overlaying the graphene/Cu foil over the epoxy would transfer the graphene to the lens. However, roughness from the FLG samples, such as copper processing lines (*ca*. 200 nm roughness) templated onto the epoxy, therefore creating a rough surface (Figure 93). In addition, "pressing" the foil into the flexible epoxy also caused the thickness of the adhesive to

be uneven. Therefore, the resulting surface on the SFB lens from this technique was far from a usable roughness for SFB experiments, despite the successful graphene transfer.

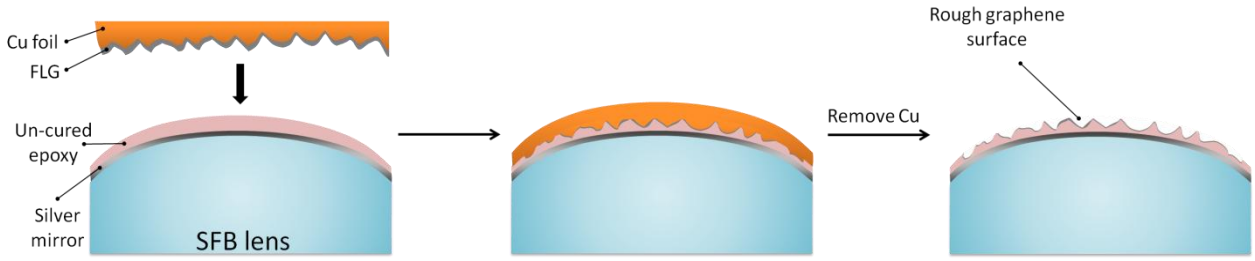


Figure 93) Schematic of direct epoxy transfer of graphene from Cu foil onto an epoxy covered SFB lens. The resultant graphene and epoxy on the SFB lens mimics Cu foil roughness.

A common transfer technique of graphene utilises PMMA (as outlined in Chapter 2). If this transfer technique was employed in conjunction with the epoxy covered lens, and the graphene/PMMA stack was laid over the epoxy, the large roughness from the Cu processing lines could be eliminated, as shown by the schematic in Figure 94. Using a flexible polymer support and removing the original rough copper surface allowed the graphene to relax, eliminating the large roughness from the Cu processing lines.

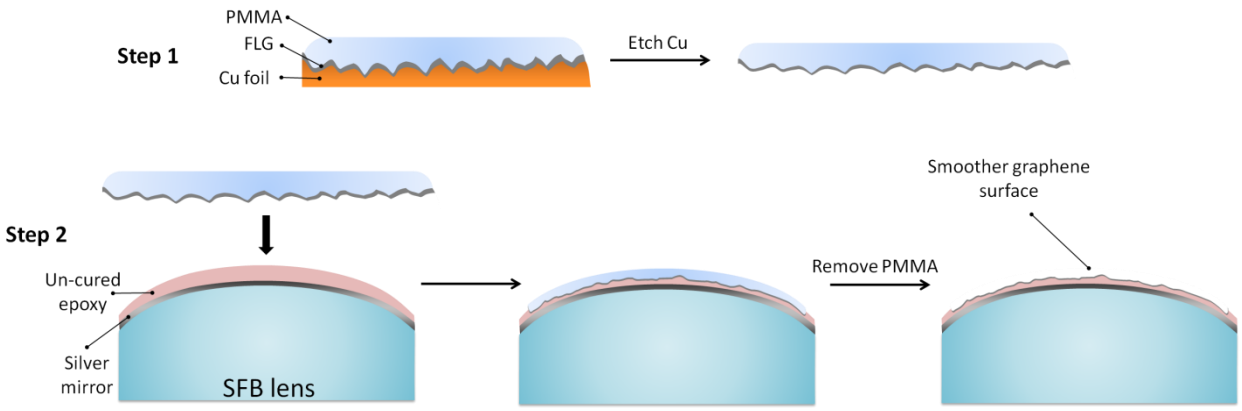


Figure 94) Schematic of PMMA/epoxy transfer of graphene from Cu foil onto a SFB lens. Step 2 demonstrates how the large roughness from the Cu foil is decreased by using the PMMA support, but still yields a rough surface on the SFB lens.

Although the graphene transferred via the PMMA/epoxy method as shown in Figure 94 allowed for a smoother graphene surface compared to the procedure used in Figure 93, some roughness was still apparent. An AFM scan (Figure 95) was taken of one of the smoothest areas on a graphene-covered SFB lens that was produced by the method as shown in Figure 94.

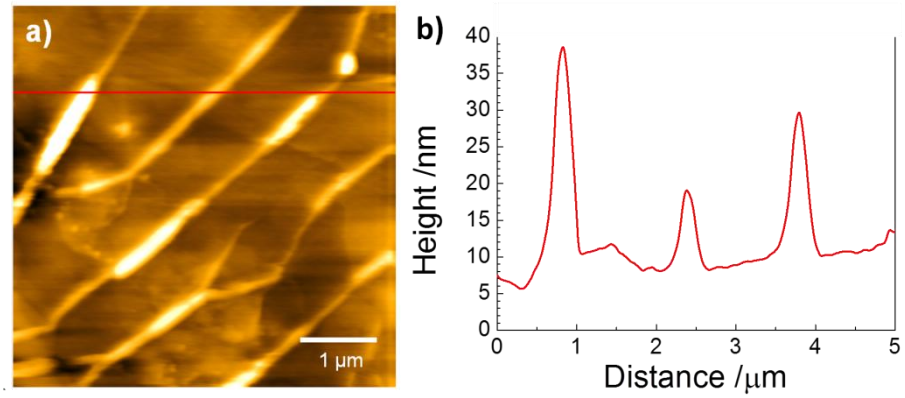


Figure 95a) AFM scan of transferred graphene to a SFB lens using the transfer technique outlined in Figure 94. b) Corresponding line profile of red line in a) showing positive protrusions from graphene wrinkles equating to *ca*. 20 nm.

Figure 95 shows that the transferred lens exhibits as roughness of *ca*. 20 nm. Roughness from processing lines was largely eliminated, however, the transfer did not achieved the usable <5 nm roughness. This surface roughness would yield a case where both SFB lenses have positive protrusions, leading to multiple contact points when the lenses are brought closer together (Figure 96). In addition, the drawbacks of using the polymer transfer, as previously discussed in Chapter 2, still remain: notably PMMA residue would still exist on the transferred surface.

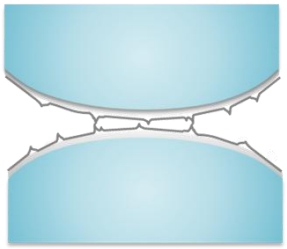


Figure 96) Schematic of how positive protrusions on a pair of SFB lenses demonstrating how such a scenario leads to multiple contact points upon bringing lenses closer together.

The PMMA transfer method was therefore also not ideal for graphene SFB lens fabrication. In this case, where multiple positive protrusions on lenses existed, interpretable interference fringes could not be obtained.

6.3 Approach 2: Graphene synthesis on thin films

In parallel to studies with Approach 1, investigations were made to find a way to synthesise FLG on ultra-flat surfaces from the outset. Approach 2 describes the FLG synthesis investigation in

more detail than in subsequent approaches to demonstrate the thought process behind gaining high-quality graphene growth.

It was hypothesised that eliminating copper roughness and obtaining ultra-flat Cu/graphene surfaces prior to transfer would hence reduce the resulting roughness of the transferred sample on the SFB lenses.

In Approach 2, graphene was synthesised on thin films of copper that were evaporated onto a layer of freshly cleaved mica. Using mica as a substrate for copper was believed to have two advantages: (i) the copper would mirror the smoothness of the atomically flat mica and (ii) the mica could be cleaved to be flexible. If FLG existed on a flexible substrate, when using adhesive to transfer the graphene, the sample could follow the SFB lens curvature and avoid having to be "pressed" into the epoxy, which could induce unevenness in the epoxy layer.

The growth of graphene on thin films is also of interest in the wider graphene field. If high quality synthesis can be demonstrated on such samples, it could lower the cost of materials for graphene synthesis, and in addition lead to the growth of "transfer free" CVD graphene. It has been shown that graphene growth on thin films substrates can allow the metallic catalyst to be evaporated off during or immediately after synthesis, enabling the graphene to be left on an underlying, insulating substrate[120]. This approach is a very important area in the use of graphene in microelectronics, where clean graphene transfer can be a significant problem.

6.3.1 Substrate preparation

Thin films of copper were prepared by evaporating copper onto freshly cleaved pieces of mica, as described in more detail in the experimental section. The thickness of copper was kept thin enough to avoid the need for vigorous etching and still retain substrate flexibility. In addition, the thickness was controlled so that de-wetting did not occur.

500 nm of Cu was first used for graphene growth experiments following the literature[265] and was increased to 700 nm due to reasons that will be discussed in the following section. A schematic and an example of the Cu/mica substrate are shown in Figure 97.



Figure 97a) Diagram of evaporated Cu/mica substrates b) Photograph of an example Cu/mica substrate.

Analogous to other CVD methods, the Cu/mica substrates were annealed prior to graphene growth to allow for the formation of larger copper grains and further cleanse the surface[25,88]. Due to the significant decreased thickness of the substrates compared to standard Cu foils, normal synthesis parameters could not be used; both temperature and time were decreased as described more specifically in the following section. Figure 98 shows SEM images of the Cu/mica substrates before and after annealing. The sample shown in Figure 98 was annealed at 700 °C for 30 minutes, after which the temperature was gradually increased to 900°C over 20 minutes and kept at 900°C for another 10 minutes. These parameters were the starting point for growth experiments so annealing experiments initially mirrored this scheme to determine the state of the substrates without the presence of carbon. It is worth noting that imaging Cu/mica samples in the SEM often proved problematic due to the insulating nature of the mica.

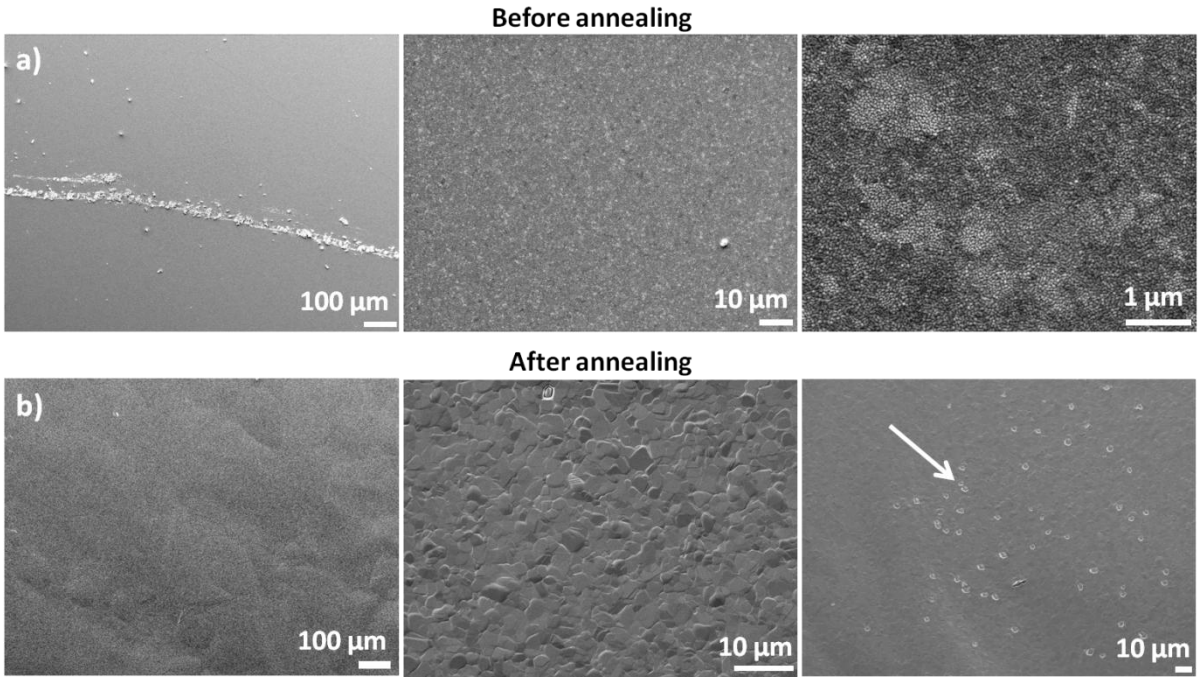


Figure 98) SEM images of prepared Cu/mica substrates. a) Cu/mica substrates as received from evaporation, before annealing. b) Cu/mica substrates post annealing. Cu grains become larger with annealing, with some areas of hole formation as highlighted by the white arrow in b).

Figure 98 shows that prior to annealing, the copper surface is made up of very small features that do not yet resemble copper grains. In addition, some contamination is also present. The surface is however very flat, and devoid of any features similar to that of processing lines that would be seen in normal copper foils. After annealing, the SEM images show the formation of small copper grains (*ca*. 5 µm in size) and the copper surface appeared to be cleaner. Furthermore, some holes through to the mica could be observed, highlighted by the white arrow in Figure 98f. These "mica holes" are areas where the copper has evaporated due to the high temperatures in the furnace. It was evident that these were holes through to the mica during imaging as at higher magnifications, the mica underneath the copper charged under the electron beam. Mica holes will be discussed in more detail in the following section.

Due to the formation of copper grains, it could be concluded that annealing the substrates provides a higher quality copper surface for graphene growth versus the pre-annealed sample. However, because these grains were still very small compared to copper foils, graphene growth was likely to be less controllable. Larger grain sizes of copper are often preferred to gain high-quality graphene synthesis[25,64,104]. To gain a comparable grain size to Cu foils in these samples, a

very slow annealing time at lower temperatures would be necessary; otherwise the small amount of copper could be lost at high temperatures. It was not possible to treat samples in such a way due to the timescale of this project.

6.3.2 Graphene growth

The majority of CVD graphene synthesis studies focus on thicker metal foils, and hence growth at higher temperatures. It is understood that largely higher quality graphene can be gained more easily at higher temperatures starting from 1000°C[25,30,64]. Thin films of metals can often not remain stable at these temperatures, therefore a new synthesis scheme must be employed to gain high quality synthesis.

Producing high-quality graphene nucleation on thin films of copper is an area requiring further development. There has been research using thin films of Ru[65,77] and work with e-beam[98,120,265] and thermally evaporated[266,267] Cu but all on SiO_2/Si substrates. In addition, not all of these papers produced "high quality" monolayer graphene growth, as indicative from the SEM and Raman analysis.

The temperature scheme used in Approach 2 was first based on work by Howsare *et al*.[265]. They noted the difference in temperatures needed for graphene synthesis on Cu thin films versus Cu foils, as shown in Figure 99.

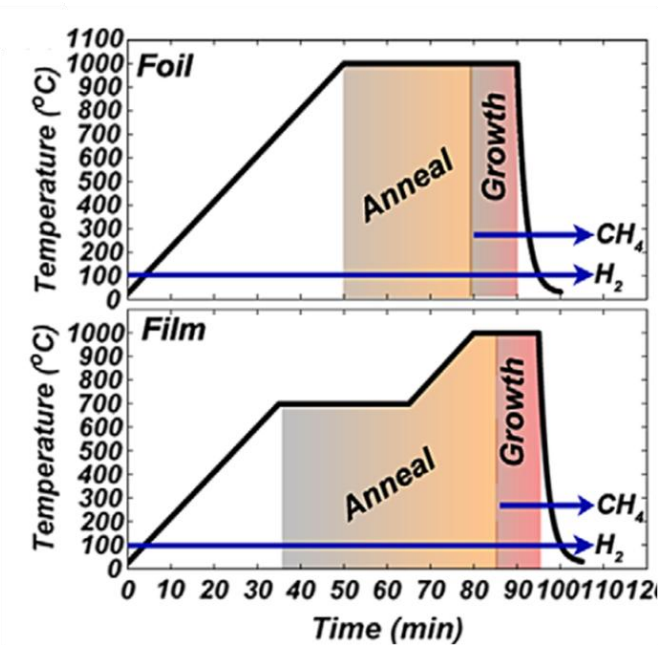


Figure 99) Reproduced with permission from ref[265]. Temperature and time scheme difference between Cu foil and Cu thin film growth.

Howsare *et al.*[265] synthesised graphene on Cu thin films by annealing at a lower temperature prior to graphene growth before increasing the temperature to a higher growth temperature. This is unlike the procedure employed with Cu foils when annealing and growth is usually undertaken at the same high temperatures. Throughout the experimental work in this chapter, a similar scheme was employed. Generally, it was found that limiting the time the Cu/mica substrates were exposed to high temperatures was beneficial.

The experimental parameters that can effect graphene nucleation, and were hence investigated, are:

- Cu thin film thickness
- Substrate orientation (Cu on top or bottom)
- Annealing temperature
- Annealing time
- Experimental temperature
- Experimental time
- Methane/hydrogen ratio

As per the paper of Hosware *et al*., 500 nm of Cu was initially used and the annealing time and temperatures were also mimicked (See Table 3). Gas flow parameters similar to those used in the previous experiments in Approach 1 were initially used in an attempt to obtain graphene nucleation.

In the following experimental tables, experiment number represents a set of identical experiments. Hence, the SEM and Raman results indicate average results across an experimental set number and any anomalies were discounted. Units for gas flows are in standard cubic centimetres per minute (sccm). Bold text highlights key changes from the previous experimental set. Green boxes highlight a positive result in moving towards full-coverage, FLG growth on Cu/mica substrates. SEM analysis was undertaken for all samples. Key SEM images that aid in the explanation of experimental results and thought process are shown from Figure 100.

Table 3 describes the first set of experiments for the Cu/Mica substrates to obtain graphene nucleation and growth.

No.	Cu thickness	Logistics	Annealing	Growth	SEM	Raman
1	500 nm Cu	Cu on top	> 30 mins 700°C under 500 H_2 > Gradual increase to 900°C over ca. 20 minutes under 500H_2	> 10 mins 900°C > 5 CH_4, 300H_2	Small Cu grains Mica holes	No graphitic peaks
2	500 nm Cu	Cu on **bottom**	> 30 mins 700°C under 500 H_2 > Gradual increase to 900°C over ca. 20 minutes under 500H_2	> 10 mins 900°C > 5 CH_4, 300H_2	Small Cu grains Mica holes	No graphitic peaks
3	500 nm Cu	Cu on bottom	> 30 mins 700°C under 500 H_2 > Gradual increase to 900°C over ca. 20 minutes under 500H_2	> 10 mins 900°C > 5 CH_4, **100H_2**	Small Cu grains Mica holes Small black features	No graphitic peaks
4	500 nm Cu	Cu on bottom	> 30 mins 700°C under 500 H_2 > Gradual increase to 900°C over ca. 20 minutes under 500H_2	> **30 mins** 900°C > **20 CH_4**, 100H_2	Cu: decreased significantly, mica holes more abundant ca. 60%. Graphene present: more nucleation around mica holes.	Graphitic peaks present, inc. D peak. Peaks only observed on Cu areas, not holes.

Table 3) Experimental details for 500 nm Cu/Mica substrates, experiment set No.s 1-4. Initial graphene nucleation was achieved in experiment set No. 4.

Across all experiment set No.s 1-4, one feature was concurrent; the presence of mica holes (Figure 100). No significant difference was observed between experiment set No.s 1-2, so it was concluded that substrate orientation was not a key factor at this point and was kept with Cu on the bottom surface for consistency in subsequent experiments.

In experiment set No. 3, the hydrogen concentration during the growth phase was reduced. As described in Chapter 2, hydrogen can act as a graphene etchant. Therefore reducing the H_2 concentration was the first step in accessing preliminary carbon deposits. Experiment set No. 3 yielded small black dot features in the SEM of <1 μm in size, see Figure 100h and i. However, Raman analysis could not confirm these features as graphitic, possibly due to their small size.

Therefore, for experiment set No. 4, the methane concentration was significantly increased, as well as growth time, to determine if nucleation on such substrates would occur at all. As can be seen in Figure 100, SEM images show a large increase in the amount of mica holes in the substrate, but also the presence of grey deposits around the holes. Raman spectroscopy confirmed the presence of graphitic material. The ratio between the G and 2D peak is indicative of FLG. A D peak is also present indicating a slightly defective material. This is to be expected with the observed growth in the SEM; the graphitic deposits are not uniform. However, confirming the synthesis of graphitic deposits on the thin Cu/mica films was a positive result.

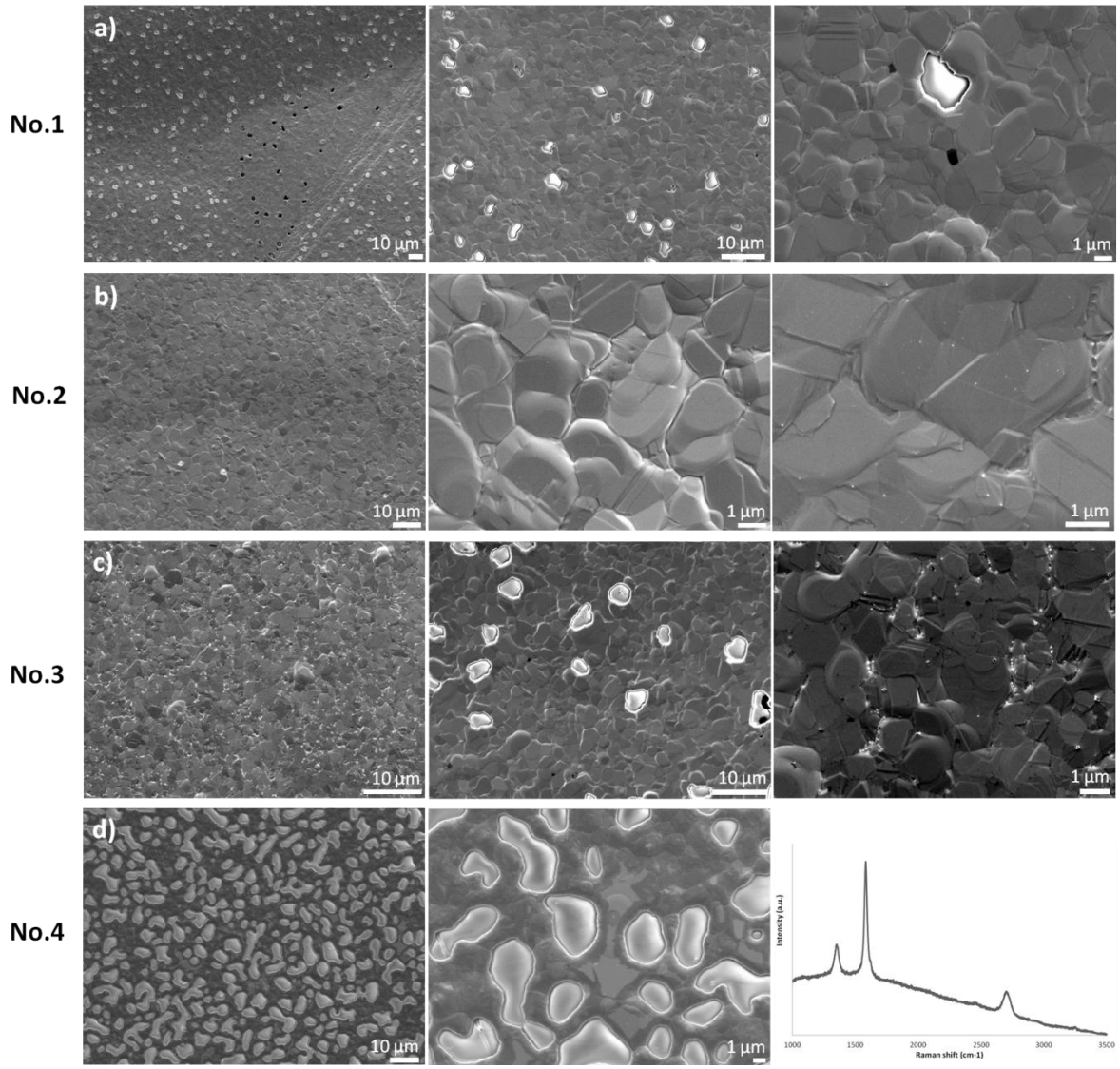


Figure 100) Key SEM images from experiments conducted in Table 3. d) Raman spectra from experiment set No. 4 showing graphitic peaks indicating FLG deposits.

Despite the positive graphene nucleation obtained from experiment set No. 4, all 500 nm Cu/mica samples yielded significant amounts of mica holes. One of the material criteria for this work was that the material must be full-coverage across the SFB lens and hence "holes" in the graphene would not be usable.

Although the previous work of Hosware *et al*. obtained graphene growth on 500 nm thin films of Cu[265], it was decided that the thickness of the Cu would be increased in an attempt to eliminate the formation of mica holes. At 600 nm Cu, the substrates still retained the mica flexibility that was useful for the SFB transfer. Table 4 details the first experiment set for 600 nm Cu.

No.	Cu thickness	Logistics	Annealing	Growth	SEM	Raman
5	**600 nm Cu**	Cu on bottom	> 30 mins 700°C under 500 H_2 > Gradual increase to 900°C over ca. 20 minutes under 500H_2	> **15 mins** 900°C > 20 CH_4, 100H_2	Irregular graphene domains observed (ca. 0.5 µm) Cu features observed: some graphene observed on them Some mica holes still present in areas	Few-layer graphene present Normal Cu areas: D and G peak present Cu features: D, G and 2D peak present i.e. Potentially higher quality graphene on features

Table 4) Experimental details for the first 600 nm Cu/mica substrate experiment set No. 5. Cu features as well as graphitic deposits were observed.

Experiment set No. 5 yielded a new characteristic in the SEM images, the appearance of Cu "features", as shown in Figure 101 (elemental composition was confirmed by EDX, as described in Appendix D). These features were most often present when the mica holes were not. Further investigation of these features will be discussed later in this section. Graphitic nucleation was also gained at these parameters, however, the Raman analysis showed this was highly defective compared to the previous growth (Figure 101e), with a strong D peak.

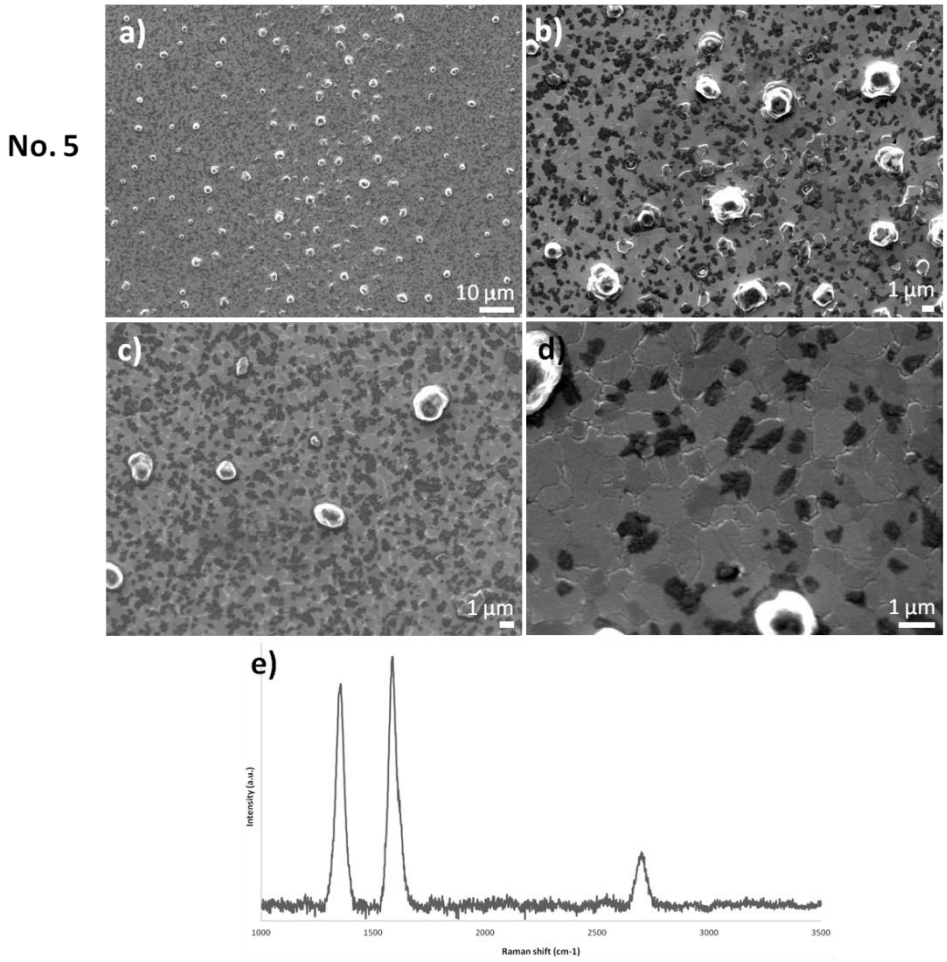


Figure 101a-d) Key SEM images from Table 4 experiments yielding Cu features. e) Corresponding Raman spectrum showing a large D peak indicating a highly defective graphitic material

Unfortunately, some mica holes were still present in this sample. In addition, the coverage of the graphitic deposits in many areas was fairly low, indicating that to obtain full coverage, the sample needed increased time at the highest temperature stage. It was therefore hypothesised that the sample needed less time in the furnace at high temperatures to ensure that mica holes were eliminated. Therefore, a "shift" scheme was developed, where the sample, still under a hydrogen atmosphere, was shifted out of hot zone of the furnace, while the temperature was increased from 700°C to 900°C.

A typical "shift" scheme is as follows:

- Anneal stage at 700°C (e.g. 30 minutes)
- Sample shifted out of furnace (still under H_2)
- Furnace brought up to growth temperature of 900°C (e.g. 20 minutes)
- Sample shifted back into furnace (still under H_2)
- Growth stage at 900°C (e.g. 20 minutes)

This process significantly decreased the time the sample spent at high temperatures, and it was thought that this could eliminate the presence of mica holes. A set of experiments using this method with 600 nm Cu yielded a significant decrease in mica holes but the continued formation of the Cu features. These experiments and corresponding SEM analysis has been described in Appendix D. Crucially however, graphitic material was obtained on all samples using this new method. The Cu thickness was further increased to 700 nm to ascertain if an increased Cu film decreased the appearance of the Cu features. More detailed experimental discussion is described in the appendix however the key result is shown in Figure 102 which shows a sample exhibiting full-coverage FLG with a smaller D peak.

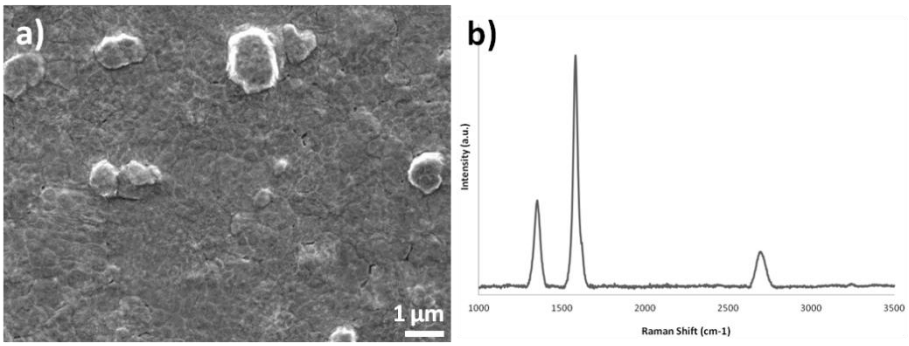


Figure 102a) SEM of 700nm Cu experiment yielding full-coverage FLG with Cu features b) Raman spectra of product in experiment set No. 12 (see Appendix D) showing FLG with D peak.

However, despite this positive result, the Cu features were still present (Figure 102a). It was concluded that all experiments where the sample had been subjected to *ca.* 900°C with methane and hydrogen gas flows yielded one of two scenarios: mica holes or Cu features.

It is possible to think therefore that the Cu features are a precursor to the mica holes, and that Cu features are solidified droplets of Cu which would evaporate to form mica holes if the temperature or experimental time is increased. Investigation of the Cu features was necessary before undertaking further growth experiments. If the mechanism of formation of the Cu features and/or mica holes could be understood, it would provide further insight into the feasibility of future synthesis experiments.

It was imperative to first confirm that the Cu features were indeed copper and not contamination. Contamination is a common feature in copper foils (as described in Chapter 2), however it was originally thought that direct substrate preparation from thermal evaporation on freshly cleaved mica would help alleviate this issue. As shown in Appendix D, EDX analysis confirmed that the Cu features consisted of copper.

Further annealing experiments were undertaken to try to determine the mechanism by which Cu features were forming. From these experiments (see Appendix D) it was concluded that the methane gas flow, the substrate orientation and the shift scheme did not contribute to the Cu features. The observations indicated that Cu features occur at higher temperatures (800-900°C),

and not from the annealing step. Mica holes were apparent at longer timescales and hence Cu features may be precursors to mica holes.

Further SEM imaging undertaken at various tilt angles (Figure 103) showed that the Cu features protrude out of the surface, some with a pyramidal shape. In addition, upon sample titling it was possible to observe some small holes in the Cu surface next to the Cu features, as highlighted by white arrows in Figure 103e.

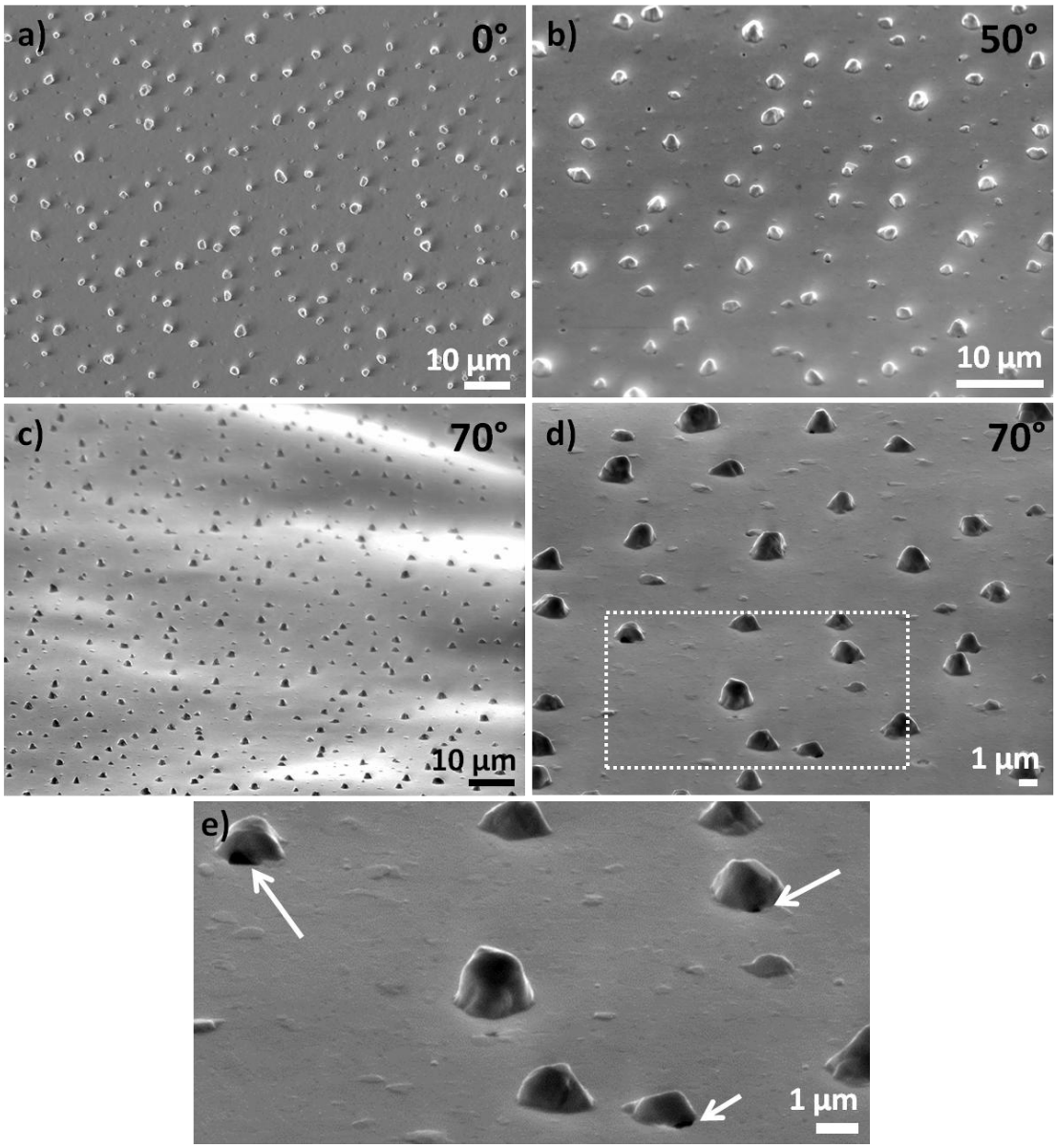


Figure 103) SEM images of Cu features at various tilt angles as specified in the top right corner of each image. a) 0° tilt, b) 50° tilt and c) and d) 70° at different magnifications. Cu features appear to be coming out of a very smooth surface. e) higher-magnification image of area highlighted by white box in d), white arrows highlight holes that are visible next to some Cu features.

EBSD analysis (with thanks to Dr. David Collins) was thought to provide information on any preferential grain orientation of Cu features, however due to the sample roughness it proved difficult to obtain wholly conclusive data. Nonetheless, the EBSD analysis (shown in Appendix D) indicates that the bulk surface is largely Cu(111) and the Cu features are of a different orientation. As an aside, the EBSD results are also interesting for Cu single crystal formation on thin films. Such a material would be a desirable substrate as it would utilise less copper and the same orientation could allow for more controllable synthesis[104].

Cu features similar to those observed in these experiments have been rarely reported in the literature. However, similar features have been discussed by Galindo *et al*.[268] in helium implanted copper foils (Figure 104a-d). Their work focussed on thin films of Cu implanted with helium in an attempt to study the interface between metal thin films and rigid substrates. Galindo *et al.* found that two phenomena occurred upon heating the helium implanted copper samples; i) the helium escaped through small, pore like holes, or ii) larger "protrusions", *ca*. 1μm in size, occurred. They speculated that the protrusions formed due to the helium agglomerating under the Cu, causing a larger bubble to form. They suggest that in such features, the thermal creep induced by the pressure within the bubble is dominant and therefore it is gas bubble formation that creates such protrusions.

It has been shown that muscovite mica (as is used in the experiments in this thesis) dehydroxylates at the high temperatures[269,270] used in the CVD synthesis scheme. This implies that water vapour would exist in the Cu/Mica system at 800-900°C. It is possible that this water vapour travels to the nearest free surface to escape, therefore travelling directly through the copper thin film. This may start to occur during the annealing stage, when smaller holes have been observed (see Appendix D, Figure 131) and continues to happen at a faster rate with elevated temperatures during the growth stage, where bubbles, akin to Galindo *et al*. are formed, alongside the holes seen next to the features in Figure 103e where gas has escaped.

Comparing the Cu features to the literature, Figure 104 shows that although Galindo's Cu protrusions seem more faceted than those which are observed in the Cu/mica samples, there are distinct resemblances in size and shape. It is worth noting that imaging individual Cu features in the Cu/mica samples was often problematic due to charging of the sample, so it is possible that such facets exists. One anomaly is the appearance of a more pyramidal shape in the Cu features compared to those observed by Galindo et al. With Cu on the bottom surface in these images, it is possible that thermal creep of the copper is enhanced by gravity at such temperatures, causing a more elongated shape to form.

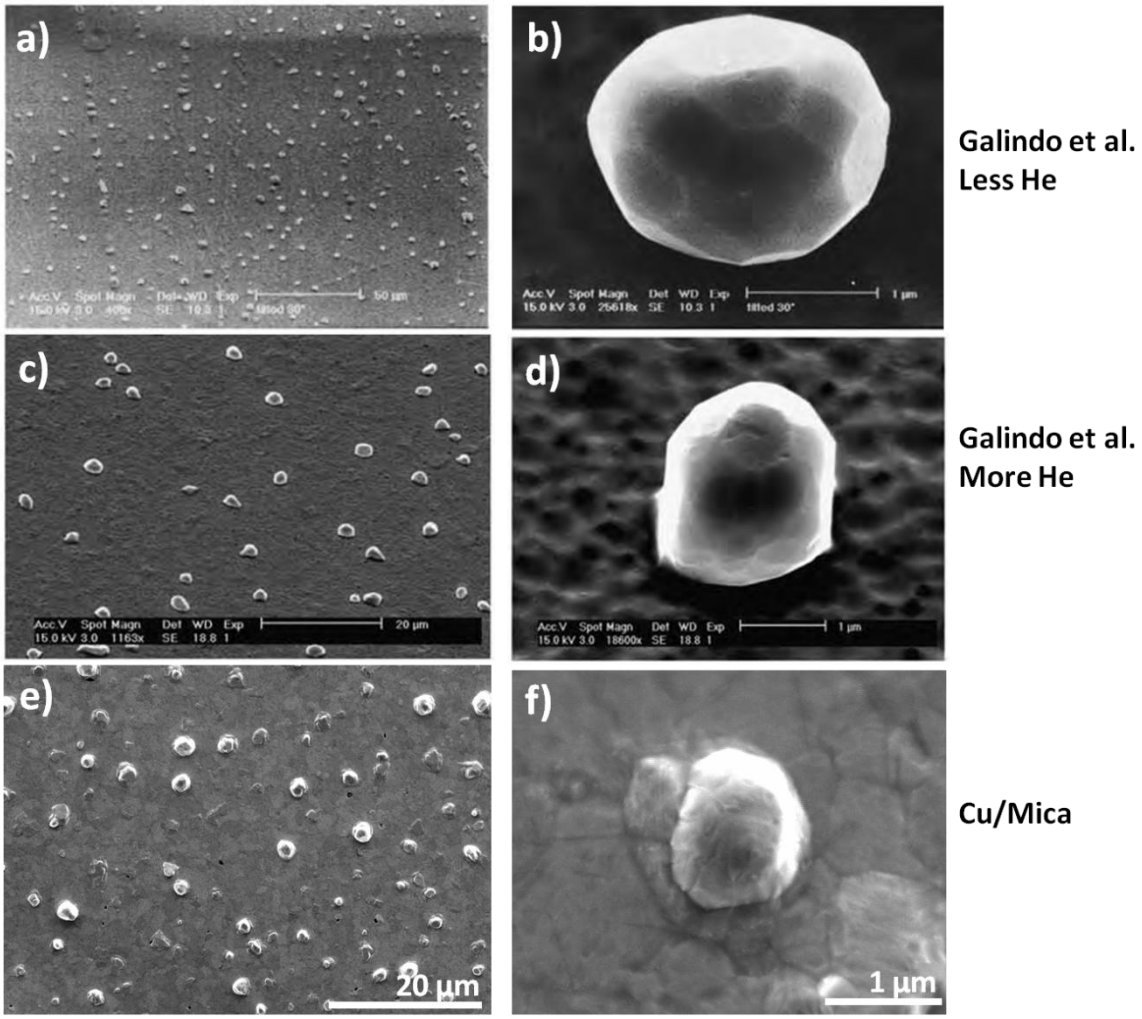


Figure 104) SEM images of a-d) helium implanted Cu bubble formation, reprinted from Galindo *et al.*[268] and e-f) similar Cu features from Cu/Mica experiments for comparison.

Despite some differences, both Cu protrusions are similar in size and coverage across the thin Cu film, and gas was present in both systems at high temperatures. This could therefore suggest a similar mechanism of formation.

However, due to the consistent formation of Cu features in these experiments, it was decided that under the temperature conditions it would be very difficult to curb their formation, and hence any benefits of using the smooth Cu/mica substrate would be lost altogether.

In summary, Approach 2: Thin film synthesis was not suitable as a means for producing flat graphene for SFB due to either the mica holes or Cu features that were consistently present in samples. It is likely that Cu feature formation occurs due to the water vapour that is released from the mica breakdown at high temperatures.

However, FLG growth was nonetheless obtained on thin Cu films on mica and is interesting progress in terms of CVD graphene thin film synthesis which is currently understudied compared with other substrates. It is possible that higher quality graphene synthesis could be gained at lower temperatures by using solid precursors, which is discussed further in Chapter 7: Further Work. For this thesis, such an investigation was not in the scope of this project. However, as will be outlined in this section in due course, it is possible that the samples which produced FLG on thin films can be employed in the SFB using the technique outlined in Approach 5.

6.4 Approach 3: Substrate Electropolishing

Approach 3 follows on from Approach 2 to obtain very smooth graphene from the outset on the Cu substrate. This approach attempted to smooth the Cu foil prior to graphene growth.

Electropolishing is a widely used technique to induce smoothness in metallic surfaces. This is achieved by the preferential dissolution of the higher surface energy sites from the metallic positive protrusions versus negative protrusions as demonstrated in Figure 105. Increased

mass transport away from the positive protrusions occurs therefore metal ion concentration is higher in the negative protrusions. This ensures that dissolution from such crevices is much slower and hence the positive asperities are dissolved away at a faster rate, eventually leading to a smooth surface[271].

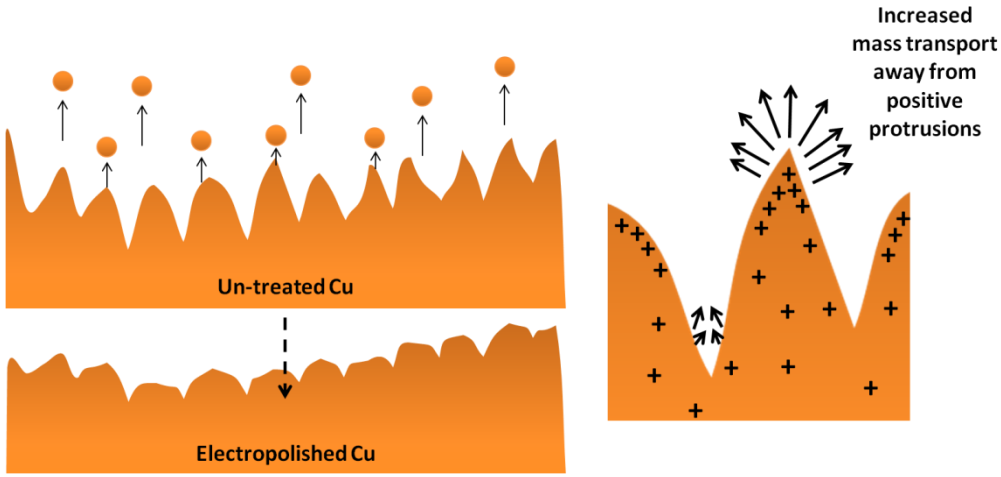


Figure 105) Schematic demonstrating electropolishing of Cu foil showing increased mass transport away from positive asperities, resulting in their preferential dissolution to create a smoother surface.

Electropolished Cu foils have been used for CVD graphene growth previously[105,272,273].Therefore several recipes could be used with the copper foils for this thesis. It was found that no significant improvement was made on a very simple technique as reported by Zhang *et al*.[105] This set up allowed the anodic dissolution of copper into an electropolishing solution of phosphoric acid. They reported obtaining roughness of Cu foils of RMS roughness of 64 nm from the >200 nm roughness of their original Cu foils. Figure 106 shows an AFM scan of a typical electropolished foil using the method similar to Zhang *et al*. (outlined in more detail in the experimental section). Using this recipe Cu foils of RMS values from 70-150 nm were obtained.

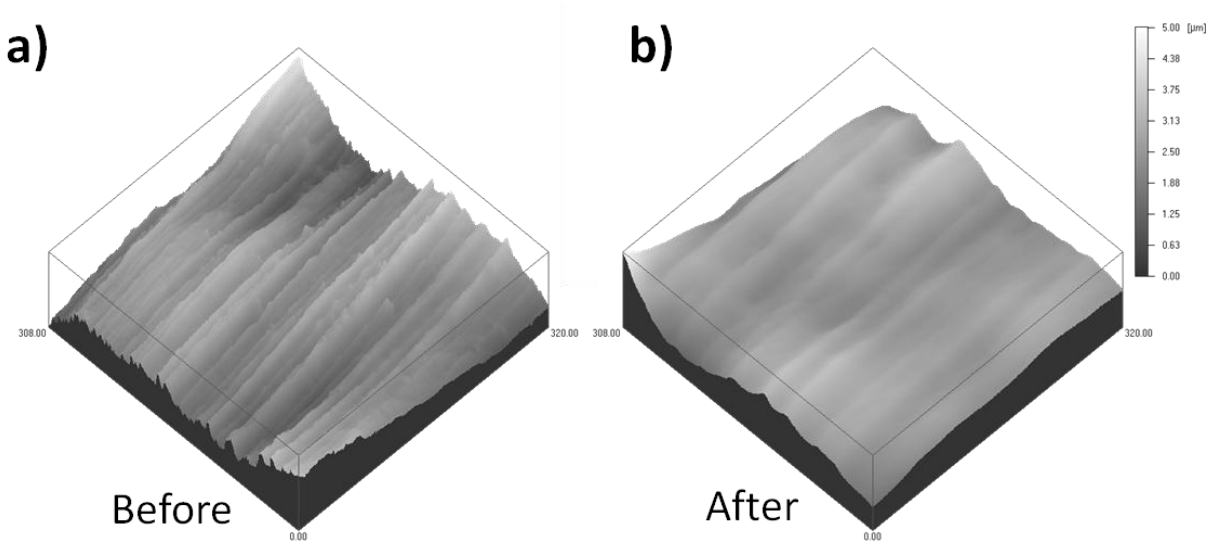


Figure 106) AFM scans of Cu foils a) before electropolishing and b) after electropolishing. With thanks to Christian van Engers for AFM operation.

6.4.1 Graphene growth on electropolished foils

It was possible to obtain graphene growth on the electropolished foils as shown in Figure 107. Electropolishing for 3 minutes provided the optimum time to produce foils for full-coverage FLG growth. Raman analysis indicates that it is possible to gain high quality FLG on the electropolished foils denoted by the absence of a large D peak.

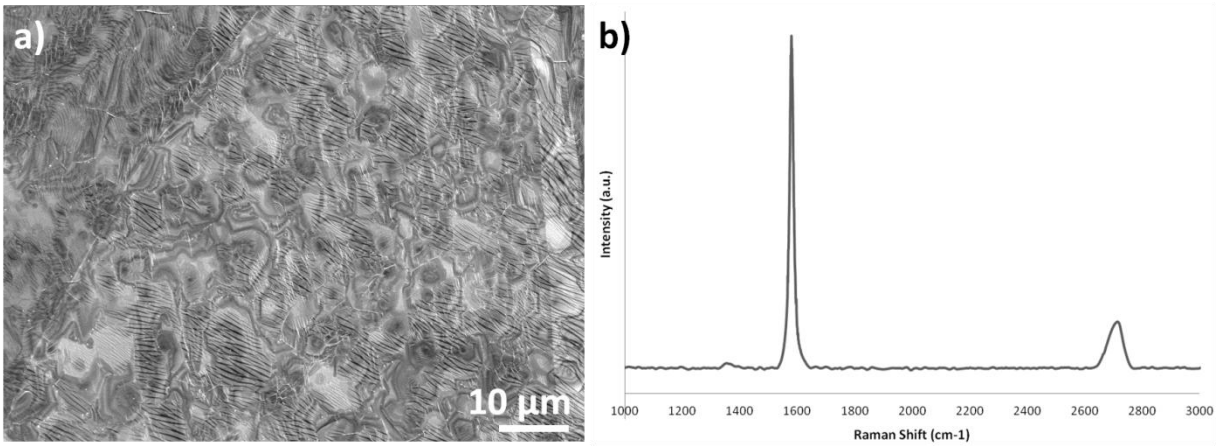


Figure 107a) Typical SEM image of high-quality FLG on electropolished foils and b) corresponding Raman spectrum with very small D peak.

However, despite the high-quality FLG produced on some electropolished foils, it was apparent that gaining reproducible high-quality FLG proved problematic and showed more inconsistencies than growth from Approach 1. Figure 108a-c shows some examples of the

varied growth that was obtained along with a comparison to the growth in the literature (Figure 108d).

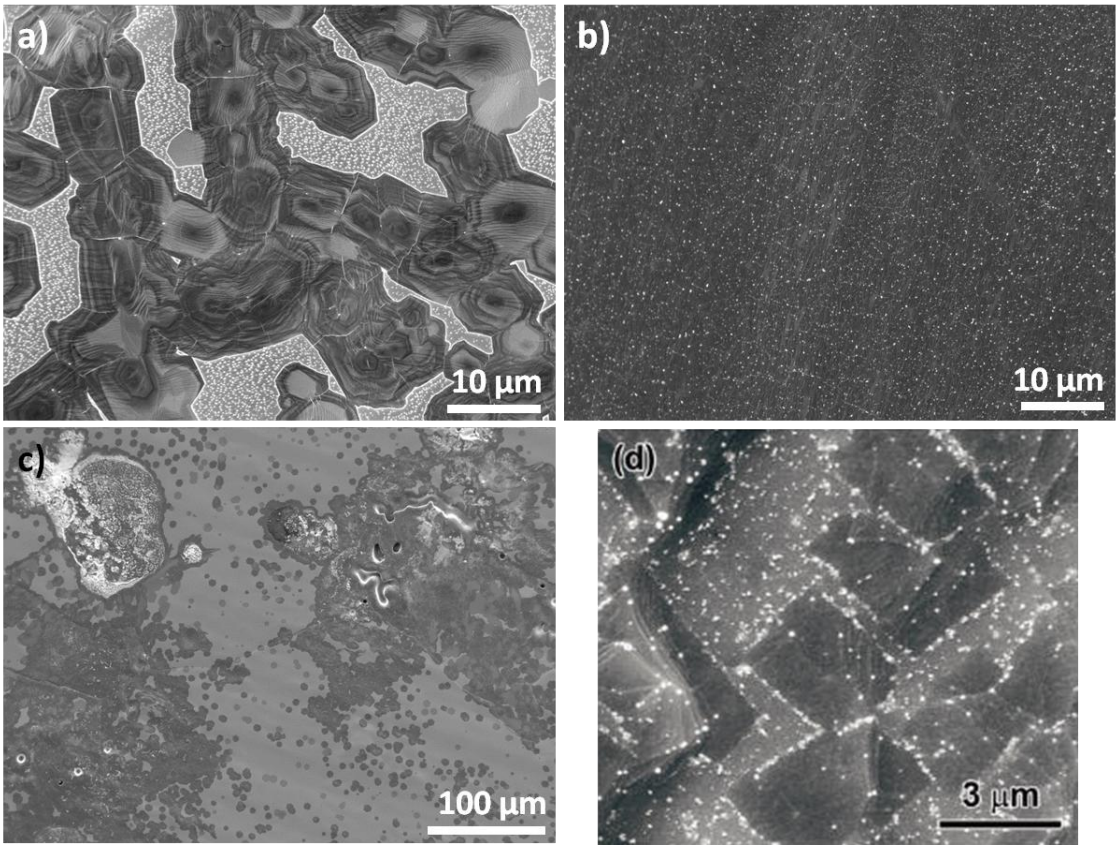


Figure 108a-c) SEM images of contamination on electropolished Cu foils. d) Reproduced with permission from Zhang et al.[105]. A SEM image of graphene on an electropolished Cu foil showing the extent of contamination present in the literature.

In addition, contamination also seemed to be increased in electropolished systems as shown in Figure 108. Zhang *et al*. obtained graphene growth on their electropolished foils at low temperatures (from 400°C) and also observed large amounts of contamination (Figure 108d)[105]. In electropolished samples in this thesis, both larger particles (Figure 108c) and finer, consistent contamination (Figure 108a and b) were often observed.

Although electropolishing produced high-quality FLG on smoother films and eradicated large roughness from Cu processing lines, the smoothest RMS roughness obtained was *ca*. 70 nm, which was again, difficult to consistently reproduce. In addition, the large amount of contamination, as previously discussed, would be hugely detrimental to SFB experiments. It was therefore concluded that much work was needed to consistently reproduce high-quality

synthesis, decrease roughness to the 5 nm range and rid the excessive contamination. Therefore further investigation into electropolishing was not carried forward.

6.5 Approach 4: Substrate pressing

Another approach to reduce the roughness of the copper surface was through substrate pressing. Copper is a relatively soft metal and therefore deforms easily under stress. Approach 3 decreased Cu roughness by simply using a press and placing the Cu foil between mica sheets. In doing so, the foil was being flattened onto a freshly cleaved, clean, atomically smooth template.

6.5.1 Substrate preparation

Cu pressing was undertaken using a bench top, hand operated press. Figure 109 shows a schematic of the experiment, with red arrows highlighting the force acting upon the mica sheets and copper foil. More specific experimental details are outlined in the experimental section.

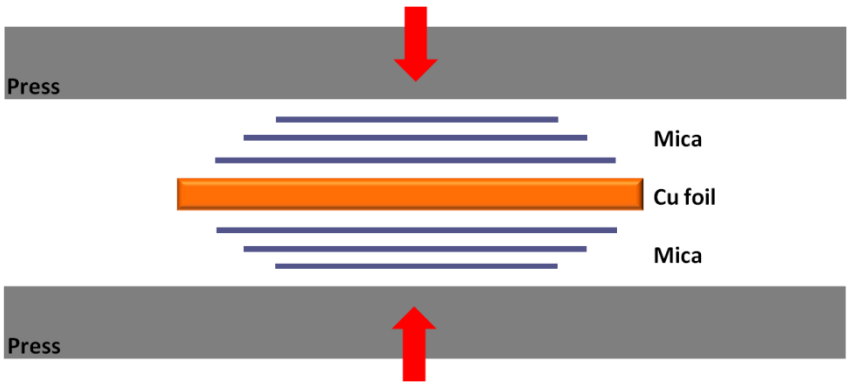


Figure 109) Schematic of Cu pressing experiment. Three layers of mica were placed either side of the Cu foil. The red arrows represent the force acting upon the materials during pressing.

Various arrangements of the copper and mica were investigated. Freshly cleaved mica was always used in direct contact with the copper foil to eliminate excess contamination. Initially, pressing experiments were conducted with one sheet of freshly cleaved mica, roughly the same size as the foil, on either side of the copper. This did not provide a uniform pressing area due to the variation in the force from the press over larger areas, as shown in Figure 110a where a pressed foil only exhibits optimum smoothest in some areas, as highlighted by the green arrows. However, these first experiments still yielded much smoother Cu than the original foil as shown

by the optical image in Figure 110c where the Cu processing lines have been completely eradicated.

In an attempt to further improve the pressing uniformity, the mica was first reduced in size to much smaller than the copper foil. This provided visibly extremely flat copper with a flawless mirror finish. However, the increased pressure on a smaller area caused the foil to break apart, leaving a very small, and hence difficult to handle, smooth copper square, as shown in Figure 110b. In addition, with the increased force, the small mica piece sometimes cracked under the pressure which in turn induced roughness in the Cu foil.

It was found that the optimal scheme for mica flattening was therefore to dissipate this very large force by utilising the flexibility of additional mica layers, but still maintain a smaller "smoothest" area using a smaller piece of mica initially, as shown by the schematic in Figure 109. This layout enabled; (i) the foil to remain intact, so it was easy to handle, (ii) the force to be sufficiently lessened so that the mica did not break and create roughness, (iii) the highest pressure area to be large enough to be useful for SFB measurements (*ca*. 1 cm^2) and (iv) the highest pressure area to be small enough so that the pressure was sufficiently high for uniform contact at a pressure which induced ultra-smooth copper. This method yielded a Cu foil with a uniformly smooth area in the middle of the Cu foil. An AFM scan of such a surface (as shown in Figure 110d) shows that the pressed surface exhibits areas of roughness of < 20 nm. This was a significant improvement on the roughness from Cu processing lines (*ca*. 200nm) despite the very simple method used.

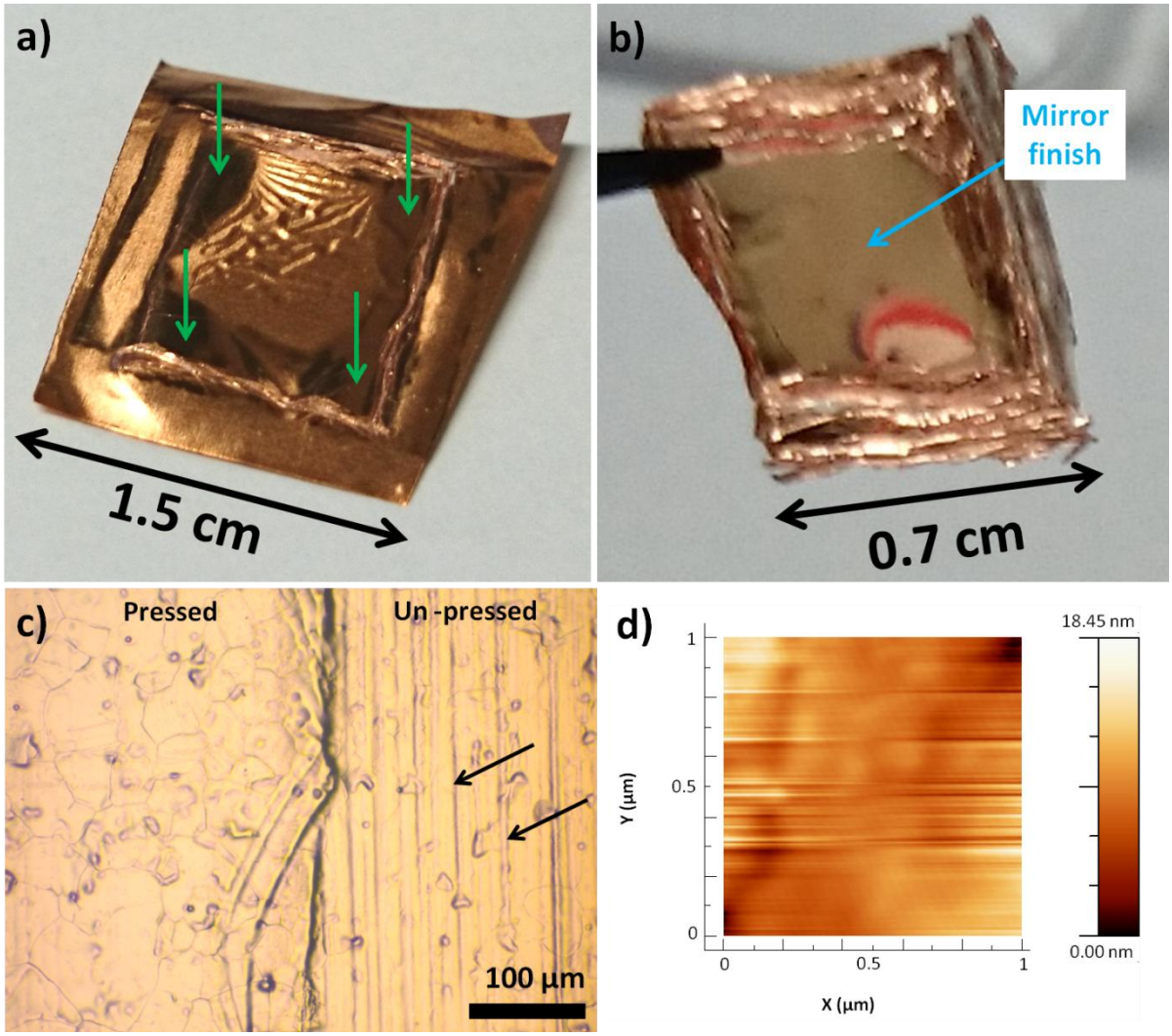


Figure 110a) Photograph of pressed Cu foil using larger mica pieces, resulting in non-uniform pressing. Green arrows highlight well pressed areas with mirror finishes. b) Photograph of pressed Cu foil using a small mica piece which caused Cu to break around the pressing area. Blue arrow highlights very smooth, uniform pressed area with mirror finish. c) Optical image of foil similar to that shown in a), showing the clear elimination of Cu processing lines which are highlighted by black arrows in the un-pressed area of the foil. d) 1 x 1µm AFM scan of pressed Cu foil with mirror finish showing no sharp features and a maximum change in roughness of <20 nm.

It is also worth noting that the copper was cleaned both prior to pressing and after. It was determined that cleaning the copper foil before pressing retained smoothness more reliably as the sonication process in the cleaning procedure can induce some copper etching or rippling in the foil.

6.5.2 Graphene growth on pressed substrates

FLG synthesis was investigated on pressed Cu foils. Interestingly, graphene nucleation on different suppliers of copper varied hugely in this case. Using parameters outlined in Approach 1, Table 2, the growth on pressed Alfa Aesar (99.8%) copper foils was more inconsistent and

often of lower quality and coverage than that on copper foils supplied from Goodfellow (99.9%), see Figure 111.

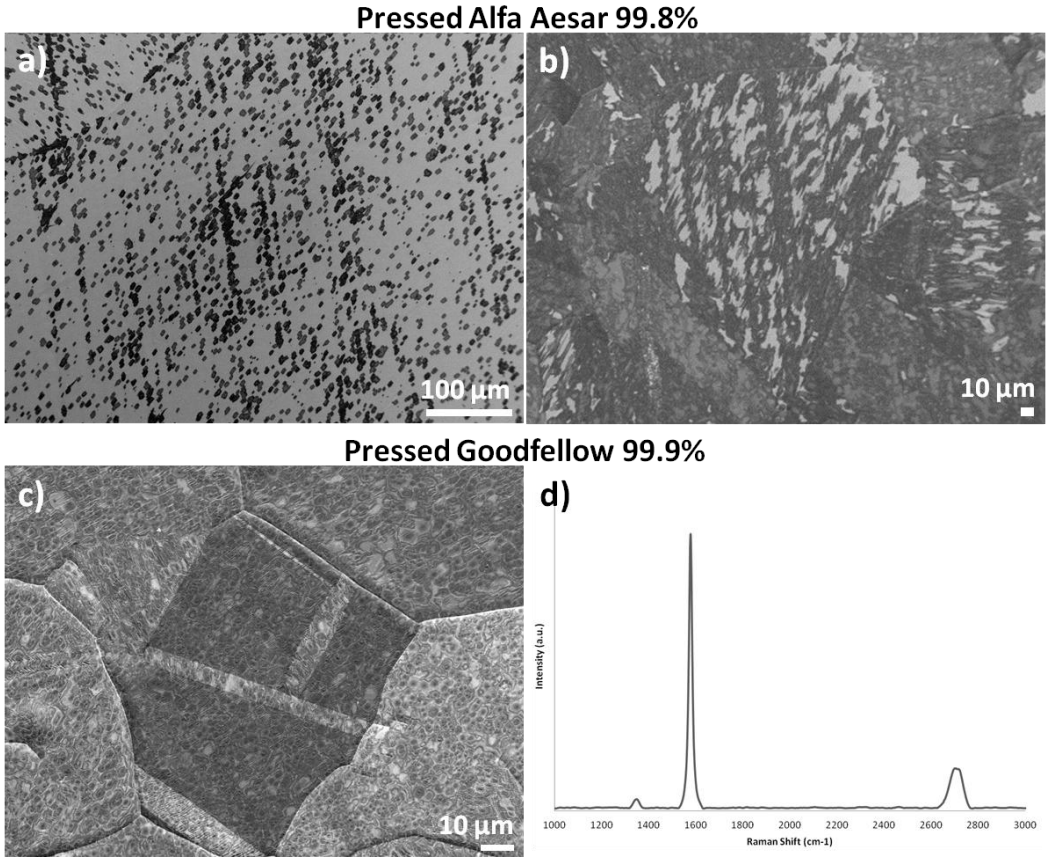


Figure 111) Comparing graphene growth on pressed Alfa Aesar and Goodfellow Cu foils using experimental parameters outlined in Table 2. a-b) SEM images of growth on pressed Alfa Aesar 99.8% Cu foil. Graphene coverage is generally lower and there are areas of daggered graphene growth. c) SEM image of growth on pressed Goodfellow 99.9% Cu foil. SEM shows full coverage FLG growth. d) Raman spectrum of sample c) showing evidence of FLG with a small D peak indicative of good quality graphene.

Alfa Aesar foils produced low and varied coverage, few-layer graphitic deposits that were often not uniform in size or shape (Figure 111a, b). By contrast, Goodfellow foils produced full-coverage, FLG graphene of high quality, with Raman analysis showing only a small D-peak in some areas (Figure 111c ,d).

As shown in Chapter 2, both these copper suppliers are made up of distinctly different copper grains at the foil surface. In addition, it is known that both copper foils contain different contamination particles which could in turn influence nucleation. This could explain the difference in growth that is observed from both of the pressed foils. On Alfa Aesar foils, although some hexagonal growth is present, coverage is generally much lower and there is a high

presence of daggered growth as shown more clearly in Figure 112.

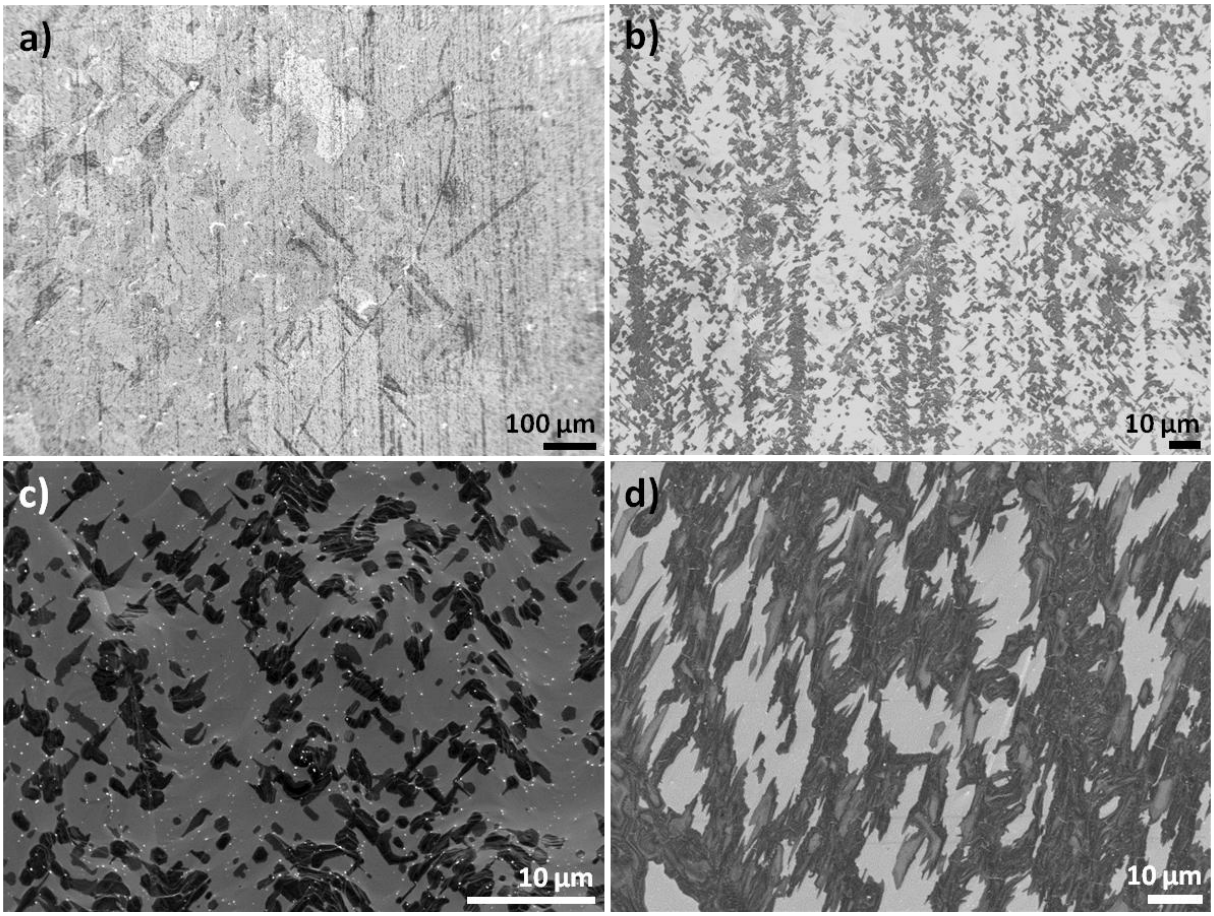


Figure 112) SEM images of daggered growth on pressed Alfa Aesar copper foils.

As discussed in more detail in Chapter 2, the formation of graphene daggers is primarily governed by contamination particles. It is possible that pressing the Alfa Aesar foil causes contamination particles to aggregate to the surface, inducing graphene dagger formation. In these experiments, pressed Alfa Aesar foils contained more visible contamination compared to pressed Goodfellow foils. This is likely why dagger formation is not seen on Goodfellow substrates and hence a more reliable synthesis could be obtained.

It is probable that with changed parameters graphene growth on the pressed Alfa Aesar copper could be tailored to be high-quality FLG. However, as high-quality material was obtained on pressed Goodfellow copper foils, further experiments were not carried out.

In summary, high-quality FLG has been obtained on pressed Cu foils with *ca.* 20 nm RMS roughness, a huge improvement on the Cu processing lines and electropolishing experiments.

However, despite this achievement, it is worth stating that the FLG obtained on the pressed Goodfellow foils were not successful in forming a gSFB. This was due to the remaining inherent level of roughness from the dense coverage of the FLG growth as shown visually in Figure 113.

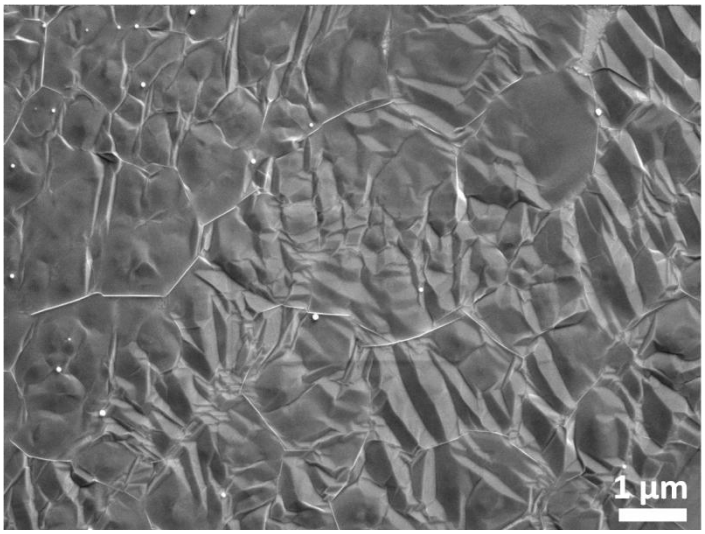


Figure 113) Higher magnification SEM of FLG grown on pressed Goodfellow Cu foil. SEM shows a high level of wrinkles from the FLG growth.

It became apparent that such roughness consistently existed on dense, full-coverage FLG samples. Therefore, although it has been possible to grow high quality FLG on pressed Cu foils and eradicate large roughness from Cu processing lines, roughness from dense coverage, such as wrinkling, still remained. This remaining roughness of FLG is discussed in more detail in Approach 5.

6.6 Overall analysis of Approaches 1-4 for SFB modification

All approaches were analysed in terms of their contribution to the development of a conductive material for the SFB. Brief summaries of each approach are outlined below:

Approach 1: FLG of very high-quality (absence of D-peak in Raman) on cleaned Cu foils was obtained. Significant roughness from the copper existed in processing lines. This could be limited with the epoxy transfer technique by using PMMA, but the resulting surface was still too rough for SFB measurements.

Approach 2: Thin-film synthesis investigations yielded some samples of high-quality FLG (small D peak in Raman), however roughness from the features on the thin film of Cu that evolved during synthesis provided no improvement on the initial roughness from the very high-quality FLG obtained in Approach 1.

Approach 3: Electropolishing the copper substrate also yielded smoother surfaces that could be tailored to produce FLG of high-quality (small D peak in Raman). However, synthesis was not as reliable as Approach 1 and often contained more contamination.

Approach 4: Pressing of the copper substrate also enabled the synthesis of high quality FLG (small D peak in Raman) on much smoother copper than that in Approach 1. However, roughness from the FLG itself, such as graphene wrinkles, was still present and resulting samples proved unsuccessful in gSFB fabrication.

From this information, all approaches achieved the synthesis of a material that was usable for SFB implementation with the exception of the desired roughness. Improvements on roughness had included the eradication of Cu processing lines (Approach 2-4) , however, < 5 nm roughness had not been achieved on SFB lenses. In addition, FLG synthesised in Approach 1, despite the highest levels of roughness, still remained the most reliable method of production and of the highest quality. Additionally, the smoothest transfer onto an SFB lens remained at *ca*. 20 nm (epoxy/PMMA transfer; Approach 1). With this transfer technique, in addition to the roughness, the PMMA residue is almost impossible to completely remove (as discussed in Chapter 2).

It became apparent that a new transfer technique was necessary if < 5nm roughness was to be achieved. Research into synthesising the smoothest graphene would not be useful without a transfer method that retained this quality and desired roughness.

As described in Chapter 2, graphene transfer is not a simple procedure; wrinkles, folds and contamination can all be introduced during the process. Such features would be detrimental for graphene SFB lens fabrication and therefore must be avoided. Therefore a new transfer

technique had to retain graphene quality, be exceptionally clean and obtain the vital smoothness necessary for high resolution SFB measurements.

6.7 Approach 5: New ultra-flat transfer technique

(Please see the attached paper: "A Graphene Surface Force Balance" in Appendix E for the peer reviewed published article[243].)

Approach 5 denotes the invention of a transfer procedure suitable for implementation of graphene in a SFB. The new transfer method exploits both the benefits of providing an alternative support for graphene compared to the substrate, as well as the smoothness and cleanliness of mica. The method is an adapted version of the conventional polymer method but with a key extra step.

The graphene used in this study is the FLG that was synthesised in Approach 1, the parameters of which are detailed in Table 2. As previously stated, this FLG was the highest quality product that was synthesised in this project, and hence is ideal for use as a conductive material for the SFB.

6.7.1 Ultra-flat transfer of FLG

From Approaches 1-4, it has been observed that the FLG necessary for the SFB, although the right thickness and quality, was essentially too rough for use in the SFB from the outset. This case is represented by the schematic in Figure 114a.

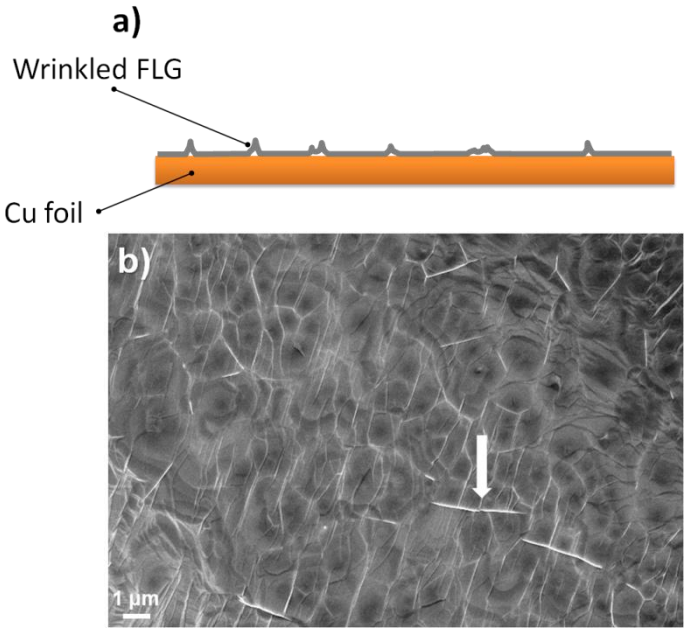


Figure 114a) Schematic of as synthesised FLG on Cu foil highlighting presence of roughness in FLG from synthesis. b) SEM image of typical FLG used in this study with white arrow highlighting a typical wrinkle that would cause roughness as represented in schematic a).

This roughness can come from the Cu foil roughness itself (which Approaches 2-4 have eliminated) but also the graphene. It became apparent that with dense, full-coverage FLG, it is probable that wrinkling occurs during growth. Figure 114b shows a typical SEM image of rough FLG as synthesised using the experimental from Approach 1. The SEM image highlights a wrinkle that would mimic the roughness as seen in the above schematic. Therefore, although Approaches 2-4 had been successful in FLG growth on smooth copper, an inherent problem is still the roughness of the FLG itself, which is can equate to *ca*. 20-30 nm. It is suspected that the *ca.* 20 nm roughness achieved on a SFB lens in Approach 1, derived from FLG coverage not the Cu substrate.

It is this roughness that the new transfer technique attempts to eliminate and has thus far, not been achieved in the literature.

The new method adapted for the transfer of graphene to an SFB lens is as follows:

Step 1: Drop coat PMMA onto FLG/Cu.

Step 2: Etch away Cu leaving PMMA/FLG stack.

Step 3: Lie PMMA/FLG onto freshly cleaved mica.

Step 4: Dissolve away the PMMA leaving a FLG/mica stack.

Step 5: Lay the FLG/mica stack over an epoxy coated SFB lens FLG side down.

Step 6: Peel off the mica at any time revealing a smooth, clean graphene surface.

Figure 115 shows the corresponding schematic of these steps.

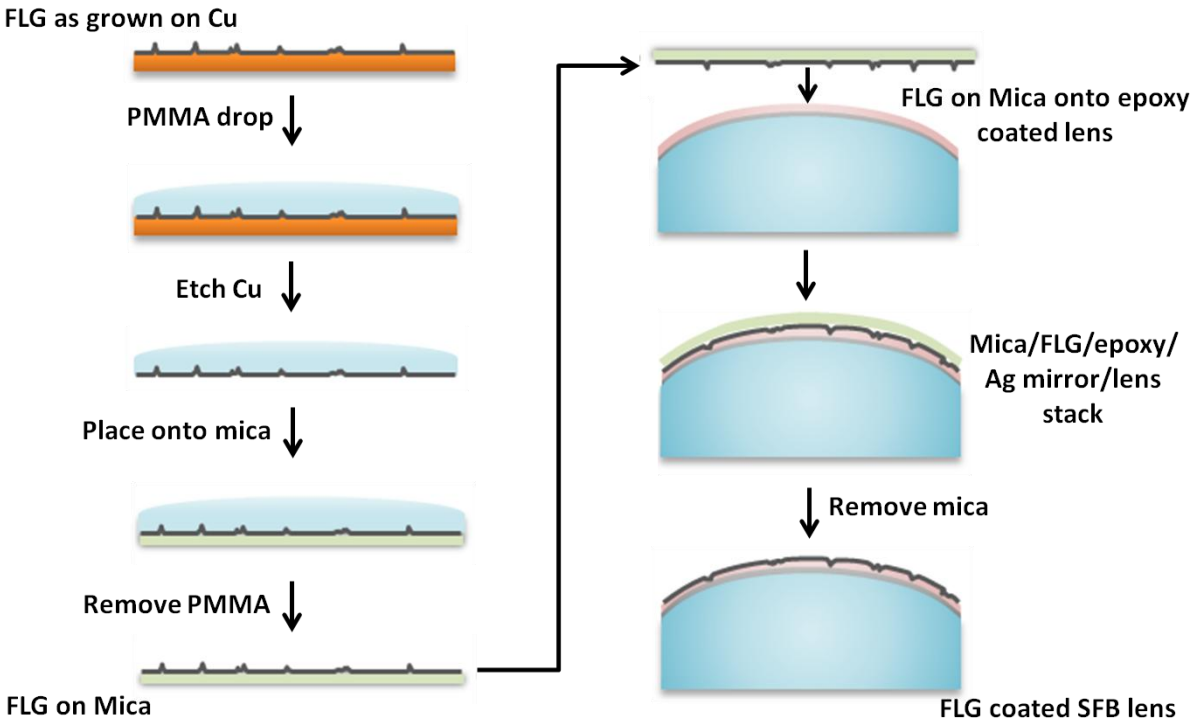


Figure 115) Transfer schematic of the new ultra-flat transfer technique. The key new step is placing the PMMA/FLG stack onto freshly cleaved mica.

Figure 116b and c show the corresponding AFM measurements of an example graphene transferred on a SFB lens using the scheme outlined in Figure 115. It is possible to see a negative protrusion in Figure 116b. Figure 116b and c show a clear improvement in roughness compared to Figure 95, using the conventional PMMA transfer technique. The RMS roughness of the SFB lens surface transferred by the new technique is 0.44 nm over 5 μm^2 and 0.19 nm over 1 μm^2, which is not only approaching the roughness of mica itself[274], but is also well below the threshold of < 5nm needed for SFB measurements.

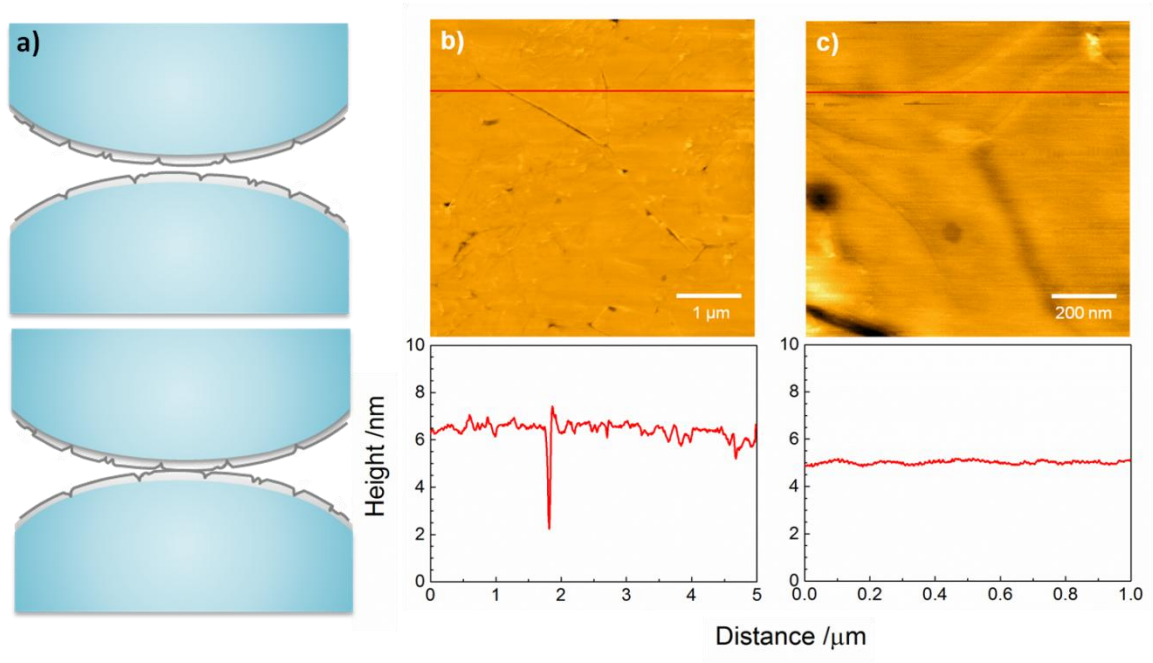


Figure 116a) Schematic of two sets of lenses showing negative protrusions from new transfer method. The lower set of lenses shows how it is possible to obtain a contact spot with no interfering roughness. b) and c) AFM images with corresponding line profiles of the red lines across each image, b) is a 5 µm scan including a negative protrusion. c) is a 1 µm scan showing <1nm RMS roughness.

The advantages from this relatively simple transfer scheme largely nucleate from Step 3, the "extra" step that involves the use of freshly cleaved mica. This step has been imperative in the success of the new transfer technique and its benefits are four-fold:

(i) Freshly cleaved mica is firstly atomically smooth. This is useful as it immediately provides an exceptionally smooth surface for the PMMA/graphene to relax onto. When peeling off the mica, it reveals an atomically smooth surface that has replicated the mica, therefore enabling the same high-resolution characterisation as previous SFB experiments.

(ii) Secondly, freshly cleaved mica is incredibly clean therefore no additional contamination is introduced into the system.

(iii) Thirdly, mica's thickness can be tailored easily depending on how thick it is cleaved. The ability to cleave mica to a thickness that is strong enough to hold the graphene, and flexible enough to relax over the epoxy/lens is a benefit which enables strong adherence between the graphene and the epoxy.

(iv) Finally, the mica can be removed from the mica/graphene/epoxy/lens stack at any point, i.e. it can be removed immediately prior to use in the SFB, hence additionally controlling contamination from the atmosphere and allowing SFB lenses to be produced in batches.

An additional advantage of this "double-transfer" procedure is that the side of the graphene exposed to the SFB is that which was originally attached to the Cu surface. This is unlike other conventional graphene transfer methods. Conventional graphene methods utilise the "top" side of the graphene, that which has been exposed to the atmosphere post synthesis, and often the side of the graphene that has been coated with a polymer support. The new transfer technique essentially "flips" the graphene. This is hugely beneficial in terms of cleanliness as the graphene side exposed in the SFB has only been exposed to an ambient etchant environment (Step 2) that can be washed thoroughly and more controlled. In addition, although PMMA is used in the new transfer method, because the other side of the graphene is measured in the SFB, any residual polymer contamination becomes obsolete. In short, the newly transferred graphene surface is protected by the mica up until the point at which it is being used, then the mica can be simply removed.

Finally, this transfer technique exploits the flexibility of the un-cured epoxy with the smoothness of the mica. Because of these features, any positive protrusions that exist as shown in Figure 96 protrude into the epoxy, creating negative protrusions. For the SFB, these negative protrusions have no effect on finding a single contact point as demonstrated in Figure 116a.

These results indicate that the newly developed transfer technique produced the desired roughness to enable the production of usable graphene SFB lenses. A proof-of-principle measurement confirms whether such graphene lenses can used to make high-resolution SFB measurements.

6.8 SFB results

The FLG growth as reported in Approach 1 was transferred by the ultra-flat transfer technique to SFB lenses. SFB experiments and data analysis were conducted by Dr. Nico Cousens.

6.8.1 Proof-of-principle experiment

To demonstrate the feasibility of the newly transferred gSFB lenses in a SFB it was imperative to conduct a "proof-of-principle" measurement under controlled surface potential.

To do this, a simple SFB experiment was adapted. The forces were measured between two graphene sheets on SFB lenses across an aqueous solution of 0.1 mM $KClO_4$ whilst the surface potential was externally controlled (Figure 117a).

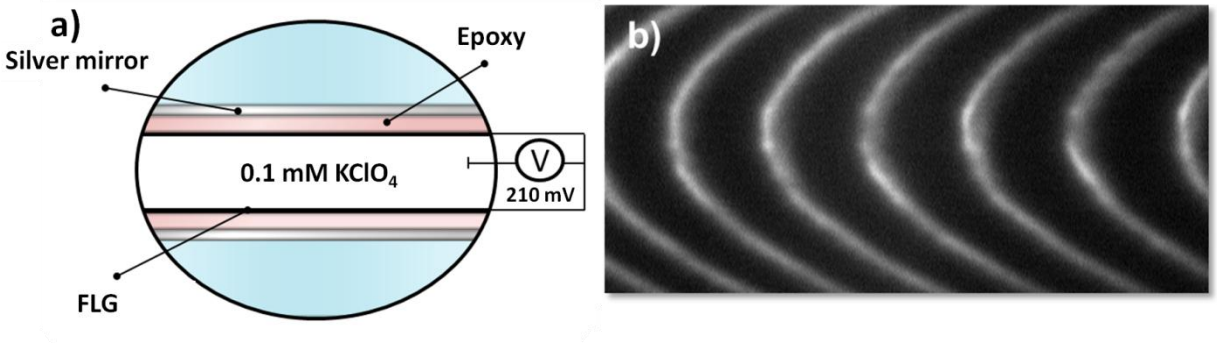


Figure 117a) Schematic of proof-of-principle SFB experiment using $KClO_4$ and 210 mV. b) Example of interference fringes obtained from the experiment, from which a surface force profile is obtained.

Plotting force and separation distance can provide information on the concentration of electrolytes in solution and surface charges. Surface charge can be calculated from the y-intercept and the gradient of a curve can be indicative of the electrolyte concentration. Figure 118 shows the force-distance profile obtained from the experiment shown in Figure 117a. Steeper gradients at lesser distances are indicative of repulsive forces, likely resulting from the two symmetrical overlapping electrical double-layers of both graphene lenses.

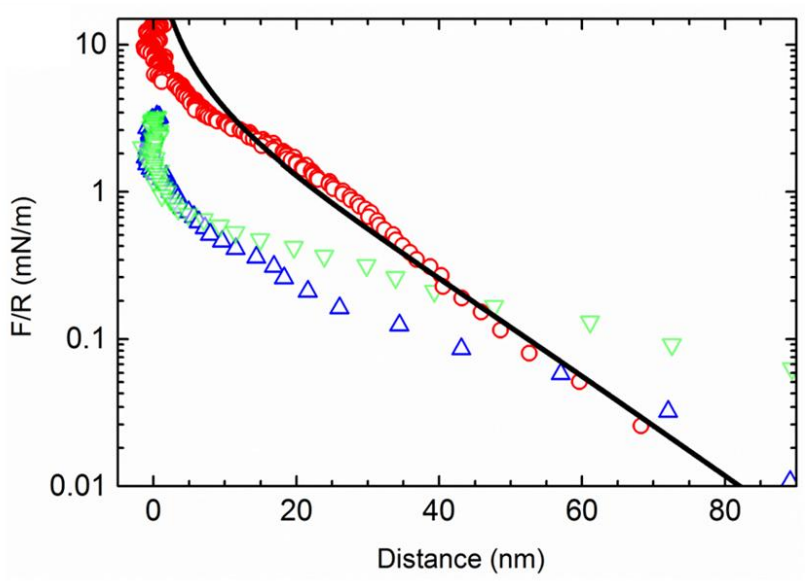


Figure 118) Surface force profile of experimental set up as shown in Figure 117. The blue triangles show the system at open circuit, red circles show the system at a -210 mV surface potential, green triangles show the system returned to open circuit after the -210 mV potential had been applied. The black line corresponds to the theoretically predicted force profile for a 0.6 mM 1:1 electrolyte solution with -210 mV surface potential.

The force was measured as a function of separation distance between the lenses (range *ca*. 0 – 200 nm), first at open circuit, with no externally applied potential. This measurement is shown by the blue triangles in Figure 118. The sharper gradient at low separation distance (tens of nanometres) is indicative of weak repulsive electric double-layer forces to the point of contact, whereas at larger distances no force is detected.

After this initial measurement, the gSFB surfaces were retracted and a potential of -210 (±10) mV was applied to both gSFB surfaces. The force profile (represented by the red circles in Figure 118) shows a much larger repulsive interaction that exponentially increases with decreasing separation distance of the gSFB surfaces. The force increased with a large applied surface potential, as expected with standard Derjaguin, Landau, Verwey, Overbeek (DLVO) theory.

This curve is closely matched with the solution of the non-linear Poisson-Boltzmann (PB) equation for a 1:1 electrolyte between identical, charged surfaces with a sphere-on-flat geometry at -210 mV, but with 0.6 mM salt concentration, not 0.1 mM[275] (see black line in Figure 118). Therefore, the experimentally observed curve at -210 mV is indicative of a higher salt

concentration (0.6 mM) compared with the concentration used. It is likely that this is due to the presence of additional ions in the double-layer region which may result from a small 350 nA background current at applied potential. This current would cause an approximately 10 nM increase in overall concentration of the solution over the duration of the experiment so although background current will have a largely insignificant effect on the overall concentration, it is possible that a larger increase in concentration at the surface is present, where the electrochemical reaction itself occurs. It is worth noting that at open circuit, the PB solution agrees with the 0.1 mM concentration as used, indicating that the concentration increase at the surface occurs only at applied surface potential. The PB solution seems to overstate the force compared with the experimental data at smaller separation distances. It is noted that this is also observed in the case of electrochemical SFB measurements between gold surfaces made by Kasuya *et al.*[276] and the cause of this is, as yet, unclear.

However, was it crucial from this data is that, upon returning to open circuit, the original surface force profile was recovered, illustrating the reversibility of the system and hence its ability to be used numerous times for multiple experiments. A weak charging of the graphene in the aqueous electrolyte environment is implied by the presence of non-zero forces detected at open circuit potential; this could be due to specific adsorption and would also need further investigation.

However, regarding the experiment in terms of a proof-of-principle measurement the results indicate that a usable gSFB has been created and the new transfer technique was successful. This conclusion is further proven by noting three key points:

1. The direct measurement of double-layer forces, without additional repulsive forces, at nanometre separation distances indicate that the two graphene coated lenses are indeed smooth enough, over the entire area of interaction, to be suitable for high resolution SFB measurements, akin to that of mica.

2. The increase in repulsive forces when an external potential is applied is indicative of the conductive, continuous nature of the graphene surfaces and their ability to support the applied external potential.
3. The appearance of high quality fringes of equal chromatic order (FECO) and the their use in successfully calculating the surface force separation and surface force to nanometre resolution undeniably demonstrates the feasibility of using the new ultra-flat transfer to fabricate gSFB lenses.

This data is the first ever measurement conducted with graphene coated SFB lenses and is hence the first example of a graphene surface force balance.

6.8.2 SFB Summary

In summary, the new ultra-flat transfer technique of graphene has enabled the formation of the first graphene SFB. The transfer has been able to eliminate problems with sample roughness that would have been detrimental to any SFB measurement at high resolution and yielded graphene surfaces of micron-sized areas with 0.44 nm RMS roughness. In addition, the transfer technique produces graphene surfaces that are free from polymer residues and can be easily kept clean until the point of SFB measurement by using mica as the protective layer.

Furthermore, if the medium in between the gSFB lenses is removed (e.g. the ionic liquid) the gSFB becomes a new characterisation technique for graphene itself. The interaction force between two graphene sheets is yet to measured experimentally[277]. With the gSFB, pioneering measurements such as adhesion and friction measurements between graphene sheets could be probed as well as liquid film structure at the graphene surface.

Moreover, the new transfer method is widely applicable beyond SFB use, for example for graphene and other 2D material applications where sample cleanliness and roughness are significant obstacles.

6.9 Chapter summary

In conclusion, Approaches 1-5 have outlined several avenues to gain ultra-flat FLG to work towards the formation of the first graphene surface force balance.

As outlined in section 6.6: Overall approaches[...], Approaches 1-4 have proven that smooth FLG can be grown on a multitude of Cu surfaces. In addition, with the transfer technique developed in Approach 5, it is possible that these approaches can be used in conjunction with one another. For example, the FLG synthesised on thin films in Approach 2 could be transferred with the new technique, onto the SFB lenses. It is possible, that the final roughness of the gSFB could be further improved over large areas by combining such approaches.

With regards to gSFB formation, this has undoubtedly been achieved, and is a key milestone for this thesis. The resulting lenses exhibit the required transparency, conductivity, cleanliness and roughness for reliable, and pioneering SFB measurements to be undertaken. In addition, this set-up has provided a new avenue for the characterisation of graphene. The increased use of graphene in a multitude of different areas ensures that a deeper understanding of the material is necessary. The gSFB can provide such measurements.

6.10 Experimental details

All chemicals were obtained from *Sigma Aldrich* unless otherwise stated.

6.10.1 General graphene synthesis via CVD

Graphene was synthesised using atmospheric-pressure chemical vapour deposition of CH_4 in the presence of H_2.10 x 25 mm Cu foils (*Alfa Aesar,* 99.8 %, 25 μm thick) were used as substrates unless otherwise stated in the main text. Substrates were cleaned prior to graphene synthesis to remove contamination from supplier processing using acetic acid[105] as described previously in Chapter 2. The CVD set-up consisted of a quartz tube (20 mm inner-diameter) located inside a horizontal cylindrical furnace, as described in more detail in Chapter 2. The Cu substrate was placed inside the quartz tube at 1035 °C and annealed for 30 min in the presence of 500 sccm H_2

unless otherwise stated. Hydrogen flow was then reduced and CH_4 was introduced as stated for specific samples in the text.

6.10.2 Cu/Mica substrate preparation

(Courtesy of Robert Jacobs, Department of Chemistry)

Muscovite mica was freshly cleaved and cut into *ca*. 10 x 25mm pieces. Cu (*Alfa Aesar*, 99.995%) was then evaporated onto the mica with a specified thickness between (500-700nm) to create Cu/Mica substrates for graphene growth. Substrates were stored under vacuum between preparation and heating in the furnace to reduce risk of contamination.

6.10.3 Cu pressing

Cu foils (*Alfa Aesar* 99.8% and *Goodfellow* 99.9%) were pressed both before and after the acetic acid cleaning procedure outlined previously. The foils were pressed between cleaved muscovite mica sheets using a cool, hydraulic press (Graseby Specac). Samples were pressed with a load of up to 10 tons, which eased off over 1-2 minutes. The sample was then removed from between the mica and blown with N_2 to remove any mica particulates. Mica sheets ranged from 10 x 20 mm and 5 x 5 mm. Any stacking of mica sheets for pressing is described in the main text.

6.10.4 Cu electropolishing

Cu foils were electropolished using a procedure adapted from that reported by Zhang et al.[105] Cu foil ca. 10 x 25 mm (*Alfa Aesar* 99.8% and *Goodfellow* 99.9%) was used as the anode and a bulk amount of Cu foil was used as the cathode. Each electrode was connected by crocodile clips and held in the electropolishing solution. The solution was made up of 200 ml deionised water, 100 ml phosphoric acid, 100 ml ethanol, 20 ml isopropyl alcohol and 2 g urea. A DC power supply supplying consistent voltage and current and was used for 1-3 minutes at a voltage of 6 V. After electropolishing, the polished foil was rinsed thoroughly with deionised water, trimmed from the area with which it was held in the clip, and dried gently with a nitrogen gun.

6.10.5 Ultra-flat transfer of CVD graphene from Cu foils onto glass/Ag lenses

Graphene transfer from Cu foils onto mica: PMMA (Mw: 996,000 dissolved in chlorobenzene) was drop coated onto one side of the Graphene/Cu foil and the Cu was etched in 0.1 M

ammonium persulphate solution. The resultant PMMA/graphene was then removed from the etchant solution and washed thoroughly with ultrapure water. The PMMA/graphene was then placed onto freshly cleaved mica, graphene side downwards, and pressed between clean, glass microscope slides at 110 °C for 30 minutes. The PMMA was removed by leaving the PMMA/graphene/mica in glacial acetic acid (*Fisher*, Extra Pure) for 2 hours.

Lens preparation: Hemispherical quartz lenses (1 cm diameter, 1 cm radius of curvature) were coated in 40 nm of Ag (Alfa Aesar, 99.999 %) using thermal evaporation under vacuum (0.3 Å s^{-1}, 10^{-6} mbar). Buelher EpoThin epoxy diluted with ethanol (1:2 ratio by volume) was then spin coated onto the Ag surface of the lens with a Laurel WS650 Mz-23NPP/LITE spin coater. Spin cycle: acceleration at 100 rpm s^{-1} for 5 s, followed by acceleration to 3000 rpm at 300 rpm s^{-1} for 30 s.

PMMA-free graphene/mica was then laid onto the lens/Ag/epoxy surface and the epoxy was left to cure overnight. The mica could be removed at any time to reveal an ultra-flat graphene surface. For SFB work, this was done immediately prior to use. The removal of mica could be eased by submerging the gSFB lens in ultrapure water.

6.10.6 SFB measurements

The set up for the standard SFB used in this work has been adapted from ref[278].

The SFB set up comprised of two silver-epoxy-graphene coated hemi-cylindrical lenses, as described previously, that were mounted in a crossed-cylinder geometry within the SFB. Using a motor and a differential spring mechanism for fine control, the lenses were translated towards or away from the other to achieve the single point of contact. Forces were detected using the change in the bend of the spring upon which one lens is attached. The epoxy layer was compressed under the high loads and hence lead to a systematic error in separation distance under such loads. This was corrected for by subtracting a linear fit to the measured compressive behavior of the system.

White light interferometry was used to measure the separation distance between the SFB lenses using 'fringes of equal chromatic order' (FECO) that arose from the reflection of the two silver mirrors on the respective lenses. These fringes were observed in a grating spectrometer and captured using a CCD camera. A method similar to that reported previously[279]was used to extrapolate the shape and location of the fringes recorded. Each row of pixels in the image is fitted separately to produce a map of the fringe. The method in this work differs from the previous procedure in using the algorithm with one dimensional centre of mass centroid fit as opposed to a Gaussian fit.

In this case, it was assumed that the two layers of epoxy were approximately the same thickness. In addition, it was noted that the epoxy thickness was far greater than that of the graphene, and hence the interferometer was assumed to behave as a three-layer symmetric interferometer system. Based on this assumption, it allowed the use of a standard analytical solution for a three-layer interferometer as described by Fisher *et al*.[280] to convert the fringe locations recorded into a reliable separation distance of the lenses. The DVLO fitting process was used to calculate a surface curvature of the graphene of 2 cm and the epoxy's refractive index used in this case was 1.532.

To produce the conductive SFB with the transferred graphene surface, electrical connections were made with conductive silver paint (RS components). Graphene surface potential was controlled with a Metrohm μAutolabIII potentiostat. The proof-of-principle SFB experiment was carried out with potassium perchlorate.

7 Further work

In general, this thesis has focussed on the characterisation and understanding of graphene as an imperfect material. Chapters 3-5 have focussed on the characterisation of imperfections, whereas Chapter 6 has demonstrated methods to overcome those limitations and hence developed a new graphene application. This thesis therefore puts forward that it is imperative for both researchers and industry to understand that graphene is a defective material and commercially available samples are likely to also contain these commonly observed imperfections.

This chapter outlines several examples of further work that could be taken forward from the results discussed in this thesis. More specific experiments that could be undertaken will first be discussed, before describing future work from a broader outlook followed by some concluding remarks.

7.1 Further experiments

7.1.1 Graphene daggers investigation

The formation of graphene daggers as described in Chapter 2 is an interesting phenomenon that has not been reported in the literature. Graphene nucleation mechanisms in CVD are often the subject of debate and as shown in Chapter 2, contamination can play an integral role in nucleation. Investigations into graphene daggers, which are unequivocally affected by contamination particles, could therefore provide further insight into graphene nucleation mechanisms as a whole.

To do this, it would first be of interest to explicitly define the elemental composition of contamination particles to ascertain both the chemical reactivity and the origin. This could be done using EDX at higher resolution, such as in a TEM.

To understand the growth mechanism of the graphene daggers, it would be extremely beneficial to use *in situ* SEM to monitor to the real-time growth, as Wang *et al*. have demonsrated[281]. They also observed the movement of contamination particles in their systems. This would enable the direct observation of growth rate, the point of nucleation and any changes the contamination particle undergoes during synthesis. This technique could also provide information on the origin of the contamination.

7.1.2 Graphene synthesis analysis using ultra-flat transfer

An additional tool to understand, particularly few-layer, graphene synthesis would be the use of the newly developed ultra-flat transfer technique. As well as its use in SFB research and the minimal amount of contamination it provides, the transfer technique differs from others as the resultant side of the graphene exposed is the "under-side" of the material, i.e. the side exposed to the Cu surface, not the atmosphere, after growth. The transfer method could therefore be used to investigate graphene nucleation from this perspective.

AFM could be employed to analyse the point of nucleation, to determine any contamination particles present and whether it is raised or defective compared to the rest of the domain. More specifically, the spiral FLG growth briefly shown in Chapter 2, and again shown in Figure 119, could also be investigated by this technique.

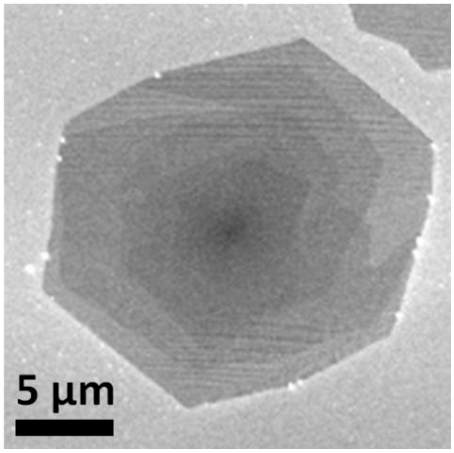


Figure 119) SEM image of FLG "spiral" domain.

Characterising the under-side of graphene domains could be a very interesting approach to graphene nucleation studies.

7.1.3 Graphene/hBN HRTEM further work

To further the HRTEM studies in this thesis, as previously mentioned, the first step would be to support the observations with simulations. Features such as the sideline periodicity and the inter-graphitic plane contrast could be conclusively understood with further image processing methods such as using exit wave restorations.

Secondly, the structure of the imperfections observed could be modelled to understand changes in electronic properties. Modelling changes in layers such as overlapping and the formation of strain and wrinkles would be of interest to both determine changes in properties and assess the significance of those changes for graphene applications. This may be difficult as larger systems are more difficult to accurately model. The majority of graphene modelling is limited to monolayer graphene. Specifically modelling FLG and its imperfections would be of interest as not only is it used in applications, but monolayer graphene often contains areas of FLG, as seen from the commercially available sample discussed in Chapter 1. These experiments could therefore have an impact on the wider graphene field, not just for FLG.

Modelling changing properties, together with the results seen in Chapters 3-5, could aim to prove whether "imperfect" graphene is still suitable for certain applications. The results may suggest that although the large-scale material may not exhibit the strength and electronic properties gained on the pristine nanometre-scale, it may still prove to be a highly useful material.

7.1.4 Thin film synthesis - Solid precursor investigation

The following work is based on the results obtained from the Cu/mica thin film synthesis study described in Chapter 6.

It was concluded that Cu features on the Cu/mica films were consistently formed when using 900°C as the growth temperature. CVD graphene synthesis from methane as the carbon source generally requires high temperatures to produce high-quality deposition of graphitic material. Therefore using a different carbon precursor, that breaks down at lower temperatures, would

be a worthwhile investigation. Li *et al*. reported on CVD graphene growth at lower temperatures using PMMA[282], hence PMMA (M_w 960,000, *Sigma-Aldrich*) was used as the carbon source in some preliminary experiments which were undertaken at 800°C, the results of which are shown in Figure 120.

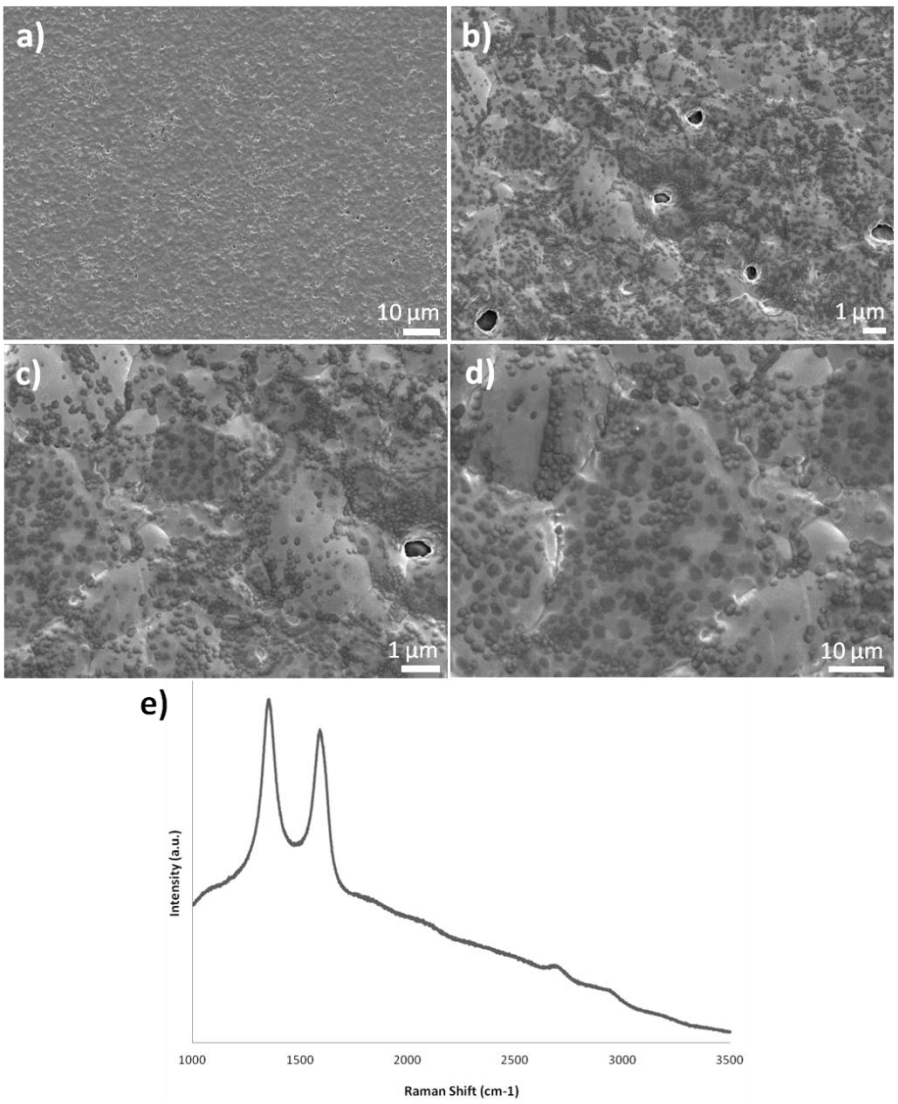


Figure 120) Solid precursor synthesis on Cu/mica substrates: preliminary results. a-d) SEM images of carbon deposits on Cu/mica substrate. e) Corresponding Raman spectrum showing amorphous carbon peaks.

Figure 120a shows that the Cu has retained large-area smoothness and no larger Cu features on the Cu are observed. Figure 120b-d shows some darker deposits approximately 0.1- 1µm in size. The Raman spectrum in Figure 120e suggests these deposits are amorphous carbon. However, the deposits appear uniform across the substrate and hence this preliminary experiment shows

potential for refinement to gain graphene growth on the Cu/mica substrates at lower temperature, without Cu feature formation.

7.1.5 Hot-pressing Cu

Pressing the Cu foils has been shown to provide remarkably smoother substrates for graphene growth with a relatively simple technique. It is likely that graphene synthesis on smoother substrates will further benefit the transfer for SFB. It has been shown recently that hot-pressing has a similar effect[283] so it would be of interest to introduce heat when pressing to create an even smoother surface. Mun *et al*. pressed a Cu substrate between two silicon dioxide wafers and annealed at 900°C[283]. This temperature seems relatively high considering the promising results obtained initially in this thesis without heat. It may therefore be possible to gain additional smoothness by first heating at much lower temperatures which would be both easier to upscale and more energy efficient.

7.1.6 Graphene SFB investigations

As previously described, the gSFB will enable a whole host of new experiments to be performed, including all the SFB experiments to date, but under potential control. Aside from these experiments, for the relevancy of this thesis, the potential for the gSFB to contribute to the graphene field itself is promising.

As eluded to in Chapter 6, the gSFB enables graphene-graphene surface force characterisation. Fundamental properties such as friction and adhesion measurements will provide an insight into how graphene interacts with itself which may be central to FLG studies.

Additionally, the gSFB could have the ability to probe interactions of graphene with other 2D materials. For examples, transferring hBN onto one of the SFB lenses will enable studies into the interaction of graphene with hBN, which can be directly related to the layered heterostructures containing both materials[200,208,218,284–287].

Investigations into this area are currently being continued by Christian van Engers.

7.2 Broader outlook

7.2.1 Overlooked parameters

Chapter 2 detailed several examples of how relatively simple changes in a CVD system can substantially affect CVD graphene growth. Additionally, other often overlooked factors have been suggested to effect graphene growth in CVD, such as impurities from gas bottles[288]. From presenting this work at conferences, it attracts much attention from researchers who synthesise graphene and want to optimise their systems, notably because work advertising synthesis imperfections is not often the subject of published science.

From these responses, and the significance of the effect of these parameters on the growth, it can be concluded that the field needs to develop an integral awareness of the difficulties in CVD synthesis. A list of easily controlled, but overlooked, parameters that effect graphene growth could then be publicised, both for researchers and those in industry to monitor, to enable efficient synthesis. This mindset corresponds to the need for a realisation in the general field that graphene is indeed not a "perfect" material and imperfections are common. If this approach is more widely accepted, additional overlooked parameters are more likely to be discussed and understood to ultimately achieve more controlled graphene synthesis.

7.2.2 Other 2D nanomaterials

With the discovery of graphene, 2D nanomaterial research has spread into a multitude of materials. Due to the similarities seen between hBN and graphene in Chapters 3-5 , it would be of interest to ascertain if similarities exist in additional 2D nanomaterials. For example, transition metal dichalcogenides (TMCs), such as MoS_2 or WS_2. Similarly to graphene, these materials can be readily synthesised and have shown promise in a multitude of applications[285–287,289]. Additionally, characterisation of their imperfections on the larger scale, outside the pristine nanometre range, is limited. It would therefore be beneficial to extend the more realistic characterisation scheme employed in this thesis to these materials.

Furthermore, with the increased expectation of these materials' potential it could be interesting to extend the SFB work to other 2D materials. A similar transfer method could be employed to allow for the creation of a TMC SFB and hence surface force measurements could be obtained for a multitude of materials, enabling further understanding of fundamental properties, including their interaction with one another.

7.3 Concluding remarks

This further work will help to contribute to more specific graphene fields and aims to further the broader approach that was introduced in this thesis. Imperfect graphene is "real" graphene. Work in this thesis has proven that graphene is not a "miracle" material. The impact of this work looks at being the bridge between the perfect, pristine graphene lattice described in the literature, and real material that is, and will be, utilised in an industrial context. Industry will be using an imperfect material and therefore recognition of the defects and publishing work surrounding both their characterisation and investigation is paramount. It is imperative that a distinction is made between the fundamental properties of graphene that is flawless, and the larger scale material that industry must work with.

8 List of Figures/Tables

Where relevant, all reproduced material has been reproduced with permission from one of the following; the American Chemical Society, Wiley Publishing, IOP Publishing, OSA Publishing, AIP publishing LLC, the American Physical Society, Elsevier, the Royal Society of Chemistry, the PCCP Owner Societies and Macmillan Publishers Ltd. All rights reserved. All reproduced material has been clearly cited.

Figure 1) Graphene brownie. vi
Figure 2) Graphene is viewed as the building block of other carbon nanomaterials such as fullerenes, CNTs and graphite. Reproduced with permission from ref[5] 14
Figure 3) A PET/graphene touch panel assembled by Bae *et al*. demonstrating flexibility and transparency. Reproduced with permission from ref[30] 20
Figure 4) SEM image of a sample of commercially available graphene as advertised[82]. 21
Figure 5) SEM images of both sides of a sample of commercially available CVD "monolayer" graphene grown on Cu foil. Inset of d) is the magnified image of the area of the white box highlighting the presence of areas of FLG growth. 22
Figure 6) Schematic of the basic principles of CVD graphene synthesis. 26
Figure 7) Schematic of the CVD experimental set up. 27
Figure 8) Example SEM image of graphene grown on Cu foil with key features highlighted: Cu substrate, Cu grain boundary, a graphene domain and contamination particles. 30
Figure 9a) Raman spectra at 514 nm comparing bulk graphite and graphene. b) Changes in Raman spectra at 514 nm with increasing number of graphene layers. c) Changes in Raman spectra at 633 nm with increasing number of graphene layers. d) Development of four components of the G' peak in bi layer graphene at 514 and 633 nm, explaining the development of an increasing band with increasing layers. Reproduced with permission from ref[110]. 32
Figure 10) SEM images of example CVD graphene grown in Cu foils. a) Hexagonal graphene growth. b) and c) Individual hexagonal domains with FLG growth visible within the domain. White arrows in b) highlight two growth points in one domain. c) Example of possible "spiral" FLG growth. d) Hexagonal growth of largely monolayer graphene. e) Full-coverage FLG with white box highlighting area of magnified inset. 34
Figure 11) Difference in graphene growth across CVD furnace due to substrate position. a) Example SEM images shown from 25%, 50%, 60% and 75% through the furnace. b) Corresponding Raman spectra taken from samples 25%, 50-60% and 85% through the furnace. Raman data shows the evolution of graphene growth from bi-layer to monolayer to defective FLG throughout the furnace. A red arrow in the Raman spectrum for 85% highlights the D peak. c) Temperature distribution of CVD furnace which is likely to be a factor that influences the changes in graphene growth. 36
Figure 12) SEM images of varied graphene growth due to influences from the Cu substrate. a) Alignment of hexagonal domains in one Cu orientation. Inset shows a graphene domain with an additional graphene domain, at a different orientation, within it. b) Example of different graphene growth on different Cu grains. c) Graphene growth dominated by Cu processing lines. d) Graphene growth more prevalent on grain boundaries between Cu orientations. 37
Figure 13) EBSD scans of Cu foils from two copper supplies with corresponding SEM images of graphene grown from the same synthesis conditions. 39
Figure 14) SEM images of contamination observed after graphene growth on Cu foils. a) Full-coverage graphene with contamination particles visible as a continuous deposit on top of the graphene. b) Contamination visible on Cu foil and bordering graphene domains. c) and d) Examples of large contamination particles inducing substantial nucleation. e) Large contamination particle both inducing nucleation and hindering growth (inset at higher magnification). 40
Figure 15) SEM images of graphene daggers. a-f) Examples of graphene daggers terminating in contamination particles. c-f) Examples of graphene daggers at higher magnification. g-h) Examples of graphene daggers occurring within regular FLG growth. Inset of h) is shown at higher resolution in f). 41
Figure 16 a) HRSTEM image of substitutional Si dopant in graphene lattice, with two adjacent five-fold rings. Reproduced with permission from ref[127]. b) HRSTEM image of substitutional N dopant with c) corresponding line profile illustrating the contrast difference between carbon and nitrogen atoms. Reproduced with permission from ref[128]. 43
Figure 17) Schematic of general polymer transfer of CVD graphene onto a different substrate. 45

Figure 18a) TEM image of graphene exhibiting polymer contaminating after PMMA support was used for graphene transfer and annealed for removal. b) shows corresponding false colour image with polymer contamination highlighted in blue. Reproduced with permission from ref[132] 45
Figure 19) Schematic of graphene transfer process for TEM using process from ref[133] 46
Figure 20) Example of a visualisation of a CTF from a HRTEM. Point resolution is highlighted by a red star. 48
Figure 21) HRTEM images of graphene at different focuses resulting in a) bright atomic contrast and b) dark atomic contrast. All scale bars are 1 nm. 49
Figure 22) Left – aberration corrector software analysis of Right – tableau of FFTs to produce a sweet spot of 26 mrad. Outer tableau limit (maximum tilt angle) was 35 mrad 50
Figure 23 a) Beam damage observed in the exact shape of b) the electron beam used during beam showering. c) Higher magnification image of accumulation of nanoparticles in damaged area of graphene. 54
Figure 24 a-c) Sequence of nanoparticle mobility; red circles highlight the position of one moving nanoparticle, black arrows illustrate the direction of movement. 55
Figure 25 a) Representation of a NanoBud (fullerene attached to a SWCNT), corresponding with c) starting material. b) Representation of transient structure of evolved NanoBud (c-h) TEM images of evolution of NanoBud structure under electron irradiation. 55
Figure 26) HRTEM images of evolving hole in FLG during beam irradiation. 56
Figure 27a) Monolayer FFT with indexed diffraction spots. b) FFT of misaligned FLG. c) Reproduced with permission from ref[143]. Diffraction of monolayer and bi-layer graphene with corresponding contrast profiles of arrowed regions in the diffraction pattern. d) FFT of an un-strained graphene lattice. e) FFT of a strained graphene lattice with a deviation from the symmetry of the white dotted circle, highlighted by white arrows. 58
Figure 28a) Raw TEM image where a graphene lattice is not visible through amorphous contamination. b) FFT of image a). c-d) Procedure of masking of lattice spots. e) Final modified FFT with masks in place. f-g) Inverse of masked FFT to produce image visualising lattice. g) Higher magnification image of inversed masked FFT, showing moiré fringes and confirmation of misaligned bi-layer graphene, previously invisible in raw data a). 59
Figure 29) Reproduced and adapted with permission from refs[84,152]: three defect structures of graphene. a) a ripple, b) a simple wrinkle and c) a folded wrinkle. 65
Figure 30) Reproduced with permission from ref[84]. a) SEM image of CVD graphene on SiO_2/Si substrate. b) Raman G band intensity map of the same area demonstrating a change in Raman signal over wrinkles. 66
Figure 31) TEM characterisation of wrinkle defects in the literature. a) Reproduced with permission from ref[125] b) reproduced with permission from ref[84] c) reproduced and adapted with permission from ref[164]. 67
Figure 32a-c) TEM images of overlapping areas of monolayer and few-layer graphene. Corresponding FFTs of above (upper) and below (lower) the overlap are pictured below the relevant image. In all cases, the FFTs from below the feature show more lattice spots, along with those seen in the above FFT (highlighted by yellow circles), indicating an overlapped region. 68
Figure 33a and b) TEM image of area of folded wrinkle. The lines of the fold are highlighted in b) by white dotted lines. The insets in b) are FFTs of the above, central and below areas of the feature. c) Schematic of a folded wrinkle. 69
Figure 34a) TEM image of a non-parallel folded wrinkle with FFT insets from respective areas in the image. b) TEM image of the same area at higher resolution showing a moiré pattern in the central area with corresponding FFT of whole image. Inset indicates angle difference between the non-parallel two-line contrast. 70
Figure 35) Reproduced and adapted with permission from ref[164]. a) Low magnification TEM image of folded wrinkle, highlighted in green. b) Schematic of likely structure of the rotation fold in a tri-layer graphene sheet. c) High-resolution TEM image of tip of folded wrinkle, highlighting change in rotation between the two rotated lattices. 71
Figure 36) Images depicting the change in angle measurement across non-parallel folded wrinkles, including the discrepancy in determining the angle at the tip of the fold. a) Low magnification TEM image of a rotated folded wrinkle, highlighted in green. b) and c) Higher magnification images of the middle and end of the feature shown in a). d) and e) Second folded wrinkle with various rotation angles highlighted. e) Feature in d) at lower magnification highlighting the curvature that occurs lower down the feature. f) Image from Figure 35c with alternative rotation highlighted equating to 10°. This angle differs from that denoted by the yellow dotted lines equating to 22.4°. 72
Figure 37) Non-parallel folded wrinkle with FFTs showing change in lattice rotations and strain. a) TEM image of rotation fold with corresponding FFTs from above, central and below fold. b) TEM image of same fold at tip, showing corresponding FFTs. White dotted circles mark a regular, un-strained lattice with red arrows highlighting non-uniformity in the FFT. Yellow and blue lines highlight the angles of the top and bottom lattices either side of the fold respectively 74
Figure 38a) TEM image of wrinkle in FLG with turquoise box highlighting area where b) line profile was taken. b) Indicates the contrast of the 8 lines. c) Schematic of a similar wrinkle feature. 76

Figure 39a-b) TEM images of graphene wrinkles where a periodicity can be observed within the contrast of the graphitic layers. c) TEM image (courtesy of Dr. Rebecca Nicholls) of a CNT where a white arrow highlights a similar contrast. 77
Figure 40a) Schematic of a graphene lattice gradually titling perpendicular to the zig-zag axis. The last diagram in this series is enlarged in b) where the contrast and spacing corresponding to the contrast observed experimentally is highlighted. 78
Figure 41a and b) TEM example images of periodic "sideline" spacing seen in FLG. White arrows highlight some areas of this contrast. c) possible sideline example images from literature ref[164]. Bottom image is feature at higher magnification with corresponding line profile of area ii. Spacing in the paper is quoted as 0.12 nm. From the image, it seems that in *ca.* 1nm, 5 spacings occur, indicative of a *ca.* 0.2 nm spacing. 79
Figure 42a) TEM image of area of sidelines showing interesting contrast similarities between the periodicity along graphitic planes and the sidelines contrast. The white arrow highlights an area with prominent sidelines, the blue arrows highlight areas of periodicity along graphitic planes and the red arrow highlights an area where it appears one feature derives from the other. The spacings of all periodicities in this image equate to *ca.* 0.2 nm. b) Reproduced with permission from ref[170], simulation of multi-wall CNT TEM image at various chiral indices showing appearance of similar sideline contrast on the side of a CNT. 80
Figure 43)TEM image of a folded wrinkle with sideline features. Inset shows how the angle of incline can be calculated if the change in focus and length of the sidelines is known. The top left of the inset depicts how this could relate to the arrangement of FLG in this scenario. Angles on the image depict how the change in incline has been calculated throughout the image. 82
Figure 44a-c) TEM images and corresponding line profiles (below each image) of areas highlighted by a turquoise box. White arrows point to areas of inter-graphitic plane contrast between the graphitic plane spacing. a) and b) Images of a simple wrinkle features. c) Image of a folded wrinkle, both sides of which exhibit an inter-graphitic plane contrast. In c) line profiles 1 and 2 correspond to the numbered boxes in the image. The red arrows in the line profile for image b) highlight two sets of contrast; off-centre and central. 83
Figure 45a) TEM image of wrinkle with several examples of inter-graphitic plane contrast, highlighted by white arrows. Turquoise boxes correspond to the contrast profiles above the image. b) TEM image of the same area at different focus highlighting the change in focus across the feature. Inset shows a schematic of similar periodic change in height over a lattice. 84
Figure 46a) TEM image of large wrinkle feature with turquoise boxes highlighting numbered contrast profiles; 1 and 2 (insets). b) TEM image at lower magnification of the same area, with red arrows highlighting graphitic layers appearing and disappearing from contrast. 85
Figure 47a) Hexagonal moiré pattern observed in bi-layer graphene. b) the same moiré pattern with unit cell of superlattice highlighted and defined with superlattice constant, 4.93 nm. c) FFT of a) showing lattice rotation of 2.5° ±0.3. 88
Figure 48a) Raw data of observed linear Moiré pattern. b) Filtered image of a) to highlight linear Moiré features with a spacing of *ca*. 3.7 nm. 89
Figure 49) Reproduced with permission from Jasinski *et al*.[181] a) Hexagonal and linear moiré patterns observed in a TEM image of bi-layer graphene and b) corresponding FFT measuring a 1.3° rotation between the two layers. c) Modelling demonstration of how a distorted graphene lattice can produce a linear moiré effect without bond breaking occurring. The modelled distorted lattice is distorted by 5 °. 90
Figure 50) General procedure for the distortion of a graphene lattice in this thesis and corresponding calculation method for new unit cell parameters. The distorted graphene unit cell is highlighted in red dashed lines on the lattice. As θ is changed, *x* is also altered to result in a distorted graphene lattice. 91
Figure 51a) FFT of raw data shown in Figure 48. b) Symmetrical circle drawn over FFT to emphasise the distortion visible in both sets of lattice spots. White arrows highlight how some lattice spots do not lie within this symmetry so could therefore be evident of a distorted lattice. c) FFT angle measurements from Lattice 1, the least distorted lattice. d) FFT angle measurements from Lattice 2, the most distorted lattice. All angles in c) and d) respectively total 360°. 92
Figure 52) Modelled linear moiré pattern of distorted lattices recreated from measurements in Figure 51. Resulting linear spacing is *ca*. 4.5 nm. 93
Figure 53) Modelled linear moiré patterns with one regular graphene lattice and a) with a 2° distorted lattice overlaid, resulting in *ca.* 1.4 nm spacing, compared with b) with 1.94° distorted lattice overlaid, resulting in a *ca*. 5.2 nm spacing. 94
Figure 54a) Raw image of the sample area top left of observed linear moiré pattern. Inset shows where the linear pattern was observed in relation to a). b) Reduced FFT of raw data shows two sets of spots similar to the FFT of the linear moiré pattern. c) Masking of FFT of a) to produce d) an inverse FFT image which highlights the change in the lattice in the bottom right hand corner, highlighted by the red arrow, where the linear moiré pattern is produced. 95

Figure 55a) Raw image with red box highlighting area where FFT b) is taken. FFT implies monolayer graphene from lattice spot intensity. Inset shows intensity profile of FFT lattice spots. c) Raw image with red box highlighting area where d) FFT is taken. Extra spots in the FFT highlighted by a red arrow imply an addition of another graphene layer, off-axis from the original monolayer. 96
Figure 56a) TEM image as in Figure 55a with highlighted change in alignment of graphene lattice with the addition of a secondary layer. b-c) SEM image of a potential similar scenario; a bi-layer hexagonal domain in the grown sample with c) where two hexagonal layers are highlighted to emphasise the distortion. Distortion between the red and blue hexagons is between 1.5-10.5 °..... 98
Figure 57a) HRTEM image of an atomically bonded graphene domain boundary, reproduced with permission from ref[182] b-c) HRSTEM images of similar graphene grain boundaries, reproduced with permission from ref[87]. All images show a change in carbon ring size at the domain boundary. 102
Figure 58) Schematics and TEM images reproduced with permission from ref[165]. a) Low magnification TEM image of an area of sample. b) and c) Schematics of atomically bonded and overlapping graphene layers respectively. d) and e) TEM images of one overlapping area with one layer highlighted in yellow in e). f) TEM image of FLG with several overlapping areas (highlighted by red and yellow). g) TEM image of overlapping example with inset showing the high-resolution Moiré pattern produced on one side.....104
Figure 59) SEM image of two, on axis, hexagonal merging domains. White arrow highlights a feature which has likely resulting from the domain boundary.....107
Figure 60a) Low magnification TEM image of merging domain area. White arrow highlights area of inset which shows a wrinkle at the boundary at higher resolution where the change in graphene lattices occurs. Yellow and blue boxes correspond to where FFTs b) and c) were taken. 108
Figure 61) Schematic of potential domain boundary. 109
Figure 62) Low magnification TEM image of domain boundary. Red arrow highlights wrinkle, white arrow highlights the area where subsequent HRTEM data is obtained. It is possible to see a join here. 110
Figure 63) TEM images of potential boundary at higher magnifications. Inset in a) shows area of image b). Inset in b) shows area of image c). White arrows in a) and b) highlight region of the boundary. Image d) is the same image as c) but has highlighted a hexagonal feature which can be observed in c) equating to a *ca*. 140° angle. Graphene holes are apparent in b-d).....111
Figure 64a) TEM image of potential boundary with white dotted lines highlighting the change in direction as can be observed by eye on the image and the boundary. b) Corresponding FFT of a) showing two hexagonal lattices slightly misaligned, inset highlights the difference between two lattice spots. c-e) TEM image a) with white boxes corresponding to the relative FFT below. Insets in FFTs c) and e) correspond to spot intensity line profiles of monolayer graphene lattices.....112
Figure 65) Low magnification TEM image of domain boundary. White arrow highlights area of join, red arrow highlights large defective area which has likely resulted from this join. b) Is image a) with a white dotted line highlighting the nanoparticle contrast that connects the two areas. 114
Figure 66a) Low magnification TEM image of feature, the white arrow highlights where subsequent data is obtained. b) is image a) with hexagonal features and corresponding angles highlighted. A small red arrow highlights features that are characteristic of FLG growth. 115
Figure 67a) Low magnification TEM image of area of interest with white arrow highlighting area where TEM image b) is shown at higher magnification. White dotted lines highlight visible misorientation. c) TEM image of the boxed area in b) where a white dotted box highlights a linear feature. The turquoise box highlights the region where the contrast profile (inset) is taken which shows the periodicity present within the linear feature. d) is the corresponding FFT of TEM image b).....116
Figure 68a-c) TEM images of area of interest where white boxes highlight the areas of corresponding FFTs d-e). g) FFT of the entire image. h-j) IFFT images corresponding to positively masked sets of FFT lattice spots as highlighted in g). White arrows highlight the presence of one lattice in specific areas of the sample.....118
Figure 69a) FFT of Figure 67b. Inset shows the spot intensity line profile corresponding to the consistent monolayer lattice throughout the image. b) Schematic of possible domain boundary scenario. Red area represents the continuous monolayer. Yellow and blue hexagons represent merging graphene domains. c) SEM image of a similar feature that would be the prelude to his phenomenon, observed in a commercially available graphene sample. 119
Figure 70a) TEM image at low magnification of merging domain area. White arrow highlights first area of interest, red arrow highlights second area of interest b) the same TEM image with hexagonal angles highlighted. c) TEM image of area highlighted by larger white arrow in a), white arrows highlight the directions of the hexagonal corner in the centre of the image. This area contains nanoparticle contamination which is caused sample damage. d) Reduced FFT of image c), white arrows highlight two strong lattice spots with hexagonal symmetry.....121

Figure 71a-c) TEM images of boundary region with yellow/blue boxes corresponding to where FFTs d-f are taken. More distortion in the FFTs is highlighted from d-f by variation from the perfect circle. Yellow/blue lines on FFTs indicate how different lattices are present either side of the boundary. 122
Figure 72a) TEM image of wrinkle feature, with b) at higher magnification. Insets are number line profiles across image. c-f) FFTs of corresponding coloured boxes in image a)....123
Figure 73a) Low magnification TEM image of graphene domain boundary. White lines highlight how features equate to a hexagonal angle of 120° b) SEM image of a similar feature. c) and d) increasing magnification TEM images of the feature, with more wrinkles becoming apparent as resolution increases....125
Figure 74a) High-resolution TEM image of domain boundary. b) Same TEM image as a) with insets highlights where FFTs c-e were taken. c-e) FFTs taken from respective places on b). Blue lines highlight a lattice that is present in FFTs c-d, yellow lines highlight a lattice that is present across FFTs d-e. 126
Figure 75) Low magnification TEM image of domain boundary with the arrangement of two merging domains highlighted, showing overlapping. White arrow – points to edge of 'blue' lattice which does not match up with the straight edge due to beam catalysed degradation during imaging. Red arrow – highlights the extra buckling occuring when the two domain are joining. Inset: Schematic of possible scenario occurring. 128
Figure 76) A sample of examples of SEM images from the literature of full-coverage graphene surfaces displaying defects. a) Reproduced with permission from ref[191]. b) Reproduced with permission from ref[192]. c) Reproduced with permission from ref[145]. d) Reproduced with permission from ref[193]. e) Reproduced with permission from ref[164]. f) Reproduced with permission from ref[125]. g) Reproduced with permission from ref[194]....132
Figure 77) Schematics of hBN and graphene. Reproduced with permission from ref[198]. 133
Figure 78) Examples of SEM images (except e which is an AFM image) of hBN domains and films from the literature. a) Reproduced with permission from ref[216], hBN domains grown on Cu foil. b) Reproduced with permission from ref[220], hBN domains grown in Cu foil. c) Reproduced with permission from ref[215], monolayer hBN domain on Cu foil. d) Reproduced with permission from ref[220]. hBN domains merging on Cu foil, with grain (domain) boundaries highlighted) Reproduced with permission from ref[219]. AFM image of few-layer hBN. f) Reproduced with permission from ref[224]. Few-layer hBN film on Cu. Images c-f) show visible wrinkles in the hBN film. 134
Figure 79) Reproduced with permission from ref[233]. HRTEM image of an atomically bonded domain boundary in hBN. a) Region of interest with FFTs showing the difference in two lattices. b) atomic resolution imaging of boundary seen in a) highlighting the 5-7 membered rings at the boundary. 136
Figure 80a) SEM image of hBN film. Inset shows film at higher magnification. b) hBN film transferred to TEM grid with corresponding diffraction pattern. Images are courtesy of Vitaly Babenko and George Lane. 138
Figure 81) TEM images with corresponding FFT in the insets of a) Few-layer hBN, b) bi-layer hBN and c) monolayer hBN where a white arrow highlights the zig-zag edge structure. 139
Figure 82a) TEM image of edge of hBN flake. Inset shows magnified area where green and red arrows highlight hBN layer additions and subtractions respectively. b) shows same TEM image as in a) with corresponding reduced FFTs. Green lines highlight common lattice spots with new additional layers, whereas a red line highlights lattice spots which are not present in the top FFT. c) shows another hBN edge showing the evolving change from 7-8 layers to 2-3 layers....140
Figure 83) TEM images and corresponding line profiles of hBN examples of a) sideline periodicity b) periodicity along hBN planes, c) inter-hBN plane contrast....142
Figure 84a) TEM image of area showing a linear moiré pattern in hBN. The white box shows the area of b). b) Linear moiré patterns at higher resolution with arrows marking different spacings of two sets of linear features. c) TEM image of a) with red boxes corresponding to the areas where FFTs e-g) are taken. d) Schematic of the area demonstrating the overlapping of two lattices occurring, the left in yellow, the right in blue. e-g) FFTs from the image. The first row shows how the lattices from both left and right sides are in the central FFT. The last row shows the same FFTs with white dotted circles to demonstrate strain. White arrows highlight any areas of strain. 143
Figure 85) Two simple examples of imperfect domain boundaries in hBN. Left and right columns show different examples. a-b) Low magnification TEM images where the white arrow on b) highlights the long straight line of the boundary. c-d) TEM images at higher resolution showing boundary and red boxes where FFTs are taken. e-h) FFTs of areas either side of both boundaries where a white line on the lattice on the left FFT is shown in the right as a dotted line, demonstrating how the domains differ. 146
Figure 86) Reproduced with permission from ref[243]. Schematic of a simplified mica SFB set-up illustrating the cross-cylinder lens geometry of the silver and mica covered lenses. The semi-transparent silver mirrors allow white light interferometry to be used to measure the surface separation of the lenses using the interference fringes gained. Forces at the lens surface can be simultaneously measured by recording the deflection of a spring as the surfaces are brought together. 151

Figure 87) Schematic of MBI. Constructive interference leads to amplified, sharp signals. Destructive interference yields no signal. *n*= number of nodes present within waves, highlighted by green circles in amplified wavelengths. 152
Figure 88) Representative schematic of mica-SFB lenses demonstrating how distance between lenses is calculated. X_{M1+M2} represent mica thickness and X_A represents lens separation. R_{A+M} represent corresponding refractive indexes. 153
Figure 89) Schematic of MBI in the curved SFB set up demonstrating that the resulting fringes represent the local geometry of the interferometer. 154
Figure 90) Adapted from refs[244,245]. Force profiles showing the interaction force as a function of film thickness between mica surfaces. a) and b) are surface force profiles from two different ionic liquids. Force oscillations indicate layered structures in the liquid film. Insets show possible example structures for different film thicknesses. 155
Figure 91) Schematics of various pairs of SFB lenses. a) Conventional mica SFB depicting formation of negatively charged lens surfaces after potassium ion dissociation in solution. b) and c) SFB with one lens replaced with a gold surface holding a positive charge. The red arrow depicts how the gold surfaces exhibit increasing roughness in solution. d) The target lens set up for SFB potential control. The material on the lenses should be smooth, transparent and conductive, akin to mica but with the ability to support potential control. 157
Figure 92a) SEM image of typical FLG synthesised using the experimental procedure outlined in Table 2. b) Corresponding Raman spectrum of the as synthesised graphene on copper. No D peak at 1350 cm^{-1} is indicative of very high quality graphene. The 2D to G ratio is characteristic of FLG. 160
Figure 93) Schematic of direct epoxy transfer of graphene from Cu foil onto an epoxy covered SFB lens. The resultant graphene and epoxy on the SFB lens mimics Cu foil roughness. 161
Figure 94) Schematic of PMMA/epoxy transfer of graphene from Cu foil onto a SFB lens. Step 2 demonstrates how the large roughness from the Cu foil is decreased by using the PMMA support, but still yields a rough surface on the SFB lens. 161
Figure 95a) AFM scan of transferred graphene to a SFB lens using the transfer technique outlined in Figure 94. b) Corresponding line profile of red line in a) showing positive protrusions from graphene wrinkles equating to *ca*. 20 nm 162
Figure 96) Schematic of how positive protrusions on a pair of SFB lenses demonstrating how such a scenario leads to multiple contact points upon bringing lenses closer together. 162
Figure 97a) Diagram of evaporated Cu/mica substrates b) Photograph of an example Cu/mica substrate. 164
Figure 98) SEM images of prepared Cu/mica substrates. a) Cu/mica substrates as received from evaporation, before annealing. b) Cu/mica substrates post annealing. Cu grains become larger with annealing, with some areas of hole formation as highlighted by the white arrow in b). 165
Figure 99) Reproduced with permission from ref[265]. Temperature and time scheme difference between Cu foil and Cu thin film growth. 167
Figure 100) Key SEM images from experiments conducted in Table 3. d) Raman spectra from experiment set No. 4 showing graphitic peaks indicating FLG deposits. 170
Figure 101a-d) Key SEM images from Table 4 experiments yielding Cu features. e) Corresponding Raman spectrum showing a large D peak indicating a highly defective graphitic material 171
Figure 102a) SEM of 700nm Cu experiment yielding full-coverage FLG with Cu features b) Raman spectra of product in experiment set No. 12 (see Appendix D) showing FLG with D peak. 173
Figure 103) SEM images of Cu features at various tilt angles as specified in the top right corner of each image. a) 0° tilt, b) 50° tilt and c) and d) 70° at different magnifications. Cu features appear to be coming out of a very smooth surface. e) higher-magnification image of area highlighted by white box in d), white arrows highlight holes that are visible next to some Cu features. 174
Figure 104) SEM images of a-d) helium implanted Cu bubble formation, reprinted from Galindo *et al*.[268] and e-f) similar Cu features from Cu/Mica experiments for comparison. 176
Figure 105) Schematic demonstrating electropolishing of Cu foil showing increased mass transport away from positive asperities, resulting in their preferential dissolution to create a smoother surface. 178
Figure 106) AFM scans of Cu foils a) before electropolishing and b) after electropolishing. With thanks to Christian van Engers for AFM operation 179
Figure 107a) Typical SEM image of high-quality FLG on electropolished foils and b) corresponding Raman spectrum with very small D peak. 179
Figure 108a-c) SEM images of contamination on electropolished Cu foils. d) Reproduced with permission from Zhang et al.[105]. A SEM image of graphene on an electropolished Cu foil showing the extent of contamination present in the literature. 180
Figure 109) Schematic of Cu pressing experiment. Three layers of mica were placed either side of the Cu foil. The red arrows represent the force acting upon the materials during pressing. 181

Figure 110a) Photograph of pressed Cu foil using larger mica pieces, resulting in non-uniform pressing. Green arrows highlight well pressed areas with mirror finishes. b) Photograph of pressed Cu foil using a small mica piece which caused Cu to break around the pressing area. Blue arrow highlights very smooth, uniform pressed area with mirror finish. c) Optical image of foil similar to that shown in a), showing the clear elimination of Cu processing lines which are highlighted by black arrows in the un-pressed area of the foil. d) 1 x 1μm AFM scan of pressed Cu foil with mirror finish showing no sharp features and a maximum change in roughness of <20 nm. 183
Figure 111) Comparing graphene growth on pressed Alfa Aesar and Goodfellow Cu foils using experimental parameters outlined in Table 2. a-b) SEM images of growth on pressed Alfa Aesar 99.8% Cu foil. Graphene coverage is generally lower and there are areas of daggered graphene growth. c) SEM image of growth on pressed Goodfellow 99.9% Cu foil. SEM shows full coverage FLG growth. d) Raman spectrum of sample c) showing evidence of FLG with a small D peak indicative of good quality graphene. 184
Figure 112) SEM images of daggered growth on pressed Alfa Aesar copper foils. 185
Figure 113) Higher magnification SEM of FLG grown on pressed Goodfellow Cu foil. SEM shows a high level of wrinkles from the FLG growth. 186
Figure 114a) Schematic of as synthesised FLG on Cu foil highlighting presence of roughness in FLG from synthesis. b) SEM image of typical FLG used in this study with white arrow highlighting a typical wrinkle that would cause roughness as represented in schematic a). 189
Figure 115) Transfer schematic of the new ultra-flat transfer technique. The key new step is placing the PMMA/FLG stack onto freshly cleaved mica. 190
Figure 116a) Schematic of two sets of lenses showing negative protrusions from new transfer method. The lower set of lenses shows how it is possible to obtain a contact spot with no interfering roughness. b) and c) AFM images with corresponding line profiles of the red lines across each image, b) is a 5 μm scan including a negative protrusion. c) is a 1 μm scan showing <1nm RMS roughness. 191
Figure 117a) Schematic of proof-of-principle SFB experiment using $KClO_4$ and 210 mV. b) Example of interference fringes obtained from the experiment, from which a surface force profile is obtained. 193
Figure 118) Surface force profile of experimental set up as shown in Figure 117. The blue triangles show the system at open circuit, red circles show the system at a -210 mV surface potential, green triangles show the system returned to open circuit after the -210 mV potential had been applied. The black line corresponds to the theoretically predicted force profile for a 0.6 mM 1:1 electrolyte solution with -210 mV surface potential. 194
Figure 119) SEM image of FLG "spiral" domain 202
Figure 120) Solid precursor synthesis on Cu/mica substrates: preliminary results. a-d) SEM images of carbon deposits on Cu/mica substrate. e) Corresponding Raman spectrum showing amorphous carbon peaks. 204
Figure 121) Schematic of a SEM. Reproduced from ref[291] 216
Figure 122) Schematic of three types of scattering with light. Reproduced from ref[293] 217
Figure 123) Schematic of an AFM. Reproduced from ref[295] 218
Figure 124) Schematic of a TEM. Reproduced from ref[296] 219
Figure 125) Examples 6 and 7 of imperfect merging graphene domains. 223
Figure 126) Examples 8 and 9 of imperfect merging graphene domains. 224
Figure 127) Examples 10 of imperfect merging graphene domain. 225
Figure 128a, b, d, e, g, h) Key SEM images from Table 5 showing mica holes and Cu features. c, f, i) Corresponding Raman spectra from experiment set No.s 6, 8 and 9 showing defective graphitic deposits are present. 228
Figure 129a-c) Key SEM images from Table 6 showing consistent appearance of Cu features. d) Raman spectra of product in experiment set No. 12 showing few-layer graphene with D peak. 230
Figure 130) EDX spectra from sample from experiment set No. 12. Left images show an SEM image with red areas highlighting where EDX spectra were taken. On the right shows corresponding EDX spectra from a-c, Cu and Fe peaks are highlighted. With thanks to Gabriella Chapman for aiding in the acquirement of this data. 231
Figure 131) Key SEM images from Table 7, annealing experiments depicting both Cu features and smaller holes in Cu thin film in experiment set No. 17. 233
Figure 132) SEM images of examples of Cu features where copper appears to come out of plane. 234
Figure 133) EBSD data from Cu features. a) and b) are SEM and EBSD images respectively at a lower magnification and c) and d) are SEM and EBSD images respectively at a higher magnification of a flatter Cu feature. e) is a quality of data point map from scan d) demonstrating that due to the sample's roughness, data from the roughest areas may not be reliable. With thanks to Dr. David Collins for EBSD operation. 235

Table 1) A summary of graphene synthesis methods using information from refs[54,63,64,66–69,71–74,77]. 18
Table 2) General experimental procedure for full-coverage, few-layer graphene synthesis on standard Cu foils. 159
Table 3) Experimental details for 500 nm Cu/Mica substrates, experiment set No.s 1-4. Initial graphene nucleation was achieved in experiment set No. 4.....168
Table 4) Experimental details for the first 600 nm Cu/mica substrate experiment set No. 5. Cu features as well as graphitic deposits were observed. 171
Table 5) Experimental details for first shift scheme experiments; experiment set No.s 6-9. Cu features were still prevalent.....226
Table 6) Experimental details of first experiments with 700 nm Cu/mica substrates; experiment set No.s 10-12. Cu features were still present.....229
Table 7) Experimental details of the annealing experiments conducted to understand Cu feature formation; experiment set No.s 13-17. 232

9 Appendix

9.1 Appendix A: Further explanations of experimental techniques

Appendix A details the basic concepts behind the characterisation techniques used in this thesis (described initially in Chapter 2).

Scanning electron microscopy[290]

Scanning electron microscopy is a technique where a high energy electron beam is rastered over the surface of a sample (see schematic in Figure 121). The interaction between the electron beam and the sample produces multiple signals. The intensity of these various signals is measured as a function of the beam location, yielding spatially resolved information. For SEM imaging, the useful signal derives from secondary electrons. Secondary electrons originate when the electron beam interaction has caused electrons within the sample to gain energy, exceeding their work function. They are therefore "knocked out" of the sample into the SEM chamber. A small positive field then accelerates them to a detector. The intensity of this signal is dependent upon multiple factors including sample topography. An SEM operating in secondary electron mode is thus able to image topographic features.

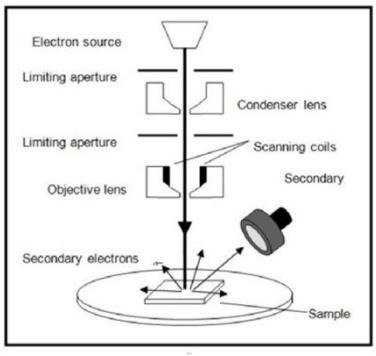


Figure 121) Schematic of a SEM. Reproduced from ref[291]

Secondary electron emission is surface specific (the penetration depth of secondary electrons is approximately 100 nm) and hence produce solely topographic contrast in images.

Electron back scattered diffraction[290]

Used in conjunction with SEM, EBSD takes advantage of the sample interaction with the electron beam during ion bombardment. EBSD concerns the analysis of back-scattered electrons (BSE) which have a much higher interaction volume (*ca*. 1 μm) compared to the secondary electrons used in SEM imaging. Therefore, information can be obtained from a larger proportion of the sample than just the surface. BSE have a very high energy and hence some can exit the sample even at this larger penetration depth. If the, essentially elastically scattered, BSE exit the sample near to the Bragg angle, they diffract to form Kikuchi lines which are characteristic of specific lattice orientations. If Kikuchi lines are adequate in signal from several point measurements, a reliable picture of crystallographic orientation can be produced

Raman spectroscopy[292]

Raman scattering describes the inelastic scattering of light as shown schematically in Figure 122 (compared to elastic Rayleigh scattering). Photons can gain or lose energy and hence a resultant wavelength can be increased or decreased (anti-Stokes and Stokes Raman scattering respectively).

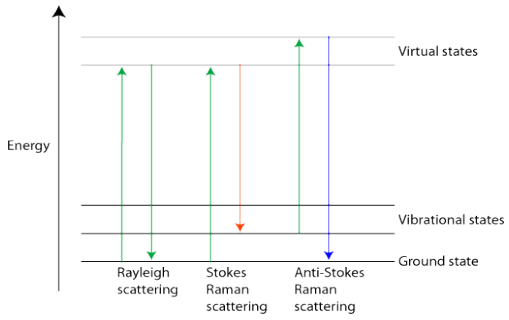


Figure 122) Schematic of three types of scattering with light. Reproduced from ref[293]

Stokes scattering exhibits a greater intensity than anti-Stokes and therefore the spectrum that is primarily used in Raman characterisation relies on Stokes signal (this is due to the relative populations in each state initially).

Raman spectroscopy is therefore a technique which is based on the interaction between a laser and the vibrational modes in a sample. Different chemical bonds within a sample will have different, characteristic, vibrational modes, which will be able to absorb, or emit, characteristic

amounts of energy. The energy of the transmitted laser will only be able to change by amounts determined by these vibrational modes. The energy spectra of the transmitted laser will thus be dependent on the bonding types present in the material. Hence Raman spectroscopy can be used as a technique to produce a "fingerprint" analysis of a sample.

Atomic force microscopy[294]

AFM works on the principle of a cantilever's interaction with the surface of a sample. A cantilever is scanned over a sample surface, and is deflected depending on the sample's topography. The cantilever's deflection is detected by a laser which is reflected from the cantilever's tip onto a photodiode (see Figure 123). As cantilever tips can be synthesised to terminate in a single atom, AFM can gain atomic resolution images.

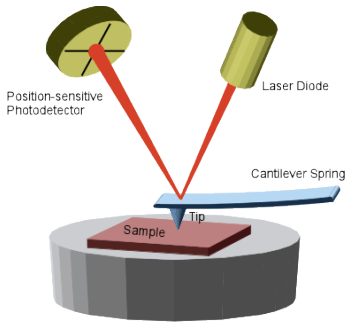


Figure 123) Schematic of an AFM. Reproduced from ref[295]

Transmission electron microscopy[134]

TEM is similar to SEM with the difference that a focussed beam of electrons is transmitted through a thin sample, as opposed to SEM which measures the backscattered electrons. The focussed electron beam interacts with the thin sample and produces a resultant beam of varying energies which is seen as contrast in a TEM image.

TEM uses higher accelerating voltages compared to SEM and therefore a higher resolution can be obtained (due to the de Broglie relation). TEMs also require more careful alignment of the electron beam to achieve interpretable resolutions. Figure 124 shows a schematic of TEM where several lenses are shown. Condenser lenses ensure the formation of an initial electron beam, and the objective lenses focus the beam that has passed through the sample. Projector lenses ensure that this information is expanded onto the imaging surface (e.g. a phosphor screen).

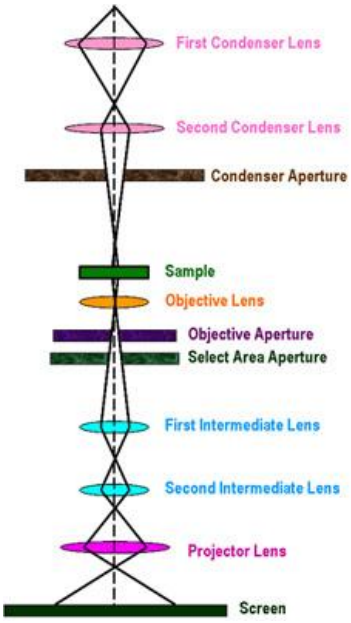


Figure 124) Schematic of a TEM. Reproduced from ref[296]

As TEM analysis utilises the beam's interaction through the entirety of the sample, TEM can provide details on a sample's composition such as crystallinity information, areas of stress and atomic defect sites.

9.2 Appendix B: NanoBud publication

ChemComm

RSC Publishing

COMMUNICATION

View Article Online
View Journal | View Issue

In situ engineering of NanoBud geometries†

Rebecca J. Nicholls,* Jude Britton, Seyyed Shayan Meysami, Antal A. Koós and Nicole Grobert

Cite this: *Chem. Commun.*, 2013, **49**, 10956

Received 8th August 2013,
Accepted 14th October 2013

DOI: 10.1039/c3cc46064a

www.rsc.org/chemcomm

Published on 14 October 2013. Downloaded by University of Oxford on 01/11/2013 11:26:36.

NanoBuds exist in a variety of stable structures. Our studies show that engineering NanoBud geometries is indeed possible and we visualise the transformation of one Nanobud geometry to another using *in situ* aberration corrected imaging techniques. Such NanoBuds are precursors for generating nanotube junctions which could be used in composite and electronic applications.

Carbon nanostructures, such as carbon nanotubes, graphene and fullerenes, are the focus of world-wide research with the aim of tailoring their properties for use in dedicated applications ranging from electronics[1,2] to drug delivery devices.[2] Carbon NanoBuds, first characterised in 2007 by Nasibulin *et al.*,[3] combine two of these carbon allotropes into one structure and consist of single-wall carbon nanotubes (SWCNTs) with fullerenes covalently bonded to the outer surface. NanoBuds exhibit enhanced field-emission properties[3] and it has been suggested that the fullerenes could act as anchors for SWCNTs providing more efficient reinforcement in composite materials.[4] Nasibulin *et al.*[3] theoretically predicted several different stable NanoBud configurations. In this work we show that the NanoBud geometry can be changed from one configuration to another. We use aberration-corrected transmission electron microscopy (TEM) to monitor *in situ* the evolution of NanoBuds and observe that electron beam irradiation can cause the fullerenes to transform into tube-like branches attached to the nanotube wall. The resulting nanostructure has potential uses in composite materials and as a precursor for the production of nanotube junctions.

We synthesised samples of SWCNTs which include NanoBuds using an aerosol-assisted chemical vapour deposition (CVD) setup described elsewhere.[5–10] An aerosol of toluene with 5 wt% ferrocene was used as the carbon source and the growth conditions were optimised to maximise the NanoBud yield. The synthesis was carried out at 800 °C for 15 minutes after which sample was collected on a substrate placed at the end of the reactor. Without any post-synthesis treatment, the deposit on the substrate was collected, dispersed in acetone, sonicated and transferred onto TEM grids.

The sample was imaged using an aberration-corrected JEOL 2200 MCO operated at 80 kV in order to reduce the knock-on damage caused by the electron beam.[11] Imaging of the NanoBuds, which can stretch unsupported over relatively large distances, is challenging due to sample vibrations. TEM imaging of the NanoBuds (Fig. 1) showed SWCNTs with fullerenes of various sizes attached which is in agreement with previous work on carbon NanoBuds.[3,12–14]

Defect-free SWCNTs are generally found to be stable when imaged with TEM using a microscope acceleration voltage of 80 kV,[11] but SWCNTs with defects[15] and fullerenes[16–18] are still susceptible to damage under these conditions. We observed that the structure of the NanoBuds changed with time and the evolution of one particular fullerene (marked by an arrow in Fig. 1) is shown in Fig. 2. The electron beam provides the sample with enough energy to allow the fullerene to evolve into a tube-like structure (Fig. 2f) before collapsing entirely (Fig. 2h). The carbon used to fuel the growth of the fullerene is likely to be released from the nanotube in the immediate vicinity of the fullerene (where the nanotube wall has disappeared, marked by an arrow in Fig. 2f). An additional supply of carbon could originate from mobile fullerene fragments or carbon structures on the surface of the nanotube. Unlike the other structures also attached to the nanotube, the nanotube away from the immediate vicinity

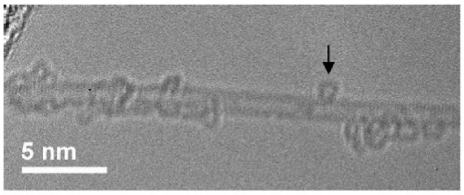


Fig. 1 Transmission electron micrograph of a typical NanoBud. The arrow indicated a single isolated fullerene attached to the side-wall of the single-wall carbon nanotube.

Department of Materials, University of Oxford, Oxford OX1 3PH, UK.
E-mail: rebecca.nicholls@materials.ox.ac.uk

† Electronic supplementary information (ESI) available. See DOI: 10.1039/c3cc46064a

This journal is © The Royal Society of Chemistry 2013

Published on 14 October 2013. Downloaded by University of Oxford on 01/11/2013 11:26:36.

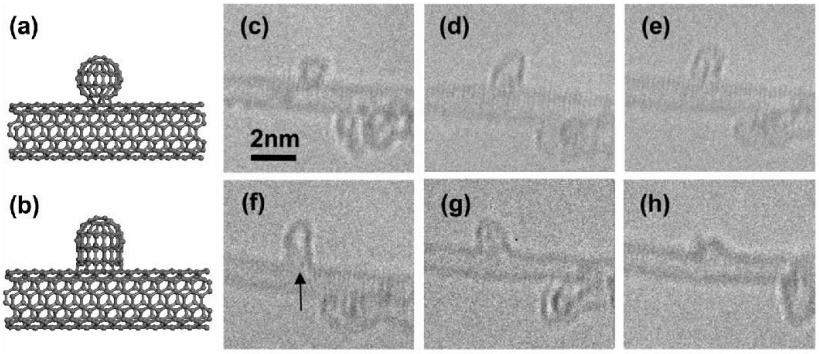


Fig. 2 Schematics showing a fullerene attached to a diagram (a) and a transient structure of a short, capped nanotube attached to a larger nanotube (b). TEM images (c–h) showing the evolution of a carbon NanoBud under the electron beam.

of the fullerene appears unaffected by the transformation and remains straight until the tube-like structure starts to collapse. The evolution seems to occur without the presence of metal catalyst particles or atoms, although single metal atoms may be difficult to identify.

Füller and Banhart[17] observed the behaviour of fullerenes when irradiated by an electron beam and found that whilst C_{60} fullerenes in a crystal were damaged very easily and tended to coalesce, single fullerene molecules formed by beam damage to graphite were very stable. They suggested that the mobile single fullerenes could repair the damage caused by the beam using carbon atoms weakly bonded to the defective graphite surface on which they were sitting. This argument is supported by the observation by Koshino *et al.*[19] that C_{60} molecules encapsulated inside a nanotube (where no weekly bonded carbon atoms would be expected to reside) damage at a similar rate to C_{60} molecules in a crystal. In NanoBuds the fullerenes are not mobile as they are covalently bonded to the outer surface of a nanotube.[3] As a result, the fullerenes in a NanoBud would be expected to be susceptible to damage from the beam since the supply of freely available carbon atoms on a pristine SWCNT is limited. Furthermore, for these anchored fullerenes to obtain carbon atoms to repair the damage caused by the electron beam, any weekly bonded carbon atoms would need to migrate over the surface of the nanotube towards the fullerene and are likely to get trapped by the presence of large amorphous carbon structures on the outer surface on the nanotube instead.

Chamberlain *et al.*[18] have reported the formation of nano-protrusions on SWCNTs resulting from the reaction of encapsulated fullerenes with the surrounding nanotube. In that case, the reaction was catalysed by rhenium atoms bonded onto the outside of the fullerene cages. The resulting protrusion is a stable feature, similar in appearance to a partial fullerene grafted onto the SWCNT.

Atomistic simulations carried out by Ding *et al.*[20] showed that fullerenes trapped inside a nanotube coalesce *via* the motion of defects. In addition, experimental work carried out on double-wall carbon nanotubes showed that defects, such as large vacancy clusters, initiate the coalescence of these nanotubes at room temperature.[21] The evolution of the NanoBuds observed here is likely to have been initiated by the production of defects by the electron beam.

Fig. 2 shows how a fullerene evolves into a tube-like structure consisting of a partial fullerene bonded to a defective nanotube and several groups have investigated such structures theoretically. Nasibulin *et al.*[3] used density functional theory to examine imperfect fullerenes covalently bonded to defective SWCNTs and Wu and Zeng[22] compared several models of full or fragmented fullerene molecules fused onto a graphene sheet. These theoretical investigations suggest that whilst a tube-like structure similar to that seen in Fig. 2g could be stable, the stability would depend on the defects present. However, both sets of modelling work were carried out for static structures, whereas we have observed a dynamic process. The tube-like structure formed may be initially stable but as the irradiation continues further defects form which destabilise it. By irradiating samples of NanoBuds with a specific dose, it may be possible to freeze the evolution of the fullerenes and hence create stable, protruding tube-like structures.

Electron beam irradiation, without the presence of a catalyst, triggers fullerenes to bond and coalesce with the nanotube wall due to the formation of defects which induce a change in the electronic structure of the fullerenes before any visual change can be observed. This change in electronic structure can be monitored *in situ* using electron energy loss spectroscopy (EELS) which probes the unoccupied density of states (DOS). Therefore, EELS can be used to differentiate between visually similar fullerenes by tracking the changes in the bonding.[23,24] Nicholls[25] showed that successive EELS spectra from C_{60} fullerites revealed that the electron beam irradiation indeed induces a change in the electronic structure of the fullerite.

The potential uses of NanoBuds include composites where the fullerenes may provide extra anchorage for the SWCNT in the matrix.[4] Therefore these new, engineered NanoBuds could provide more efficient anchorage as there is a greater number of bonds between the protrusions and the nanotube in the irradiated structures than for the initial NanoBud. In addition, several authors have proposed electron beam irradiation as a method of producing nanotubes junctions.[21,26] The observed

Published on 14 October 2013. Downloaded by University of Oxford on 01/11/2013 11:26:36.

evolution reported here indicates that NanoBuds may be preferred to pristine SWCNTs as a starting material for junction production. Currently NanoBuds form a relatively small percentage of the nanotubes synthesized, therefore in order for any of these applications to become viable, the scale-up of the production of NanoBuds must first be investigated.

In summary, we have reported experimental evidence of a NanoBud transforming from one geometry to another. Using aberration corrected microscopy, we have observed a fullerene bonded to a SWCNT changing into a tube-like structure in a process which is likely to be driven by the creation of defects by the electron beam. The structures created have potential uses in composites and the evolution observed demonstrates that NanoBuds have the potential to act as a starting material for nanotube junction formation *via* irradiation methods.

We are grateful to the The Royal Society, the European Research Council (ERC) (Starting Grant ERC-2009-StG-240500 DEDIGROWTH and Proof of Concept grant ERC-2012-PoC 309786 DEVICE), the European Community's Seventh Framework Programme (FP7/2007-2013): the Marie Curie CONTACT Project under grant agreement no. 238363 and the Engineering and Physical Sciences Research Council (EPSRC Pathways to Impact Awards) for financial support.

Notes and references

1 K. S. Novoselev, V. I. Fal'ko, L. Colombos, P. R. Gellert, M. G. Schwab and K. Kim, *Nature*, 2012, **490**, 192–200.
2 A. Hirsch, *Phys. Status Solidi B*, 2006, **243**, 3209–3212.
3 A. G. Nasibulin, P. V. Pikhitsa, H. Jiang, D. P. Brown, A. V. Krasheninnikov, A. S. Anisimov, P. Queipo, A. Moisala, D. Gonzalez, G. Lientschnig, A. Hassanien, S. D. Shandakov, G. Lolli, D. E. Resasco, M. Choi, D. Tománek and E. I. Kauppinen, *Nat. Nanotechnol.*, 2007, **2**, 156–161.
4 X. Wu and X. C. Zeng, *ACS Nano*, 2008, **2**, 1459–1465.
5 A. A. Koós, M. Dowling, K. Jurkschat, A. Crossley and N. Grobert, *Carbon*, 2009, **47**, 30–37.
6 A. A. Koós, F. Dillon, E. A. Obraztsova, A. Crossley and N. Grobert, *Carbon*, 2010, **48**, 3033–3041.
7 A. A. Koós, R. J. Nicholls, F. Dillon, K. Kertész, L. P. Biró, A. Crossley and N. Grobert, *Carbon*, 2012, **50**, 2816–2823.
8 A. A. Koós, F. Dillon, R. J. Nicholls, L. Bulusheva and N. Grobert, *Chem. Phys. Lett.*, 2012, **538**, 108–111.
9 S. S. Meysami, F. Dillon, A. A. Koós, Z. Aslam and N. Grobert, *Carbon*, 2013, **58**, 151–158.
10 S. S. Meysami, A. A. Koós, F. Dillon, Z. Aslam and N. Grobert, *Carbon*, 2013, **58**, 159–169.
11 B. W. Smith and D. E. Luzzi, Electron Irradiation Effects in Single Wall Carbon Nanotubes, *J. Appl. Phys.*, 2001, **90**, 3509–3515.
12 A. G. Nasibulin, A. S. Anisimov, P. V. Pikhitsa, H. Jiang, D. P. Brown, M. Choi and E. I. Kauppinen, *Chem. Phys. Lett.*, 2007, **446**, 109–114.
13 Y. Tian, D. Chassaing, A. G. Nasibulin, P. Ayala, H. Jiang, A. S. Anisimov and E. I. Kauppinen, *J. Am. Chem. Soc.*, 2008, **130**, 7188–7189.
14 Y. Tian, D. Chassaing, A. G. Nasibulin, P. Ayala, H. Jiang, A. S. Anisimov, A. Hassanien and E. I. Kauppinen, *Phys. Status Solidi B*, 2008, **245**, 2047–2050.
15 T. Susi, J. Kotakoshi, R. Arenal, S. Kurasch, H. Jiang, V. Skakalova, O. Stephan, A. V. Krasheninnikov, E. I. Kauppinen, U. Kaiser and J. C. Mayer, *ACS Nano*, 2012, **6**, 8837–8846.
16 F. Banhart, *Rep. Prog. Phys.*, 1999, **62**, 1181–1221.
17 T. Füller and F. Banhart, *Chem. Phys. Lett.*, 1996, **254**, 372–378.
18 T. W. Chamberlain, J. C. Meyer, J. Biskupek, J. Leschner, A. Santana, N. A. Besley, E. Bichoutskaia, U. Kaiser and A. N. Khlobystov, *Nat. Chem.*, 2011, **3**, 732–737.
19 M. Koshino, K. Suenaga and E. Nakamura, *Microsc. Microanal.*, 2006, **12**, 586–587.
20 F. Ding, Z. Xu, B. I. Yakobson, R. J. Young, I. A. Kinloch, S. Chu, L. Deng, P. Puech and M. Monthioux, *Phys. Rev. B*, 2010, **82**, 041403.
21 A. Nie, P. Wang, N. Wang and S. X. Mao, *Nanotechnology*, 2010, **21**, 245302.
22 X. Wu and X. C. Zeng, *Nano Lett.*, 2009, **9**, 250–256.
23 R. J. Nicholls, D. Nguyen-Manh, D. J. H. Cockayne and S. Lazar, *Chem. Phys. Lett.*, 2009, **470**, 116.
24 S. M. Lee, R. J. Nicholls, D. Nguyen-Manh, D. G. Pettifor, G. A. D. Briggs, S. Lazar, D. A. Pankhurst and D. J. H. Cockayne, *Chem. Phys. Lett.*, 2005, **404**, 206.
25 R. J. Nicholls, D.Phil thesis, *Electron energy loss spectroscopy of fullerene materials*, University of Oxford, 2006.
26 M. Terrones, F. Banhart, N. Grobert, J.-C. Charlier, H. Terrones and P. M. Ajayan, *Phys. Rev. Lett.*, 2002, **89**, 075505.

This journal is © The Royal Society of Chemistry 2013

9.3 Appendix C: Five further examples of imperfect merging domains

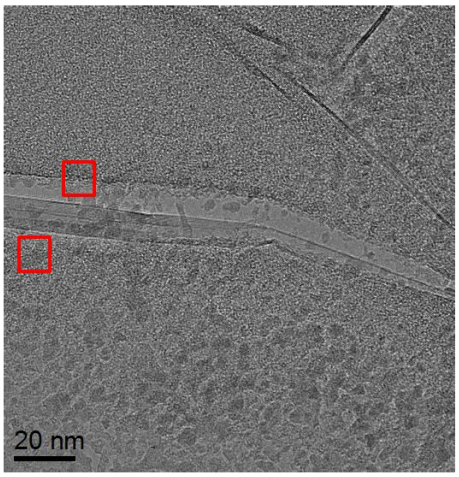
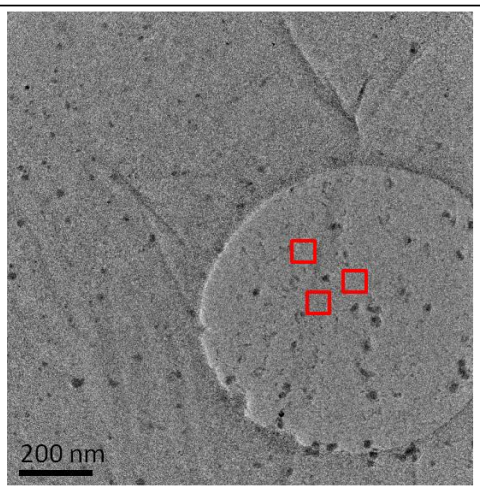
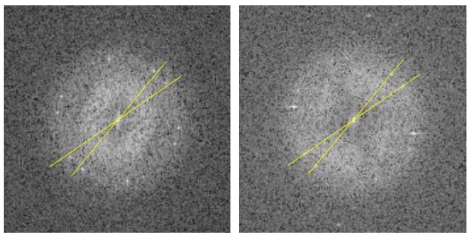
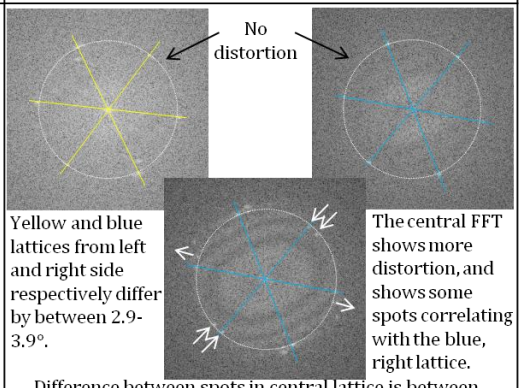
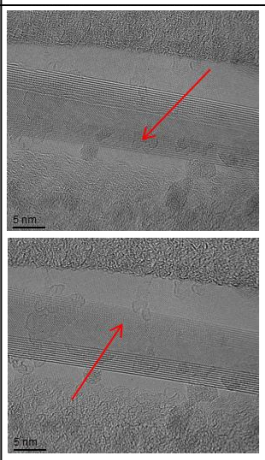
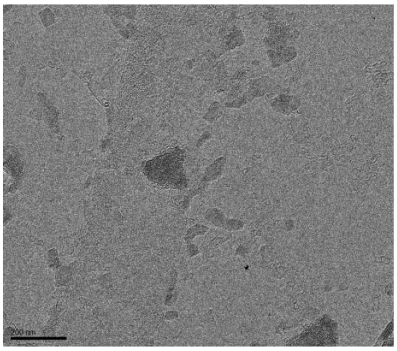
No.	6	7
Representative image with red boxes highlighting areas where FFTs are taken		
FFT Evidence	Top Bottom  Yellow lines highlight how lattice spots from the bottom FFT do not match with the FFT pattern from the top lattice. Rotation between the lattices was measured to be between 3.8-4.9°.	 Yellow and blue lattices from left and right side respectively differ by between 2.9-3.9°. The central FFT shows more distortion, and shows some spots correlating with the blue, right lattice. Difference between spots in central lattice is between 8.4-9.7°.
Further analysis or information	 Zooming into the area where the FFTs were taken; the feature, which consists of ca. 8 layers either side, comes into focus at distinctly different heights. The images shown here show both the bottom and top features in focus in the two images, highlighted by red arrows. The difference in height between the images is ca. 20 nm.	 Central feature is very parallel, but is also connected with an area of defects above the hole in lacy carbon as seen in the first image. It could be possible that the domain boundary has caused thesis additional defects.
Description	The FFT implies that the image shows two different graphene domains above and below the wrinkle feature. On closer look at this feature, two "edges" come into focus 20nm in height from each other. This could imply an overlap of FLG, as in the schematic below. 	It is possible that the central feature is caused by a domain boundary. Either side of the feature shows a different FFT. Visually, the central feature resembles an overlap, however, the FFT from this area does not match exactly with the lattices either side. However, the central feature still shows two sets of spots, one which closely correlates to the right hand lattice. In addition, the central FFT patterns exhibit distortion. It could therefore be hypothesised that a domain overlap causes a distortion in both lattices, much like what is observed in the case of what causes linear Moiré patterns.

Figure 125) Examples 6 and 7 of imperfect merging graphene domains.

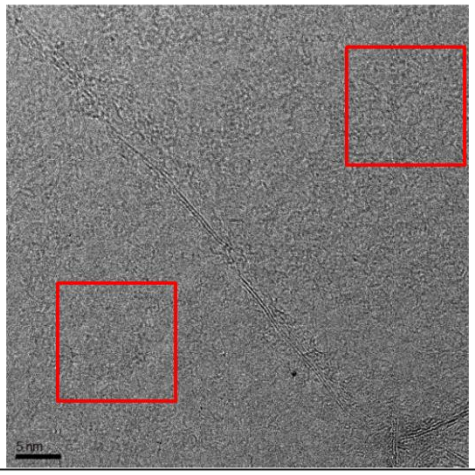
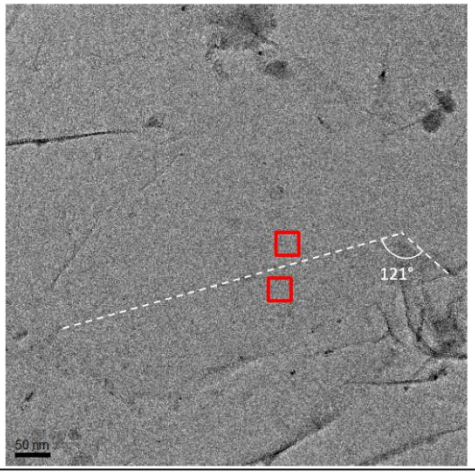
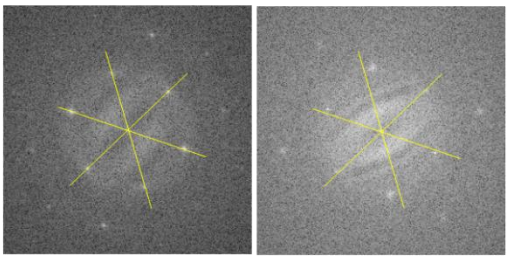
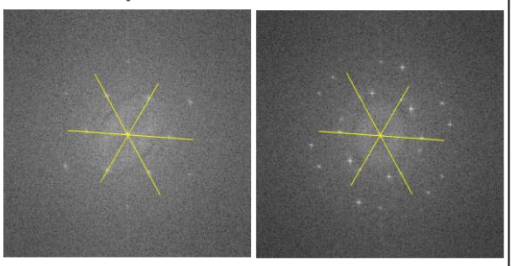
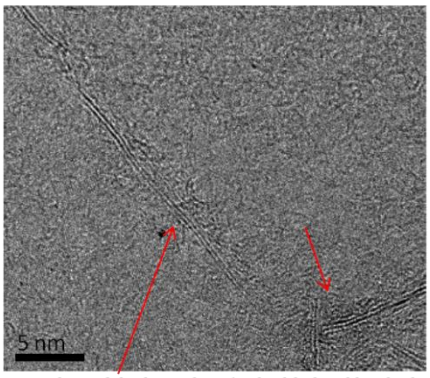
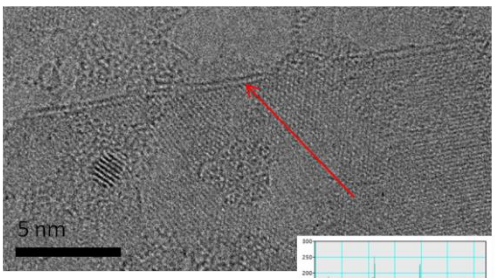
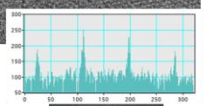
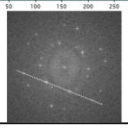
No.	8	9
Representative image with red boxes highlighting areas where FFTs are taken		
FFT Evidence	Left Right  Yellow lines highlight how lattice spots from the left FFT do not match with the right hand lattice. Rotation between the lattices was measured to be between 1.4-8.2°.	Top Bottom  Yellow lines highlight how lattice spots from the top FFT are also seen in the bottom FFT, with another set of lattice spots. Rotation between the lattices in the bottom FFT was measured to be ca. 18.2°.
Further analysis or information	 The main line of the boundary (as highlighted by the long red arrow) was observed for more than 200 nm, terminating in the cluster of wrinkles (small red arrow.)	   Red arrow highlights boundary. Line profiles of both top and bottom FFTs indicate that each set of lattice spots corresponds to monolayer graphene. The line profile of the bottom lattice is shown.
Description	A low magnification image was not shown as the contrast of the main boundary was difficult to see. However, was it clear from the FFT evidence is that a defect exists where two different graphene boundaries meet. The defect appears as a wrinkle feature that is observed for over 200 nm and is likely the case of an additional cluster of wrinkles at the base of the image.	This example seems to indicate the a domain boundary that exists as an overlap. At low magnification, a hexagonal angle can be observed and the boundary is observable between the two monolayer domains. The overlap was observed to continue for over 200 nm.

Figure 126) Examples 8 and 9 of imperfect merging graphene domains.

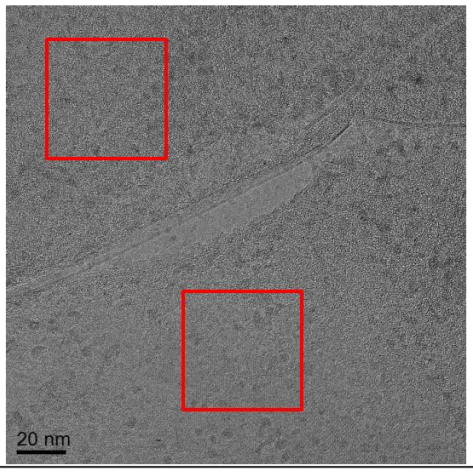
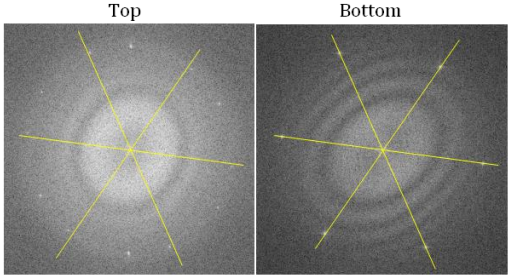
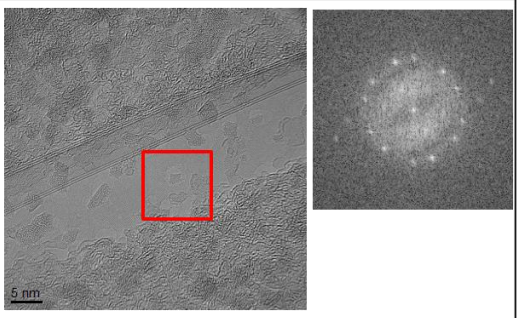
No.	10
Representative image with red boxes highlighting areas where FFTs are taken	
FFT Evidence	Top Bottom  Yellow lines highlight how lattice spots from the bottom FFT are slightly off axis from one set of spots in the top FFT. The difference between these spots is between 1.4-2.8°. Rotation between both lattices on the top FFT was measured to be ca. 24. 1°.
Further analysis or information	 At higher resolution, an FFT was taken from just below the feature, as shown in the red box above. This FFT corresponds to the top FFT pattern. It was observed that the bottom FFT pattern began within the contaminated area as highlighted by the red arrow.
Description	The difference between the initial top and bottom FFTs indicate that this is a domain boundary. From further FFT analysis, it seems that the dominant defect appears just after the boundary. It is possible that this wrinkle defect, and others wrinkles as shown in the first image, were caused by the merging domain.

Figure 127) Examples 10 of imperfect merging graphene domain.

9.4 Appendix D: Additional information from Chapter 6: Approach 2: Cu/mica thin film synthesis.

Table 5 shows the first set of experiments that employ the "shift" scheme, also using samples of 600 nm Cu.

No.	Cu thickness	Logistics	Annealing	Growth	SEM	Raman
6	600 nm Cu	Cu on bottom	> **2 hour 700°C under 500 H_2** > **SAMPLE SHIFTED OUT OF FURNACE** > Gradual increase to 900°C over ca. 20 minutes still under 500H_2 > **SAMPLE SHIFTED BACK IN**	> **15 mins** 900°C > 20 CH_4, 100H_2	Graphene-like deposits on Cu Abundant mica holes	Multilayer graphene peaks Some areas of amorphous carbon
7	600 nm Cu	Cu on bottom	> **30 min** 700°C under 500 H_2 > SAMPLE SHIFTED OUT OF FURNACE > Gradual increase to 900°C over ca. 20 minutes still under 500H_2 > SAMPLE SHIFTED BACK IN	> **20 mins** 900°C > **15 CH_4,** 100H_2	Cu features Graphene-like deposits on Cu No mica holes	Amorphous carbon on Cu Cu features: Sometimes 3 graphitic peaks, but poor 2D peak
8	600 nm Cu	Cu on bottom	> **1 hour** 700°C under 500 H_2 > SAMPLE SHIFTED OUT OF FURNACE > Gradual increase to 900°C over ca. 20 minutes still under 500H_2 > SAMPLE SHIFTED BACK IN	> 20 mins 900°C > 15 CH_4, 100H_2	Cu features increased Full coverage graphene-deposits No mica holes	3 graphitic peaks, sometimes without D peak (higher quality) on Cu features
9	600 nm Cu	Cu on bottom	> **30 min** 700°C under 500 H_2 > SAMPLE SHIFTED OUT OF FURNACE > Gradual increase to **880°C** over ca. 20 minutes still under 500H_2 > SAMPLE SHIFTED BACK IN	> 15 mins **880°C** > 15 CH_4, 100H2	Cu features Full coverage graphene-deposits No mica holes	3 graphitic peaks, but poor 2D

Table 5) Experimental details for first shift scheme experiments; experiment set No.s 6-9. Cu features were still prevalent.

The first experiment set, No. 6, was an ambitious attempt at a longer annealing stage (2 hours) prior to growth, in the thought that the shift scheme would decrease the time at high temperature enough to allow this annealing time. A longer annealing time is likely to make the Cu substrate cleaner with a larger grain size. Unfortunately, significant mica holes were again observed (see Figure 128a,b). Although graphitic material was gained (see Raman Figure 128c), the mica holes made the long annealing time not useful for SFB experiments.

However, if the annealing time was kept the same (30 minutes), as expected, significantly limiting the time the sample spent at high temperatures eliminated the appearance of mica holes, across all experiment set No.s 7-9. This was an important result to gain control of the copper coverage in these samples. However, although mica holes had been eradicated, the Cu features instead became prevalent (see Figure 128d-e, g-h).

Graphitic deposits were gained across all samples detailed in Table 5. In experiment set No. 6, as well as defective graphitic material, areas of amorphous carbon were observed. Hence, in experiment set No. 7, the methane was decreased in the hope to gain a higher quality material. In set No. 7, although defective graphitic material was obtained, there seemed to be no amorphous areas. To try to increase the quality of the material further, the annealing time was slightly increased to 1 hour in experiment set No. 8. This produced the first full coverage of graphitic material across the sample. A D peak was still present in the Raman spectrum (Figure 128f) and the ratio of the G and 2D peak implied that few-layer graphene was present. However, it seemed that with the increased anneal more Cu features could be observed compared to other samples (Figure 128d). This further increased the roughness of the samples which was not a positive result for the target SFB application. Hence, in set No. 9, the annealing stage was decreased back to 30 minutes, and the growth temperature decreased in the hope that the Cu features would decrease. Although the Cu features were less abundant than in set No. 8, they were nevertheless still observable. In addition, the low growth temperature significantly decreased the quality of the graphitic material produced, with a large increase in the D peak in the Raman spectrum (Figure 128i).

It is worth noting that SEM imaging of experiments sets No. 8 and No. 9 produced clearer images due to the fully conducting, full coverage of graphitic deposits. This was a useful indicator during SEM imaging that graphitic deposits were present.

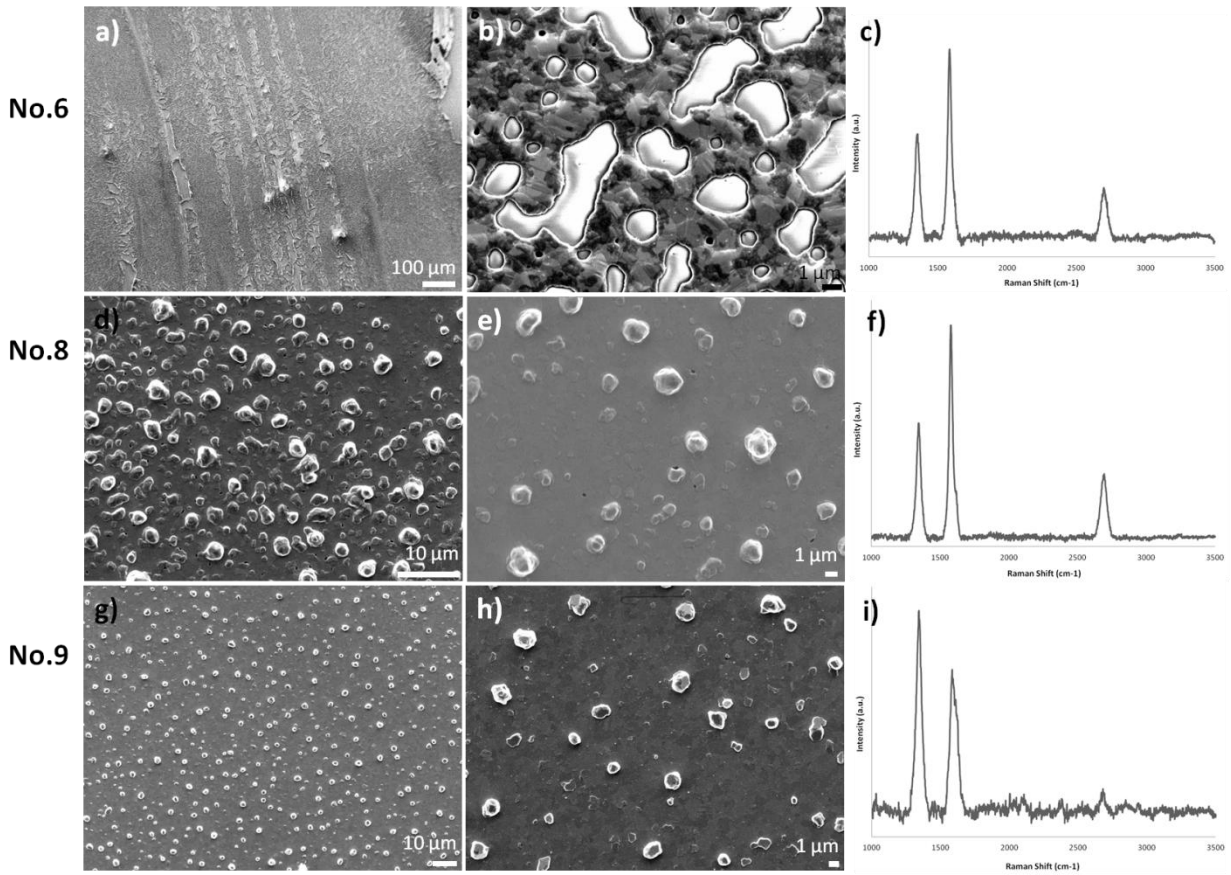


Figure 128a, b, d, e, g, h) Key SEM images from Table 5 showing mica holes and Cu features. c, f, i) Corresponding Raman spectra from experiment set No.s 6, 8 and 9 showing defective graphitic deposits are present.

Due to the decreased quality of graphene growth at 880°C, and the increased Cu features with a longer anneal time, the next option was to see if a further increase in Cu thickness could eliminate the Cu features as both temperature and time were not decreasing their formation. Table 6 shows the experiments conducted with 700 nm Cu on mica. Experiment set No. 10 was conducted with 15 sccm methane, like experiment set No. 8, to attempt to access the higher quality, full coverage graphene growth obtained previously, but without the increased Cu features.

No.	Cu thickness	Logistics	Annealing	Growth	SEM	Raman
10	**700 nm Cu**	Cu on bottom	> 30 min 700°C under 500 H_2 > SAMPLE SHIFTED OUT OF FURNACE > Gradual increase to 900°C over ca. 20 minutes still under 500H_2 > SAMPLE SHIFTED BACK IN	> 20 mins 900°C > **15 CH_4**, 100H_2	Cu features present Potentially very small graphene domains No mica holes	Amorphous carbon peaks
11	700 nm Cu	Cu on bottom	> 30 min 700°C under 500 H_2 > SAMPLE SHIFTED OUT OF FURNACE > Gradual increase to 900°C over ca. 20 minutes still under 500H_2 > SAMPLE SHIFTED BACK IN	> 20 mins 900°C > **10 CH_4**, 100H_2	Cu features present Possible ca. 0.2 µm graphene hexagons	No signal, domains possibly too small
12	700 nm Cu	Cu on bottom	> 30 min 700°C under 500 H_2 > SAMPLE SHIFTED OUT OF FURNACE > Gradual increase to 900°C over ca. 20 minutes still under 500H_2 > SAMPLE SHIFTED BACK IN	> 20 mins 900°C > 10 CH_4, **50H_2**	Cu features present Full coverage graphene	Few-layer graphene signal across all Cu with D peak

Table 6) Experimental details of first experiments with 700 nm Cu/mica substrates; experiment set No.s 10-12. Cu features were still present.

Experiment set No. 10 did not yield higher quality graphene, as in the case of set No. 8, amorphous carbon peaks were observed. In addition, in set No. 8, the highest quality growth was in fact observed on the Cu features, not the bulk. This implies that it was the longer annealing time (that produced more Cu features) that was the cause of this growth compared to the methane to hydrogen ratio. Therefore, this ratio was changed again in an attempt to access higher quality, graphitic deposits.

Figure 129 shows some key SEM images from Table 6. On reducing the methane concentration further, set No. 11 showed the presence of some possible small, graphene domains (*ca*. 0.2 µm), some of which looked more hexagonal (Figure 129b). However, Raman analysis did detect any carbon deposits, possibly due to the low coverage and small domain size. In light of this, for experiment set No. 12, the hydrogen concentration was halved to eliminate excessive domain etching. In doing so, full coverage few-layer graphene was produced, with the smallest D peak obtained on a Cu/mica sample to date without mica holes.

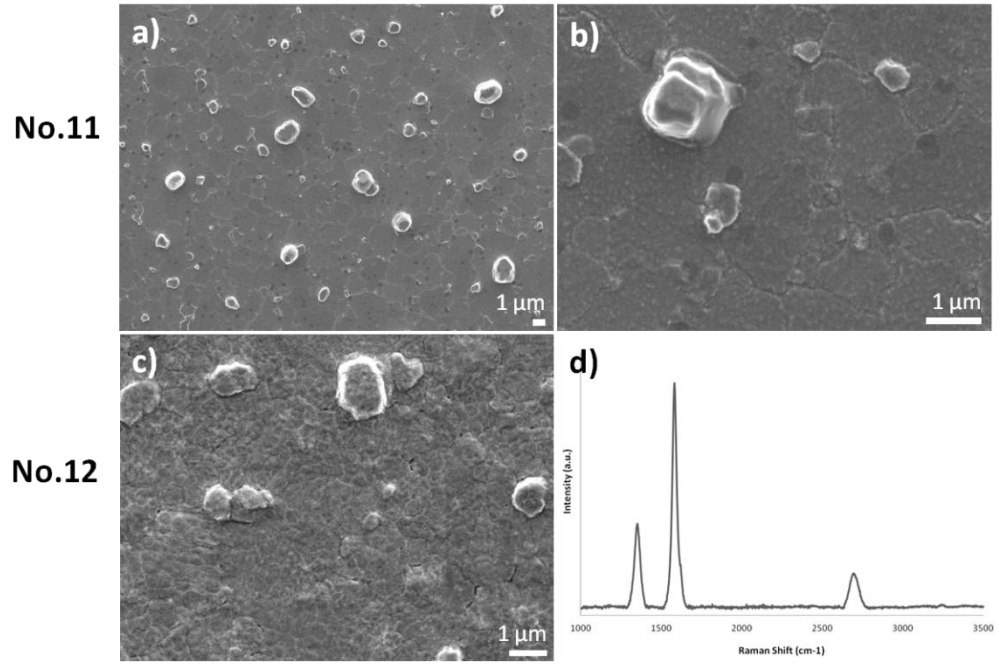


Figure 129a-c) Key SEM images from Table 6 showing consistent appearance of Cu features. d) Raman spectra of product in experiment set No. 12 showing few-layer graphene with D peak.

To further investigate the presence of Cu features, EDX analysis was undertaken. Figure 130 shows EDX spectra from various regions on a Cu/mica sample from experiment set No. 12. Figure 130a shows a spectra from the bulk sample (non-Cu feature), whereas Figure 130b and c show EDX analysis from two separate Cu features. Full scale for each spectrum was 2977 counts.

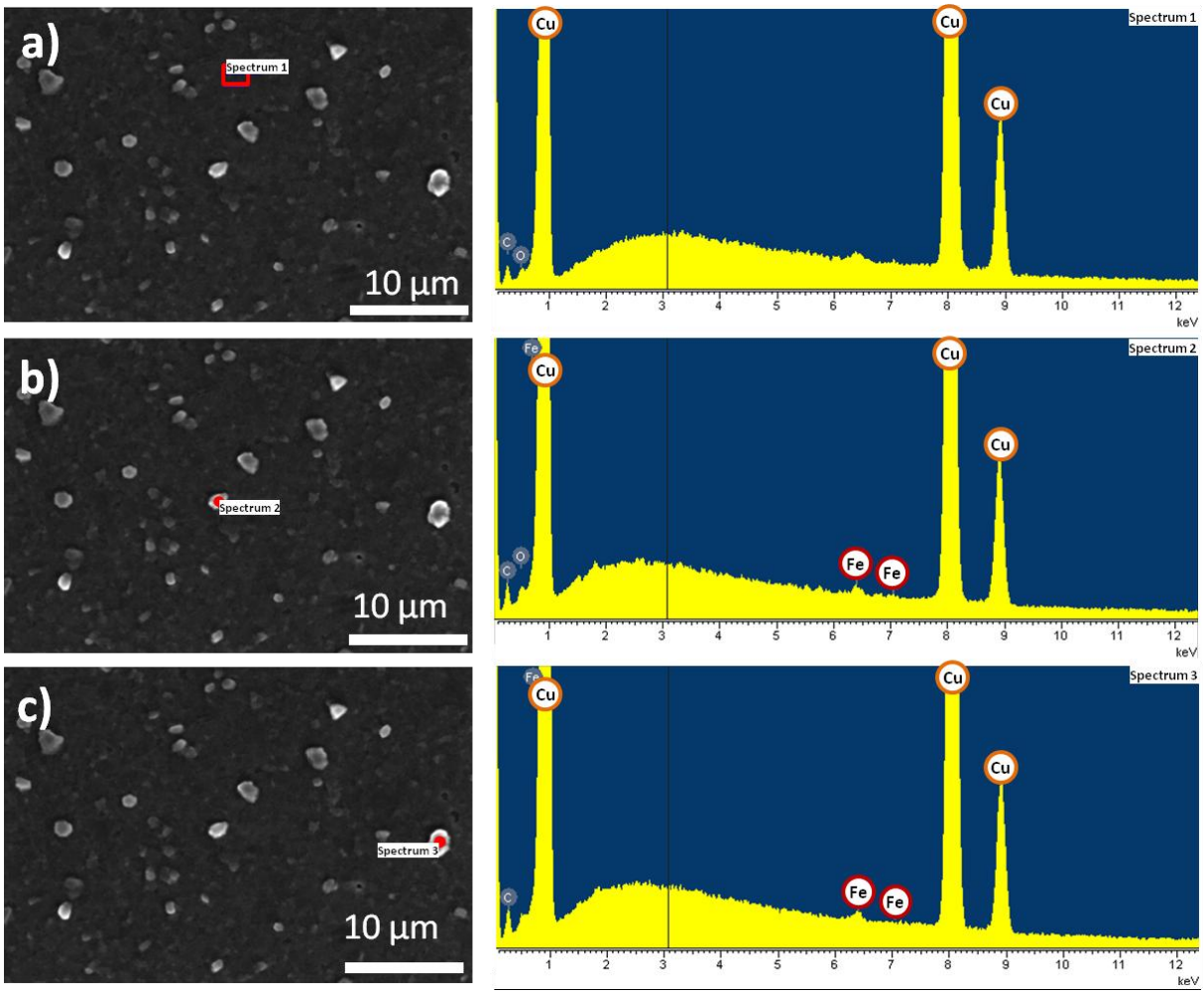


Figure 130) EDX spectra from sample from experiment set No. 12. Left images show an SEM image with red areas highlighting where EDX spectra were taken. On the right shows corresponding EDX spectra from a-c, Cu and Fe peaks are highlighted. With thanks to Gabriella Chapman for aiding in the acquirement of this data.

The EDX analysis explicitly shows that the Cu features are not contamination. The spectra hardly changes from the bulk sample to the Cu features. Peaks from Fe are present but most likely to come from the SEM stub on which the Cu/mica sample is mounted. The only other, visibly very dominant peak is from copper. It could therefore be confirmed that the Cu features that have been observed are copper and derive from the copper substrate during annealing and growth. This was to be expected with graphene growth already being observed on the Cu features.

Further annealing experiments were undertaken to determine the cause of the Cu features, as outlined in Table 7.

No.	Cu thickness	Logistics	Annealing	Growth	SEM	Raman
13	700 nm Cu	Cu on bottom	> 30 min 700°C under 500 H_2 > SAMPLE SHIFTED OUT OF FURNACE > Gradual increase to 900°C over ca. 20 minutes still under 500H_2 > SAMPLE SHIFTED BACK IN	> 20 mins 900°C > **NO CH_4**, 50H_2	Cu features present (Graphene nucleation/CH_4 not cause)	ANNEALING EXP ONLY
14	700 nm Cu	Cu on **top**	> 30 min 700°C under 500 H_2 > SAMPLE SHIFTED OUT OF FURNACE > Gradual increase to 900°C over ca. 20 minutes still under 500H_2 > SAMPLE SHIFTED BACK IN	> 20 mins 900°C > **NO CH_4**, 50H_2	Cu features present (Top/bottom not cause)	ANNEALING EXP ONLY
15: **"Growth step"**	700 nm Cu	Cu on top	-	> 20 mins 900°C > NO CH_4, 50H_2	Cu features present Rest of Cu flat	ANNEALING EXP ONLY
16: **"Growth step lower T"**	700 nm Cu	Cu on top	-	> 20 mins **800°C** > NO CH_4, 50H_2	Cu features present Rest of Cu very flat	ANNEALING EXP ONLY
17: **"Anneal step"**	700 nm Cu	Cu on top	> 30 min 700°C under 500 H_2	-	Small Cu grains forming No features as before, but small holes	ANNEALING EXP ONLY

Table 7) Experimental details of the annealing experiments conducted to understand Cu feature formation; experiment set No.s 13-17.

Experiment set No. 13 was done to determine whether the methane gas flow, and perhaps carbon deposit, had any effect on Cu feature formation. After the Cu/mica sample was subjected to the same conditions as synthesis, without the addition of methane, the Cu features were present as before.

Cu/mica substrate orientation was revisited again in experiment set No. 14 as Cu features had only been thus far observed when Cu was on the bottom surface. When the Cu/mica sample was subjected to the same synthesis conditions, without the methane, with the copper on the top surface, Cu features were still present.

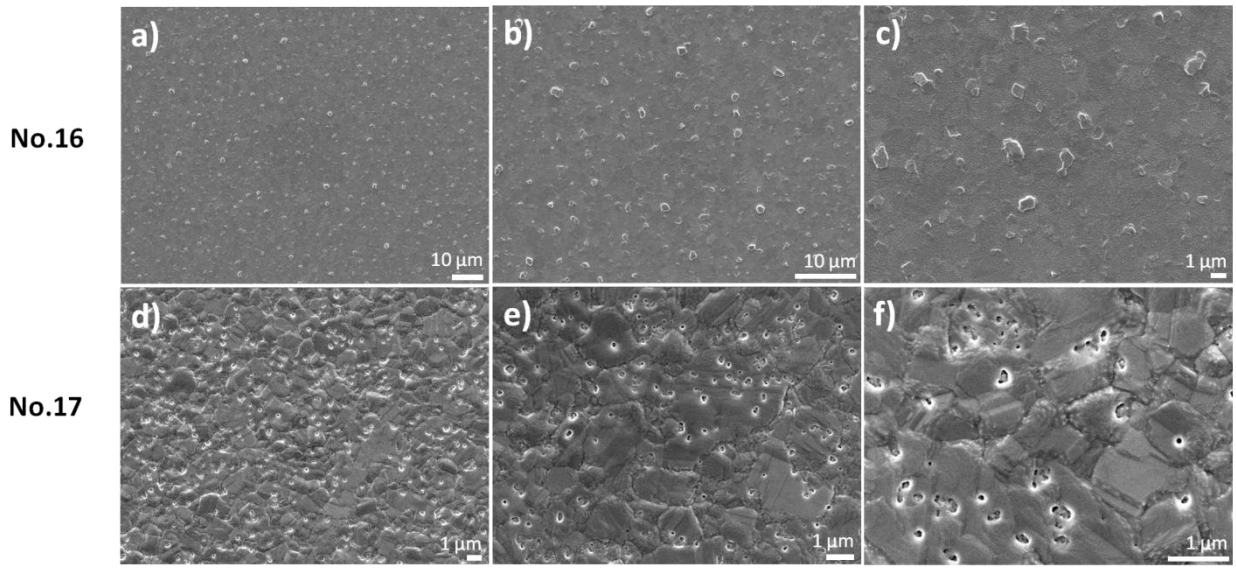


Figure 131) Key SEM images from Table 7, annealing experiments depicting both Cu features and smaller holes in Cu thin film in experiment set No. 17.

From experiment set No. 15, which was essentially just the "Growth step" without annealing at 900°C, Cu features were also apparent. This implies that the "shift" scheme was not the cause of Cu feature formation. Cu features were also observed in set No. 16, where the temperature was decreased to 800°C in a similar "Growth step".

When a sample was subjected to only the "Annealing step" (No. 17) at 700°C, no Cu features are observed, but some small holes and visibly different grains (Figure 131d-f). The small holes observed seem to be unlike mica holes in that they do not charge during SEM imaging and they are much smaller, implying that the holes are shallower and do not go through to the underlying mica layer. The small holes may however be a precursor to the larger mica holes.

Further analysis of the Cu features with SEM (Figure 132) shows that the Cu can be fairly flat on the top of the features. In addition, it Figure 132b seems to "come out" vertically from the bulk Cu.

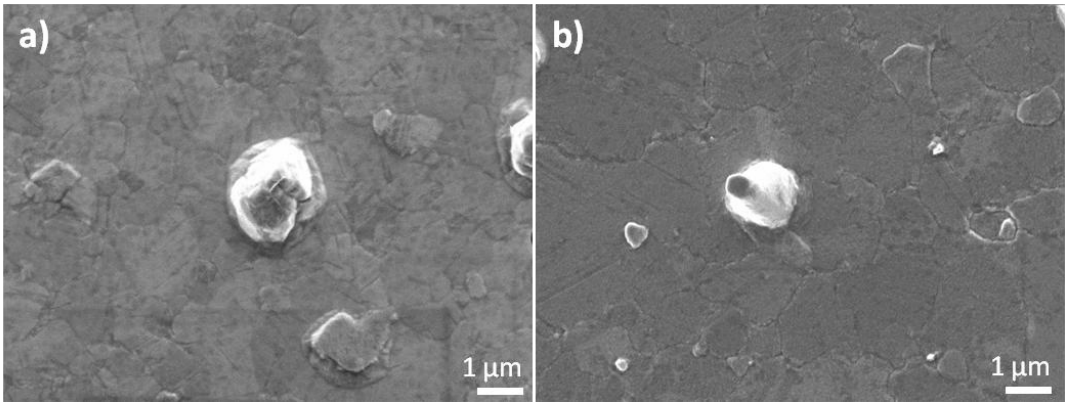


Figure 132) SEM images of examples of Cu features where copper appears to come out of plane.

The observations indicate that Cu features occur at higher temperatures (800-900°C), and not from the annealing step. They occur both with and without the shift scheme, and still occur when the Cu is both on the top and bottom surfaces. Mica holes seem to occur at longer timescales, so the Cu features may be precursors to mica holes. It is also possible that an increased hydrogen flow rate encourages mica holes as opposed to features, aiding with Cu evaporation. It could be possible that for Cu feature formation at lower flow rates, Cu atoms are mobile on the surface, and build upon preferential grains or defect sites, such as protruding areas. In addition, another theory could be that protrusion growth is chemistry driven, leading to accelerated growth of certain Cu domains, potentially driven by contamination particles in the system.

Although it was possible to speculate the formation of the Cu features, further analysis would provide more information.

Figure 133a, b show an EBSD scan and corresponding SEM image at lower magnification of the Cu features (with thanks to Dr. David Collins for EBSD operation). This data implies that the bulk Cu is largely Cu(111), but orientation differs on the Cu features. However, the quality of the data from the features is questionable, due to high roughness which will do not allow the electron beam to be reflected into the EBSD detector at high angles. Figure 133c, d show a higher magnification EBSD scan and SEM image, with Figure 133e denoting the "quality" of the EBSD scan. In this image darker areas represent orientation information based on very little

signal. It is clear therefore from Figure 133e that the data from the Cu features is largely constructed from very low signal. However, observing the kikuchi lines during EBSD scanning, it is possible to speculate the darker grey areas have reliable and hence interpretable data to make an orientation assumption. It could therefore be assumed that the "pink" area in Figure 133d is reliable EBSD data. The Cu feature chosen in this case was much shallower to allow for more reliable data extraction. If this assumption is correct, it implies that the Cu features are indeed made up of a different Cu orientation to the bulk.

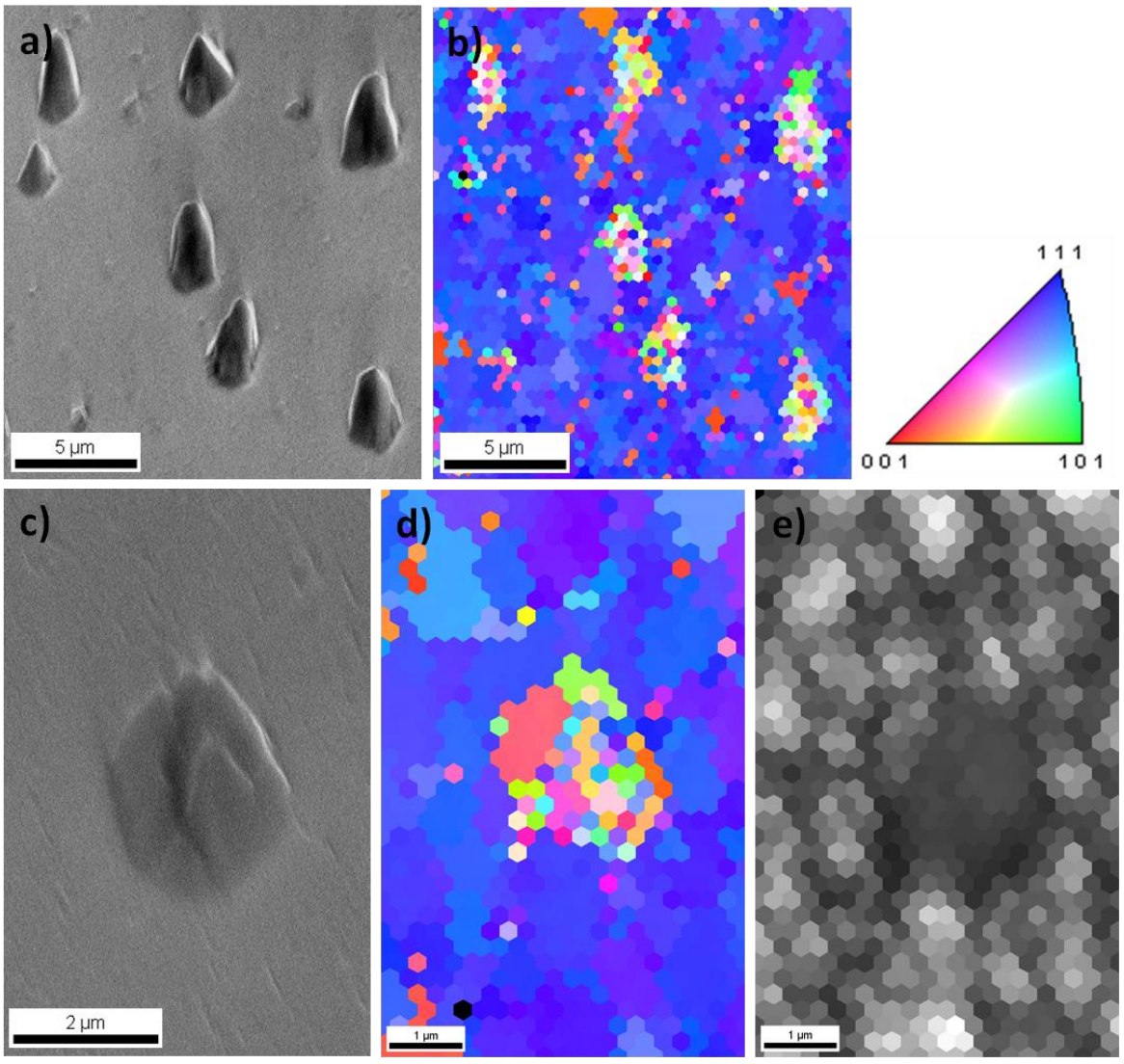


Figure 133) EBSD data from Cu features. a) and b) are SEM and EBSD images respectively at a lower magnification and c) and d) are SEM and EBSD images respectively at a higher magnification of a flatter Cu feature. e) is a quality of data point map from scan d) demonstrating that due to the sample's roughness, data from the roughest areas may not be reliable. With thanks to Dr. David Collins for EBSD operation.

This could be indicative that the local composition in the Cu features has been changed, either through interaction with gases in the system or contamination, causing a change in melting point. EDX analysis would not be able to detect such a small composition change and without further analysis of the detailed composition of the features, this is only speculation.

A theory of Cu feature formation is put forward in the main text.

9.5 Appendix E: gSFB publication

Langmuir

Article

pubs.acs.org/Langmuir

A Graphene Surface Force Balance

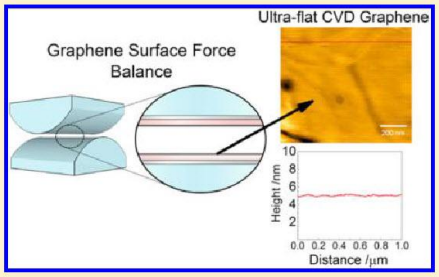
Jude Britton,[†,‡] Nico E. A. Cousens,[†,§] Samuel W. Coles,[§] Christian D. van Engers,[‡] Vitaliy Babenko,[‡] Adrian T. Murdock,[‡] Antal Koós,[‡] Susan Perkin,*[,§] and Nicole Grobert*[,‡]

[‡]Department of Materials, University of Oxford, Parks Road, Oxford OX1 3PH, United Kingdom

[§]Department of Chemistry, University of Oxford, South Parks Road, Oxford OX1 3QZ, United Kingdom

Supporting Information

ABSTRACT: We report a method for transferring graphene, grown by chemical vapor deposition, which produces ultraflat graphene surfaces (root-mean-square roughness of 0.19 nm) free from polymer residues over macroscopic areas (>1 cm^2). The critical step in preparing such surfaces involves the use of an intermediate mica template, which itself is atomically smooth. We demonstrate the compatibility of these model surfaces with the surface force balance, opening up the possibility of measuring normal and lateral forces, including friction and adhesion, between two graphene sheets either in contact or across a liquid medium. The conductivity of the graphene surfaces allows forces to be measured while controlling the surface potential. This new apparatus, the graphene surface force balance, is expected to be of importance to the future understanding of graphene in applications from lubrication to electrochemical energy storage systems.



INTRODUCTION

Graphene is likely to play a key role in a broad range of electronic, electrochemical, and structural applications. Because the study of these systems continues to focus on the nanoscale, understanding the interaction of graphene with ultrathin films, molecular assemblies, and even individual molecules becomes increasingly important.[1−4] To reliably investigate such structures with techniques, such as atomic force microscopy and scanning tunneling microscopy, smooth substrates, devoid of contamination and large features, are required.[5] Similarly, surface force measurements, which require smooth surfaces over macroscopic areas, are also constrained by these requirements.[6] Graphene can be prepared directly from graphite, either mechanically[7] or via chemical exfoliation;[8] however, the characteristics of the graphene flakes produced are largely uncontrollable, and the mean flake size is limited to only a few micrometers. Conversely, graphene synthesized by chemical vapor deposition (CVD) provides much larger surface areas with control over the number of graphene layers (Vlassiouk et al. report growth on 40 in. copper foils[9]). Nonetheless, difficulties arise in transferring graphene from the growth substrate to the target material, with polymer contamination of the graphene surface common when using current transfer methods.[10−15] Furthermore, graphene is generally wrinkled because of a difference in thermal expansion coefficients of graphene and the growth substrate upon cooling after synthesis.[16,17]

Here, we present a new and facile method of transferring CVD graphene to produce clean, molecularly smooth surfaces on the order of 1 cm^2 in area. This is made possible by a "double-transfer" procedure, where an intermediate step uses freshly cleaved and atomically smooth mica as a template to flatten the graphene. Mica is a naturally occurring mineral, which can be cleaved to reveal a perfectly clean and flat surface over macroscopic areas, making it ideal for this process. For SFB applications, it is imperative that graphene exhibits a close to molecularly smooth roughness and polymer contamination is explicitly avoided. As a final step in this work, we demonstrate that the resulting graphene surfaces are indeed sufficiently smooth to allow for force measurements in a surface force balance (SFB), by presenting a proof-of-principle measurement. The modified instrument is referred to as a graphene surface force balance (gSFB). Some features of the resulting force profiles across aqueous solution are as yet unexplained, and future work in our laboratories will investigate the interaction between graphene sheets with externally applied potential.

The SFB[18−20] [also called surface force apparatus (SFA)] has provided pioneering measurements over the past half-century of surface and colloidal forces in liquids: electrostatic surface forces,[21−23] Lifshitz/van der Waals forces,[18,24] solvation forces,[25] forces because of adsorbed and grafted polymers,[26,27] and forces because of surfactants/lipids and biological molecules[28] were all first characterized using this technique. The power of the method arises from the molecular (often sub-molecular) resolution in separation between two identical and atomically smooth mica sheets of precisely known contact

Received: July 18, 2014
Revised: August 26, 2014
Published: August 29, 2014

 © 2014 American Chemical Society dx.doi.org/10.1021/la5028493 | Langmuir 2014, 30, 11485−11492

geometry, obtained using white-light interferometry. Key features of the SFB setup are shown in Figure 1. Although a

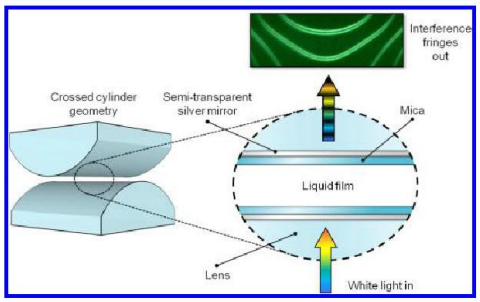


Figure 1. Schematic of the conventional mica SFB illustrating the crossed-cylinder geometry of the mica-covered lenses. Semi-transparent silver mirrors behind the mica form a white light interferometer, which is used to measure the surface separation with sub-nanometer precision. Forces at the mica surface are simultaneously measured by recording the deflection of a spring as the surfaces are brought together.

number of modifications have been made to explore different substrate materials, including the hugely desirable move to use conducting materials, it has not been possible to replace both surfaces with conducting layers of (sub)molecular roughness over the square-centimeter-sized areas as required.[6,29−31] The difficulty arises from the simultaneous need for optical transparency, good conductivity, and molecular-scale smoothness over macroscopic (~cm^2) areas. It is the aim of this work to provide such surfaces using CVD graphene and demonstrate their potential for future surface force measurements.

In summary, we propose a new ultraflat transfer for graphene, which produces molecularly smooth, clean model surfaces. Although graphene has attracted a huge amount of attention in recent years, it has never before been used in SFB measurements. This technique facilitates a modification to the classical SFB to produce a gSFB that allows for graphene−graphene interactions to be measured across air and across liquids with simultaneous detection of their separation with sub-nanometer resolution.

■ MATERIALS AND METHODS

CVD Graphene Synthesis. Few-layer graphene was synthesized using atmospheric pressure chemical vapor deposition of CH_4 in the presence of H_2 on 10 × 25 mm Cu foils (Alfa Aesar, 99.8%, 25 μm thick). The CVD setup consisted of a quartz tube (20 mm inner diameter) located inside a horizontal cylindrical furnace and connected to an acetone bubbler. Contamination from supplier processing was removed before synthesis by sonicating copper in acetic acid for 10 min and then rinsing with deionized water.[32] Copper foil was placed inside the quartz tube at 1035 °C and annealed for 30 min in the presence of 500 standard cubic centimeters per minute (sccm) H_2 to further clean the copper surface and increase the copper grain size. Hydrogen flow was then reduced to 300 sccm, and 5 sccm CH_4 was introduced for 50 min for few-layer graphene growth.

Graphene to Mica Transfer. Graphene was transferred from the copper foil by drop-coating poly(methyl methacrylate) (PMMA; molecular weight = 996 000, dissolved in chlorobenzene) onto one side of the foil and then etching the copper in 0.1 M ammonium persulfate solution. The PMMA/graphene was then removed from the etchant solution and washed thoroughly with ultrapure water [18.2 MΩ resistivity, <1 ppb total organic carbon (TOC)]. It was then placed onto freshly cleaved mica, graphene side down, and pressed between glass microscope slides at 110 °C for 30 min. PMMA was removed by submerging the sample in glacial acetic acid (Fisher, extra pure) for 2 h.

Lens Preparation. A total of 40 nm of Ag (Alfa Aesar, 99.999%) was thermally evaporated under vacuum (0.3 Å s^{-1}, 10^{-6} mbar) onto hemispherical quartz lenses (1 cm diameter, 1 cm radius of curvature). Fringes arising from silver mirrors evaporated onto quartz lenses were similar to fringes arising from back-silvered mica and smooth enough to resolve long-range forces. Alternatively, the mirrors can also be prepared via the template stripping method, which produces atomically smooth mirrors with potentially increased resolution. Buelher EpoThin epoxy diluted with ethanol (Sigma-Aldrich, >99.8%, 1:2 ratio by volume) was spin-coated onto the Ag surface with a Laurel WS650 Mz-23NPP/LITE spin coater. The following spin cycle was used: accelerate at 100 rpm s^{-1} for 5 s and then accelerate to 3000 at 300 rpm s^{-1} for 30 s.

Graphene on mica was then laid onto the surface, and the epoxy was left to cure overnight. The mica could then be removed, and the ultraflat graphene was exposed immediately prior to use in the SFB. Submerging the lens in ultrapure water facilitated removal of the mica.

SFB. The SFB used has been described in detail elsewhere;[20] a full paper describing the setup and operation of the modified gSFB will be communicated in due course. Essential details of the setup relating to this proof-of-principle experiment are as follows. Two hemicylindrical lenses, with graphene sheets attached as described in the text, were mounted in crossed-cylinder configuration inside the SFB. One lens was translated toward or away from the other, in the perpendicular direction, using a motor and a differential spring mechanism to achieve fine control. Forces were detected via the bending of a spring upon which one surface is mounted. Under high applied loads, the glue layer was compressed, leading to a systematic error in the separation distance under high load; this was corrected by subtraction of a linear fit to the compressive behavior from the measured data points.

The separation distance between the lenses was measured using white-light interferometry. Fringes arising from reflection between the silver layers on the lenses ["fringes of equal chromatic order" (FECO)] were observed in a grating spectrometer and captured using a charge-coupled device (CCD) camera. The shape and location of the fringes within these images were extrapolated using a method similar to that used by Quon et al.[33] In this method, each row of the pixels is fitted separately to map the fringe. However, in contrast to previous work, the algorithm here used a one-dimensional center of mass centroid fit instead of a Gaussian fit.

By approximating that the two glue layers are of the same thickness and noting that the thickness of the glue is far greater than that of graphene, the interferometer was estimated to behave as a three-layer symmetric interferometer. This allowed for the fringe locations from within the images to be converted into distance separation using the standard analytical solution for a three-layer interferometer described elsewhere.[34] The refractive index used for the epoxy was 1.532. The surface curvature of the graphene was calculated from the Derjaguin−Landau−Verwey−Overbeek (DLVO) fitting process and was found to be 2 cm in this case.

The potential of the graphene surfaces was controlled with a Metrohm μAutolabIII potentiostat, with Pt wire as the reference electrode, and the effective surface potential at the region of interaction was measured from the minimum point of an electrocapillary curve obtained through electrochemical impedance spectroscopy (see Figure S1 of the Supporting Information). Electrical connections to the graphene surfaces were made with silver conductive paint (RS Components). Potassium perchlorate (99.99+%) from Sigma-Aldrich was used as supplied.

Sample Characterization. CVD graphene was characterized by scanning electron microscopy (SEM), Raman spectroscopy and atomic force microscopy (AFM). For SEM imaging, a JEOL JSM-6500F was operated at 5 kV. Raman spectroscopy was conducted at room temperature using a JY Horiba LabRAM Aramis Raman spectrometer equipped with a 532 nm laser. Atomic force micrographs

dx.doi.org/10.1021/la5028493 | Langmuir 2014, 30, 11485−11492

were recorded with a NanoScope MultiMode AFM in contact mode (Nanosensors PointProbe Plus Contact Mode probes).

RESULTS AND DISCUSSION

Outline of the Procedure (Full Details Are Provided in the Materials and Methods). We present a new five-layer interferometer setup, analogous to the traditional mica–film–mica interferometer used in SFB, consisting of epoxy–graphene–film–graphene–epoxy (where the film can be air, vapor, or a liquid), as shown in Figure 2a. The key to the success of the graphene-coated lenses for force measurement and interferometry are (i) chemical cleanliness (e.g., absence of polymer residues from graphene transfer) and (ii) absence of "positive protrusions" in the graphene, as indicated in panels b and c of Figure 2. This was achieved by way of a new double-transfer procedure, making use of an atomically smooth and clean mica surface as a template. Individual steps in this double-transfer procedure were as follows (see the Materials and Methods for full details, and a schematic of the procedure is shown in Figure 3):

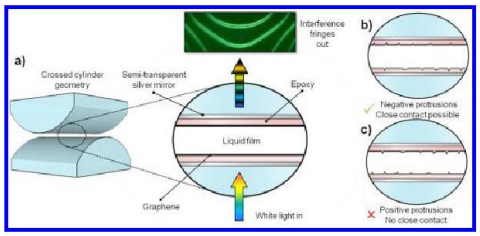


Figure 2. (a) Illustration of gSFB lens structure detailing the five-layer interferometer setup consisting of epoxy–graphene–film–graphene–epoxy. (b and c) Two sets of graphene lens surfaces showing the detrimental effect of positive protrusions on finding a contact point.

CVD Graphene Growth. Graphene was synthesized using atmospheric-pressure CVD of CH_4 in the presence of H_2 on Cu foils at 1035 °C. Gas concentrations and experimental times were tailored to synthesize high-quality, few-layer graphene. Full characterization of the graphene is described in the Graphene Characterization section.

Graphene Transfer to Mica. Graphene was transferred from the Cu foil by adapting and incorporating additional steps to a well-established conventional polymer transfer method.[10,11] PMMA was deposited onto the graphene/Cu foil, followed by copper substrate etching. The PMMA/graphene was then removed from the etchant solution, thoroughly rinsed with ultrapure water (18.2 MΩ cm resistivity, <1 ppb total organic content), and placed onto freshly cleaved mica. The mica was cleaved such that it was thin and flexible enough to lie over a curved SFB lens. Following this, the PMMA/graphene was pressed into the mica surface at 110 °C, after which PMMA was removed with glacial acetic acid.

Graphene Transfer to Silver-Coated Lens with Necessary 2–10 μm Interferometer Thickness. To detect separation distance and interaction force, the SFB requires each of the hemicylindrical optical lenses to be covered by a partially reflective mirror, which was achieved by evaporating 40 nm of silver onto the SFB lenses. The thin silver film enables the FECO interference method to be used. Furthermore, the silver mirrors must still be separated by 2–10 μm when the graphene surfaces are in contact. To achieve this precise separation of the mirrors, the epoxy used to fix the graphene to the mirror was spin-coated. The resulting epoxy thickness (1–10 μm) was precisely controlled by diluting the epoxy and varying the speed and duration of the spin cycle. At this stage, the mica/graphene was laid over the epoxy-covered lenses. After the epoxy had cured, the mica was peeled off, revealing an ultraflat graphene surface, which mirrored the low roughness of the mica template. Submerging the lens in ultrapure water greatly facilitated the mica removal, presumably because of favorable interactions between water and the high-energy mica surface. The mica removal step was performed immediately prior to using the lenses in the gSFB to minimize exposure to airborne contamination and ensure that the surface was as clean as possible. For electrochemical experiments, electrical connections to the graphene sheets were made.

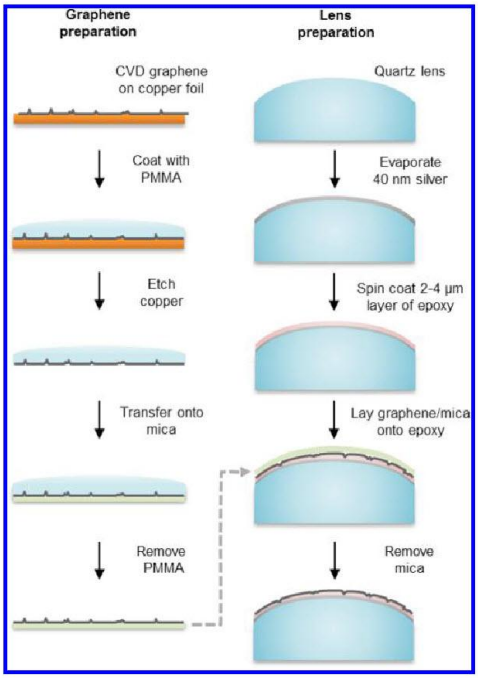


Figure 3. Schematic of graphene SFB lens fabrication. (Left) Transfer of CVD graphene onto the mica template. After CVD growth of graphene on copper, the graphene surface is coated with PMMA to provide a mechanical support for the graphene film during etching. After etching, the graphene is laid onto freshly cleaved mica. Finally, PMMA is removed with glacial acetic acid. (Right) Preparation of SFB lens with the ultraflat graphene surface suitable for the FECO interference method. A total of 40 nm of silver is evaporated onto a clean SFB lens. Subsequently, the epoxy adhesive is spin-coated onto the silver layer onto which the graphene mica stack is placed. After curing, removal of the mica with water exposes a clean, smooth, graphene surface with no positive protrusions.

Graphene Characterization. CVD-synthesized graphene allows for the production of large area graphene films with precise control over the number of graphene layers.[12,35−42]

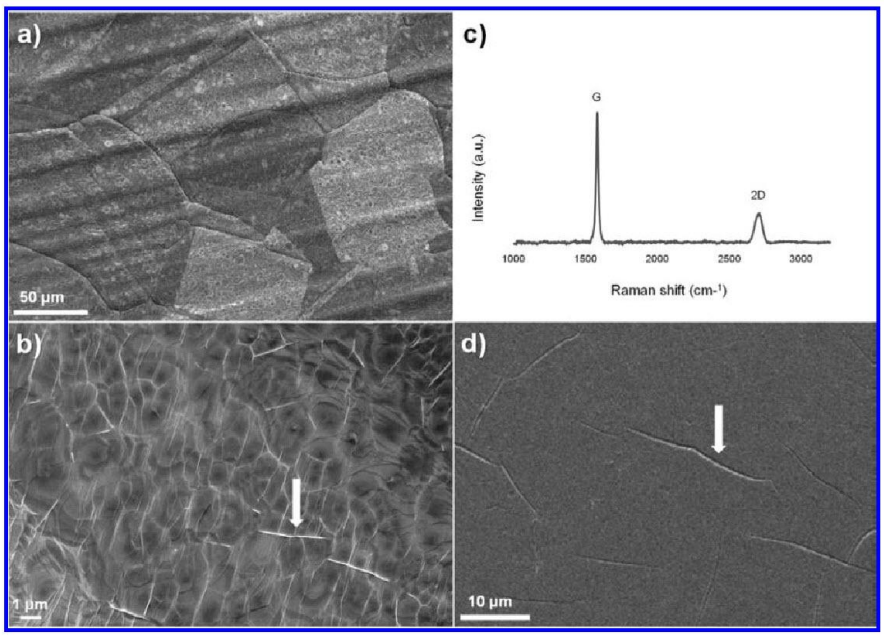


Figure 4. (a and b) SEM images of few-layer graphene (white arrow highlights an example of a wrinkle). (c) Raman spectrum of as-synthesized graphene on copper. The 2D/G ratio is characteristic of few-layer graphene. The absence of a D peak at 1350 cm^{-1} is indicative of a low-defect density. (d) SEM image of graphene transferred to a glass slide using the ultraflat technique (white arrow highlights a now inverted wrinkle, embedded in the epoxy below, as in the schematic in Figure 2b).

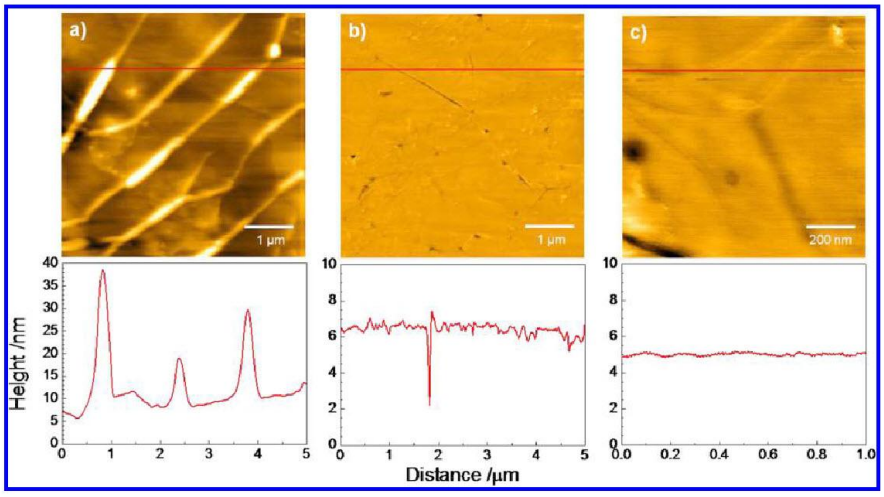


Figure 5. (Top) AFM micrographs of (a) 5 μm^2 scan of the top surface of CVD graphene transferred onto mica using a conventional polymer transfer method, with 4.43 nm RMS roughness, (b) 5 μm^2 scan of ultraflat CVD graphene transferred onto SFB lens using a double-transfer procedure, with 0.44 nm RMS roughness, and (c) 1 μm^2 scan of ultraflat CVD graphene transferred onto SFB lens using a double-transfer procedure, with 0.19 nm RMS roughness. The dark areas in the bottom left of the scan are negative protrusions. (Bottom) Height profiles corresponding to the lines in the top images.

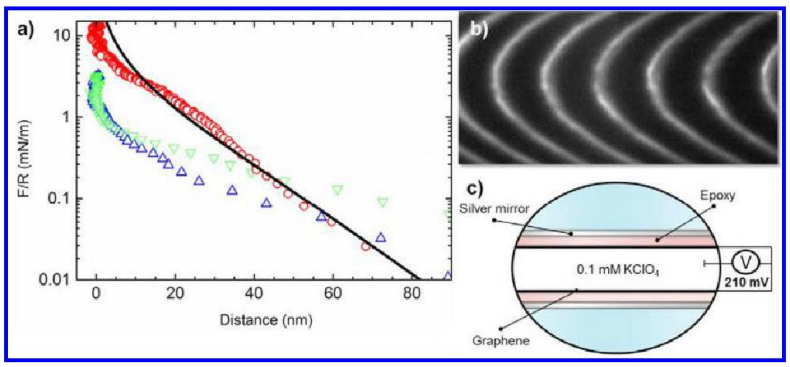


Figure 6. (a) Force–distance profile of graphene surfaces under potential control in the gSFB with 0.1 mM $KClO_4$ solution. Blue triangles show the system at open circuit; red circles show a −210 mV surface potential; and green triangles show the system at open circuit after the −210 mV potential had been switched off. The black line corresponds to the theoretically predicted force profile for a 0.6 mM 1:1 electrolyte solution with −210 mV surface potential. The solid green and blue lines correspond to fits for 0.1 mM 1:1 electrolyte solution. (b) Example of interference fringes used to extract the force profile. (c) Diagram of the experimental setup.

Panels a and b of Figure 4 show typical SEM images of fully covered copper substrates with few-layer (approximately 3–5) CVD graphene used in these experiments. Figure 4a demonstrates the uniform coverage of the few-layer graphene across several copper grains. As highlighted by a white arrow in Figure 4b, wrinkles were observed in these SEM images as expected for dense coverage of few-layer graphene. Regardless of this level of roughness, the proposed transfer technique still allows for molecularly smooth surfaces to be obtained.

Figure 4c shows a typical Raman spectrum of the graphene used in this study. The ratio of the 2D/G peak is indicative of few-layer graphene.[43−45] There is no appearance of a D peak in the spectrum (~1350 cm^{-1}), indicating high-quality (low-defect) graphene.[46] Figure 4d shows a SEM image of graphene that was transferred onto a glass slide, as opposed to a SFB lens, via the ultraflat transfer process as outlined in Figure 3. A white arrow highlights a wrinkle that can be seen protruding into the epoxy below, as shown schematically in Figure 2c. A Raman spectrum of the graphene after transfer onto a SFB lens is shown in Figure S2 of the Supporting Information.

The resistance across the lens, measured with a two-point probe, was 0.5–2 kΩ, indicating that moderate currents (up to ~1 μA) could be passed through the lens without significant voltage drops or Joule heating occurring.

Full coverage of graphene across the copper foil was preferred for SFB purposes to ensure that only graphene–graphene interactions were probed rather than graphene–epoxy interactions. The benefits of few-layer graphene in SFB experiments are expected to be twofold: increased screening of intermolecular forces from the underlying epoxy and increased conductivity of the surface.[47] It has been shown that monolayer graphene is essentially "transparent" to the van der Waals forces of the underlying support material; however, as the number of graphene layers increases, the contact angle of a water droplet approaches that of water on graphite.[48]

Conductivity of the surface is of interest because a conductive surface permits external control of the surface potential. The recorded resistance affirms the viability of using the gSFB for electrochemical and other potential-dependent experiments.

Roughness Analysis of Ultraflat Surfaces. Graphene surfaces were imaged with AFM. Figure 5a shows CVD graphene transferred onto mica before transfer to the lens (see the left-hand side of Figure 3 for transfer details). This image is representative of CVD graphene, which has been transferred to an arbitrary substrate, such as a silicon wafer, using the conventional polymer transfer method. The surface exhibits graphene wrinkles ca. 20 nm tall. Such a surface is unsuitable for surface force measurements because the protrusions prevent close contact of the surfaces (see Figure 2c).

When the graphene is flipped, adhered onto a quartz lens, and the mica is removed, the resulting graphene surface replicates the flatness of the mica. Indeed, from the AFM images (Figure 5), it is clear that graphene as laid onto the SFB lens using the transfer method (panels b and c of Figure 5) is significantly smoother than graphene transferred using a conventional transfer method (Figure 5a). The root-mean-square (RMS) roughness of the double-transferred surface is 0.44 nm over 5 μm^2 and 0.19 nm over 1 μm^2, approaching the roughness of mica itself.[49] This is an order of magnitude less than the roughness of the non-templated surface (4.43 nm). Furthermore, the dominant features in Figure 5b, as seen from the height profile, are negative protrusions or "valleys", enabling surfaces to come into contact during SFB measurements (Figure 2b). Low surface roughness is essential for insightful SFB experiments because the roughness essentially limits the resolution of the experiment: if the surface is rough, forces arising from liquid film structure at small surface separation will be obscured by the force required to compress surface asperities (Figure 2).

The resultant graphene surface is also free from commonly encountered polymer residue contamination because this side of graphene is never in contact with PMMA.[50] Furthermore, there is no evidence of the presence of metal nanoparticle contamination arising from incomplete etching of the copper.[15] Finally, the surface is free from airborne particulates. This is because, unlike conventional transfer methods, the final graphene surface has had only brief exposure to the ambient environment. The graphene surface is protected by the mica up until the point at which it is required, and the mica is removed.

In contrast, the final surface in ordinary transfer techniques is the "top" side of the graphene, the side exposed to the air after synthesis and any polymer support.[10−12]

Interferometry with Graphene Lenses: The gSFB. To confirm the feasibility of measuring surface forces between graphene sheets with external control of the surface potential in the gSFB, the interaction between graphene sheets across an aqueous solution of 0.1 mM $KClO_4$ was investigated (Figure 6; procedure detailed in the Materials and Methods). The force, as a function of surface separation in the range of ∼200 nm down to 0 nm, was first measured at open circuit. At large separation, no force is detected (within the resolution of the measurement), and then very weak repulsive double-layer forces are detected in the range from tens of nanometers to the point of surface contact. The surfaces were then retracted, and a potential of -210 ± 10 mV versus the point of zero charge (see Figure S1 of the Supporting Information) was applied to both graphene surfaces. The subsequent force profile shows a large repulsive interaction, exponentially increasing with decreasing surface separation. The magnitude of force is much greater with the large applied surface potential, as expected within the standard DLVO theory. The data adheres closely to the solution of the nonlinear Poisson−Boltzmann (PB) equation for a 1:1 electrolyte between identical, charged surfaces with a sphere-on-flat geometry at −210 mV and with 0.6 mM salt concentration.[51] The higher salt concentration (steeper gradient) of the PB fit compared to that expected for 0.1 mM ionic strength indicates the presence of additional ions in the double-layer region. This may result from the small 350 nA background current at this potential. This current will have an insignificant effect on the overall concentration (approximately 10 nM increase in the concentration over the duration of the experiment), but there may be an increase in the concentration at the surface where the electrochemical reaction occurs. In the absence of an applied potential, the PB fit agrees with the expected 0.1 mM ionic strength. At small separations, the fit overestimates the force compared to the measured data; the origin of this non-PB behavior is not yet clear, although we note it is also present in the electrochemical SFB measurements between gold surfaces by Kasuya and Kurihara.[52] Crucially, upon relaxation of the surface potential (a return to open circuit), the original surface force profile was recovered, illustrating the reversibility of the system. The non-zero forces detected at open circuit potential indicate a weak charging of the graphene in the aqueous electrolyte environment, possibly because of specific adsorption.

With regard to the objective of this work, viz. demonstrating the feasibility of graphene−SFB measurements, three key points are noted: (i) The appearance of double-layer forces (and no additional repulsive force) down to nanometer separation between the two graphene sheets indicates that the surfaces are indeed sufficiently smooth, over the whole interacting area, for gSFB measurements. (ii) The strong repulsive force observed when symmetric potential is applied to the graphene surfaces indicates that the graphene sheets are continuous across the surfaces and able to support the external potential as expected. (iii) The successful use of FECO interference fringes to calculate the surface force and surface separation, with nanometer precision, demonstrates the feasibility of using the procedures outlined above for the preparation of graphene lenses and subsequent force measurement in the gSFB.

CONCLUSION

A new double-transfer procedure has been demonstrated for preparation of ultraflat graphene surfaces over macroscopic areas. This was achieved by modifying the conventional polymer transfer method with an additional transfer step using freshly cleaved mica as a perfectly clean and flat support. Graphene surfaces produced by the double-transfer procedure have a RMS roughness of less than half a nanometer (0.44 nm) over micrometer-sized areas. In comparison, surfaces produced by the conventional polymer transfer method have a RMS roughness an order of magnitude higher (4.43 nm). Furthermore, the double-transfer procedure yields graphene surfaces that are free from polymer residues commonly encountered when using conventional transfer methods.

These ultraflat graphene surfaces have been integrated into a new apparatus, the gSFB, an instrument for the measurement of surface forces and surface liquid structure at the nanoscale. We show that the graphene surfaces can be brought into clean contact and their separation and interaction force measured with subnanometer resolution by white-light interferometry. This opens up the possibility of a multitude of measurements, including graphene−graphene adhesion and friction, liquid film structure at the graphene surface, and owing to the high conductivity of graphene, potential-dependent and electrochemical effects on normal interaction forces and shear forces.

We note that the graphene transfer method reported here, the key enabling step in the process, is widely applicable for graphene and other two-dimensional (2D) material applications where macroscopic graphene sheets are required and where cleanliness and roughness are key hurdles.

ASSOCIATED CONTENT

Supporting Information

Electrocapillary curve of CVD graphene in 0.1 mM $KClO_4$ (on SFB lens) (Figure S1) and unfiltered Raman spectra of graphene SFB lens, confirming the success of the transfer and demonstrating the retained quality of the few-layer graphene (Figure S2). This material is available free of charge via the Internet at http://pubs.acs.org.

AUTHOR INFORMATION

Corresponding Authors

*E-mail: susan.perkin@chem.ox.ac.uk.
*E-mail: nicole.grobert@materials.ox.ac.uk.

Author Contributions

†Jude Britton and Nico E. A. Cousens contributed equally to this work.

Notes

The authors declare no competing financial interest.

ACKNOWLEDGMENTS

The authors are grateful to the Royal Society, the European Research Council (ERC) (Starting Grant ERC-2009-StG-240500 DEDIGROWTH and Proof of Concept Grant ERC-2012-PoC 309786 DEVICE), the Engineering and Physical Sciences Research Council (EPSRC Pathways to Impact Awards), the Leverhulme Trust (F/07 134/DK and F/07 134/DN), and the John Fell Fund (Oxford University) for financial support.

REFERENCES

(1) Geim, A. K.; Novoselov, K. S. The rise of graphene. *Nat. Mater.* **2007**, *6*, 183−191.
(2) Ivanišťšev, V.; Fedorov, M. V.; Lynden-Bell, R. M. Screening of ion−graphene electrode interactions by ionic liquids: The effects of liquid structure. *J. Phys. Chem. C* **2014**, *118*, 5841−5847.
(3) Lee, C.; Li, Q.; Kalb, W.; Liu, X.-Z.; Berger, H.; Carpick, R. W.; Hone, J. Frictional characteristics of atomically thin sheets. *Science* **2010**, *328*, 76−80.
(4) Englert, J. M.; Dotzer, C.; Yang, G.; Schmid, M.; Papp, C.; Spiecker, E.; Hauke, F.; Hirsch, A.; Gottfried, J. M.; Steinrı, H.-P. Covalent bulk functionalization of graphene. *Nat. Chem.* **2011**, *3*, 279−286.
(5) Vogel, N.; Zieleniecki, J.; Köper, I. As flat as it gets: Ultrasmooth surfaces from template-stripping procedures. *Nanoscale* **2012**, *4*, 3820−3832.
(6) Chai, L.; Klein, J. Large area, molecularly smooth (0.2 nm rms) gold films for surface forces and other studies. *Langmuir* **2007**, *23*, 7777−7783.
(7) Novoselov, K.S.; Geim, A. K.; Morozov, S. V.; Jiang, D.; Zhang, Y.; Dubonos, S. V.; Grigorieva, I. V.; Firsov, A. A. Electric field effect in atomically thin carbon films. *Science* **2004**, *306*, 666−669.
(8) Ciesielski, A.; Samorì, P. Graphene via sonication assisted liquid-phase exfoliation. *Chem. Soc. Rev.* **2014**, *43*, 381−398.
(9) Vlassiouk, I.; Fulvio, P.; Meyer, H.; Lavrik, N.; Dai, S.; Datskos, P.; Smirnov, S. Large scale atmospheric pressure chemical vapor deposition of graphene. *Carbon* **2013**, *54*, 58−67.
(10) Reina, A.; Son, H.; Jiao, L.; Fan, B.; Dresselhaus, M. S.; Liu, Z.; Kong, J. Transferring and identification of single- and few-layer graphene on arbitrary substrates. *J. Phys. Chem. C* **2008**, *112*, 17741−17744.
(11) Li, X.; Zhu, Y.; Cai, W.; Borysiak, M.; Han, B.; Chen, D.; Piner, R. D.; Colombo, L.; Ruoff, R. S. Transfer of large-area graphene films for high-performance transparent conductive electrodes. *Nano Lett.* **2009**, *9*, 4359−4363.
(12) Bae, S.; Kim, H.; Lee, Y.; Xu, X.; Park, J.-S.; Zheng, Y.; Balakrishnan, J.; Lei, T.; Kim, H. R.; Song, Y. I.; Kim, Y.-J.; Kim, K. S.; Ozyilmaz, B.; Ahn, J.-H.; Hong, B. H.; Iijima, S. Roll-to-roll production of 30-in. graphene films for transparent electrodes. *Nat. Nanotechnol.* **2010**, *5*, 574−578.
(13) Lin, Y.-C.; Jin, C.; Lee, J.-C.; Jen, S.-F.; Suenaga, K.; Chiu, P.-W. Clean transfer of graphene for isolation and suspension. *ACS Nano* **2011**, *5*, 2362−2368.
(14) Geringer, V.; Subramaniam, D.; Michel, A. K.; Szafranek, B.; Schall, D.; Georgi, A.; Mashoff, T.; Neumaier, D.; Liebmann, M.; Morgenstern, M. Electrical transport and low-temperature scanning tunneling microscopy of microsoldered graphene. *Appl. Phys. Lett.* **2010**, *96*, 082114.
(15) Liang, X.; Sperling, B. A.; Calizo, I.; Cheng, G.; Hacker, C. A.; Zhang, Q.; Obeng, Y.; Yan, K.; Peng, H.; Li, Q.; Zhu, X.; Yuan, H.; Walker, A. R. H.; Liu, Z.; Peng, L.-M.; Richter, C. A. Toward clean and crackless transfer of graphene. *ACS Nano* **2011**, *5*, 9144−9153.
(16) Chae, S. J.; Güneş, F.; Kim, K. K.; Kim, E. S.; Han, G. H.; Kim, S. M.; Shin, H.-J.; Yoon, S.-M.; Choi, J.-Y.; Park, M. H.; Yang, C. W.; Pribat, D.; Lee, Y. H. Synthesis of large-area graphene layers on poly-nickel substrate by chemical vapor deposition: Wrinkle formation. *Adv. Mater.* **2009**, *21*, 2328−2333.
(17) Zhu, W.; Low, T.; Perebeinos, V.; Bol, A. A.; Zhu, Y.; Yan, H.; Tersoff, J.; Avouris, P. Structure and electronic transport in graphene wrinkles. *Nano Lett.* **2012**, *12*, 3431−3436.
(18) Tabor, D.; Winterton, R. H. S. The direct measurement of normal and retarded van der Waals forces. *Proc. R. Soc. London, Ser. A* **1969**, *312*, 435−450.
(19) Israelachvili, J. N. Thin film studies using multiple-beam interferometry. *J. Colloid Interface Sci.* **1973**, *44*, 259−272.
(20) Klein, J.; Kumacheva, E. Simple liquids confined to molecularly thin layers. I. Confinement-induced liquid-to-solid phase transitions. *J. Chem. Phys.* **1998**, *108*, 6996−7009.
(21) Pashley, R. M. DLVO and hydration forces between mica surfaces in Li^+, Na^+, K^+ and Cs^+ electrolyte solutions: A correlation of double-layer and hydration forces with surface cation exchange properties. *J. Colloid Interface Sci.* **1981**, *83*, 531−546.
(22) Pashley, R. M. Hydration forces between mica surfaces in aqueous electrolyte solutions. *J. Colloid Interface Sci.* **1981**, *80*, 153−162.
(23) Perkin, S.; Goldberg, R.; Chai, L.; Kampf, N.; Klein, J. Dynamic properties of confined hydration layers. *Faraday Discuss.* **2009**, *141*, 399−413.
(24) Israelachvili, J. N.; Tabor, D. Measurement of van der Waals dispersion forces in the range 1.4 to 130 nm. *Nat. Phys. Sci.* **1972**, *236*, 106.
(25) Horn, R. G.; Israelachvili, J. N. Direct measurement of structural forces between two surfaces in a nonpolar liquid. *J. Chem. Phys.* **1981**, *75*, 1400−1411.
(26) Klein, J. Forces between mica surfaces bearing layers of adsorbed polystyrene in cyclohexane. *Nature* **1980**, *288*, 248−250.
(27) Klein, J.; Kumacheva, E.; Mahalu, D.; Perahia, D.; Fetters, L. J. Reduction of frictional forces between solid surfaces bearing polymer brushes. *Nature* **1994**, *370*, 634−636.
(28) Horn, R. G. Direct measurement of the force between two lipid bilayers and observation of their fusion. *Biochim. Biophys. Acta, Biomembr.* **1984**, *778*, 224−228.
(29) Connor, J. N.; Horn, R. G. Measurement of aqueous film thickness between charged mercury and mica surfaces: A direct experimental probe of the Poisson−Boltzmann distribution. *Langmuir* **2001**, *17*, 7194−7197.
(30) Fréchette, J.; Vanderlick, T. K. Double layer forces over large potential ranges as measured in an electrochemical surface forces apparatus. *Langmuir* **2001**, *17*, 7620−7627.
(31) Shrestha, B. R.; Baimpos, T.; Raman, S.; Valtiner, M. Angstrom-resolved real-time dissection of electrochemically active noble metal interfaces. *ACS Nano* **2014**, *8*, 5979−5987.
(32) Zhang, B.; Lee, W. H.; Piner, R.; Kholmanov, I.; Wu, Y.; Li, H.; Ji, H.; Ruoff, R. S. Low-temperature chemical vapor deposition growth of graphene from toluene on electropolished copper foils. *ACS Nano* **2012**, *6*, 2471−2476.
(33) Quon, R. A.; Levins, J. M.; Vanderlick, T. K. High-precision automated measurement of surface separation for the surface force apparatus. *J. Colloid Interface Sci.* **1995**, *171*, 474−482.
(34) Fisher, L. R.; Israelachvili, J. N. Direct experimental verification of the Kelvin equation for capillary condensation. *Nature* **1979**, *277*, 548−549.
(35) Reina, A.; Jia, X.; Ho, J.; Nezich, D.; Son, H.; Bulovic, V.; Dresselhaus, M. S.; Kong, J. Large area, few-layer graphene films on arbitrary substrates by chemical vapor deposition. *Nano Lett.* **2009**, *9*, 30−35.
(36) Li, X.; Cai, W.; An, J.; Kim, S.; Nah, J.; Yang, D.; Piner, R.; Velamakanni, A.; Jung, I.; Tutuc, E.; Banerjee, S. K.; Colombo, L.; Ruoff, R. S. Large-area synthesis of high-quality and uniform graphene films on copper foils. *Science* **2009**, *324*, 1312−1314.
(37) Reina, A.; Thiele, S.; Jia, X.; Bhaviripudi, S.; Dresselhaus, M. S.; Schaefer, J.A.; Kong, J. Growth of large-area single- and bi-layer graphene by controlled carbon precipitation on polycrystalline Ni surfaces. *Nano Res.* **2010**, *2*, 509−516.
(38) Zhou, H.; Yu, W. J.; Liu, L.; Cheng, R.; Chen, Y.; Huang, X.; Liu, Y.; Wang, Y.; Huang, Y.; Duan, X. Chemical vapour deposition growth of large single crystals of monolayer and bilayer graphene. *Nat. Commun.* **2013**, *4*, 2096.
(39) Li, X.; Magnuson, C. W.; Venugopal, A.; Tromp, R. M.; Hannon, J.B.; Vogel, E. M.; Colombo, L.; Ruoff, R. S. Large-area graphene single crystals grown by low-pressure chemical vapor deposition of methane on copper. *J. Am. Chem. Soc.* **2011**, *133*, 2816−2819.
(40) Liu, W.; Kraemer, S.; Sarkar, D.; Li, H.; Ajayan, P. M.; Banerjee, K. Controllable and rapid synthesis of high-quality and large-area Bernal stacked bilayer graphene using chemical vapor deposition. *Chem. Mater.* **2014**, *26*, 907−915.

(41) Bhaviripudi, S.; Jia, X.; Dresselhaus, M. S.; Kong, J. Role of kinetic factors in chemical vapor deposition synthesis of uniform large area graphene using copper catalyst. *Nano Lett.* **2010**, *10*, 4128−4133.
(42) Murdock, A. T.; Koos, A.; Britton, T. B.; Houben, L.; Batten, T.; Zhang, T.; Wilkinson, A. J.; Dunin-Borkowski, R. E.; Lekka, C. E.; Grobert, N. Controlling the orientation, edge geometry, and thickness of chemical vapor deposition graphene. *ACS Nano* **2013**, *7*, 1351−1359.
(43) Ferrari, A. C.; Meyer, J. C.; Scardaci, V.; Casiraghi, C.; Lazzeri, M.; Mauri, F.; Piscanec, S.; Jiang, D.; Novoselov, K. S.; Roth, S.; Geim, A. K. Raman spectrum of graphene and graphene layers. *Phys. Rev. Lett.* **2006**, *97*, 1−4.
(44) Ferrari, A. C. Raman spectroscopy of graphene and graphite: Disorder, electron−phonon coupling, doping and nonadiabatic effects. *Solid State Commun.* **2007**, *143*, 47−57.
(45) Graf, D.; Molitor, F.; Ensslin, K.; Stampfer, C.; Jungen, A.; Hierold, C.; Wirtz, L. Spatially resolved Raman spectroscopy of single- and few-layer graphene. *Nano Lett.* **2007**, *7*, 238−242.
(46) Dresselhaus, M. S.; Jorio, A.; Hofmann, M.; Dresselhaus, G.; Saito, R. Perspectives on carbon nanotubes and graphene Raman spectroscopy. *Nano Lett.* **2010**, *10*, 751−758.
(47) Chen, S.; Cai, W.; Piner, R. D.; Suk, J. W.; Wu, Y.; Ren, Y.; Kang, J.; Ruoff, R. S. Synthesis and characterization of large-area graphene and graphite films on commercial Cu−Ni alloy foils. *Nano Lett.* **2011**, *11*, 3519−3525.
(48) Rafiee, J.; Mi, X.; Gullapalli, H.; Thomas, A. V.; Yavari, F.; Shi, Y.; Ajayan, P.M.; Koratkar, N. A. Wetting transparency of graphene. *Nat. Mater.* **2012**, *11*, 217−222.
(49) Senden, T. J.; Ducker, W. A. Surface roughness of plasma-treated mica. *Langmuir* **1992**, *8*, 733−735.
(50) Ishigami, M.; Chen, J. H.; Cullen, W. G.; Fuhrer, M. S.; Williams, E. D. Atomic structure of graphene on SiO_2. *Nano Lett.* **2007**, *7*, 1643−1648.
(51) Chan, D. Y. C.; Pashley, R. M.; White, L. R. A simple algorithm for the calculation of the electrostatic repulsion between identical charged surfaces in electrolyte. *J. Colloid Interface Sci.* **1980**, *77*, 283−285.
(52) Kasuya, M.; Kurihara, K. Characterization of ferrocene modified electrode using electrochemical surface forces apparatus. *Langmuir* **2014**, *30*, 7093−7097.

10 References

1. Geim, A. K. Graphene: status and prospects. *Science* **324,** 1530–4 (2009).

2. Novoselov, K. S. *et al.* Electric field effect in atomically thin carbon films. *Science* **306,** 666–9 (2004).

3. Dresselhaus, M. S. *et al.* Intercalation compounds of graphite. *Adv. Phys.* **51,** 1–186 (2002).

4. Shenderova, O. A. *et al.* Carbon nanostructures. *Crit. Rev. Solid State Mater. Sci.* **27,** 227–356 (2002).

5. Geim, A. K. *et al.* The rise of graphene. *Nat. Mater.* **6,** 183–91 (2007).

6. Partoens, B. *et al.* From graphene to graphite: Electronic structure around the K point. *Phys. Rev. B* **74,** 075404 (2006).

7. Wang, S. *et al.* Wettability and surface free energy of graphene films. *Langmuir* **25,** 11078–81 (2009).

8. Park, H. J. *et al.* Growth and properties of few-layer graphene prepared by chemical vapor deposition. *Carbon N. Y.* **48,** 1088–1094 (2010).

9. Geim, a K. *et al.* Van der Waals heterostructures. *Nature* **499,** 419–25 (2013).

10. Lee, C. *et al.* Measurement of the elastic properties and intrinsic strength of monolayer graphene. *Science* **321,** 385–8 (2008).

11. Bunch, J. S. *et al.* Impermeable atomic membranes from graphene sheets. *Nano Lett.* **8,** 2458–2462 (2008).

12. Balandin, A. a *et al.* Superior thermal conductivity of single-layer graphene. *Nano Lett.* **8,** 902–7 (2008).

13. Novoselov, K. S. *et al.* Two-dimensional gas of massless Dirac fermions in graphene. *Nature* **438,** 197–200 (2005).

14. Bolotin, K. I. *et al.* Temperature-dependent transport in suspended graphene. *Phys. Rev. Lett.* **101,** 096802 (2008).

15. Zhang, Y. *et al.* Experimental observation of the quantum Hall effect and Berry's phase in graphene. *Nature* **438,** 201–4 (2005).

16. Casiraghi, C. *et al.* Raman fingerprint of charged impurities in graphene. *Appl. Phys. Lett.* **91,** 233108 (2007).

17. Pisana, S. *et al.* Breakdown of the adiabatic Born-Oppenheimer approximation in graphene. *Nat. Mater.* **6,** 198–201 (2007).

18. Nair, R. R. *et al.* Fine structure constant defines visual transparency of graphene. *Science* **320,** 1308 (2008).

19. Ma, P. *et al.* Chemical vapour deposition graphene radio-frequency field-effect transistors. *Chinese Phys. Lett.* **29,** 057302 (2012).

20. Tang, Y. B. *et al.* High-quality graphenes via a facile quenching method for field-effect transistors. *Nano Lett.* **9,** 1374–1377 (2009).

21. Lim, S. *et al.* Inkjet-printed reduced graphene oxide/poly(vinyl alcohol) composite electrodes for flexible transparent organic field-effect transistors. *J. Phys. Chem. C* **116,** 7520–7525 (2012).

22. Kim, T. *et al.* Large-scale graphene micropatterns via self-assembly-mediated process for flexible device application. *Nano Lett.* **12,** 743–8 (2012).

23. Lee, Y. *et al.* Wafer-scale synthesis and transfer of graphene films. *Nano Lett.* **10,** 490–3 (2010).

24. Li, H. *et al.* Layer-by-layer assembly and UV photoreduction of graphene-polyoxometalate composite films for electronics. *J. Am. Chem. Soc.* **133,** 9423–9 (2011).

25. Li, X. *et al.* Large-area synthesis of high-quality and uniform graphene films on copper foils. *Science* **324,** 1312–4 (2009).

26. Liu, W. *et al.* Synthesis of high-quality monolayer and bilayer graphene on copper using chemical vapor deposition. *Carbon N. Y.* **49,** 4122–4130 (2011).

27. Kasry, A. *et al.* Chemical doping of large-area stacked graphene films for use as transparent, conducting electrodes. *ACS Nano* **4,** 3839–44 (2010).

28. Li, X. *et al.* Transfer of large-area graphene films for high-performance transparent conductive electrodes. *Nano Lett.* **9,** 4359–63 (2009).

29. Wang, X. *et al.* Transparent, conductive graphene electrodes for dye-sensitized solar cells. *Nano Lett.* **8,** 323–7 (2008).

30. Bae, S. *et al.* Roll-to-roll production of 30-inch graphene films for transparent electrodes. *Nat. Nanotechnol.* **5,** 574–8 (2010).

31. Kim, K. S. *et al.* Large-scale pattern growth of graphene films for stretchable transparent electrodes. *Nature* **457,** 706–10 (2009).

32. Zhu, Y. *et al.* High throughput preparation of large area transparent electrodes using non-functionalized graphene nanoribbons. *Chem. Mater.* **23,** 935–939 (2011).

33. Kim, H. M. *et al.* Transparent and high gas barrier films based on poly(vinyl alcohol)/graphene oxide composites. *Thin Solid Films* **519,** 7766–7771 (2011).

34. Kim, H. *et al.* Graphene/polyurethane nanocomposites for improved gas barrier and electrical conductivity. *Chem. Mater.* **22,** 3441–3450 (2010).

35. Kim, H. *et al.* Processing-property relationships of polycarbonate/graphene composites. *Polymer (Guildf).* **50,** 3797–3809 (2009).

36. Kim, H. *et al.* Morphology and properties of polyester / exfoliated graphite nanocomposites. *Macromolecules* **41,** 3317–3327 (2008).

37. Bajpai, R. *et al.* Graphene supported nickel nanoparticle as a viable replacement for platinum in dye sensitized solar cells. *Nanoscale* **4,** 926–30 (2012).

38. Bajpai, R. *et al.* Graphene supported platinum nanoparticle counter-electrode for enhanced performance of dye-sensitized solar cells. *ACS Appl. Mater. Interfaces* **3,** 3884–9 (2011).

39. Kavitha, T. *et al.* Glucose sensing, photocatalytic and antibacterial properties of graphene–ZnO nanoparticle hybrids. *Carbon N. Y.* **50,** 2994–3000 (2012).

40. Muszynski, R. *et al.* Decorating graphene sheets with gold nanoparticles. *J. Phys. Chem. C* **112,** 5263–5266 (2008).

41. Wu, Z.-S. *et al.* Graphene/metal oxide composite electrode materials for energy storage. *Nano Energy* **1,** 107–131 (2012).

42. Murugan, A. V. *et al.* Rapid, facile microwave-solvothermal synthesis of graphene nanosheets and their polyaniline nanocomposites for energy strorage. *Chem. Mater.* **21,** 5004–5006 (2009).

43. Wu, Z.-S. *et al.* Doped graphene sheets as anode materials with superhigh rate and large capacity for lithium ion batteries. *ACS Nano* **5,** 5463–71 (2011).

44. Hong, W. G. *et al.* Agent-free synthesis of graphene oxide/transition metal oxide composites and its application for hydrogen storage. *Int. J. Hydrogen Energy* **37,** 7594–7599 (2012).

45. Wan, X. *et al.* Focusing on energy and optoelectronic applications: a journey for graphene and graphene oxide at large scale. *Acc. Chem. Res.* **45,** 598–607 (2012).

46. Kandanur, S. S. *et al.* Suppression of wear in graphene polymer composites. *Carbon N. Y.* **50,** 3178–3183 (2012).

47. Murariu, M. *et al.* The production and properties of polylactide composites filled with expanded graphite. *Polym. Degrad. Stab.* **95,** 889–900 (2010).

48. Kim, H. *et al.* Graphene/polymer nanocomposites. *Macromolecules* **43,** 6515–6530 (2010).

49. Pumera, M. Electrochemistry of graphene: new horizons for sensing and energy storage. *Chem. Rec.* **9,** 211–23 (2009).

50. Liang, J. *et al.* Electromagnetic interference shielding of graphene/epoxy composites. *Carbon N. Y.* **47,** 922–925 (2009).

51. Yin, J. *et al.* Harvesting Energy from Water Flow over Graphene? *Nano Lett.* **12,** 1736–41 (2012).

52. Prasai, D. *et al.* Graphene: corrosion-inhibiting coating. *ACS Nano* **6,** 1102–8 (2012).

53. Wang, S. *et al.* Synthesis, growth mechanism and thermal stability of copper nanoparticles encapsulated by multi-layer graphene. *Carbon N. Y.* **50,** 2119–2125 (2012).

54. Tassinari, O. *Graphene : Near-term opportunities and long-term ambitions*. *Lux Research Report* (2009).

55. Koh, Y. K. *et al.* Reliably counting atomic planes of few-layer graphene (n>4). *ACS Nano* **5,** 269–274 (2011).

56. Miller, D. L. *et al.* Observing the quantization of zero mass carriers in graphene. *Science* **324,** 924–7 (2009).

57. Orlita, M. *et al.* Approaching the dirac point in high-mobility multilayer epitaxial graphene. *Phys. Rev. Lett.* **101,** 267601 (2008).

58. Bolotin, K. I. *et al.* Observation of the fractional quantum Hall effect in graphene. *Nature* **462,** 196–9 (2009).

59. Sadowski, M. L. *et al.* Magnetospectroscopy of epitaxial few-layer graphene. *Solid State Commun.* **143,** 123–125 (2007).

60. Sprinkle, M. *et al.* First direct observation of a nearly ideal graphene band structure. *Phys. Rev. Lett.* **103,** 226803 (2009).

61. Gava, P. *et al.* Ab initio study of gap opening and screening effects in gated bilayer graphene. *Phys. Rev. B* **79,** 165431 (2009).

62. Chen, S. *et al.* Synthesis and characterization of large-area graphene and graphite films on commercial Cu-Ni alloy foils. *Nano Lett.* **11,** 3519–25 (2011).

63. Reina, A. *et al.* Large area, few-layer graphene films on arbitrary substrates by chemical vapor deposition. *Nano Lett.* **9,** 30–35 (2009).

64. Mattevi, C. *et al.* A review of chemical vapour deposition of graphene on copper. *J. Mater. Chem.* **21,** 3324–3334 (2011).

65. Sutter, P. W. *et al.* Epitaxial graphene on ruthenium. *Nat. Mater.* **7,** 406–11 (2008).

66. Shivaraman, S. *et al.* Free-standing epitaxial graphene. *Nano Lett.* **9,** 3100–5 (2009).

67. Levchenko, I. *et al.* The large-scale production of graphene flakes using magnetically-enhanced arc discharge between carbon electrodes. *Carbon N. Y.* **48,** 4570–4574 (2010).

68. Wu, C. *et al.* Production of graphene sheets by a simple helium arc-discharge. *Phys. E* **42,** 1267–1271 (2010).

69. Hernandez, Y. *et al.* High-yield production of graphene by liquid-phase exfoliation of graphite. *Nat. Nanotechnol.* **3,** 563–8 (2008).

70. Lotya, M. *et al.* Liquid phase production of graphene by exfoliation of graphite in surfactant/water solutions. *J. Am. Chem. Soc.* **131,** 3611–20 (2009).

71. Janowska, I. *et al.* Mechanical thinning to make few-layer graphene from pencil lead. *Carbon N. Y.* **50,** 3106–3110 (2012).

72. Kosynkin, D. V *et al.* Longitudinal unzipping of carbon nanotubes to form graphene nanoribbons. *Nature* **458,** 872–6 (2009).

73. Jiao, L. *et al.* Narrow graphene nanoribbons from carbon nanotubes. *Nature* **458,** 877–80 (2009).

74. Yang, X. *et al.* Two-dimensional graphene nanoribbons. *J. Am. Chem. Soc.* **130,** 4216–7 (2008).

75. Zhang, W. *et al.* A strategy for producing pure single-layer graphene sheets based on a confined self-assembly approach. *Angew. Chem. Int. Ed. Engl.* **48,** 5864–8 (2009).

76. Ruan, G. *et al.* Growth of graphene from food, insects, and waste. *ACS Nano* **5,** 7601–7607 (2011).

77. Sutter, E. *et al.* Graphene growth on polycrystalline Ru thin films. *Appl. Phys. Lett.* **95,** 133109 (2009).

78. Haigh, S. J. *et al.* Cross-sectional imaging of individual layers and buried interfaces of graphene-based heterostructures and superlattices. *Nat. Mater.* **11,** 1–4 (2012).

79. Wang, Z. *et al.* Flexible graphene-based electroluminescent devices. *ACS Nano* **5,** 7149–54 (2011).

80. Chung, K. *et al.* High-quality GaN films grown on chemical vapor-deposited graphene films. *NPG Asia Mater.* **4,** e24 (2012).

81. Li, X. *et al.* Multifunctional graphene woven fabrics. *Sci. Rep.* **2,** 395 (2012).

82. Graphene Supermarket. Single Layer Graphene on Copper foil: 2'x2'. (2015). at <https://graphene-supermarket.com/Single-Layer-Graphene-on-Copper-foil-2inch.html>

83. Alnemer, O. *et al.* Electrical characteristics of graphene wrinkles extracted by conductive atomic force microscopy and electrical measurements on Kelvin structures. in *8th International Conference on DTIS in Nanoscale Era* 182–183 (2013).

84. Zhu, W. *et al.* Structure and electronic transport in graphene wrinkles. *Nano Lett.* **12,** 3431–3436 (2012).

85. Obraztsov, a. N. *et al.* Chemical vapor deposition of thin graphite films of nanometer thickness. *Carbon N. Y.* **45,** 2017–2021 (2007).

86. Vlassiouk, I. *et al.* Role of hydrogen in chemical vapor deposition growth of large single-crystal graphene. *ACS Nano* **5,** 6069–6076 (2011).

87. Huang, P. Y. *et al.* Grains and grain boundaries in single-layer graphene atomic patchwork quilts. *Nature* **469,** 389–92 (2011).

88. Trehan, Y. N. The reduction of copper oxides by molecular hydrogen. *Zeitschrift fuer Anorg. und Allg. Chemie* **318,** 107–112 (1962).

89. Calleja, F. *et al.* Periodically rippled graphene: growth and spatially resolved electronic structure. *Phys. Rev. Lett.* **100,** 056807 (2008).

90. Marchini, S. *et al.* Scanning tunneling microscopy of graphene on Ru(0001). *Phys. Rev. B* **76,** 075429 (2007).

91. Coraux, J. *et al.* Structural coherency of graphene on Ir(111). *Nano Lett.* **8,** 565–70 (2008).

92. Gall', N. R. *et al.* Interaction of silver atoms with iridium and with a two-dimensional graphite film on iridium: Adsorption, desorption, and dissolution. *Phys. Solid State* **46,** 371–377 (2004).

93. Starr, D. E. *et al.* Carbon films grown on Pt(111) as supports for model gold catalysts. *Surf. Sci.* **600,** 2688–2695 (2006).

94. Ueta, H. *et al.* Highly oriented monolayer graphite formation on Pt(111) by a supersonic methane beam. *Surf. Sci.* **560,** 183–190 (2004).

95. Gamo, Y. *et al.* Atomic structure of monolayer graphite formed on Ni(111). *Surf. Sci.* **374,** 61–64 (1997).

96. Kawano, T. *et al.* Preparation of layered B/C/N thin films on nickel single crystal by LPCVD. *Solid State Sci.* **4,** 1521–1527 (2002).

97. Wu, W. *et al.* Wafer-scale synthesis of graphene by chemical vapor deposition and its application in hydrogen sensing. *Sensors Actuators B Chem.* **150,** 296–300 (2010).

98. Lee, Y. *et al.* Wafer-scale synthesis and transfer of graphene films. *Nano Lett.* **10,** 490–3 (2010).

99. Gao, L. *et al.* Repeated growth and bubbling transfer of graphene with millimetre-size single-crystal grains using platinum. *Nat. Commun.* **3,** 699 (2012).

100. Li, X. *et al.* Large-area graphene single crystals grown by low-pressure chemical vapor deposition of methane on copper. *J. Am. Chem. Soc.* **133,** 2816–9 (2011).

101. Han, G. H. *et al.* Influence of copper morphology in forming nucleation seeds for graphene growth. *Nano Lett.* **11,** 4144–8 (2011).

102. Zhao, L. *et al.* Influence of copper crystal surface on the CVD growth of large area monolayer graphene. *Solid State Commun.* **151,** 509–513 (2011).

103. Robertson, A. W. *et al.* Hexagonal single crystal domains of few-layer graphene on copper foils. *Nano Lett.* **11,** 1182–9 (2011).

104. Murdock, A. T. *et al.* Controlling the orientation, edge geometry, and thickness of chemical vapor deposition graphene. *ACS Nano* **7,** 1351–9 (2013).

105. Zhang, B. *et al.* Low-temperature chemical vapor deposition growth of graphene from toluene on electropolished copper foils. *ACS Nano* **6,** 2471–6 (2012).

106. Li, X. *et al.* Evolution of graphene growth on Ni and Cu by carbon isotope labeling. *Nano Lett.* **9,** 4268–4272 (2009).

107. Zhang, W. *et al.* First-principles thermodynamics of graphene growth on Cu surfaces. *J. Phys. Chem. C* **115,** 17782–17787 (2011).

108. Ago, H. *et al.* Catalytic growth of graphene: toward large-area single-crystalline graphene. *J. Phys. Chem. C* **3,** 2228–2236 (2012).

109. Jin, Y. *et al.* Roles of H2 in annealing and growth times of graphene CVD synthesis over copper foil. *J. Mater. Chem. A* **2,** 16208–16216 (2014).

110. Ferrari, A. C. *et al.* Raman spectrum of graphene and graphene layers. *Phys. Rev. Lett.* **97,** 187401 (2006).

111. Ferrari, A. C. Raman spectroscopy of graphene and graphite: Disorder, electron–phonon coupling, doping and nonadiabatic effects. *Solid State Commun.* **143,** 47–57 (2007).

112. Graf, D. *et al.* Spatially resolved Raman spectroscopy of single- and few-layer graphene. *Nano Lett.* **7,** 238–42 (2007).

113. Dresselhaus, M. S. *et al.* Perspectives on carbon nanotubes and graphene Raman spectroscopy. *Nano Lett.* **10,** 751–8 (2010).

114. Zhao, L. *et al.* Visualizing individual nitrogen dopants in monolayer graphene. *Science* **333,** 999–1003 (2011).

115. Chae, D. H. *et al.* Hot phonons in an electrically biased graphene constriction. *Nano Lett.* **10,** 466–471 (2010).

116. Das, A. *et al. Raman spectroscopy of graphene on different substrates and influence of defects*. *arXiv:0710.4160* (2007).

117. Voloshina, E. N. *et al.* Graphene on Rh(111): STM and AFM studies. *Appl. Phys. Lett.* **100,** 241606 (2012).

118. Kertész, K. *et al.* Polarized light microscopy of chemical-vapor-deposition-grown graphene on copper. *Appl. Phys. Lett.* **100,** 213103 (2012).

119. Brown, L. *et al.* Twinning and twisting of tri- and bilayer graphene. *Nano Lett.* **12,** 1609–15 (2012).

120. Ismach, A. *et al.* Direct chemical vapor deposition of graphene on dielectric surfaces. *Nano Lett.* **10,** 1542–8 (2010).

121. Ogawa, Y. *et al.* Structure and transport properties of the interface between CVD-grown graphene domains. *Nanoscale* **6,** 7288–94 (2014).

122. Choi, J. *et al.* Growth of wrinkle-free graphene on texture-controlled platinum films and thermal-assisted transfer of large-scale patterned graphene. *ACS Nano* **9,** 679–686 (2015).

123. Wang, F. *et al.* Evaporation induced wrinkling of graphene oxide at the nanoparticle interface. *Nanoscale* **7,** 919–923 (2015).

124. Paronyan, T. M. *et al.* Formation of ripples in graphene as a result of interfacial instabilities. *ACS Nano* **5,** 9619–27 (2011).

125. Chae, S. J. *et al.* Synthesis of large-area graphene layers on poly-nickel substrate by chemical vapor deposition: wrinkle formation. *Adv. Mater.* **21,** 2328–2333 (2009).

126. Nicholls, R. J. *et al.* In situ engineering of NanoBud geometries. *Chem. Commun.* **49,** 10956–8 (2013).

127. Zhou, W. *et al.* Probing the electronic structure and optical response of a graphene quantum disk supported on monolayer graphene. *J. Phys. Condens. Matter* **24,** 314213 (2012).

128. Nicholls, R. J. *et al.* Probing the bonding in nitrogen-doped graphene using electron energy loss spectroscopy. *ACS Nano* **7,** 7145–50 (2013).

129. Suk, J. W. *et al.* Transfer of CVD-grown monolayer graphene onto arbitrary substrates. *ACS Nano* **5,** 6916–24 (2011).

130. Liang, X. *et al.* Toward clean and crackless transfer of graphene. *ACS Nano* **5,** 9144–53 (2011).

131. Lin, Y.-C. *et al.* Clean transfer of graphene for isolation and suspension. *ACS Nano* **5,** 2362–8 (2011).

132. Lin, Y.-C. *et al.* Graphene annealing: how clean can it be? *Nano Lett.* **12,** 414–9 (2012).

133. Regan, W. *et al.* A direct transfer of layer-area graphene. *Appl. Phys. Lett.* **96,** 113102 (2010).

134. Williams, D. B. *et al. Transmission electron microscopy: A textbook for materials science (second edition)*. (2009).

135. Jiang, W. *et al.* Web-based simulation for contrast transfer function and envelope functions. *Microsc. Microanal.* **7,** 329–334 (2001).

136. Smith, B. W. *et al.* Electron irradiation effects in single wall carbon nanotubes. *J. Appl. Phys.* **90,** 3509–3515 (2001).

137. Füller, T. *et al.* In situ observation of the formation and stability of single fullerene molecules under electron irradiation. *Chem. Phys. Lett.* **254,** 372–378 (1996).

138. Banhart, F. Irradiation effects in carbon nanostructures. *Reports Prog. Phys.* **62,** 1181–1221 (1999).

139. Chamberlain, T. W. *et al.* Reactions of the inner surface of carbon nanotubes and nanoprotrusion processes imaged at the atomic scale. *Nat. Chem.* **3,** 732–737 (2011).

140. Susi, T. *et al.* Atomistic description of electron beam damage in nitrogen-doped graphene and single-walled carbon nanotubes. *ACS Nano* **6,** 8837–8846 (2012).

141. Robertson, A. W. *et al.* Spatial control of defect creation in graphene at the nanoscale. *Nat. Commun.* **3,** 1144 (2012).

142. He, K. *et al.* Hydrogen-free graphene edges. *Nat. Commun.* **5,** 3040 (2014).

143. Meyer, J. C. *et al.* On the roughness of single- and bi-layer graphene membranes. *Solid State Commun.* **143,** 101–109 (2007).

144. Shen, X. *et al.* Wrinkling in graphene sheets and graphene oxide papers. *Carbon N. Y.* **66,** 84–92 (2014).

145. Kim, K. *et al.* Multiply folded graphene. *Phys. Rev. B* **83,** 245433 (2011).

146. Wang, C. *et al.* Graphene wrinkling: formation, evolution and collapse. *Nanoscale* **5,** 4454–61 (2013).

147. Wang, C. *et al.* The physics of wrinkling in graphene membranes under local tension. *Phys. Chem. Chem. Phys.* **15,** 2764–2773 (2013).

148. Chopra, N. G. *et al.* Fully collapsed carbon nanotubes. *Nature* (1995).

149. Liu, X. *et al.* Anisotropic growth of buckling-driven wrinkles in graphene monolayer. *Nanotechnology* **26,** 65701 (2015).

150. Zhang, K. *et al.* Understanding and strain-engineering wrinkle networks in supported graphene through simulations. *J. Mech. Phys. Solids* **72,** 61–74 (2014).

151. Runte, S. *et al.* Graphene buckles under stress: An x-ray standing wave and scanning tunneling microscopy study. *Phys. Rev. B* **89,** 155427 (2014).

152. Yu, S. U. *et al.* Simultaneous visualization of graphene grain boundaries and wrinkles with structural information by gold deposition. *ACS Nano* **8,** 8662–8668 (2014).

153. Guo, Y. *et al.* Electronic and field emission properties of wrinkled graphene. *J. Phys. Chem. C* **117,** 692–696 (2013).

154. Yan, W. *et al.* Strain and curvature induced evolution of electronic band structures in twisted graphene bilayer. *Nat. Commun.* **4,** 2159 (2013).

155. Guinea, F. *et al.* Midgap states and charge inhomogeneities in corrugated graphene. *Phys. Rev. B* **77,** 075422 (2008).

156. Rochford, C. *et al.* All-optical technique to correlate defect structure and carrier transport in transferred graphene films. *ACS Appl. Mater. Interfaces* **5,** 7176–7180 (2013).

157. Grosse, K. L. *et al.* Direct observation of resistive heating at graphene wrinkles and grain boundaries. *Appl. Phys. Lett.* **105,** 143109 (2014).

158. Wang, C. *et al.* Anisotropic thermal conductivity of graphene wrinkles. *Nanoscale* **6,** 5703–7 (2014).

159. Zhang, Y. H. *et al.* Role of wrinkles in the corrosion of graphene domain-coated Cu surfaces. *Appl. Phys. Lett.* **104,** 143110 (2014).

160. Zhang, Y. H. *et al.* The distribution of wrinkles and their effects on the oxidation resistance of chemical vapor deposition graphene. *Carbon N. Y.* **70,** 81–86 (2014).

161. Bai, S. *et al.* The influence of wrinkling in reduced graphene oxide on their adsorption and catalytic properties. *Carbon N. Y.* **60,** 157–168 (2013).

162. Wang, B. *et al.* Wrinkle-dependent hydrogen etching of chemical vapor deposition-grown graphene domains. *Carbon N. Y.* **70,** 75–80 (2014).

163. Zhang, Y. *et al.* Defect-like structures of graphene on copper foils for strain relief investigated by high-resolution scanning tunneling microscopy. *ACS Nano* **5,** 4014–22 (2011).

164. Robertson, A. W. *et al.* Structural distortions in few-layer graphene creases. *ACS Nano* **5,** 9984–91 (2011).

165. Robertson, A. W. *et al.* Atomic structure of interconnected few-layer graphene domains. *ACS Nano* **5,** 6610–8 (2011).

166. Yuk, J. M. *et al.* Superstructural defects and superlattice domains in stacked graphene. *Carbon N. Y.* **80,** 755–761 (2014).

167. Ortolani, L. *et al.* Folded graphene membranes: mapping curvature at the nanoscale. *Nano Lett.* **12,** 5207–12 (2012).

168. Hattab, H. *et al.* Interplay of wrinkles, strain, and lattice parameter in graphene on iridium. *Nano Lett.* (2012).

169. Norimatsu, W. *et al.* Selective formation of ABC-stacked graphene layers on SiC(0001). *Phys. Rev. B* **81,** 161410 (2010).

170. Hayashi, T. *et al.* Determination of the stacking order of curved few-layered graphene systems. *Nanoscale* **4,** 6419–24 (2012).

171. Kuwabara, M. *et al.* Anomalous superperiodicity in scanning tunneling microscope images of graphite. *Appl. Phys. Lett.* **56,** 2396 (1990).

172. Miller, D. L. *et al.* Structural analysis of multilayer graphene via atomic moiré interferometry. *Phys. Rev. B* **81,** 125427 (2010).

173. Meng, L. *et al.* Multi-oriented moiré superstructures of graphene on Ir(111): experimental observations and theoretical models. *J. Phys. Condens. Matter* **24,** 314214 (2012).

174. Luican, A. *et al.* Single-layer behavior and its breakdown in twisted graphene layers. *Phys. Rev. Lett.* **106,** 126802 (2011).

175. Pong, W.-T. *et al.* A review and outlook for an anomaly of scanning tunnelling microscopy (STM): superlattices on graphite. *J. Phys. D. Appl. Phys.* **38,** R329–R355 (2005).

176. Xhie, J. *et al.* Giant and supergiant lattices on graphite. *Phys. Rev. B* **47,** 15835–15841 (1993).

177. Land, T. A. *et al.* STM investigation of single layer graphite structures produced on Pt (111) by hydrocarbon decomposition. *Surf. Sci.* **264,** 261–270 (1992).

178. First, P. N. *et al.* Epitaxial Graphenes on Silicon Carbide. *MRS Bull.* **35,** 296 (2010).

179. Gao, M. *et al.* Epitaxial growth and structural property of graphene on Pt(111). *Appl. Phys. Lett.* **98,** 033101 (2011).

180. McCann, E. *et al.* Landau-level degeneracy and quantum hall effect in a graphite bilayer. *Phys. Rev. Lett.* **96,** 086805 (2006).

181. Jasinski, J. B. *et al.* Observation and interpretation of adjacent moiré patterns of different shapes in bilayer graphene. *Appl. Phys. Lett.* **99,** 073104 (2011).

182. Graphene, P. *et al.* Grain boundary mapping in polycrystalline graphene. *ACS Nano* **5,** 2142–2146 (2011).

183. Yazyev, O. V *et al.* Electronic transport in polycrystalline graphene. *Nat. Mater.* **9,** 806–9 (2010).

184. Tsen, A. W. *et al.* Tailoring electrical transport across grain boundaries in polycrystalline graphene. *Science* **336,** 1143–6 (2012).

185. Rao, R. *et al.* Probing inhomogeneous doping in overlapped graphene grain boundaries by Raman spectroscopy. *Carbon N. Y.* **80,** 513–522 (2014).

186. Li, X. *et al.* Graphene films with large domain size by a two-step chemical vapor deposition process. *Nano Lett.* **10,** 4328–34 (2010).

187. Zhou, H. *et al.* Chemical vapour deposition growth of large single crystals of monolayer and bilayer graphene. *Nat. Commun.* **4,** 2096 (2013).

188. Gan, L. *et al.* Turning off hydrogen to realize seeded growth of subcentimeter single-crystal graphene grains on copper. *ACS Nano* **7,** 9480–8 (2013).

189. Wu, Y. a *et al.* Large single crystals of graphene on melted copper using chemical vapor deposition. *ACS Nano* **6,** 5010–7 (2012).

190. Geng, D. *et al.* Uniform hexagonal graphene flakes and films grown on liquid copper surface. *Proc. Natl. Acad. Sci.* **109,** 7992–7996 (2012).

191. Bykov, A. Y. *et al.* Probing structural inhomogeneity of graphene layers via nonlinear optical scattering. *Opt. Lett.* **38,** 4589–92 (2013).

192. Yan, Z. *et al.* Hexagonal graphene onion rings. *J. Am. Chem. Soc.* **135,** 10755–62 (2013).

193. Juang, Z.-Y. *et al.* Graphene synthesis by chemical vapor deposition and transfer by a roll-to-roll process. *Carbon N. Y.* **48,** 3169–3174 (2010).

194. Yao, Y. *et al.* Controlled growth of multilayer, few-layer, and single-layer graphene on metal substrates. *J. Phys. Chem. C* **115,** 5232–5238 (2011).

195. Pauling, L. The structure and properties of graphite and boron nitride. *Proc. Natl. Acad. Sci.* **56,** 1646–1652 (1966).

196. Zhi, C. *et al.* Large-scale fabrication of boron nitride nanosheets and their utilization in polymeric composites with improved thermal and mechanical properties. *Adv. Mater.* **21,** 2889–2893 (2009).

197. Blase, X. *et al.* Frustration effects and microscopic growth mechanisms for BN nanotubes. *Phys. Rev. Lett.* **80,** 1666–1669 (1998).

198. Pakdel, A. *et al.* Nano boron nitride flatland. *Chem. Soc. Rev.* **43,** 934–59 (2014).

199. Watanabe, K. *et al.* Direct-bandgap properties and evidence for ultraviolet lasing of hexagonal boron nitride single crystal. *Nat. Mater.* **3,** 404–409 (2004).

200. Dean, C. R. *et al.* Boron nitride substrates for high-quality graphene electronics. *Nat. Nanotechnol.* **5,** 722–6 (2010).

201. Gannett, W. *et al.* Boron nitride substrates for high mobility chemical vapor deposited graphene. *Appl. Phys. Lett.* **98,** (2011).

202. Pacilé, D. *et al.* The two-dimensional phase of boron nitride: Few-atomic-layer sheets and suspended membranes. *Appl. Phys. Lett.* **92,** 28–31 (2008).

203. Han, W. Q. *et al.* Structure of chemically derived mono- and few-atomic-layer boron nitride sheets. *Appl. Phys. Lett.* **93,** 10–13 (2008).

204. Warner, J. H. *et al.* Atomic resolution imaging and topography of boron nitride sheets produced by chemical exfoliation. *ACS Nano* **4,** 1299–1304 (2010).

205. Wang, Y. *et al.* Boron nitride nanosheets: large-scale exfoliation in methanesulfonic acid and their composites with polybenzimidazole. *J. Mater. Chem.* **21,** 11371 (2011).

206. Zeng, H. *et al.* 'White graphenes': Boron nitride nanoribbons via boron nitride nanotube unwrapping. *Nano Lett.* **10,** 5049–5055 (2010).

207. Erickson, K. J. *et al.* Longitudinal splitting of boron nitride nanotubes for the facile synthesis of high quality boron nitride nanoribbons. *Nano Lett.* **11,** 3221–3226 (2011).

208. Ding, X. *et al.* Direct growth of few layer graphene on hexagonal boron nitride by chemical vapor deposition. *Carbon N. Y.* **49,** 2522–2525 (2011).

209. Preobrajenski, A. B. *et al.* Influence of chemical interaction at the lattice-mismatched h-BN/Rh(111) and h-BN/Pt(111) interfaces on the overlayer morphology. *Phys. Rev. B* **75,** 245412 (2007).

210. Sutter, P. *et al.* Chemical vapor deposition and etching of high-quality monolayer hexagonal boron nitride films. *ACS Nano* **5,** 7303–7309 (2011).

211. Preobrajenski, a. B. *et al.* Monolayer of h-BN chemisorbed on Cu(111) and Ni(111): The role of the transition metal 3d states. *Surf. Sci.* **582,** 21–30 (2005).

212. Chatterjee, S. *et al.* Chemical vapor deposition of boron nitride nanosheets on metallic substrates via decaborane/ammonia reactions. *Chem. Mater.* **23,** 4414–4416 (2011).

213. Ismach, A. *et al.* Toward the controlled synthesis of hexagonal boron nitride films. *ACS Nano* **6,** 6378–85 (2012).

214. Suter, H. *et al.* Synthesis of one monolayer of hexagonal boron nitride on Ni (111) from B-trichloroborazine (ClBNH)3. *Chem. Mater.* **16,** 343–345 (2004).

215. Kim, K. K. *et al.* Synthesis of monolayer boron nitride on Cu foil using chemical vapor deposition. *Nano Lett.* **12,** 161–166 (2011).

216. Wang, L. *et al.* Monolayer hexagonal boron nitride films with large domain size and clean interface for enhancing the mobility of graphene-based field-effect transistors. *Adv. Mater.* **26,** 1559–1564 (2014).

217. Gao, Y. *et al.* Repeated and controlled growth of monolayer, bilayer and few-layer hexagonal boron nitride on Pt foils. *ACS Nano* **7,** 5199–5206 (2013).

218. Lee, K. H. *et al.* Large-scale synthesis of high-quality hexagonal boron nitride nanosheets for large-area graphene electronics. *Nano Lett.* **12,** 714–718 (2012).

219. Song, L. *et al.* Large scale growth and characterization of atomic hexagonal boron nitride layers. *Nano Lett.* **10,** 3209–15 (2010).

220. Guo, N. *et al.* Controllable growth of triangular hexagonal boron nitride domains on copper foils by an improved low-pressure chemical vapor deposition method. *Nanotechnology* **23,** 415605 (2012).

221. Kim, K. K. *et al.* Synthesis and characterization of hexagonal boron nitride film as a dielectric layer for graphene devices. *ACS Nano* **6,** 8583–8590 (2012).

222. Tay, R. Y. *et al.* Growth of large single-crystalline two-dimensional boron nitride hexagons on electropolished copper. *Nano Lett.* **14,** 839–846 (2014).

223. Khan, M. H. *et al.* Synthesis of large and few atomic layers of hexagonal boron nitride on melted copper. *Sci. Rep.* **5,** 7743 (2015).

224. Han, J. *et al.* Synthesis of wafer-scale hexagonal boron nitride monolayers free of aminoborane nanoparticles by chemical vapor deposition. *Nanotechnology* **25,** 145604 (2014).

225. Song, Y. *et al.* Triggering the atomic layers control of hexagonal boron nitride films. *Appl. Surf. Sci.* **313,** 647–653 (2014).

226. Liu, Z. *et al.* Ultrathin high-temperature oxidation-resistant coatings of hexagonal boron nitride. *Nat. Commun.* **4,** 2541 (2013).

227. Sainsbury, T. *et al.* Oxygen radical functionalization of boron nitride nanosheets. *J. Am. Chem. Soc.* **134,** 18758–18771 (2012).

228. Kim, G. *et al.* Growth of high-crystalline, single-layer hexagonal boron nitride on recyclable platinum foil. *Nano Lett.* **13,** 1834–1839 (2013).

229. Mitome, M. *et al.* Element discrimination in a hexagonal boron nitride nanosheet by aberration corrected transmission electron microscopy. *Ultramicroscopy* **122,** 6–11 (2012).

230. Jin, C. *et al.* Fabrication of a freestanding boron nitride single layer and its defect assignments. *Phys. Rev. Lett.* **102,** 195505 (2009).

231. Meyer, J. C. *et al.* Selective sputtering and atomic resolution imaging of atomically thin boron nitride membranes. *Nano Lett.* **9,** 2683–2689 (2009).

232. Kotakoski, J. *et al.* Electron knock-on damage in hexagonal boron nitride monolayers. *Phys. Rev. B* **82,** 113404 (2010).

233. Gibb, A. L. *et al.* Atomic resolution imaging of grain boundary defects in monolayer chemical vapor deposition-grown hexagonal boron nitride. *J. Am. Chem. Soc.* **135,** 6758–6761 (2013).

234. Liu, Y. *et al.* Dislocations and grain boundaries in two-dimensional boron nitride. *ACS Nano* **6,** 7053–7058 (2012).

235. Chen, W. *et al.* Electronic structure and reactivity of boron nitride nanoribbons with stone-wales defects. *J. Chem. Theory Comput.* **5,** 3088–3095 (2009).

236. Gao, J. *et al.* Reduced stability of copper interconnects due to wrinkles and steps on hexagonal boron nitride substrates. *Appl. Phys. Lett.* **105,** 123108 (2014).

237. Song, L. *et al.* Large scale growth and characterization of atomic hexagonal boron nitride layers. *Nano Lett.* **10,** 3209–3215 (2010).

238. Wang, Y. *et al.* Electrochemical delamination of CVD-grown graphene film: toward the recyclable use of copper catalyst. *ACS Nano* **5,** 9927–33 (2011).

239. Odlyzko, M. L. *et al.* Identifying hexagonal boron nitride monolayers by transmission electron microscopy. *Microsc. Microanal.* **18,** 558–67 (2012).

240. Qin, L. *et al.* Catalyst-free growth of mono- and few-atomic-layer boron nitride sheets by chemical vapor deposition. *Nanotechnology* **22,** 215602 (2011).

241. Tabor, D. *et al.* The direct neasurement of normal and retarded van der Waals Forces. *Proc. R. Soc. A Math. Phys. Eng. Sci.* **312,** 435–450 (1969).

242. Israelachvili, J. N. Thin film studies using multiple-beam interferometry. *J. Colloid Interface Sci.* **44,** 259–272 (1973).

243. Britton, J. *et al.* A graphene surface force balance. *Langmuir* **30,** 11485–11492 (2014).

244. Perkin, S. *et al.* Self-assembly in the electrical double layer of ionic liquids. *Chem. Commun. (Camb).* **47,** 6572–4 (2011).

245. Perkin, S. Ionic liquids in confined geometries. *Phys. Chem. Chem. Phys.* **14,** 5052–62 (2012).

246. Smith, A. M. *et al.* Monolayer to bilayer structural transition in confined pyrrolidinium-based ionic liquids. *J. Phys. Chem. Lett.* **4,** 378–382 (2013).

247. Segura, J. J. *et al.* Adsorbed and near surface structure of ionic liquids at a solid interface. *Phys. Chem. Chem. Phys.* **15,** 3320–8 (2013).

248. Bazant, M. Z. *et al.* Double layer in ionic liquids: overscreening versus crowding. *Phys. Rev. Lett.* **106,** 46102–4 (2011).

249. Israelachvili, J. N. *et al.* Measurement of van der Waals dispersion forces in the range 1.4 to 130 nm. *Nat. Phys. Sci.* **236,** 106 (1972).

250. Horn, R. G. *et al.* Direct measurement of structural forces between two surfaces in a nonpolar liquid. *J. Chem. Phys.* **75,** 1400–1411 (1981).

251. Pashley, R. M. DLVO and hydration forces between mica surfaces in Li+, Na+, K+ and Cs+ electrolyte solutions : a correlation of double-layer and hydration forces with surface cation exchange properties. *J. Colloid Interface Sci.* **83,** 531–546 (1981).

252. Pashley, R. M. Hydration forces between mica surfaces in aqueous electrolyte solutions. *J. Colloid Interface Sci.* **80,** 153–162 (1981).

253. Perkin, S. *et al.* Dynamic properties of confined hydration layers. *Faraday Discuss.* **141,** 399–413 (2009).

254. Klein, J. Forces between mica surfaces bearing layers of adsorbed polystyrene in cyclohexane. *Nature* **288,** 248–250 (1980).

255. Klein, J. *et al.* Reduction of frictional forces between solid surfaces bearing polymer brushes. *Nature* **370,** 634–636 (1994).

256. Horn, R. G. Direct Measurement of the force between two lipid bilayers and observation of their fusion. *Biochim. Biophys. Acta - Biomembr.* **778,** 224–228 (1984).

257. Israelachvili, J. *et al.* Recent advances in the surface forces apparatus (SFA) technique. *Reports Prog. Phys.* **73,** 036601 (2010).

258. Chai, L. *et al.* Large area, molecularly smooth (0.2 nm rms) gold films for surface forces and other studies. *Langmuir* **23,** 7777–7783 (2007).

259. Connor, J. N. *et al.* Measurement of aqueous film thickness between charged mercury and mica surfaces : a direct experimental probe of the Poisson - Boltzmann distribution. *Langmuir* **17,** 7194–7197 (2001).

260. Fréchette, J. *et al.* Double layer forces over large potential ranges as measured in an electrochemical surface forces apparatus. *Langmuir* **17,** 7620–7627 (2001).

261. Shrestha, B. R. *et al.* Angstrom-resolved real-time dissection of electrochemically active noble metal interfaces. *ACS Nano* **8,** 5979–5987 (2014).

262. Smith, C. P. *et al.* Ultrathin platinum films on mica and the measurement of forces at the platinum/water interface. *J. Phys. Chem.* **92,** 199–205 (1988).

263. Rafiee, J. *et al.* Wetting transparency of graphene. *Nat. Mater.* **11,** 217–22 (2012).

264. Novoselov, K. S. *et al.* Electric field effect in atomically thin carbon films. *Science* **306,** 666–9 (2004).

265. Howsare, C. a *et al.* Substrate considerations for graphene synthesis on thin copper films. *Nanotechnology* **23,** 135601 (2012).

266. Levendorf, M. P. *et al.* Transfer-free batch fabrication of single layer graphene transistors. *Nano Lett.* **9,** 4479–83 (2009).

267. Lee, Y.-H. *et al.* Scalable growth of free-standing graphene wafers with copper(Cu) catalyst on SiO2/Si substrate: Thermal conductivity of the wafers. *Appl. Phys. Lett.* **96,** 83101–3 (2010).

268. Escobar Galindo, R. *et al.* Protrusion formation and surface porosity development on thermally annealed helium implanted copper. *Nucl. Instruments Methods Phys. Res. Sect. B* **217,** 262–275 (2004).

269. Barlow, S. G. *et al.* Influence of time and temperature on reactions and transformations of muscovite mica. *Br. Ceram. Trans.* **98,** 122–126 (1999).

270. Guggenheim, S. *et al.* Muscovite dehydroxylation : high-temperature studies. *Am. Mineral.* **72,** 537–550 (1987).

271. Palmieri, V. Fundamentals of electrochemistry - The electrolytic polishing of metals: Application to copper and niobium. in *SRF Workshop* (2003).

272. Vlassiouk, I. *et al.* Large scale atmospheric pressure chemical vapor deposition of graphene. *Carbon N. Y.* **54,** 58–67 (2013).

273. Kim, H. *et al.* Activation energy paths for graphene nucleation and growth on Cu. *ACS Nano* **6,** 3614–23 (2012).

274. Senden, T. J. *et al.* Surface roughness of plasma-treated mica. *Langmuir* **8,** 733–735 (1992).

275. Chan, D. Y. C. *et al.* A simple algorithm for the calculation of the electrostatic repulsion between identical charged surfaces in electrolyte. *J. Colloid Interface Sci.* **77,** 283–285 (1980).

276. Kasuya, M. *et al.* Characterization of ferrocene modified electrode using electrochemical surface forces apparatus. *Langmuir* **30,** 7093–7097 (2014).

277. Klimchitskaya, G. *et al.* van der Waals and Casimir interactions between two graphene sheets. *Phys. Rev. B* **87,** 075439 (2013).

278. Klein, J. *et al.* Simple liquids confined to molecularly thin layers. I. Confinement-induced liquid-to-solid phase transitions. *J. Chem. Phys.* **108,** 6996–7009 (1998).

279. Quon, R. A. *et al.* High-precision automated measurement of surface separation for the surface force apparatus. *J. Colloid Interface Sci.* **171,** 474–482 (1995).

280. Fisher, L. R. *et al.* Direct experimental verification of the Kelvin equation for capillary condensation. *Nature* **277,** 548–549 (1979).

281. Wang, Z.-J. *et al.* Direct observation of graphene growth and associated copper substrate dynamics by in situ scanning electron microscopy. *ACS Nano* **9,** 1506–1519 (2015).

282. Li, Z. *et al.* Low-temperature growth of graphene by chemical vapor deposition using solid and liquid carbon sources. *ACS Nano* **5,** 3385–90 (2011).

283. Mun, J. H. *et al.* Wrinkle-free graphene with spatially uniform electrical properties grown on hot-pressed copper. *Nano Res.* **8,** 1075–1080 (2015).

284. Haigh, S. J. *et al.* Cross-sectional imaging of individual layers and buried interfaces of graphene-based heterostructures and superlattices. *Nat. Mater.* **11,** 764–767 (2012).

285. Geim, a K. *et al.* Van der Waals heterostructures. *Nature* **499,** 419–25 (2013).

286. Wang, H. *et al.* Graphene and graphene-like layered transition metal dichalcogenides in energy conversion and storage. *Small* **10,** 2165–2181 (2014).

287. Jariwala, D. *et al.* Emerging device applications for semiconducting two-dimensional transition metal dichalcogenides. *ACS Nano* **8,** 1102–1120 (2014).

288. Reckinger, N. *et al.* The influence of residual oxidizing impurities on the synthesis of graphene by atmospheric pressure chemical vapor deposition. *Carbon N. Y.* **63,** 84–91 (2013).

289. Tan, C. *et al.* Two-dimensional transition metal dichalcogenide nanosheet-based composites. *Chem. Soc. Rev.* **44,** 2713–2731 (2015).

290. Goodhew, P. J. *et al. Electron Microscopy and Analysis*. (2000).

291. Kalantar-zadeh, K. *et al. Nanotechnology-Enabled Sensors*. (2007).

292. Ferraro, J. *et al. Introduction to Raman Spectroscopy (Third Edition)*. (2003).

293. Sandeman, K. *et al.* www.doitpoms.ac.uk. *TLP: Raman Spectroscopy* (2014).

294. Haugstad, G. *Atomic Force Microscopy: Understanding Basic Modes and Advanced Applications*. (2012).

295. Myers, D. www.undergrad.research.ucsb.edu. *Atomic Force Microscope: A Tiny Record Player* (2014).

296. Ding, Y. www.nanoscience.gatech.edu. *Fundamental Theory of Transmission Electronic Microscopy* (2015).

"*Absolutely packed with fun-stuffed memories. But I'm off to bed now*."

–Bernard Black